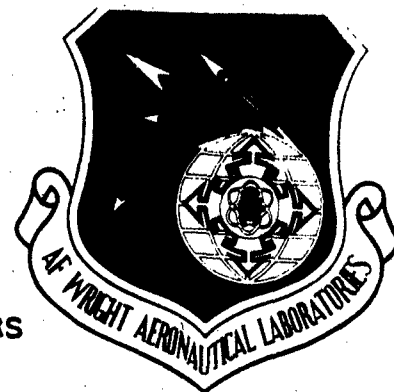MLBP

AFWAL-TR-84-4033
ADA145549

PHYSICAL-CHEMICAL PROPERTIES OF ARTICULATED RODLIKE POLYMERS

G. C. Berry
R. Furukawa
S. Mohan
C. Wei

Carnegie-Mellon University
4400 Fifth Avenue
Pittsburgh, PA   15213

April, 1984

Final Report for Period 1 March 1982 to 30 August 1983
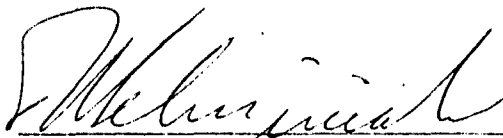
Best Available Copy

20040219056

NOTICE

When Government drawings, specifications, or other data are used for any purpose other than in connection with a definitely related Government procurement operation, the United States Government thereby incurs no responsibility nor any obligation whatsoever; and the fact that the Government may have formulated, furnished, or in any way supplied the said drawings, specifications, or other data, is not to be regarded by implication or otherwise as in any manner licensing the holder or any other person or corporation, or conveying any rights or permission to manufacture, use, or sell any patented invention that may in any way be related thereto.

This report has been reviewed by the Office of Public Affairs (ASD/PA) and is releasable to the National Technical Information Service (NTIS). At NTIS, it will be available to the general public, including foreign nations.

This technical report has been reviewed and is approved for publication.

THADDEUS E. HELMINIAK
Project Scientist

R. L. VAN DEUSEN
Chief, Polymer Branch

FOR THE COMMANDER

FRANKLIN D. CHERRY, Chief
Nonmetallic Materials Division

REPORT DOCUMENTATION PAGE	READ INSTRUCTIONS BEFORE COMPLETING FORM

1. REPORT NUMBER AFWAL-TR 84-4033	2. GOVT ACCESSION NO.	3. RECIPIENT'S CATALOG NUMBER

4. TITLE (and Subtitle) PHYSICAL-CHEMICAL PROPERTIES OF ARTICULATED RODLIKE POLYMERS	5. TYPE OF REPORT & PERIOD COVERED Final Report March 1982--August 1983
	6. PERFORMING ORG. REPORT NUMBER

7. AUTHOR(s) G. C. Berry S. Mohan R. Furukawa C. Wei	8. CONTRACT OR GRANT NUMBER(s) F33615-81K-5043

9. PERFORMING ORGANIZATION NAME AND ADDRESS Carnegie-Mellon University 5000 Forbes Avenue Pittsburgh, PA 15213	10. PROGRAM ELEMENT, PROJECT, TASK AREA & WORK UNIT NUMBERS 24190420

11. CONTROLLING OFFICE NAME AND ADDRESS Materials Laboratory (AFWAL/MLBP) Air Force Wright Aeronautical Labs (AFSC) Wright-Patterson AFB, Ohio 45433	12. REPORT DATE April 1984
	13. NUMBER OF PAGES 330

14. MONITORING AGENCY NAME & ADDRESS(if different from Controlling Office)	15. SECURITY CLASS. (of this report) UNCLASSIFIED
	15a. DECLASSIFICATION/DOWNGRADING SCHEDULE N/A

16. DISTRIBUTION STATEMENT (of this Report)

Approved for Public Release, Distribution Unlimited

17. DISTRIBUTION STATEMENT (of the abstract entered in Block 20, if different from Report)

18. SUPPLEMENTARY NOTES

19. KEY WORDS (Continue on reverse side if necessary and identify by block number)

20. ABSTRACT (Continue on reverse side if necessary and identify by block number)

    Rheological and rheo-optical studies are reported for isotropic solution of the mesogenic rodlike poly(1,4-phenylene-2,6-benzobisthiazole), PBT. Several PBT samples are used, with average contour lengths from 95 to 135 nm. Concentrations were varied over a range just below the concentration c_c for the formation of an ordered (nematic) state. The predictions of a single-integral constitutive equation of the BKZ-type utilizing experimental estimates of the distribution of discrete relaxation time is compared with

DD $_{1 \text{ JAN } 73}^{\text{FORM}}$ 1473   EDITION OF 1 NOV 65 IS OBSOLETE

experimental data on the steady-state viscosity $\eta_{\varkappa}$, the recoverable compliance function $R_{\varkappa}$ and the steady-state flow birefringence as functions of the shear rate $\varkappa$, with satisfactory results. The relaxation of the shear stress and the flow birefringence on cessation of steady-state flow at shear rate $\varkappa$ are also compared with the single-integral constitutive, and it is found that in the nonlinear response range the data can be superposed over a wide range in $\varkappa$. The overall behavior is qualitatively similar to that for flexible coil chains, which can also be fitted by the single-integral constitutive equation over similar ranges of $\eta_0 R_0 \varkappa$, with η_0 and R_0 the limiting values of $\eta_{\varkappa}$ and $R_{\varkappa}$ for small $\varkappa$. Of course, the dependence of η_0 and R_0 on concentration and molecular weight differs markedly for rodlike and flexible chain polymers.

Total intensity and photon correlation light scattering data are reported for dilute solutions of several mesogenic rodlike copolymers. The latter have a preponderance of rodlike monomers together with a small fraction of a flexible chain-like monomer. The results are discussed in terms of chain conformations and tendency for interchain association. It is found that the copolymers studied do not adopt a rodlike conformation in dilute solution, but do exhibit varying degrees of aggregation. The solutions may be brought to a state of phase separation by the addition of a low molecular weight salt to the methane sulfonic acid solution. Prior to phase separation the depolarized scattering increases sharply, along with the appearance of slowly diffusing species in the photon correlation light scattering. This behavior indicates the existence of some degree of flocculation prior to phase separation. These flocs may be metastable, and appear to be organized with the rodlike chain elements in partial parallel array. This tendency may have importance in the coagulation step used in the solution processing of more concentrated solutions.

Foreword

This report on the "Physical-Chemical Properties of Articulated Rodlike Polymers" was prepard in the Department of Chemistry, Carnegie-Mellon University, 4400 Fifth Avenue, Pittsburgh, Pennsylvania 15213, under Contract F33615-81K-5043 (Project No. 24190420). It was administered under the direction of the Materials Laboratory, Air Force Wright Aeronautical Laboratories, Wright-Patterson Air Force Base, Ohio, Dr. T. E. Helminiak.

The report covers work conducted from I March 1982 to 30 August 1983. It was submitted in January, 1984. Authors are G. C. Berry, Principal Investigator, R. Furukawa, S. Mohan and C. Wei.

Table of Contents

List of Figures

List of Tables

1. PART I

1.1 INTRODUCTION

1.1.1 Summary

The properties of PBT, 'articulated' copolymers of PBT (SPBT), and PBO (SPBO), and copolymers of PBT and PBO in dilute solutions are discussed in the following. Light scattering methods are used to determine the molecular weight M_w, the second virial coefficient A_2, the root-mean-square radius of gyration R_G, and a hydrodynamic radius $R_H = \Xi/6\pi\nu_s$, with Ξ the molecular friction factor. Photon correlation scattering is used to determine the other parameters. The anisotropic light scattering is used to determine an optical molecular anisotropy δ which provides information on the rodlike nature of the chain. Detailed expressions for these quantities are given in the next section.

Several salient features emerge from this study:

1. The data on δ show that the articulated copolymers are not rodlike chains in dilute solution in methane sulfonic acid (MSA). Data on R_G and R_H suggest that these adopt a coil-like conformation.

2. The addition of salt to solutions of PBT or articulated PBT's causes pronounced enhancement of the anisotropic light scattering. With PBT, this behavior is interpreted in terms of aggregated flocs, with an appreciable extent of parallelism between the rodlike chains. With the articulated PBT's, the anisotropic scattering is attributed to increased rodlike conformation of chains held in aggregated supramolecular structures.

3. All of the solutions studied exhibited some degree of intermolecular association in MSA; this behavior was particularly pronounced with the PBT-PBO copolymers

The behavior of the PBT and articulated PBT copolymers on the addition of salt is intriguinh, and suggest that aggregation phenomena may be expected in general as the solution properties are changed in the direction toward decreasing A_2. The formation of such aggregates may play a dominant role in the properties of a solid of these polymers formed by coagulation from solution, as is the usual solution processing methods used with PBT.

1.1.2 Theoretical Relations

Polarized and depolarized absolute intensity and polarized dynamic light scattering are used in this study. The analysis employs the intensity correlation function $g^{(2)}(\tau,\Delta\tau)$ and the second factorial moment $n^{(2)}(\Delta\tau)$, both determined in the self-beating photon correlation mode . Here $\Delta\tau$ is the sampling interval and τ is the correlation time. For monodispersed solutes[1-4]

$$g^{(2)}(\tau,\Delta\tau) -1=f(A)q(2\gamma)\left| g^{(1)}(\tau,\Delta\tau)\right|^2 \tag{1.1}$$

$$n^{(2)}(\tau\Delta\tau)- 1 = f(A)h(2\gamma) \tag{1.2}$$

where $f(A)$ is a coherence factor fixed by the optical system (typically $0.1< f(A) <0.7$), $\gamma= \Delta\tau/\tau_h$ where τ_h is the coherence time at scattering angle θ with the wave vector modulus $q=(4\pi/\lambda)\sin\theta/2$, and

$$q(2\gamma) = \left(\frac{\sinh\gamma}{\gamma} \right)^2 \tag{1.3}$$

$$h(\gamma) = \frac{2}{\gamma} - \frac{2}{\gamma^2}(1 - \exp(-\gamma)) \tag{1.4}$$

In obtaining Eqns. 3 and 4, the magnitude $\left| g^{(1)}(\tau,\Delta,\tau)\right|$ the electric field correlation function has been set equal to $\exp(-\gamma\tau/\Delta\tau)$; this approximation will used throughout the following. For a collection comprising components characterized by γ_i, each contributing a fraction r_i of the scattered light,[5]

$$g^{(2)}(\tau,\Delta\tau)- 1 = f(A) \sum\sum_{i\,j}r_i r_j q(\gamma_i+\gamma_j)\tau/\Delta\tau \tag{1.5}$$

$$n^{(2)}(\Delta\tau) - 1 =f(A) \sum\sum_{i\,j}r_i r_j h(\gamma_i +\gamma_j) \tag{1.6}$$

2

With the neglect of $q(\gamma_i + \gamma_j)$ which is essentially unity unless the γ_i are very large, eq. 5 can be written in the more convenient form

$$[g^{(2)}(\tau,\Delta\tau)-1]^{1/2} = f^{1/2}(A)\Sigma_i r_i \exp(-\gamma_i \tau/\Delta\tau) \tag{1.7}$$

for the analysis of data to obtain r_i and γ_i. If the solution comprises unassociated and aggregated components, it may appear to be a quasi-multiple component mixture since the γ_i for these components can be expected to differ significantly. In this case, simple methods of data analysis may be used to estimate r_1, γ_i, r_2, γ_2, r_3, γ_3, etc. for the "components". Sophisticated methods (eg., see ref 2)) have been proposed to deal with more complex situations. In general, if the γ_i are closely spaced and numerous (as with a distribution of chain lengths) estimation of the r_i and γ_i set will be imprecise and may not be unique since the problem is ill posed.

The r_i are related to integrated scattered intensity. For vertically polarized scattering with vertically polarized incident light r_i is determined by the Rayleigh ratio $\mathbb{R}_{Vv,i}$ for component i at concentration c_i, divided by the total Rayleigh ratio $\mathbb{R}_{Vv,i}$ ratio[5]:

$$r_i = \mathbb{R}_{Vv,i}(q,c)/\mathbb{R}_{Vv}(q,c) \tag{1.8}$$

$$(Kc_i/\mathbb{R}_{Vv,i})_0^{1/2} = (Kc_i/\mathbb{R}_0)^{1/2}\left[1+\frac{A_{2,i}M_i}{(1+(4/5)\delta_i^2)}\, c_i + ...\right] \tag{1.9}$$

$$(Kc_i/\mathbb{R}_{Vv,i}^0) = M_i^{-1}(1+(4/5)\delta_i^2)^{-1}(1+\frac{1}{3} J(\delta_i)R_{G,i}^2 q^2+...) \tag{1.10}$$

with δ the molecular optical anisotropy, A_2 the second virial coefficient , M_w the weight average molecular weight, superscript and subscript 0 denoting quantities at infinite dilution and zero angle, respectively , and

3

$$J(\delta) = [1 - (4/5) f_1 \delta + (4/7)(f_2 \delta)^2]/[1 + (4/5)\delta^2] \tag{1.11}$$

The depolarized scattering $\mathbb{R}_{Hv}(h,c)$ is given by [6]

$$(Kc_i/\mathbb{R}_{Hv,i0}) = (Kc_i/\mathbb{R}^0_{Hv,i}0)_0 + O(c^2) \tag{1.12}$$

$$(Kc_i/\mathbb{R}_{Hv,i})_0 = (5/3M_i\delta_i^2)[1 + (3/7)f_3^2 R_{Gi}^2 q^2 + \ldots] \tag{1.13}$$

The coefficients $f_1, f_2,$ and f_3 are essentially unity for rodlike chains.

These expressions are valid for two types of chain models with anisotropic segments, the freely rotating chain and the worm like chain. The chain elements are intrinsically anisotropic; that is δ_o is defined in terms of the principal polarizabilities of the scattering element

$$\delta_o^2 = \frac{(\alpha_1 - \alpha_2)^2 + (\alpha_1 - \alpha_3)^2 + (\alpha_2 - \alpha_3)^2}{2(\alpha_1 + \alpha_2 + \alpha_3)^2}$$

If the polarizability is cylindrically symmetric with $\alpha_1 = \alpha$ and $\alpha_2 = \alpha_3 = \beta$ then

$$\delta_o = \frac{\alpha - \beta}{\alpha + 2\beta}$$

and $-1/2 < \delta_o < 1$. The overall anisotropy δ for a polymer chain can be defined as the average of δ_o for each chain element over all chain conformations.

The first model is a chain with free rotation about each of the N bonds of length l, anisotropy δ_o, and valence angle $\pi - \alpha$. The second model is a worm like chain with n equivalent segments of length b, anisotropy α and a persistence length $\rho = b/2\lambda$, where λ is a parameter between zero and unity. As λ goes to zero and unity, the

worm like chain behaves as a rodlike and random-coil chain respectively. The overall chain anisotropy δ has been calculated with both models with the result [6]

$$\delta^2 = \frac{\delta_o^2}{N} \left(\frac{1+b}{1-b} - \frac{2b(1-b)^N}{N(1-b)^2} \right)$$

where $b = \dfrac{3a^2-1}{2}$ and $a = \cos\alpha$ \hfill (1.14)

for the chain with free rotation and [6]

$$\delta^2 = \delta_o^2 (2/3Z)\{1-(3Z)^{-1}[1-\exp(-3Z)]\}$$

where $Z = 2\lambda n = L/\rho$ for the worm like chain, with $L = nb$ the contour length of the chain. The ratio $(\delta/\delta_o)^2$ is shown as a function of $N(1-a)/a$ in figure 1 for several values of α. For the freely rotating chain, if $Z = N(1-a)/a$, figure 1 represents equation (1.14) well.

For rodlike chains ($L/\rho = 0$), segments along the contour length are highly correlated. Recalling δ_o^2 is an average over all chain conformations and in a rod there is only one conformation, δ will equal δ_o. The high value of the optical anisotropy will give rise to a large Hv scattering component if the molecular weight is large enough. For coil like molecules $(L/\rho) \sim \infty$ δ^2 is averaged over all possible chain configurations which is a relationship proportional to N^{-1}. It is expected introduction of a few flexible segments will decrease the overall anisotropy of the molecule and the intensity of the Hv component of the scattered light.

Several estimates of the average contour length of a rodlike chain can be obtained through the used of the relations [7]

$$R_G^2 = L^2 \, W(L/\rho)/12 \tag{1.15}$$

$$R_H = \Xi^0/6\pi\eta_s = L/2 \, H(L/\rho, L/d_H) \tag{1.16}$$

$$M_L = M/L \tag{1.17}$$

Here $\lim W(L/\rho) = 1 - \dfrac{1}{5}\left(\dfrac{L}{\rho}\right) + \dfrac{1}{30}\left(\dfrac{L}{\rho}\right)^2 - \dots$

$\lim\limits_{(L/\rho)<2} H\left(\dfrac{L}{\rho}, \dfrac{L}{d_H}\right) = H\dfrac{L}{d_H} \sim 1.887\left(\dfrac{L}{d_H}\right)^{0.2}$

$F\left(\dfrac{L}{d_H}\right) \sim 0.745 H\left(\dfrac{L}{d_H}\right)$ where the power law approximations are useful for L/d_H in the range 30 to 3,000. Estimates of the contour lengths may be calculated as [8]

$$L_{\Xi} = \left\{ \dfrac{H\Xi^0}{3\pi\epsilon L^{0.2}} \right\}^{1.25} \tag{1.18}$$

$$L_{G,H} = 28\left(\dfrac{W\partial \ln(c/R_{Hv})^0}{dh^2} \right)^{1/2} \tag{1.19}$$

$$L_{G,V} = 36 J(\delta)\left(\dfrac{W\partial \ln(c/R_{Vv})^0}{\partial h^2} \right)^{1/2} \tag{1.20}$$

$$L_H = \left(\dfrac{5(R_{Hv}(0)/Kc)^0}{3\delta^2 M_L} \right) \tag{1.21}$$

$$L_V = \dfrac{(R_{Vv}(0)/Kc)^0}{(1+4/5\delta^2)M_L} \tag{1.22}$$

where $J(\delta) = (1 + 4/5 f_1 \delta + 4/7 f_2 \delta^2)$. In the rodlike limit, L becomes the rod length when L/ρ is small, f_i are unity, and the functions F, W, and H can be calculated by the above approximations.

For a polydisperse sample, the following provide representations of well-defined averages of L:

6

$$L_W = L_V = L_H \sim L_Z$$

$$(L_Z L_{Z+1})^{1/2} = L_{G,H} = L_{G,V}$$

Data on $n^{(2)}(\Delta\tau)$ obtained in self-beating experiments can also be used to determine a set of average coherence times of the form[5]

$$\langle \tau_h^{(s)} \rangle \equiv 2\Delta\tau \left\{ \Sigma\Sigma r_i r_j (\gamma_i + \gamma_j)^{-s} \right\}^{1/s} \tag{1.23}$$

Thus, $\langle \tau_h^{(1)} \rangle$ is equal to the value $\Delta\tau_N$ of $\Delta\tau$ for the crossover of $n^{(2)}(\Delta\tau) - 1$ from its limiting value f(A) at small $\Delta\tau$ to the function f(A) $\Delta\tau_G/\Delta\tau$ obtained at large $\Delta\tau$. Values of $\langle \tau_h^{(s)} \rangle$ with $-s = 1,2$, etc. are calculated from the cumulants K_γ of ln $|g^{(1)}(\gamma)|$ given by $(-1)^\gamma (\gamma!)^{-1} \partial \ln|g^{(1)}(\tau)|/\partial\tau$, so that $\langle \tau_h^{(-1)} \rangle = K_1^{-1}$ and $\langle \tau_h^{(-2)} \rangle = [K_2 + k_1^2]^{-1/2}$ in these expressions, q(2γ) is taken to be unity. The latter average coherence times may be put in the form

$$\langle \tau_h^{(-1)} \rangle = \Delta\tau \{ \Sigma r_i \gamma_i \}^{-1} \tag{1.24}$$

$$\langle \tau_h^{(-2)} \rangle = \Delta\tau \{ \tfrac{1}{2}\Sigma r_i \gamma_i^2 + \tfrac{1}{2}(\Sigma r_i \gamma_i)^2 \}^{1/2} \tag{1.25}$$

1.2 EXPERIMENTAL

1.2.1 Materials

The polymer samples investigated were subjected to different post-polymerization histories in addition to different methods of solution preparation. The monomers were polymerized in PPA (polyphosphoric acid), isolated by precipitation into water, dried, dissolved in MSA (methane sulfonic acid) and reprecipitated into water. Polymers have been studied after polymerization as a PPA solution, and dried after

each subsequent precitation. It was previously found the precipitation from MSA causes the polymer to be more aggregated. Polymer solutions were also subject to a combination of precentrifugation, sonication, and in some cases heating. For a few samples, the effect of added salt and the method of adding the salt were investigated. For purposes of clarity, Table 18 and 17 contains a summary of samples, sample composition, sample preparation, and histories.

For all polymer samples, the solutions were examined before and after centrifugation. The dynamic light scattering data were measured in the self-beating mode at 514.5 nm. The absolute intensity light scattering (AILS) were obtained at 514.5 nm or at 633 nm. Fluorescence and absorption corrections to the AILS data will be discussed below.

1.2.2 Light Scattering Apparatus

The light scattering apparatus is shown schematically in Figure 2. It is equipped with Birnboim Digital Correlation used as a data acquisition and processing system, DAPS, by Science Research Systems of Troy (Model DAS 6). Other components include an argon-ion laser with etalon (Lexel Model 85), a He-Ne laser (Spectra-Physics Model 120), a photomultiplier with an S-2 photocathode (ITT, FW-130-RF) photomultiplier, housing (Products for Research, Inc.) and a discriminator amplifier (SSR Instruments Co.) Optical components allow for beam alignment, rotation of the incident beam (one-half wave plate), beam spreading for total intensity measurements, transfer of an auxiliary light beam to the photomultiplier with an optical fiber (Oriel Corp., Model 7167), definition of the scattering volume by slits S_H and S_V, collimation of the accepted rays by pinhole P, selection of the wavelength of the light impinging on the photomultiplier (by use of interference filters for fixed or variable band pass, e.g., Oriel Corp., Model 7155, or fixed band rejection, to eliminate light with wavelength of the incident beam); and an analyzer to select the polarization of the scattered beam.

In the mode used here, the DAPS, which is based on a Texas Instruments 980B computer, acquires pulses in each of 4,736 intervals of length $\Delta\tau$, with a deadtime of 25 ns included in each interval; the number of pulses per interval can be large as 2^{15}. The full auto-correlation function $G^{(2)}$ is computed over the primary data base of 2^{12} intervals to give a correlation with up to 512 points spaced at intervals of $\Delta\tau$. Usually, a 64 point correlation was used in this work. The first point of a correlation can be shifted up to 128. After each acquisition cycle, the unnormalized correlation $G^{(2)}(k\Delta\tau)$ and the mean-count rate are calculated as

$$G^{(2)}(k\Delta\tau) = \frac{1}{T} \sum_i n_i n_{i+k} \tag{1.26}$$

$$\langle n \rangle = \left(\frac{1}{T} \sum_{i=1}^{T} n_i \right) \tag{1.27}$$

where $T = 2^{12}$ and $k = 0,1,2,...$ The acquisition and calculation cycle is repeated M times, and averaged in the form

$$G^{(2)}(k\Delta\tau) = \frac{1}{M} \sum_{j=1}^{M} G_j^{(2)}(k\Delta\tau) \tag{1.28}$$

$$\langle n \rangle^2 = \frac{1}{M} \sum_{j=1}^{M} \langle n \rangle_j^2 \tag{1.29}$$

and the unnormalized factorial moments are calculated over the data base of TM intervals as

TM

9

$$N^{(s)} = \frac{1}{TM} \sum_{i=1} \{n(n-1)...(n-s+1)\}_i \qquad (1.30)$$

$$\langle n \rangle = N^{(1)} \qquad (1.31)$$

The distribution $P(n,\gamma)$ of photon pulses per interval is also computed over the data base of TM intervals. If $P(n,\gamma)$ is the same for each of the M data sets, then $\langle \langle n \rangle^2 \rangle$ and $(N^{(1)})^2$ are equal. If the $P(n,\gamma)$ differ (e.g., because of scattering 'dust' in a few of the M sets), then $\langle \langle n \rangle^2 \rangle \geq (N^{(1)})^2$.

Further data processing includes calculations of $g^{(2)}(\tau)$ and $n^{(s)}$. For the former $\langle \langle n \rangle^2 \rangle$ is used to give

$$g^{(2)}(k\Delta\tau) = G^{(2)}(k\Delta\tau)/\langle \langle n \rangle^2 \rangle \quad ; \quad k > 0 \qquad (1.32)$$

$$g^{(2)}(0) = \frac{G^{(2)}(0) - \langle n \rangle}{\langle \langle n \rangle \rangle^2} \qquad (1.33)$$

It may be remarked that the use of $\langle \langle n \rangle^2 \rangle$ rather than $(N^{(1)})^2$ or $G_M^{(2)}(\infty)$ to normalize $G^{(2)}(\tau)$ is not trivial for realistic data, owing to the effects of noise and drift, etc. Values of $g^{(2)}(\tau)$ calculated with Eqn. (1.32) exhibit the expected property that $g^{(2)}(\infty)$ tends to unity, even under conditions for which $\langle \langle n \rangle^2 \rangle > (N^{(1)})^2$. An estimate for K_1 is calculated by least-squares fit of $\ln(g^{(2)}(\tau)-1)$ versus τ, using correlation points for k from 1 to 7. with the algorithm in use in the DAPS, the time $\Delta\tau$ per correlation point required to compute $G^{(2)}(\Delta\tau)$ is fixed (80 ms) for $\langle n \rangle$ larger than 2, but decreases with increasing $\langle n \rangle$ for smaller $\langle n \rangle$. Consequently, the efficiency $(1+C\Delta t/2^{12}\Delta\tau)^{-1}$ varies with $\Delta\tau$, Δn and the number of correlation points C, but

generally ranges from about 0.2 to nearly unity, with values being about 0.8 or greater for typical experiments.

The normalized factorial moments are calculated as

$$n^{(s)} = N^{(s)}/(N^{(1)})^s$$

Rigorous expressions for the photon distribution function $P(n,\Delta\tau)$ have only been obtained for the limiting cases at $\Delta\tau = 0$ and at $\Delta\tau = \infty$, where equations have been derived for both self-beating and reference-beam methods.[1,9,10] However, usually, $P(n;\Delta\tau)$ for self-beating measurements at arbitrary sampling interval is closely given by the approximate two parameter function.[REF 11]

$$P(n,\Delta\tau) = \frac{\Gamma(n+m)}{n!\Gamma(m)} \left(1 + \frac{\langle n \rangle}{m}\right)^{-m} \left(1 + \frac{m}{\langle n \rangle}\right)^{-n} \tag{1.34}$$

$$m = [n^{(2)}(\Delta\tau)-1]^{-1} \tag{1.35}$$

so that

$$n^{(s)} = \frac{\Gamma(m+s)}{\Gamma(s)m^s} \tag{1.36}$$

Examples of comparison of Eqn. (1.34) with experimental $P(n,\Delta\tau)$ are given in Figure 3 for several values of $\Delta\tau/\tau_h$. Distortion of $P(n,\Delta\tau)$ by excessive scattering during a few of the sampling intervals can result in values of $n^{(s)}$ ($s \geq 3$) far larger than the estimate given by Eqn. (1.36) with m calculated from $n^{(2)}$, providing a test for the internal consistency of the data. Another test is provided by comparison $g^{(2)}(0)$ with

11

$n^{(1)}$. These should be equal, but may differ if $P(n,\Delta\tau)$ varies substantially among the M data sets.

Other sources of experimental errors should also be taken into account. The experimental $P(n,\Delta\tau)$ is truncated by the digital nature of experiments at photon number n_m such that $TM\langle n\rangle\, P(n_m;\Delta\tau) < 1$. The experimental estimator $\hat{n}^{(s)}$ to $n^{(s)}$ is given by

$$\hat{n}^{(s)} = n^{(s)}\left[1 - \left(\frac{\langle n\rangle}{m+\langle n\rangle}\right)^{n_m-s+1}\left(n_m-s+j\right)\sum_{j=0}^{m+s-1}\left(\frac{m}{m+\langle n\rangle}\right)\right] \qquad (1.37)$$

using the approximate photon distribution function Eqn. (1.34) (with integer m). The photon number η_m is determined by

$$\frac{TM\langle n\rangle^{\eta_m}}{(1+\langle n\rangle)^{1+\eta_m}} \leq 1 \qquad (1.38)$$

for small $\Delta\tau$, which is the only case for which the correction is important. Thus, the correction terms in Eqn. (1.37) depend on $\langle n\rangle$ and M. They can be made sufficiently small for $n^{(2)}$ by setting the optimum conditions of data acquisition: e.g., large M or small $\langle n\rangle$.

When the average photon count rate $\langle n\rangle$ is small, contribution of dark counts from the photomultiplier to $n^{(2)}(\Delta\tau)$ and $g^{(2)}(\tau)$ becomes significant. The experimental estimators are given by

$$\hat{n}^{(2)}(\Delta\tau)-1 = [n^{(2)}(\Delta\tau)-1](1-\delta)^2+[n_d^{(2)}(\Delta\tau)-1]\delta^2 \qquad (1.39)$$

$$\hat{g}^{(2)}(\tau)-1 = [g^{(2)}(\tau)-1](1-\delta)^2+[g_d^{(2)}(\tau)-1]\delta^2 \qquad (1.40)$$

where $n_d^{(2)}$ and $g_d^{(2)}$ are the second factorial moment and correlation functions for dark counts, and δ is the fraction of dark counts in the total counts registered. Usually, $n_d^{(2)} - 1$ and $g_d^{(2)} - 1$ are not very large in the range of time scale corresponding to macromolecular diffusion. The correction terms in Eqns. (1.39) and 24, therefore, only increase the experimental values of $\hat{n}^{(2)}$ and $\hat{g}^{(2)}$ to larger values, but do not affect evaluation of $\langle \tau^{(h)} \rangle_N$ or $\langle \tau^{(h)} \rangle_G$. On the other hand, distortions by dead time of photomultiplier or computer become large at high counting rate of photons. A correction for this effect is already given in the literature.[12]

The function f(A) is fixed by the detector optics. With the optical system used in this study, f(A) is principally determined by the pinhole P and is less dependent on slits S_H and S_V. Pinholes from 100 to 1000 μm diameter are used. Typical data for f(A) as a function of the pinhole diameter are given in Figure 4 along with a theoretical estimate for f(A).[12]

1.2.3 Light Scattering Methods

In this study, all data were taken in the self-beating mode and in V_v mode (vertically polarized incident and vertically polarized scattering) at 514 nm. As discussed above, estimations for $g^{(2)}(\tau, \Delta\tau)$, $g^{(2)}(\Delta\tau, \Delta\tau)$, and $n^{(s)}(\Delta\tau)$ (s = 1-5) are calculated for each data set as a function of scattering angle θ, usually over the range 30-135 deg. In most cases, the number of M of post-autocorrelation averages was adjusted so that the total number of photon counts TM$\langle n \rangle$ was about 10^6.

In the absolute intensity experiments, the incident beam is modulated by a rotary chopper. This eliminates the count rate $\langle n \rangle_D$ due to thermionic emission, room light, electrical noise etc. The count rate $\langle n \rangle_s$ of the scattered light is determined from $G^2(\tau)$ of the modulated scattered light. Two types of rotary choppers were employed in these studies. The first consists of equal intervals of open and closed slots produces an incident beam with a square wave modulation. The count rate $\langle n \rangle_s$ determined from $G^2(\tau)$ which a triangular function with period $2\tau_s$ and peak-to-peak

amplitude $\frac{1}{2}\langle n\rangle_s^2$. The slope $\partial G^2(\tau)/\partial \tau = \langle n\rangle_s^2/2\tau_s$ determined in the range $2.5\tau_2 < \tau < 3\tau_s$ is used to compute $\langle n\rangle_s$. The second type of rotary chopper employed allowed the intensity of the incident beam to be monitored as well as the scattered light. The resultant function $G^2(\tau)$ is no longer a simple triangular function but $\langle n\rangle_i$ can nonetheless be calculated from $G^2(\tau)$. The count rate of the scattered light is determined as the ratio of $\langle n\rangle_s/\langle n\rangle_i$. Imperfections in the chopper, the finite thickness of the scattering volume, etc. produce some rounding at the extremes of the function $G^2(\tau)$ but these effects do not interfere in the evaluation of $\partial G^2(\tau)/\partial \tau$ or $\langle n\rangle_s/\langle n\rangle_i$.

The DAPS provides for automatic scan through θ and $\Delta\tau$ ranges to facilitate these measurements. The light scattering cells are immersed in a fluid with refractive index close to that of the scattered fluid. The immersion fluid is held in a cylindrical cell with flat entrance and exit windows (Brice-Phoenix, cylindrical light scattering cell) using teflon rings at the top and bottom of the light scattering cell to position it. The cylindrical cell is held in a concentric cylinder thermostat, with incident and scattered rays passing through small (6 mm dia.) ports.

Absolute Intensity Light Scattering (AILS) experiments were performed with a digital light scattering instrument with a Lexel model 85 laser tuned to the 514.5 nm line or with a Spectra-Physics model 120 laser at 632.8 nm. The intensities of the scattered and fluorescent light were measured as described above. The solutions were filtered through fine or ultra-fine sintered glass filters or teflon filters (1-3 μm) into cells of the Dandliker-Kraut design[13]. The solutions were degassed once and immediately flame sealed under vacuum (10^{-4} Torr).

The polymer solutions were all colored and absorbed light at the incident scattering wavelength even though the absorbance maxima were 440 nm to 450 nm. The elastic scattering of interest was isolated from the inelastic scattering (fluorescence) by placing a filter with a narrow wavelength band (10 nm at half peak height) before the

detector. The determination of the fluorescence will be discussed below. The excess Rayleigh ratio was calculated from (for either R_{Vv} or R_{Hv})

$$R(\theta) = k\{\mu[I(\theta) - I^{fl}(\theta)] - I^{o}(\theta)\}$$

where $I(\theta) \sin \theta$ is the observed intensity at angle θ with vertically polarized incident and scattered light, $I\theta$ is the estimated fluorescence intensity at angle θ, I^{o} is the solvent intensity at $\theta = 90^{o}$, and k is an instrument constant. The solvent scattering contribution to the Hv component was zero. The correction for the attenuation of the scattered light is given by μ

$$\mu = \exp(0.2303 \, \ell \, A_{\lambda,xs})$$

where $A_{\lambda,xs}$ is a absorbance at the incident wavelength in a 1 cm pathlength cell and ℓ is the pathlength of scattering cell, estimated as 14 mm.

For molecules such as rods, helices, or any extended chain with an asymmetric polarizability tensor, a depolarized scattering component can be observed. For molecules with a significant amount of depolarized scattering, both the polarized (Vv) and depolarized (Hv) scattering components of AILS must be measured to obtain parameters such as the molecular weight and radius of gyration. The polarizer was aligned by locating the minimum scattered intensity from a working standard of a low molecular weight (51,000 dalton) polystyrene with a narrow molecular weight distribution (Pressure Chemical Company) dissolved in either toluene or methyl ethyl ketone (MEK). The polarization of the incident was then changed from H to V by rotation of a 1/4 wave plate. The analyzer was aligned by locating the minimum scattered intensity from the polystyrene standard with the incident beam vertically polarized. The depolarized component of AILS was then measured. The polarizer

which consists of a calcite prism was then rotated 90° to allow the detection of the vertical component of light, fluorescent and scattered.

All polymer solutions studied were fluorescent over a large wavelength range which included the wavelength of the scattered light. To ascertain the magnitude of the fluorescence contribution to the intensity of the scattered light, an emission spectrum was measured as a function of wavelength. A variable monochromator was placed before the detector and the intensity was measured a a function of the monochromator setting. The monochromator was calibrated by locating the maximum scattered intensity from a working standard of polystyrene in methyl ethyl ketone at several laser wavelengths with a narrow wavelength band filter in series. A typical emission spectrum obtained in the Vv mode is shown in figure 5. The fluorescence peak is extrapolated through the scattered light peak as indicated by the dotted line in figure 5 The fluorescence contribution is related to the scattered light by the ratio of intensities at a wavelength slightly removed from the scattered light to the extrapolated value of the fluorescence at the scattering wavelength. When the excitation wavelength is 514 nm, a narrow band filter centered at 546 nm is used to measure the fluorescence contribution. If the excitation wavelength is 633 nm, a filter centered at 650 nm was used. The intensity measured at either 546 nm or 650 nm is multiplied by the ratio obtained in the emission spectrum and subtracted from the scattered intensity which was obtained by placing a narrow band filter before the detector. No attempt was made to correct for the wavelength dispersion of the monochromator,band filters or the wavelength dependence of detector. In a few cases, the fluorescence contribution was estimated as the intensity measured with a narrow band filter centered at 620 nm.

The emission spectra obtained in the Hv mode gave valuable information concerning the presence of a detectable Hv component of the scattered light. In many cases, the scattered light peak was absent or appeared as a small shoulder in the emission spectra. In these cases, the Hv component of the scattered light was not measured.

The reciprocal of the corrected Vv or Hv Rayleigh ratios were plotted as a function of $\sin^2 \theta/2$ and and extrapolated to zero scattering angle. The square root of the zero angle intercepts were plotted separately as a function of concentration and extrapolated to zero concentration. This procedure was used instead of the more familiar Zimm plot since the second virial coefficient was often so large that a linear concentration dependence could not be obtained over a larger concentration range.

1.3 RESULTS AND DISCUSSION

1.3.1 PBT-30 in PPA/MSA

ABSOLUTE INTENSITY LIGHT SCATTERING

The PPA solution of PBT-30 was diluted in MSA to form a stock solution. To facilitate dissolution, this was heated at $110^{\circ}C$ for 1-2 hours prior to sonication.

The Vv scattering component from AILS of PBT-30 is characterized by a marked deviation at low scattering angles from the linear dependence extrapolated from high angles, both prior to and after centrifugation, as seen in fig 6a and 6b. This behavior is indicative of aggregation, and indicates that this indicates the scattering moieties are large, but not large enough to sediment completely. The concentration dependence of $Kc/R_{Vv}(0)$ is shown in figure 7.

The Hv scattering component from AILS of PBT also exhibits a deviation at low scattering angles from the linear dependence extrapolated from data at higher angles in the two highest concentrations, both prior to and after centrifugation, as shown in figure 8. Upon centrifugation, the angular dependence of the Hv scattering component becomes smaller. The concentration dependence for $Kc/R_{Hv}(0)$ is shown in figure 9. The experimental parameters are listed in Table 3. The experimental parameters are listed in Table 3

DYNAMIC LIGHT SCATTERING

The results of the component analysis are presented in Figs. 10- 11 which give the weighting factors r_i and $\tau_i \sin^2 \theta/2$ for PBT as a function of concentration As the concentration increases, the scattering contribution from the larger species increases. This is true for the centrifuged and uncentrifuged samples.

If the various time constants correspond to a quasi-ternary system, the Vv scattering may be separated into three components using the values for r_i in Figs. 10 and 11. The values of $Kc/r_i R_V(\theta)$ are plotted against $\sin^2\theta/2$ for the uncentrifuged and centrifuged PBT in MSA in Figs. 12 and 13 and the concentration dependence is shown in fig 14. The experimental parameters are listed in table 3

INTERPRETATION OF LIGHT SCATTERING DATA

The weight average molecular weight M_w from the Vv and Hv scattering data respectively can be calculated from the equations 9 and 12. The mean square radius of gyration is calculated using equations 10 and 13 and the Vv and Hv scattering angular dependence respectively. These values are listed in Table 4. Comparing the molecular weight obtained from the Vv and Hv scattering data indicate that the PBT sample is aggregated. In previous studies of rodlike molecules[16], it was found that aggregation affected the results obtained from the Vv AILS component severely. The value of $(1+(4/5)\delta^2)M_{w,Vv}$ reflected the mass of the aggregated species and the angular dependence of $Kc/R_{Vv}(\theta)$ deviated markedly at low scattering angles from the linear dependence extrapolated from the high scattering angle data. Owing to the poor orientational order of the molecular axes in the aggregate, the Hv AILS component was not affected by the presence of aggregation and gave information on the single chain in solution. Thus, the value of $M_{w,Hv}$ and the mean square radius of gyration were those of the single chain regardless of whether the chain was contained in an aggregate or not. The value of δ obtained from R_{Hv}/R_{Vv} was generally smaller than expected for a rodlike chain. This measure of δ is small since the molecules in the aggregates were spatially but not orientationally correlated. The aggregates were postulated to be a 'brush-heap' of the molecules.

The solutions of PBT-30 in PPA/MSA showed the characteristics of other PBT solutions described above. The value of R_{Hv}/R_{Vv} was smaller than expected (see table TABLE). Comparison of $(1+(4/5)\delta^2)M_{w,Vv}$ and $\delta^2 M_{w,Hv}$ show that the sample is aggregated.

If we postulate that the Hv AILS component is due to single rods, we can calculate $M_{w,Hv}$, $L_{G,Hv}$ and L_H using eqns 9, (1.15),and (1.21) with the results listed in table 4. The value of L_H is a factor of two larger than $L_{G,Hv}$. If the Hv AILS component was due to single rodlike molecules, L_H and $L_{G,Hv}$ should be equal. The molecule weight expected from $L_{G,Hv}$, calculated from $M=LM_L=213$ d nm^{-1} from $\delta^2 M_{w,Hv}$ with $\delta=0.5$

where M_L is the mass per unit length, is 1.1×10^4 which is 2-3 larger than obtained. This difference could arise from aggregates which there is some degree of orientational correlation among the molecular axes, resulting in a larger than expected molecular weight as measured by $\delta^2 M_{w,Hv}$.

Application of eqns (1.9) and (1.11) gives estimates for $w_2(1+(4/5)\delta^2)M_{w,i}$ and $J_i^{1/2}R_{G,i}$. If these are interpreted in terms of a rodlike molecule with $\delta=0.5$ (eg., $f_1=f_2=f_3=1$) then the lengths entered in Table 4 are obtained (where the $w_i<1$). Since the lengths estimated from $R_{G,i}$ correspond to a $(L_z L_{z+1})^{1/2}$ average whereas those from $M_{w,i}$ are L_w average, the former should exceed the latter. Failure to observe this condition indicates that the assumed rodlike aggregates are several molecules wide, augmenting $M_{w,i}$ but not $R_{G,i}$. This is consistent with comparison with data on $L_{\Xi,3}$ =25 nm computed from $R_{H,3}$ since $L_{\Xi,3}$ vary as a weight average.

If we assume the aggregates, can be represented as ellipsoids of revolution, then the radius of gyration and the friction factor can be expressed as[14]

$$R_G^2 = (L^2/5)(1+2p_2) \tag{1.41}$$

$$\Xi_o = 3\pi\eta_s L \frac{(1-p^2)^{1/2}}{p} F(p)$$

where $p = L / d$

For a prolate ellipsoid $(p>1)$ (1.42)

$$F^{-1}(p) = \ln [(p+(p^2-1)^{1/2})/(p-(p^2-1)^{1/2}]^{-1}$$

and for an oblate ellipsoid $(p<1)$ (1.43)

$$F^{-1}(p) = \arctan (1-p^2)^{1/2}/ p$$

If L is eliminated between the expressions for R_G and Ξ_o, the resultant function $\Xi_o R_G$ depends only on p. As shown in Fig.FIG97X the function is bimodal so that for most p, a given $\Xi_o R_G$ may correspond to either an oblate and a prolate ellipsoid. In order to differentiate between these models, more information is needed. Owing to the asymmetric nature of the rodlike chains, we will assume a prolate ellipsoid is formed by aggregation.

Component two after centrifugation can be modelled as a prolate ellipsoid of length 540 nm and a diameter of 5 nm. Prior to centrifugation, the dimensions of the prolate ellipsoid would correspond to an infinitely thin rod which is unreasonable since component two is attributed to an aggregate structure many molecules thick. This result implies prior to centrifugation, component two must contain a broad distribution of species in which the weighted averages, $R_{G,2}$, a z-type of average, and $R_{H,2}$, a weight type of average, give a $R_G \Xi$ product which is too large.

The dimensions of the prolate ellipsoid of component three prior to and after centrifugation are essentially that of an infinitely thin rods of length 120 nm and 100 nm respectively.

1.3.2 PBT-PBO (90/10) in PPA/MSA

ABSOLUTE INTENSITY LIGHT SCATTERING

The PPA solution of PBT-PBO (90/10) was diluted in MSA to form a stock solution. In the initial experiments, this was not heated as part of the preparation history (see table 1). The initial solutions of PBT-PBO (90/10) in PPA were prepated by dilution in to MSA, followed by sonication for 1 hour and centrifugation for 24 hours. A portion of the centrifuged sample was used as a stock solution from which the light scattering solutions were prepared.

The preliminary AILS results were surprising in that the angular dependence of $R_{Vv}(\theta)$ displayed a strong upward curvature with decreasing angle, which is characteristic of aggregation, shown in fig 16.

A subsequent attempt was made to prepare solutions of PBT-PBO (90/10) and (75/25) in PPA by dilution with MSA. Prior to sonication, the MSA solution was heated at $110^{\circ}C$ for 1 hour, the sonication time was increased to 2 hours and the solution was centrifuged 24 hours before light scattering solutions were prepared.

The Vv scattering component of the AILS for PBT-PBO (90/10) copolymer has a remarkably linear angular dependence with the exception of the highest concentration as shown in figure 17a. Upon centrifugation, the angular dependence changes by 30% and at low scattering angles there as a large deviation from the linear angular dependence extrapolated from the data obtained at high scattering angles as shown in figure FIG34Ab. The second highest concentration (0.0385 g/dl) exhibits a different angular dependence than the other concentrations. The concentration dependence of $Kc/R_{Vv}(\theta)$ is unusual in contrast to the behavior prior to centrifugation. The concentration dependence of $Kc/R_{Vv}(0)$ is shown in figure 14. There is a large increase in $Kc/R_{Vv}(0)$ upon centrifugation. Since M_w is inversely proportional to $Kc/R_{Vv}(0)$, aggregates with a high molecular weight have been removed by sedimentation.

The angular dependence of the Hv component of AILS prior to and after centrifugation is shown in figure 19a and 19b respectively. The highest concentration (0.0491 g/dl) exhibits an angular dependence which is different than the other concentrations. After centrifugation, the angular dependence of the highest concentration does not deviate from that of other concentrations. This suggests a more ordered aggregate at the highest concentration. The concentration dependence of $Kc/R_{Vv}(0)$ is shown in figure 20. In contrast to the change of the concentration dependence of the Vv component, $Kc/R_{Hv}(0)$ changes only by 10%. This implies the aggregates by sedimentation are probably not more ordered than the supernatant.

The experimental parameters are listed in table 5

DYNAMIC LIGHT SCATTERING

The results of the component analysis are presented in Figs.21- 22, giving both the weighting factors r_i and $\tau_i \sin^2 \theta/2$ as a function of concentration As the concentration increases, the scattering

contribution from the larger species increases. This is true for both the centrifuged and uncentrifuged samples.

If the various time constants correspond to a quasi-ternary system, the Vv scattering may be separated into three components using the values for r_i in Figs. 21 and 22. The values of $Kc/R_{Vv,i}(\theta)$ are plotted against $\sin^2\theta/2$ for the uncentrifuged and centrifuged PBT-PBO(90/10) in MSA in Figs. 23 and 24 and the concentration dependence is shown in fig 25. The experimental parameters are listed in Table 5.

INTERPRETATION OF LIGHT SCATTERING DATA

It is clear from a comparison of $R_{Vv}(\theta)$ of the non-heat treated and the heat treated samples of PBT-PBO (90/10) in PPA/MSA, that heating degrades metastable aggregates. From the angular dependence of the R_{Vv} data on the heat treated sample, it is apparent that aggregation persists even after the heat treatment. This is a somewhat discouraging result as it was hoped solutions prepared directly from PPA

(avoiding the precipitation step known to produce aggregation) would be the most aggregate-free samples possible. Through the effect of heat treatment, a less aggregated solution was prepared. Perhaps a more 'molecular' solution could be prepared if a solvent with a lower ionic strength such as CSA was used or if the sample was heated at a higher temperature for a longer period of time.

As for the the PBT previously discussed, a comparison of $(1+(4/5)\delta^2)M_{w,Vv}$ and $\delta^2 M_{w,Hv}$ indicates that PBT-PBO (90/10) in PPA/MSA is aggregated. The previous conclusions about the value of δ and increased forward polarized scattering are also valid for this system. If the Hv AILS component is considered to arise from a single rodlike molecule, $L_{G,Hv}$ and L_H can be calculated and the values are listed in table 6. The value of $L_{G,Hv}$ is a factor of 2-3 smaller than L_H. The molecular weight corresponding to a rodlike molecule with contour length 60 nm is $\sim 1.3 \times 10^4$. This suggests the possibility of an aggregate of 2-3 molecules orientationally correlated, giving rise to enhanced Hv scattering.

As with the data on PBT-30 discussed above, the results for lengths computed for the components using data on $R_{G,i}$ and $w_i M_{w,i}$ indicate an overall rodlike structure several chains in diameter, and somewhat longer than the true molecular length (see Table 6). The data on $L_{\Xi,3}$ are surprisingly large in comparison with that on $L_{2,Vv}$.

With the ellipsoid model discussed above, component three can be modelled as a prolate ellipsoid of length 120 nm and a diameter of 1 nm prior to centrifugation, and a length of 93 nm and a diameter of 8.5 nm after centrifugation. From the previous of comparison of $L_{G,H}$ and L_H, the possibility of an aggregate composed of 2-3 molecules arose. Component three could be an aggregate of this type.

Component two when modelled as a prolate ellipsoid has a length of 850 nm and a diameter of less than 0.1 nm, ie. an infinitely thin rod. This is an unreasonable estimate since component two is postulated to be an aggregated species, presumably

several molecules thick. The discrepancy could arise from the weighted average of R_H and R_G. If component two is a broad distribution of sizes, then the length of a prolate ellipsoid could be overestimated. However, this suggests the aggregate is highly extended and asymmetric.

1.3.3 PBT-PBO (75/25) in PPA/MSA

ABSOLUTE INTENSITY LIGHT SCATTERING

Solutions were prepared following the procedure described for PBT-PBO (90/10). As with that polymer, the $R_{Vv}(\theta)$ data on the solutions prepared without heat treatment on the stock solution showed severe enhanced forward scattering, indicative of substantial aggregation (see fig.FIG1001). The data described below were obtained on heat treated solutions following the procedure given above.

The angular dependence of the Vv scattering component for PBT-PBO (75/25) shown in figure 27 is influenced greatly by the presence of aggregates at all but the lowest concentration. The low angle scattering is greatly enhanced, deviating from the linear angular dependence extrapolated from the data obtained at high scattering angles. At 0.0102 g/dl, the predominance of the scattering from the aggregates can be seen by the deviation of the high angle scattering data from the linear dependence extrapolated from the low angle scattering. If the linear dependence of $Kc/R_{Vv}(\theta)$ was extrapolated from the high angle scattering data, the intercept $Kc/R_{Vv}(0)$ would be negative, an unphysical result. This implies the presence of an aggregate large enough to exhibit strong intraparticle interference effects.

The concentration dependence of $Kc/R_{Vv}(0)$ shown in figure 29, the highest concentration 0.0499 g/dl deviates from the linear concentration dependence extrapolated from the other concentrations.

Upon centrifugation, the Vv scattering component exhibits a deviation at low scattering angles from the linear angular dependence extrapolated from the data obtained at high scattering angles except the lowest concentration as shown in figure 28. The lowest concentration exhibits an angular dependence similar to that prior to centrifugation. The concentration dependence of $Kc/R_{Vv}(0)$ is shown in figure 29. The weight average molecular weight is listed in table 7. The root mean square radius of gyration is concentration dependent as shown in figure 30 and listed in table 7, increasing with decreasing concentration.

26

The angular dependence of the Hv scattering component prior to and after centrifugation is shown in figure 31 and FIG35D. The concentration dependence of $Kc/R_{Hv}(0)$ shown in figure 32 does not exhibit the expected concentration independence. If a mean square radius of gyration is calculated using $\partial \ln R_{Hv}/\partial \sin^2 \theta/2$ at each concentration (listed in table 7 and indicated by **), the result is not concentration independence as shown in figure 33. The mean square radius of gyration increases with decreasing concentration except at 0.0102 g/dl with decreases sharply after centrifugation. After centrifugation, $R_{G,Hv}$ decreases with decreasing concentration. This implies the quantity $(\delta^2 M_{w,Hv})$ is concentration dependent.

DYNAMIC LIGHT SCATTERING

The results of component analysis are presented in Figs.34- 35, gives the weighting factors r_i and $\tau_i \sin^2 \theta/2$ for as a function of concentration . As the concentration increases, the scattering contribution from the larger species increases. This is true for both the centrifuged and uncentrifuged samples.

If the various time constants correspond to a quasi-ternary system, the Vv scattering may be separated into three components using the values for r_i in Figs. 34 and 35. The values of $Kc/R_{Vv,i}(\theta)$ are

plotted against $\sin^2 \theta/2$ for the uncentrifuged and centrifuged PBT-PBO (75/25) in MSA in Figs. 27 and 28 and the concentration dependence is shown in fig 31 and 37. The experimental parameters are listed in Table 7.

INTERPRETATION OF LIGHT SCATTERING RESULTS

As distinct from the data on PBT-30 and PBT-PBO (90/10), for PBT-PBO (75/25) the data on $c/R_{Hv}(0)$ depend strongly on c. This implies that the state of aggregation depends on c since intermolecular correlation effects on R_{Hv} are unexpected. Consequently, the data are difficult to interpret. Comparison of $J^{1/2}R_{G,v}$ with $f_3 R_{G,H}$ extrapolated to infinite dilution reveals that the latter is over 10 times smaller than the former, indicating severe effects of association characterized by spatial but orientational correlation of the chain comprising the aggregates. The data on $R_{H,3}$

27

correspond to a rod of length 30 nm, which may a reasonable estimate for the weight average chain length. By comparison, $R_{G,H}$ for the total sample would correspond to a $(L_z \cdot L_{z+1})^{\frac{1}{2}}$ of 45 nm.

1.3.4 PBT-7 and PBT-8

ABSOLUTE INTENSITY LIGHT SCATTERING

The effects of salt on articulated PBT copolymers have been previously investigated. Evidence for large oriented supramolecular structures included intense Hv scattering, versus nil without salt, and a change in the marked fluorescence upon the addition of salt. The analysis of 'molecular' arrangement within a supramolecular structure is complicated by the possibility of molecular conformational changes due to the presence of the articulated comonomer. Studies of rodlike PBT with added salt were initiated to remove this complication. Two PBT's were chosen to investigate the effect of aggregation with addition of salt.

As shown in Fig. 39, the intensity of the Hv scattering increases but the intensity of the fluorescence is not much affected Thus, as with the articulated copolymer, an ordered supramolecular structure appears to be formed in the rodlike case also.

The dependence of the fluorescence on polymer concentration and salt for PBT-8 and PBT-7 are shown in Figs. 40 and 41 respectively supports this postulate. The fluorescence intensity is expected to vary with concentration according to the relation

$$\frac{n_{fl}}{n_{std}} = \mu K^0 c Q(c) \exp\{-(\mu_l + \mu_{l'} l')c\} \tag{1.44}$$

if the same species is assumed to be responsible for absorption and fluorescence: Here n_{fl} and n_{std} are the photon count rates from the sample and a standard respectively, primed and unprimed quantities refer to the emitted and incident light respectively, μ is the extinction coefficient, I a pathlength, K^0 an apparent quantum efficiency and $Q(c)$ accounts for concentration dependent quenching or enhancement of the fluorescence. The data in Fig. 41 show that for PBT 7 the Vv fluorescence μK^0 is increased, and the rate of change of the fluorescence with concentration is decreased by the addition of salt. The latter implies that addition of the salt results in fluorescence enhancement that increases with increasing concentration; such an

29

effect could result from increased tendency to form supramolecular structures with increasing concentration in the presence of the salt. For the sample containing the salt, the ratio of the Hv and the Vv fluorescence intensities is about 0.4, independent of concentration.

The angular dependence of the Hv scattering obtained for the samples, PBT 7 and PBT 8 with salt is shown in figures 42 and 44. The increase of $[Kc/R_{Hv}(0)]_o^{-1}$ ∂ $(Kc/R_{Hv})/\partial \sin^2 \theta/2$, which is equal to $f_3 R_{G,Hv}$ listed in tables 8 and 9 respectively, of the solutions with added salt is an indication of oriented supramolecular species. The concentration dependence of the Hv scattering for PBT 7 and 8 with and without added salt is shown in Figs. 45 and 47. There are several interesting features to the data. Firstly, eq.(1.12) indicates that $[Kc/R_{Hv}(0)]^0$ is independent of concentration. In the case of PBT 8 with salt, the centrifuged samples are nearly independent of concentration. However, the uncentrifuged samples of PBT 8 + salt and more markedly, PBT 7+ salt show a large concentration dependence as shown in Figs. 45 and 109. The Hv intensity is much greater at the lower concentrations, for the uncentrifuged and centrifuged samples. After centrifugation, the intensity decreases but is still larger than the samples without salt.

The angular dependence of the Vv scattering of PBT 7 and 8 with salt are not independent of concentration as shown in Figs. 43, 45, 49 and 51. This combined with the concentration dependence of the Hv component could be attributed to the formation of different species of supramolecular aggregates with different degrees of intermolecular orientation. The concentration dependence of PBT 7 and 8 with and without salt are shown in Figs. 47 and 53. For the samples with salt, $[dKc/R_{Vv}(0)]/dc$ is smaller than without salt. This is the expected result with polyelectrolytes, electrostatic screening increases with increasing amounts of added salt. The apparent molecular weight obtained from $[Kc/R_{Vv}(0)]^0$ of PBT 7 and 8 with salt is greater than without salt.

The results calculated for each component of PBT 8 are given in Table8 and PBT 7 in Table 9. Meaningful interpretation of these lengths require the state of aggregation to be constant with concentration and the rodlike approximations are valid. The uncentrifuged samples of PBT 7 and 8 appear to contain different sizes of aggregates at each concentration . This can be clearly seen for PBT 7 in Figs. 49 and 51. $dKc/R_{Vv}\theta/dsin^2 \theta/2$ is extremely concentration dependent, indicating that the aggregates increase in size with increasing concentration. Interpretation of the data will be discussed later.

DYNAMIC LIGHT SCATTERING

The characteristics of dynamic light scattering, the autocorrelation function and $n^{(2)}-1$ for PBT-7 and PBT-8 with added salt are that the lowest concentration solution exhibits long time correlation behavior while the highest concentration possesses shorter correlation times as shown in figures 49 - 56 for PBT-8 and figures 57 for PBT-7. As can be seen in figure 56, the concentration dependence does not change with centrifugation. The results of the component analysis, which are the concentration dependences of r_i and $\tau_i sin^2 \theta/2$ presented in figures 59-62. The experimental parameters are listed in table 8 and 9 for PBT-8 and PBT-7 respectively.

The weighting factors r_i were used to decompose the Rayleigh ratio into components. The angular dependence of $[Kc/r_iR_{Vv}(\theta)]$ for PBT-8 are shown in figures 63-65 and for PBT-7 in figures 67-69. The concentration dependence of $[Kc/r_iR_{Vv}(0)]$ for PBT-8 and PBT-7 are shown in figures 125B and 70. The experimental parameters are listed in table 8 and 9.

31

INTERPRETATION OF LIGHT SCATTERING DATA FOR PBT-8 +SALT

It is important to note that added salt cannot change the conformation of PBT since the PBT molecule is fully extended. The optical anisotropy of a rodlike molecule such as PBT must be at its maximum value.

As discussed above, the spatial correlation of the optical components in the scatterer dominates the R_{Vv} data, whereas R_{Hv} is dominated by the orientational correlation of the components. In the preceding data was presented for which both R_{Vv} and R_{Hv} were augmented dramatically by the addition of salt for solutions of PBT-7 and 8. This is unlike the results discussed above for PBT-30, PBT-PBO (90/10), and PBT-PBO (75/25) for which it was deduced that aggregation caused pronounced effects on R_{Vv} but had much less effect on R_{Hv}. Similar conclusions were reached for data on solutions of PBT-7 and PBT-8 in MSA. With PBT-7 and 8, it appears that the addition of salt induces some enhanced R_{Vv} scattering but relatively more R_{Hv} scattering. If the aggregates developed on the addition of salt were comprised of nearly parallel arrays of the rodlike chains, then the overall anisotropy δ computed from $[R_{Hv}(0)/R_{Vv}(0)]_o$ would be equal to the molecular δ, or about 0.5. As shown in Table 8, the observed values are only slightly smaller (in distinct contrast with the results reported above for PBT-30, or the PBT-PBO polymers). Apparently, the addition of salt promotes the formation of aggregates with both spatial and orientational correlation of the rodlike molecules. A more detailed analysis of the scattering data follows.

With PBT-8, the Vv and Hv scattering for the uncentrifuged samples are essentially independent of c except for the lowest concentration. On centrifugation, the small angle Vv scattering is markedly reduced, but not much else happens to the scattering data except for the sample with the the lowest c, see below. The solution with c> 0.1 gL^{-1} contain a substantial fraction of structure in which the chains are both spatially and orientationally correlated, along with a few large aggregates with poor orientation correlation. On dilution to 0.1 gL^{-1}, surprisingly both the Vv and Hv

scattering are increased in an absolute sense! Apparently the dilution creates well ordered large structures, perhaps by agglomeration involving the polymer involved in the few large aggregates at higher c. In the photon correlation data, the decrease of c to 0.1 gL^{-1} is accompanied by the appearance of a component with a very long coherence time, as evidenced by the apparently small coherence factor.

The value of δ computed from $[R_{Hv}(0)/R_{Vv}(0)]_o$ for the PBT-8 with added salt is about 0.2, lower than the value of 0.5 expected for the PBT-8 molecule, or the value of 0.3 observed directly from $[R_{Hv}(0)/R_{Vv}(0)]_o$ for PBT-8 in MSA (including the effects of some aggregation for the latter). Thus, the aggregates exhibit appreciable but not complete orientational correlation of the rodlike axes. Comparison of $f_3 R_{G,H}$ for the samples with and without salt give similar result, ca. 20-25 nm, whereas for the centrifuged sample $\delta^2 M_{w,H}$ is increased about 3-fold on addition of salt, as is $(1+(4/5)\delta^2)M_{w,V}$.

The effects of salt induced aggregation of PBT-8 can be seen clearly from the comparison of $(1+(4/5)\delta^2)M_{w,V}$ for the uncentrifuged sample with salt to PBT-8 without salt. Although δ for the overall structures are not the same for the PBT-8 with and without salt, the error in the estimate of the increase in M_w arising by a comparison of $(1+(4/5)\delta^2)M_{w,V}$ is at most a factor of two. If δ were equal for PBT-8 with and without salt, PBT-8 with salt contains $\sim$ 25-fold more mass than PBT-8 without salt, or that the aggregate may contain about 50 molecules. By contrast, the quantity $\delta^2 M_{w,H}$ for the PBT-8 + salt is about 10-fold larger for the solution with salt than for that without salt. To a reasonable approximation, one might write

$$[\delta^2 M_{wAGGREGATE}] \sim (3\langle\cos^2 \phi\rangle - 1)\nu(\delta^2 M)_{MOLECULE}$$

where ν is the number of molecules per aggregate with $\langle\cos^2 \phi\rangle$ calculated for the angle $\phi/2$ of the molecular axis with a preferred direction. Thus, if $\nu \sim 50$, one finds $\langle\cos^2 \phi\rangle$ corresponds to $\phi/2$ of 25 °. This is not different for the case without salt for which $\nu \sim 2$-3.

33

Comparison of $J^{1/2}R_{G,V}$ for the uncentrifuged PBT-8+salt with that for PBT-8 without salt suggests that the aggregate is highly extended.

Using eqns.(1.42), Component 1, the largest aggregate species can be modelled as a prolate ellipsoid with length 800 nm and diameter 18 nm. This suggests the molecules have aggregated into an extended array, many molecules long, with only partial orientation of the axes of the molecules along the long axis of the aggregate on the average.

If component two for the centrifuged and uncentrifuged PBT-8 + salt sample is also modelled as a prolate ellipsoid then the major and minor diameters are $\sim$ 130 nm and 20-50 nm, respectively. The major diameter is larger than L_G of PBT-8 without salt. Component two apparently also corresponds to an extended aggregate with the molecules somewhat in a parallel array.

Component three corresponds to a moiety with a length $L_{\Xi,3}$ of 15 and 9 nm for the uncentrifuged and centrifuged samples respectively using a rodlike model. This component probably represents the smaller molecularly dispersed components of the overall molecular weight distribution of the sample.

INTERPRETATION OF LIGHT SCATTERING DATA FOR PBT-7+SALT

For the data on PBT-7, $\partial Kc/R_{Vv} / \partial \sin^2 \theta^2/2$ decrease appreciably with decreasing concentration indicating that the scattering entities become smaller as c decreases. In addition, $Kc/R_{Hv}(0)$ decreases with decreasing c. Since interparticle interference effects are unexpected, the latter means that $\delta^2 M_{w,H}$ increases with decreasing c! At the same time, $f_3 R_{G,H}$ is about independent of c. According to the component analysis, these solutions contain appreciable fractions of very large (large $\tau_i q^2$) moieties and the fraction of the moiety tends to decrease with decreasing c, resulting in an enhanced fraction of a scatterer with smaller $\tau_i q^2$.

When the uncentrifuged Vv AILS data of PBT-7+salt shown in figure 49 is represented in a Gunier plot, the non-parallel $Kc/R_{Vv}(0)$ versus $\sin^2 \theta/2$ become parallel in the Gunier representation. This suggests the presence of large nonpenetrable asymmetric aggregates possibly exhibiting interparticle interference effects. The quantities $J^{1/2}R_{G,V}$ and $(1+(4/5)\delta^2)M_{w,V}$ should be calculated from the small angle scattering data, not the high angle scattering data which neglects the aggregated species or particle interference effects. This aggregated species is precisely the species of interest. The apparent $J^{1/2}R_{G,V}$ and $(1+(4/5)\delta^2)M_{w,V}$ are enormous $((1+(4/5)\delta^2)M_{w,V} \sim 10^7$ d). The Hv scattered intensity is larger than PBT-7 without salt.

After centrifugation, a Gunier representation of $Kc/R_{Vv}(\theta)$ of the data shown in figure 113 versus $\sin^2 \theta/2$ also are parallel with respect to concentration. At high scattering angles $Kc/R_{Vv}(\theta)$ for the centrifuged and uncentrifuged samples almost coincide. The decreased scattered intensity at small angles as well as a decrease in the longest $\langle\tau_i\rangle q^2$ indicate large aggregates have been removed by sedimentation. If $Kc/R_{Hv}(\theta)$ for PBT-7+salt is also represented in a Gunier graph, it is apparent that R_{Hv}/Kc decreases slight at 0.025 and 0.039 g/dl, more at 0.012 g/dl and significantly at 0.49 g/dl upon centrifugation. It was found $R_{Hv}/Kc \sim R_{Vv}/Kc$ for the centrifuged

sample, suggesting δ for the scattering moiety is a constant while M_w is changing. The quantity R_{Vv}/Kc is not as sensitive to the value of δ as R_{Hv}/Kc (ie.$(1+(4/5)\delta^2)M_{w,V} \sim \delta^2 M_{w,H}$) so M_w is probably changing while δ is high and constant. This interpretation could account for the apparent concentration dependence of $Kc/R_{Hv}(0) = (\delta^2 M_{w,H}(0))^{-1}$.

The observed behavior can be understood in terms of the dissolution of large aggregates with spatial but not orientational correlation among the molecules in the structure, with simultaneous formation of dimensionally smaller structures with spatial and enhanced orientationally disorganized aggregates, but the resultant solvated specie either added to already present structures with better orientational organization, or form new such entities. Not unexpectedly, much of these very large structures are lost upon centrifugation. However, the data still show the presence of large structures with more or less the same qualitative behavior.

1.3.5 SPBT-38/MSA

ABSOLUTE INTENSITY LIGHT SCATTERING

SPBT-38/MSA showed no detectable Hv light scattering peak in the emission spectrum using either a 514 nm or 633 nm wavelength excitation as shown in figure FIG1F. The Vv component of AILS was measured using the 514 nm wavelength for convenience.

The angular dependence of $Kc/R_{Vv}(\theta)$ after centrifugation is small, except at the highest concentration as shown in figure 72. The concentration dependence of $Kc/R_{Vv}(0)$ is shown in figure 73 . Using equations (1.9),(1.10), and (1.11) the calculated M_w of $\sim 10^5$ and radius of gyration listed in Table 10,

Prior to centrifugation, there is a more pronounced deviation of $Kc/R_{Vv}(\theta)$ at low angles from the linear angular dependence extrapolated from high scattering angles as shown in figure FIG98. The radius of gyration listed in table 10 increases slightly as does the apparent molecular weight also listed in table 10 extrapolated to zero concentration from dependence of $Kc/R_{Vv}(0)$ shown in figure 73.

DYNAMIC LIGHT SCATTERING

A typical correlation function $g^{(2)}(\tau,\Delta\tau)$ for these samples is a function of $\sin^2 \theta/2$ as shown in Fig. 74 indicating a wide range of τ_i. At small angles, $g^{(2)}(\tau,\Delta\tau)$ decays very slowly, indicating the presence of an extremely large particle moving slowly. The behavior of these materials is dependent on concentration. The behavior can also be seen in $n^{(2)}-1$ shown in figure 75 This concentration dependence does not change upon centrifugation for all systems studied. The results of the component analysis are presented in Figs.76- FIG1J. The weighting factors r_i and time constants $\tau_i \sin^2 \theta/2$ are shown for SPBT-38 as a function of concentration. As the concentration increases, the scattering contribution from the larger species increases. This is true for the centrifuged and uncentrifuged samples.

Using equations 10 and 11, the Vv AILS data of SPBT 38/MSA can be decomposed

into relative contributions to the intensity using the weighting factors obtained by analysis of the photon correlation data. There were only two components present in this system, the longest time constant attributed to component one is absent. The angular dependence of two and three are shown in fig 77. Upon centrifugation, large aggregates were removed as seen by the change in the scattering curves. The remaining components diffused so rapidly that, photon correlation data were collected at 15.0° C instead of the normal 25.0° C. Decreasing the temperature has the effect of increasing solvent viscosity making data collection on the slower moving species possible. Data on the faster diffusing species were unreliable. The angular dependence of the slower species is shown in fig 78. The best estimate for component three come from the uncentrifuged Vv AILS data. The concentration dependence of the $[Kc/r_iR_{Vv}(\theta)]$ are shown in figure 79.

INTERPRETATION OF LIGHT SCATTERING DATA

The values of M_w and $R_{G,Vv}$ listed in Table 10 are biased by neglect of scattering at small angles;less so in the case of the centrifuged sample. The values of $R_{G,Vv}$ and M_w are consistent with a coil-like conformation for the chain, (remembering that molecular weight dispersion enhances $R_{G,Vv}$.

As a useful approximation, we may consider a SPBT chain as comprised of N segments with average length $\langle \ell \rangle_i$ made up of the PBT type monomers and n-1 segments of length ℓ_2=0.44 nm made up of the bipyridyl moities that break up the rodlike structures. These are connected to form fixed bond angles $\pi-\alpha$ of $2\pi/3$ radians. The average length $\langle \ell \rangle_1 \sim$ L/n where LI is the contour length of the 2n-1 segments in the chain. For a freely-rotating chain with fixed bond angles $\pi-\alpha$ and alternating bonds of length ℓ_1 and ℓ_2 (n bonds of length ℓ_1 and n-1 of length ℓ_2).

$$R_G^2 = \frac{(2n-1)}{12} (\ell_1^2 + \ell_2^2) \left[\frac{1+q}{1-q} - \frac{2(\ell_1 - \ell_2)^2}{(\ell_1^2)} (q+q^3) \right] \qquad (1.45)$$

with q= cos α. For the SPBT structures, L=M/M$_L$ with the mass per unit contour

length M_L equal to 213 d nm_1. The average number $n-1$ of articulated monomers per chain is given by xM/m_a, where x is the fraction of the articulated monomer. With the assumption of random placement, this produces n straight chain sequences of PBT of average length ℓ_1. The total contour length $L=n\ell_1 + (n-1)\ell_2$. For SPBT-38, $x=0.05$, $n=16$ and $\langle\ell\rangle_1 = 23$ nm so that $n\langle\ell\rangle_1^2/6 = 1350$ nm^2. The term in square brackets is equal to 1.58 for $\langle\ell\rangle_1 \gg \ell_2$, is found to be 1.54, to that $R_G = 45$ nm in comparison with the reported value of 25-30 nm. The differences may be within experimental error and the crude approximation used to calculate R_G. The disparity could be also indicate that the chains are aggregated to form an irregular structure somewhat similar to a randomly branched molecule so that M_w is larger than is expected for the measured R_G. The decrease of M_w and R_G on centrifugation is consistent with this proposal.

The factors r_i permit estimates of the quantity $w_i M_{w,i}$, where w_i is the weight fraction of the component with molecular weight $M_{w,i}$ and weight factor r_i. Unless w_i is known, the $M_{w,i}$ cannot be determined. On the other hand, $R_{G,i}$ can be estimated from the plots of $c/R_{Vv} r_i$ as discussed above and in reference 5. The data on the centrifuged sample shown that $R_{G,2}$ and $R_{H,2}$ are in reasonable accord for the behavior expected with coil-like chains, eg., with eqn 33 using the coil-like limit for H.

$$R_H \sim 2R_G/3$$

so that the ratio of $R_{H,2}$ to $R_{G,2}$ given in table 10 for the centrifuged solutions of SPBT-38 is consistent with a coil-like structure. On the other hand, the values reported for $R_{G,2}$ correspond to a $M_{w,2}$ of about 3×10^4 using the model described above, whereas $w_2 M_{w,2}$ is found to be 8.4×10^4. This may indicate a degree of association in excess of 3 for the centrifuged sample. The smaller $R_{H,3}$ apparently corresponds to lower M_w components of the chain length distribution.

For the uncentrifuged sample, $R_{H,2}$ is far in excess of $R_{G,2}$ estimated using the R_i for the sample. According to eqns. 32-33, R_H/R_G is expected to vary from 2/3 for a coil-like structure to $((12)^{1/2}/4)(d/L)^{1/5} \sim 1.73$ for a rodlike structure. The data on $R_{H,2}$ and $R_{G,2}$ for the uncentrifuged polymer may indicate the presence of a larger aggregate with a complex, but not rodlike structure.

In the treatment of the data to obtain $M_{w,Vv}$, the scattering at small angles is neglected-- the true M_w, including all aggregates, is greater than that reported in table--. For this reason, the values of $w_2 M_{w,2}$ and $w_3 M_{w,3}$ (with $w_2 + w_3 = 1$) do not necessarily sum to give M_w. Since w_2 is unknown, that data on $w_2 M_{w,2}$ and $w_3 M_{w,3}$ cannot be used to estimate $M_{w,2}$ or $M_{w,3}$. Data on $R_{G,2}$ can, however, be used to estimate an apparent molecular weight using the expression given above for R_G, with the result 3×10^4 for the centrifuged sample. This would suggest that the polymer remaining in the centrifuged sample is aggregated to about trimers on the average, in comparison with $M_{w,2}$, which is at least as large as the entered value $w_2 M_{w,2} = 8.4 \times 10^4$ (since $w_2 < 1$).

We conclude that prior to centrifugation, the solution contains large aggregates possibly comprised of randomly branched-like structures, together with some nearly completely dissociated chains. On centrifugation, the larger aggregates are lost, leaving a population of chains with a coil-like structure and some association.

1.3.6 SPBT-36/MSA

ABSOLUTE INTENSITY LIGHT SCATTERING

The Vv component of AILS for SPBT-36/MSA prior to centrifugation exhibits a large angular dependence except at the lowest concentration as shown in figure 80a. The scattering intensity at low angles deviate markedly from the linear angular dependence extrapolated from the high angle data except at the lowest concentration. Upon centrifugation, there is a factor of five change in the angular dependence of the scattered intensity shown in figure 80b. The concentration dependence of $Kc/R_{Vv}(0)$ is shown in figure 81. The apparent M_w and $J^{1/2}R_G$ are listed in table 11

The intensity of the Hv scattering component was small, making accurate measurements difficult. The fluorescence intensity used to correct the scattering intensity was measured at 650 nm for the Vv component but the Hv intensity was difficult to measure. The magnitude of the fluorescence correction was determined by subtracting a fraction (the ratio of the Vv fluorescence at 650 nm to the total Vv fluorescence) of the total Hv fluorescence intensity measured. The results prior to and after centrifugation are shown in figure 82a and b respectively. There is a large decrease in the Hv scattered intensity after centrifugation, suggesting the sedimented aggregates were more ordered than the supernatant. The angular dependence of the Hv scattered intensity decreases by a factor two, also indicating the ordered segments in the aggregate were large. The concentration dependence of $Kc/R_{Hv}(0)$ is shown in figure 83.

DYNAMIC LIGHT SCATTERING

As was found for SPBT-38/MSA, the autocorrelation function deviated significantly from the single exponential behavior expected for monodisperse solutes. The auto correlation functions were decomposed using equation 1.7. The results for a quasi-binary component system are shown in figure 84 and 85. The experimental results are listed in table 11.

INTERPRETATION OF LIGHT SCATTERING DATA

The principal difference between the scattering for SPBT-36 and that for SPBT-38 discussed above is the appearance of strong Hv scattering-- the intensity of the Hv scattering is seen to decrease markedly on centrifugation. Since x=0.1 for SPBT-36 and 0.05 for SPBT-38, it is not reasonable to attribute the increased Hv scattering for SPBT-36 to molecular rodlike structures.

If it is assumed that the Hv scattering arises from essentially rodlike entities, $R_{G,Hv}$ can be determined without a value for the molecular anisotropy δ with the result given in Table 11. It is seen that $R_{G,Hv}$ is decreased markedly on centrifugation indicating partial removal of large rodlike aggregates. Very likely, these comprise only a small fraction of the material, so that the concentration necessary to properly interpret the Hv data is unknown.

For the centrifuged sample, the Hv scattering is very small, so that presumably the Vv scattering reflects the properties of the coil-like moities. The ratio of $R_{H,2}$ to $R_{G,Vv}$ is similar to that expected for a coil-like molecule. With eqn. (1.45) and x=.01, the data for $M_{w,Vv}$ (calculated with $\delta=0$) correspond to a R_G of 16 nm , by comparison with the observed value of 50 nm. The discrepancy may be attributed to molecular weight heterogeneity or residual aggregation. In either case, a coil-like conformer is indicated for the dissociated chain.

1.3.7 SPBT-7/MSA

ABSOLUTE INTENSITY LIGHT SCATTERING

The scattering intensity of the Vv component of AILS of SPBT-7/MSA is much greater prior to sample centrifugation. After centrifugation, the Vv scattered intensity decreases by a factor of 2-5 as shown in fig.86. The angular dependence of $Kc/R_{Vv}(\theta)$ prior to centrifugation is large and although the magnitude of the angular dependence is smaller at the lowest concentration. At low scattering angles, for 0.0266 and 0.0378 g/dl, $Kc/R_{Vv}(\theta)$ deviates greatly from the linear angular dependence extrapolated from data obtained at the high scattering angles. This indicates the presence of large aggregates contributing to the forward scattering and that the degree of aggregation is concentration dependent. The concentration dependence of $Kc/R_{Vv}(0)$ is shown in figure87.

After centrifugation, the low angle scattering does not deviate appreciably from the linear angular dependence of $Kc/R_{Vv}(\theta)$ extrapolated from the data at high scattering angles except for the highest concentration. The decrease in intensity, the magnitude of $dKc/R_{Vv}(\theta)/dsin^2 \theta/2$ and the presence of increased low angle forward scattering indicate large aggregates have been removed by sedimentation. The concentration dependence of $Kc/R_{Vv}(0)$ is shown in figure 87. It is interesting to note $[Kc/R_{Vv}(0)]^\circ$ are the same for the sample prior to and after centrifugation although the concentration dependence of $Kc/R_{Vv}(0)$ are different.

The Hv scattering component of AILS was measurable but not reliably enough to be useful. The experimental parameters are listed in table 12.

DYNAMIC LIGHT SCATTERING

Prior to centrifugation, the contribution of r_1 extended to relatively large scattering angles (90°) in contrast to other samples where the contribution of r_1 was confined to angles less than or equal to 60° as shown in figure 88. This parallels the low scattering angle deviation from the linear angular dependence of $Kc/R_{Vv}(\theta)$ extrapolated from high scattering angles. After centrifugation ,the angular contribution of r_1 decreases to 60° as $\tau_i sin^2 \theta/2$ is shown in figure 89.

INTERPRETATION OF LIGHT SCATTERING DATA

The values of $M_{w,Vv}$ and $R_{G,Vv}$ for the uncentrifuged sample indicate an very large entity. Since these values reduce drastically on centrifugation, this is believed to be aggregated polymer. For the centrifuged polymer (assuming negligible change in c), $M_{w,Vv}$ corresponds to an $R_G = 24$ nm by the use of the expression given above ($n=39, \langle \ell \rangle_1 = 8$ nm). This is in reasonable accord with the reported value of 110 nm (considering the effects of polydispersity and experimental error), so that the value of $M_w = 6.8 \times 10^4$ appears to a satisfactory estimate, indicating a large degree of aggregation in the uncentrifuged material. The near lack of substantial Hv scattering indicate that the aggregates are not well organized. However, comparison of $R_{H,2}$ with $R_{G,2} \sim 1.4 R_{H,2}$ indicate severe departure from coil-like behavior. The large aggregates may have some overall rodlike configuration, leading to the observed ratio $R_{H,2}/R_{G,2}$ and minimal Hv scattering.

1.3.8 SPBT-12/MSA

ABSOLUTE INTENSITY LIGHT SCATTERING

There were several experimental difficulties in the investigation of this polymer. The first, a very small Hv scattering was obtained, but with poor precision. A second problem involves the absorption of the laser light in the measurement of the diffusion constant. At 514 nm, the solution absorbed so strongly that heating effects could not be avoided so that dynamic data were not collected. To minimize this difficulty, a krypton ion laser line (647 nm) was used. However, the intensity of scattered light is inversely proportional to the fourth power of the incident wavelength and the solution did not scatter enough light to be reliably detected.

A remarkable feature of the Vv component of AILS data is a lack of increased scattered intensity at low angles (except for one concentration)as shown in figure 92 for the sample prior to and after centrifugation. The quantity $d[Kc/R_{Vv}(\theta)]/d\sin^2 \theta/2$ is listed in table 13. The effect of centrifugation on the angular dependence is dramatic although there was no significant increase in the low angle scattering. This indicates a large coil or globular aggregate which dominates the scattered light. Upon centrifugation, the radius of gyration decreases by a factor of two. The concentration dependence is shown in figure 93. The molecular weight obtained by using the equation for a coil like molecule are listed in table 13. Upon centrifugation, M_w decreases by a factor of two.

INTERPRETATION OF LIGHT SCATTERING DATA

The values of M_w and $R_{G,V}$ are listed in table 13. The small Hv AILS scattering and values of $R_{G,V}$ and $M_{w,V}$ are consistent with a coil-like conformation for the chain, (remembering that molecular weight dispersion enhances $R_{G,V}$)

Using the previously discussed model of a freely-rotating chain, R_G can be calculated. For the centrifuged sample using $\langle \ell_1 \rangle$ = 5.7 nm, $\langle \ell_2 \rangle$=0.44 nm and n=59.6, $R_G \sim$ 22nm in comparison to the reported value of 30nm. The calculated value of R_G agrees well with the experimental value considering the crude model used and the experimental error involved.

For the centrifuged sample, using $\langle \ell_1 \rangle$=5.8 nm, $\langle \ell_2 \rangle$=0.44 nm and n=106.3, $R_G \sim$ 29 nm in comparison to the experimental value of 60 nm. The disparity could be due to molecules which are not highly packed in an aggregate giving the appearance of a highly expanded chain.

1.3.9 SPBT-38/MSA+salt

SPBT-38 was studied as a function of salt concentration and method of preparation. As indicated in table 18, SPBT-38 was dissolved in MSA, then a salt solution was added (indicated by (ps+s)) or dissolved in a salt solution (ps+s). The data will be discussed in terms of the concentration dependence of the Hv component of the absolute intensity light scattering (AILS) and the time constants obtained by dynamic light scattering. These data are characterized by the intense Hv scattering absent in the MSA solution, see figure 94, a large radius of gyration, and concentration dependent time constants.

ABSOLUTE INTENSITY LIGHT SCATTERING

The Vv component of the absolute intensity light scattering from SPBT 38+ 1N salt (ps+s) exhibits a large downward curvature from the data extrapolated from high angles indicating the presence of large aggregates Upon centrifugation, the aggregates contributing a large part of the scattered intensity have been lost at all concentrations except 0.0129 g/dl as shown in figure 95. The scattered intensity has decreased by a factor of 2-4. The downward curvature of $R_{Vv}(\theta)$ with $\sin^2 \theta/2$ is less severe. The angular dependence is a factor of 2 less than that for the uncentrifuged species, see fig 95. The concentration dependence is shown in fig 96.

The angular dependence of the Hv component are shown in fig 97. Prior to centrifugation, the angular dependence and scattered intensities are large. Evidently, the sedimented aggregates are extremely large and ordered, since the Hv scattered intensity decreases by a factor of 3 after centrifugation. The concentration dependence is shown in fig 98. From equations 10 and 13, M_w from the concentration dependences of the Hv and Vv scattering are calculated. Using equations 11 and 14 the radius of gyration is calculated from the angular dependence of the Hv and Vv scattering. These quantities are listed in table 14.

The intensity and angular dependence of the Vv component of the scattered light of the solution containing added salt (ps+s) is greater than for the MSA solution, as

seen by comparison of figures 72 and 95. The concentration dependence of the Vv scattering is shown in figure 96 The M_w calculated from the data for the MSA solution, along with the radius of gyration , are listed in table 10. The value obtained for M_w for the solutions with and without salt prior to centrifugation are approximately the same, even though the dependence on concentration differs. The apparent radius of gyration is greater in the salt solution than in the MSA solution. Additional information on the radius of gyration and molecular weight obtained from the Hv scattering are given in table 14. Substantial Hv scattering indicates that the sample is ordered. The addition of salt has brought about a transition from a coil like structure in MSA to a more rodlike conformation. The second virial coefficient is small to zero for the centrifuged salt solution. After centrifugation, the value of M_w calculated from the Vv scattering for the salt solution is a factor of 2 less than that for the MSA solution. This may indicate that higher molecular weight components were removed by centrifugation of the salt containing solution.

Data on the SPBT-38+1 N salt (p+ss) system exhibits some curvature of the Vv component as a function of angle but not as severe as is obtained with the ps+s system as seen in fig. 99. Upon centrifugation, the intensity decreases slightly. A more dramatic change occurs in the angular dependence and concentration dependence, as shown in fig 100. The angular dependence give a mean square radius of gyration decreased by a factor by 2 after centrifugation, whereas A_2 becomes 0. The angular dependence and intensity of the Hv component of the AILS do not change upon centrifugation (except for the 0.0500 g/dl solution) as shown in fig 101. The observation that the Hv scattering was little affected by centrifugation indicates that the substantial effects on the Vv scattering induced by centrifugation reflect a small fraction of the polymer. The concentration dependence is shown in fig 102. The experimental quantities are listed in table 15. The comparisons between data on the SPBT 38+1 N salt (ps+s) and the MSA solution are also true for the p+ss sample.

The value of M_w determined from the Vv scattering for the p+ss system is twice

as large as that with ps+s system both before and after centrifugation. M_w determined from the Hv scattering is larger for ps+s before centrifugation and comparable after. Whether before or after centrifugation, the Vv data give larger apparent M_w but comparable apparent R_G for the p+ss system as compared to the ps+s system. The Hv scattering gives larger apparent R_G for the ps+s prior to centrifugation and for the p+ss system apparent R_G is larger after. Since R_G is relatively insensitive to the diameter of the suspected rodlike supramolecular aggregates, the apparent comparable R_G but different apparent M_w value for the Vv scattering may indicate different diameters of the aggregates in the ps+s and p+ss systems.

The Vv scattering component for the SPBT 38 + 0.561N salt (p+ss) system is characterized by the absence of the downward curvature at small angles. Prior to centrifugation, the angular dependence for the three highest concentrations is large while the lowest concentration exhibits a smaller angular dependence, as shown in fig 103. This indicates the formation of distinctly different species at the lowest concentration is different, indicating distinct species at each concentration. The concentration dependence of $J^{1/2}R_{G,Vv}$ is shown in fig 104. The formation of different species with different molecular weights and $R_{G,Vv}$ with concentration may give rise to A_2 not equal zero , as seen in the concentration dependence in fig 105. All other solutions after centrifugation have $A_2=0$. The Hv component for SPBT 38+ 0.5N salt (p+ss) prior to centrifugation has large downward curvature from data extrapolated from higher angles for all but the highest concentration as shown in fig 106. This is unusual for the Hv scattering, especially since this behavior was absent from the Vv component The Hv data indicate the presence of a small fraction of large and well oriented supramolecular aggregate. The curvature observed could result if these aggregates preferentially contained the highest molecular weight components of the sample. Upon centrifugation, the Hv angular dependence changes drastically such that it is less intense by a factor of three with an angular

dependence that does not depend on concentration, as shown in fig 106. The large well-oriented aggregates are removed on centrifugation. The concentration dependence of the angular dependence shown in fig 107 is consistent with the Vv scattering.

The parameter $[Kc/R_{Hv}(0)]$ is expected to be independent of c and was so for most of the data obtained here. In some cases (indicated by ** in Table 15) $[Kc/R_{Hv}(0)]$ decreased with decreasing c, as though the supramolecular structure varied with c. In these cases, $f_3 R_G$ was calculated from $\partial \ln R_{Hv}/\partial \sin^2 \theta/2$ at each c.

The SPBT 38 + 0.53N salt system (ps+s) exhibited the same characteristics of the integrated intensity light scattering as the +0.561N system (p+ss) with the exception of the concentration dependence of the Hv scattering. The concentration dependence of the Hv scattering was not independent of concentration before or after centrifugation. The data for this system is shown in figs 108-111. The experimental parameters are listed intable 15

DYNAMIC LIGHT SCATTERING

For the systems with added salt, the lowest concentration sample exhibits long time correlation behavior as shown in $n^{(2)}-1$ in Figs. 112a , while the highest concentration possesses shorter correlation times shown in Figs. 112b. For all systems with added salt except ps+s with 0.5N salt, the highest concentration exhibits the longer time behavior as shown in Figs. 113. This concentration dependence does not change with centrifugation for all systems studied. The results of the component analysis are presented in figures 114 - 121. The weighting factors r_i and $\tau_i \sin^2 \theta/2$ are also shown as a function of concentration. As the concentration increases, the scattering contribution from the larger species increases. This is true for the centrifuged and uncentrifuged samples.

Analysis on the SPBT-38 systems with added salt was attempted to resolve the Rayleigh ratio into components with little success. The analysis assumes $[Kc/R_{Vv}(\theta)]$

can be resolved as weighted contributions to the Rayleigh ratio using the bulk concentration as a resonable approximation for the concentration of each component. In the systems with added salt, estimates of the concentration of each component are required to obtain meaningful results. It is not possible to estimate the concentration of each component without additional sources of information.

Interpretation of Light Scattering Data

It was concluded above that SPBT-38 was somewhat aggregated in methane sulfonic acid—negligible Hv scattering revealed that the rodlike subunits of the molecule have little orientational correlation in the aggregate. When the salt is added to these solution (either 0.5 or 1N) a modest enhancement in the forward scattering is obtained, the Hv scattering is increased markedly and the values of the $\tau_i \theta^2 v_s^{-1}$ are decreased somewhat. The Hv scattering remains after centrifugation but the enhanced forward scattering is lost. This behavior can be understood as a collapse of the disordered aggregates in MSA to a more highly ordered, and somewhat more dense, state together with the formation of a few larger agglomerates of the already existing aggregates. Since R_G is not much increased, and R_H appears to decrease, the articulated chains cannot be considered to be extended into fully rodlike conformers in the presence of salt. Rather, it appears that a supramolecular structure has the rodlike chain elements folded into a domain in which they pack with a substantial degree of parallelism. When the polymer is dissolved directly into the slat solution, essentially the same behavior is observed, except that the enhancement of the forward scattering is diminished. The Hv scattering is very similar, indicating a similar extent of spatial and orientational correlation irrespective of the order in which salt is added to the system.

1.3.10 SPBT-36 + salt

ABSOLUTE INTENSITY LIGHT SCATTERING

The Vv component of AILS for SPBT-36 + 1.095N salt prior to centrifugation at low scattering angles deviates from the linear angular dependence extrapolated from the data obtained at high scattering angles as shown in figure 122a. The angular dependence of $Kc/R_{Vv}(\theta)$ is large in contrast to the centrifuged sample shown in figure 122b. The angular dependence of $Kc/R_{Vv}(\theta)$ of the centrifuged sample is about a factor of 4 smaller than the uncentrifuged sample, indicating very large aggregates were removed by sedimentation. The concentration dependence of the zero angle intercept $Kc/R_{Vv}(0)$ is shown in figure FIG17. The second virial coefficient A_2 is not zero in contrast to the result $A_2 = 0$ found for other centrifuged articulated polymers with added salt.

The Hv component of AILS for SPBT-36 + 1.09N salt prior to centrifugation exhibits a large angular dependence shown in figure 124a. After centrifugation, the angular dependence of $Kc/R_{Hv}(\theta)$ is a factor of two smaller as shown in figure 124b. This indicates the aggregates lost by sedimentation were ordered. The concentration dependence of $Kc/R_{Hv}(0)$ is shown in figure 125.

The weight average molecular weight and mean square radius of gyration calculates from the Hv and Vv AILS data are listed in table 16.

DYNAMIC LIGHT SCATTERING

The time constants and weighting factors for a quasi-ternary component system of SPBT-36+salt as a function of concentration are shown in figures 126 and 127 for the uncentrifuged and centrifuged systems respectively. The experimentally accessible lengths are listed in table 16. Using the weighting factors in figure 126 and 127, the Rayleigh ratio can be decomposed into components. The angular dependence of $Kc/R_{2,Vv}(\theta)$ is shown in figures 128 and 129 for the uncentrifuged and the centrifuged sample respectively. The data corresponding to component three are too scattered to be meaningful and are hence not shown. The concentration dependence for

component two is shown in figure 130. The experimental parameters are listed in table 4.

To ascertain the origin of the molecular scattering, it is convenient to discuss the results of the Hv scattering component of AILS from SPBT-36 in MSA and those of the added salt first. Prior to centrifugation, the magnitude of $[Kc/R_{Hv}(0)]^o$ for SPBT-36 in MSA is larger than that after centrifugation. If it is postulated the Hv component of AILS is arising from the rodlike segments in the molecule, the corresponding molecular weight would be approximately 14,000 daltons. The 'molecular' weight of the ordered segments of the aggregates $[Kc/R_{Hv}(0)]^o$ prior to centrifugation is approximately 10,000 daltons while the actual 'molecular' weight is much larger as seen from $[Kc/R_{Vv}(0)]^o$. There is a loss of Hv scattered intensity upon centrifugation. In the case of added salt, the intensity of the Hv component of the scattered light remains approximately constant after centrifugation. The molecular weight corresponding to $[Kc/R_{Hv}(0)]^o$ is approximately that postulated for the molecule in MSA. It is of course not possible to assign this contribution to the molecular properties but nonetheless it is apparent the molecule or portions of the molecule are more ordered in the salt solution. It is useful to estimate the molecular dimensions from the result obtained from the Hv scattering component of AILS of SPBT-36 with added salt.

It is convenient to discuss the AILS results for component two of SPBT-36+salt first. The lengths obtained from the component analysis of the Rayleigh ratio are close to that obtained for the centrifuged sample before decomposition as seen from table 4. Furthermore, the molecular obtained for this component is approximately equal to the molecular weight from the total Vv component of the Rayleigh scattering from the centrifuged sample . This implies that this component may be the smallest aggregate formed in solution. It is interesting to note L_2 for the salt solutions is twice L_V for the centrifuged MSA sample as are the molecular weights. A speculation is the aggregate of the salt solution is formed by a dimer of the

aggregate in MSA. The length obtained using a rodlike model for the centrifuged sample is approximately equal to L_2.

From the total $[Kc/R_{Vv}(0)]^o$, the uncentrifuged and centrifuged samples for the solution with added salt differ by a factor of two. This leads to a speculation that the aggregate formed in the uncentrifuged is formed from a dimer of aggregates found in the salt solution. The intense Hv scattering suggests the rodlike segments have a high degree of orientational correlation.

The discrepancy found in the results of the lengths $L_{\equiv}$ for the uncentrifuged and centrifuged samples from $L_{G,Vv}$ leads to conclusion SPBT-36 in MSA is not a rodlike molecule.

The length $L_{\equiv}$ for component three for the centrifuged sample of SPBT-36+salt does not agree with L_3 from the Rayleigh ratio.

LOW IONIC STRENGTH STUDIES

In the early classical light scattering studies, it was found that changing the ionic strength of the solvent by the addition of low molecular weight salts or pH, the dimensions and the second virial coefficient of the polymer are changed. Although this topic is still one of current theoretical investigations, it is agreed these effects are due to long range electrostatic interactions absent in neutral polymers. In recent years, the influence of the long range electrostatic interactions on chain dynamics have been investigated. Using dynamic light scattering, studies on dilute suspensions of charged latex spheres in a low ionic strength media indicate long range order between spheres. The spheres have been found to be in regular packed geometries. As a consequence, there is a decrease in scattered intensity due to the destructive interference from the correlated scattering centers. Also studies with poly-lysine have shown an 'ordinary to extraordinary' transition where long range forces are postulated to create a lattice-like structure between molecules.

The effect of low ionic strength solvents was studied using SPBO-4 using CSA (chlorosulfonic acid) and MSA which have ionic strengths of ~ 0.02 and 0.1 respectively.

1.3.11 SPBO-4 in CSA or MSA

ABSOLUTE INTENSITY LIGHT SCATTERING

The most striking difference between data on solutions of SPBO-4 in CSA and MSA is the Hv AILS scattering. The Hv scattering peak in the emission spectrum of SPBO-4/CSA, small in SPBO-4/MSA, is large as shown in figure 131.

Another effect of utilizing the low ionic strength CSA solvent is more clearly seen in the angular dependence of the Rayleigh ratio prior to sample centrifugation, as shown in figures 132 and 142 of SPBO-4 in CSA and MSA respectively. Note the magnitude of $Kc/R_{Vv}(\theta)$ decreases by a factor of 10 in CSA. As the polymer concentration increases in CSA, the angular dependence of $Kc/R_{Vv}(\theta)$ increases, indicating aggregation which is concentration dependent. Also, the intensity which is the reciprocal of $Kc/R_{Vv}(0)$ decreases. There is increased low angle scattering causing deviation from the linear angular dependence of $Kc/R_{Vv}(\theta)$, indicative of aggregation. The concentration dependence of $Kc/R_{Vv}(0)$ is large as shown in figure 133, indicating a large second virial coefficient. These effects have been attributed to electrostatic interactions in solution. A discussion of the role of electrostatic interactions will be given after the presentation of the dynamic light scattering results.

The angular dependence of $Kc/R_{Hv}(\theta)$ is concentration dependent and parallels the behavior of the Vv AILS data as shown in figure 134. The magnitude of this intense Hv scattering is in some cases comparable to the Vv scattered intensities. This result is very unusual, but can be understood as a competition between the enhanced short-range orientational correlation, which increases R_{Hv}, and enhanced long-range spatial correlation among the scattering entities. The latter which increases with increasing concentration,causing R_{Vv} to decrease with increasing concentration due to interparticle interference. In very low ionic strength solvents, the Debye screening length increases as the inverse of square-root of the ionic strength and the molecules have a large excluded volume. At low concentrations, the scattering moieties are held in a pseudo-lattice order, As the concentration increases, the

effects of excluded volume become more pronounced. The ordering between scattering entities becomes more perfect, causing destructive interparticle interference and a decrease in the observed scattered intensity.

After centrifugation, the intensity of the Hv scattered light decreases by an order of magnitude with a decrease in the angular dependence of $Kc/R_{Hv}(\theta)$ shown in figure 134. This is to be expected if the aggregates are removed upon sedimentation. The quantity $Kc/R_{Hv}(0)$ is concentration dependent as shown in figure 135.

After centrifugation, there is also a dramatic change of $Kc/R_{Vv}(\theta)$, as shown in figure 132. The concentration dependence of the angular dependence of $Kc/R_{Vv}(\theta)$ and $Kc/R_{Vv}(0)$ are quite different. This result is consistent with the notion of large aggregates being removed by sedimentation. The increased scattering intensity at the two higher concentrations is observed while at the two lower concentrations a decrease is observed.

The effects of sonication are to increase the angular dependence of $Kc/R_{Vv}(\theta)$, as shown in figure 136, and to decrease in $[Kc/R_{Vv}(0)]^o$, as shown in figure 137. Upon centrifugation, the angular dependence of $Kc/R_{Vv}(\theta)$ and $Kc/R_{Hv}(\theta)$ decrease as shown in figure 138. Centrifugation does not affect the results obtained for $Kc/R_{Hv}(\theta)$ for the sonicated samples.

The experimental parameters are listed in table 17 for the SPBO-4/CSA prior to and after sonication respectively. The data of $Kc/R_{Hv}(0)$ was extrapolated to the same zero concentration value irrespective of sample treatment since the Hv scattering component is attributed to the molecular species and the concentration dependence of the Hv scattering component is not influenced by the second virial coefficient. The Hv scattering intensity was very weak, making extrapolation to zero concentration difficult. The second virial coefficient was extremely large, making extrapolation to zero concentration hazardous.

DYNAMIC LIGHT SCATTERING

The scattering intensity from these solutions is weak, as is observed in other experiments conducted in low ionic strength medium[2]. Owing to the weak scattering, the autocorrelation functions were not accurate enough to warrant a component analysis at all concentrations; the first cumulant could always be evaluated easily. Moreover, the lower solvent viscosity caused the time constants to be in limiting range of the correlator in use. The results of decomposition of the autocorrelation function made for a few concentrations are shown in figure 140 and 141 and listed in table 17.

INTERPRETATION OF LIGHT SCATTERING DATA

The effects of lowering the solvent ionic strength are decreased scattering intensity and increasing intermolecular association. The first effect is consistent with previous experimental observation[15-16]. With results on the rodlike counterparts studied in this laboratory the interactions were intermolecular since the chains were already fully extended. The long range nature of the electrostatic interactions created a pseudo-lattice ordering of the rodlike molecules, decreasing the scattering intensity through destructive interparticle interference effects. This resulted in a decreased absolute intensity and extremely long correlation times in the dynamic light scattering experiments.

In the present case, chain extension or an intramolecular ordering of the rodlike segments may play a role as the ionic strength is lowered, as evidenced by the presence of an Hv AILS component, small in the higher ionic strength solvent (MSA). In previous articulated copolymers studied. especially the cases where salt was added, the presence of Hv scattering was attributed to aggregation and specifically to orientational correlation between rodlike segments, primarily intermolecular in origin. This result suggests CSA is not a better solvent than MSA in spite of a large second virial coefficient in CSA. This is disappointing, since it was thought that CSA might be a better solvent in achieving a 'molecular' solvation. The solvation

mechanism requires protonation of the polymer backbone and subsequent dissolution through electrostatic repulsion. In CSA, the Debye screening length is large, creating a maximum repulsive energy and a 'molecular' solution. This was the result for the rodlike molecules, although the large second virial coefficient prevented conclusive results. Apparently, the introduction of a few flexible segments into an otherwise rodlike molecule causes aggregation. This result is also in contrast to the results found in coil-like molecules where chain expansion and a large second virial coefficient are the primary effects of lowering ionic strength. Perhaps, the 'all or nothing' solvation of the rodlike molecules is prohibited by the flexible segments. A few rodlike segments in the molecule could be protonated without molecular dissolution.

SPBO 4/MSA

ABSOLUTE INTENSITY LIGHT SCATTERING

As previously noted, the Hv emission spectrum for SPBO-4/MSA contains only a small peak at the wavelength of the incident light. This contribution is too weak to be used in the analysis of the R_{Hv} scattering.

The Vv scattering component of SPBO 4/MSA is notable for the absence of increased low angle scattering causing $Kc/R_{Vv}(\theta)$ to deviate from a linear angular dependence extrapolated from data obtained at high scattering angles as shown in figures 142a and 142b for the centrifuged and uncentrifuged samples respectively. The concentration dependence of $Kc/R_{Vv}(0)$ is shown in figure 143 for the uncentrifuged and centrifuged sample. The results of SPBO-4 in CSA are also shown for comparison. It can be seen that the second virial coefficient is smaller in MSA.

DYNAMIC LIGHT SCATTERING

The autocorrelation function displayed the characteristic deviation from a single exponential with components biasing the autocorrelation function at long times. The results of decomposition into components is shown in figure 144 . Using the weighting factors obtained through dynamic light scattering to decompose the Rayleigh ratio, a quasi-binary component system can be obtained as shown in figure 145 . The concentration dependence of $Kc/R_{Vv}(0)$ is shown in figure 146. The experimental parameters are listed in table 18.

INTERPRETATION OF LIGHT SCATTERING RESULTS

Since the Hv scattering peak is negligibly small , it is not unreasonable to postulate SPBO-4/MSA is coil-like in solution. If R_G is calculated from M_w using the model discussed previously with $\langle \ell \rangle_1 = 12.1$ nm and n=45.4, the value 40 nm is approximately equal to the experimentally observed $R_{G,Vv}$. The discrepancy between this and the measured value of $R_{G,Vv}$ is attributed to the experimental error and the crudeness of the model employed. The observed $R_{H,1}$ is consistent with the value expected for coil-like molecules. The value of $R_{H,2}$ reported for SPBO-4 is small, probably

indicative of lower molecular weight species. If this scattering moiety has a coil-like conformation, the corresponding R_G is 4 nm, which is too small to be experimentally observed, in the angular dependence of the scattered light intensity.

1.3.12 SPBO-96/MSA

ABSOLUTE INTENSITY LIGHT SCATTERING

This sample exhibits a small Hv scattering peak in the emission spectrum, typical of the articulated copolymers and consequently $Kc/R_{Hv}(\theta)$ was not measured.

The Vv component of the AILS prior to centrifugation deviated from the linear behavior extrapolated from the high scattering angles as shown in figure 147b. After centrifugation, the Vv component of AILS exhibited a linear angular dependence over the entire angular range studied.

The Vv component was examined prior to and after sonication, uncentrifuged and centrifuged. Prior to sonication, the uncentrifuged sample exhibits a large deviation at low scattering angles from the linear angular dependence of $Kc/R_{Vv}(\theta)$ extrapolated from high scattering angles, as shown in figure 147. After centrifugation, $Kc/R_{Vv}(\theta)$ is linear with scattering angle and the magnitude of $d[Kc/R_{Vv}(\theta)]/d\ sin^2/2$ becomes smaller, as shown in figure 147b, indicating aggregates have been removed by sedimentation. The value of $[Kc/R_{Vv}(0)]^o$ shown in figure 148 increases upon centrifugation, another indication large moities have been removed. The experimental parameters obtained are listed in Table 19.

After sonication, the abnormally intense low angle scattering due to aggregation is absent, as shown in figure 149. The magnitude of $dKc/R_{Vv}(\theta)/d\ sin^2/2$ is comparable to the centrifuged sample prior sonication.

The effect of sonication is illustrated after centrifugation in figure FIG54B. The magnitude of $d[Kc/R_{Vv}(\theta)]/d\ sin^2\ \theta/2$ becomes smaller. Inspection of $[Kc/R_{Vv}(0)]^o$ as a function of sample treatment shows the largest value is after sonication and centrifugation. Sonication has the effect of breaking apart the aggregates. There is also an interesting observation with the sonicated sample. The concentration dependence of $[Kc/R_{Vv}(0)]^o$ is constant ie. the second virial coefficient becomes small to zero shown in figure 150, in contrast to the value prior to sonication.

DYNAMIC LIGHT SCATTERING

The results of the decomposition of the autocorrelation function into components is shown in figures 151 and 152. The component with the longer relaxation time made the dominant contribution to the scattered intensity as a function of angle. The experimental parameter $R_{H,i}$ is listed in table 19 for each component.

The weighting factors r_i were used to decompose the Rayleigh ratio. The results are shown for the sample prior to centrifugation in figure 153a and after centrifugation in figure 153b. The magnitude of $dKc/R_{Vv,1}(\theta)/d\sin^2 \theta/2$ is essentially that of the Rayleigh ratio prior to decomposition regardless of sample treatment. The angular dependence of component two is too small to determine. The concentration dependence of each component prior to and after centrifugation is shown in figure 155. The experimental parameters are listed in table 19.

INTERPRETATION OF LIGHT SCATTERING DATA

If R_G is calculated from M_w using the the previously discussed model for the freely rotating chain using $\langle \ell \rangle_1 = 12.7$ nm, n=123 for the uncentrifuged sample, the value 58 nm is larger than $R_{G,Vv}$ experimentally observed. The differences may be within experimental error and the crude approximation used to calculate R_G, but the disparity may indicate that the chains are aggregated to form an irregular structure somewhat similar to a randomly branched molecule, so that M_w is larger than is expected for the measured R_G. The decrease of M_w and R_G on centrifugation is consistent with this proposal. From the experimentally observed $R_{G,Vv}$, the molecular weight of the moiety is calculated to be 8.1×10^4 using the above model with n=18. The aggregated species in solution can be modelled as coil-like conformers.

If R_G is calculated from the molecular weights of the uncentrifuged components, the values are consistent with the experimentally observed R_G. The components in solution can be modelled with coil-like conformations. The discrepancy in the values of R_G for the centrifuged samples could be due to the uncertainty in the concentrations of the solutions or experimental error.

The value of $R_{H,2}$ is consistent with R_G for a coil-like conformer.

1.3.13 SPBO-39/MSA

ABSOLUTE INTENSITY LIGHT SCATTERING

A nonnegligble Hv scattering component was observed for SPBO-39 in MSA which is unusual for the articulated copolymers. The fluorescence contribution to the Vv scattered light component was negligibly small, as can be seen in figure156. This is also unusual since most samples were strongly fluorescent.

The Vv component of AILS is shown in figure 157 for the uncentrifuged and centrifuged samples . The two lowest concentrations exhibit a larger $d[Kc/R_{Vv}(\theta)]/d\sin^2\theta/2$ than the two higher concentrations. After centrifugation, $d[Kc/R_{Vv}(\theta)/d\sin^2\theta/2$ becomes concentration independent. This suggests that the formation large moieties are concentration dependent and were removed upon centrifugation although the low angle scattering data did not deviate from the linear behavior of $Kc/R_{Vv}(\theta)$ extrapolated from high scattering angles versus angle. The concentration dependence of $Kc/R_{Vv}(0)$ is shown in figure158. The zero concentration intercept is the same prior to and after centrifugation. The experimental parameters are listed in table 20.

DYNAMIC LIGHT SCATTERING

The autocorrelation functions for SPBO-39/MSA show behavior characteristic of aggregation, that is long time components and deviations from an exponential decay. The results of a component analysis for the dynamic light scattering experiments are shown in figures 159 and 160. The angular dependence of the weighting factors for the two components are complementary, as the scattering angle increases, r_1 decreases. If the species corresponding to r_1 is attributed to aggregation, it is expected the contribution to the scattering factor will decrease with increasing angle. Conversely, the contribution from the smaller component will appear to increase as the contribution from the large aggregate decreases.

If the components are assumed to form a quasi-binary system, in principle, the Rayleigh ratio can be decomposed using the weighting factors r_i. The results from such an analysis are shown in figures 161-163. With the centrifuged sample did not

exhibit a physical behavior such that the values of $Kc/R_{Vv}(0)$ were not monotone functions of c, for unknown reasons. Experimental parameters are listed in table 20. The apparent experimental parameters for component one is essentially equal to that found prior to decomposition of the Rayleigh ratio.

INTERPRETATION OF LIGHT SCATTERING DATA

The strong R_{Hv} intensities, and the nature of the R_{Vv} scattering and the dynamic scattering together indicate the presence of large aggregates, with the possibility of a reasonable degree of orientational correlation among the rodlike segments comprising the aggregates. The macroscopic value of $\delta = 0.18$ for the effective scatterers is smaller than the molecular value of 0.5, indicating less than complete parallel organization in the aggregate. The large $\delta^2 M_{w,Hv}$ could result from an overall rodlike aggregate with a tendency for parallel organization of the rodlike subunits, or from a fringed micelle-like model with an overall coil-like shape and a few micellar-like crosslink loci comprising structure with a highly parallel arrangements of the components.

The observed value of $R_{G,Vv}$ is smaller than that expected for a thin rodlike structure with molecular weight $M_w = 1.3 \times 10^5$. By contrast, the ratio of the values of $R_{G,2}$ and $R_{H,2}$ for the uncentrifuged sample is in reasonable accord with that expected for a coil. Thus, we speculate an overall coil-like aggregate stabilized by micellar-like loci with the components in parallel array.

From the previous results obtained from systems with added salt, aggregation formation leads to a more ordered conformation. This is also true for the sample SPBO-80 and SPBO-88 which have been reprecipitated from MSA. These samples are characterized by a relatively large Hv scattering peak in the emission spectra shown in figures FIG66A.

1.3.14 SPBO-80/MSA

ABSOLUTE INTENSITY LIGHT SCATTERING

The angular dependence of $Kc/R_{Vv}(\theta)$ for SPBO-80/MSA after sonication and centrifugation are not independent of concentration as shown in figure 165. There is also a notable lack of increased low angle scattered intensity characteristic of aggregation. The concentration dependence of $d[Kc/R_{Vv}(\theta)]/d \sin^2/2$ could be indicative of varying degrees of aggregation. This phenomena is more pronounced in the sample prior to sonication and the sonicated sample prior to centrifugation as shown in figures 169a and 169b respectively. The concentration dependence of $Kc/R_{Vv}(0)$ is shown in figure 166.

The Hv component of AILS also exhibits a concentration dependent $d[Kc/R_{Hv}(\theta)]/d \sin^2\theta/2$ as shown for the sample prior to sonication in figure 167a, after sonication in figure 170b and the centrifuged sonicated sample in figure 167. Although the data are scattered, the trend appears to be as concentration increases the magnitude of $d[Kc/R_{Hv}(\theta)]/d \sin^2\theta/2$ increases. This suggests as the size of the aggregate increases the orientational correlation between the rodlike segments increases. The results presented here are not corrected for he fluorescence contribution. This correction is large ($\sim$ 25 % of the total scattered intensity). Although the Hv AILS data are not corrected for fluorescence and absolute magnitudes of the experimental parameters are not available, the presence of Hv AILS implies aggregation and the relative magnitudes of $Kc/R_{Hv}(\theta)$ can be interpreted.

The experimental parameters are listed in table 21.

DYNAMIC LIGHT SCATTERING DATA

The autocorrelation function $g^{(2)}-1$ contained only 16 data points instead of the usual 32 or 64 points and so the long time behavior of SPBO-80 is not known. However, the first cumulant was evaluated. The hydrodynamic radii that were obtained are listed in table 21.

INTERPRETATION OF LIGHT SCATTERING DATA

The absolute value of R_{Hv} is not known for this sample due to fluorescence contribution to the scattered intensity. However, the Hv spectra indicates a strong Hv scattering for the uncentrifuged sample. Since the Hv spectra was not measured for the centrifuged, sonicated sample, it cannot be directly ascertained whether there is any Hv scattering or not. However, the magnitude of $\partial\, Kc/R_{Hv}(\delta)/\partial\, \sin^2 \delta/2$ and $Kc/R_{Hv}\delta$ are approximately the same for the uncentrifuged, sonicated and centrifuged samples, indicating that the Hv scattering persisted for the latter two materials. By contrast, for the Vv scattering changed greatly. The strong R_{Hv} suggests aggregation persists after centrifugation. The large R_{Hv} could result from an overall rodlike aggregate with a tendency towards parallel orientation of the rodlike segments or from a fringed micelle model with an overall coil-like shape and a few micellar-like crosslinked loci comprising structure with a highly parallel arrangement of the rodlike segments. The observed value of $J^{1/2}R_{Vv}$ is smaller than expected for a rodlike structure with $(1+(4/5)\delta^2)M_w=1.8\times10^4$. The value of R_H obtained for the centrifuged sample agrees well with the value of $R_{G,Vv}$ obtained for the sonicated and centrifuged sample if the species is assumed to have a coil-like conformation.

We speculate that, after centrifugation, an aggregate with an overall coil-like structure is stabilized by micellar loci with the rodlike segments in a parallel array. This is in contrast to the elongated aggregate postulated for the uncentrifuged sample.

The aggregate probably has orientation correlation between rodlike segments. It is not possible to ascertain the degree of organization of the rodlike segments in the

aggregate as the value of δ is unknown owing to the unknown contribution of fluorescent intensity in the measured Hv response.

The value of R_H for the uncentrifuged sample agrees well with the values of $J^{1/2}R_{G,Vv}$ for a rodlike structure, that is the ratio of R_H to R_G is ~ 1.7. The observed value of $J^{1/2}R_{G,Vv}$ is larger than that expected for a rodlike structure with $M_w = 2.9 \times 10^4$ d. The disparity ($J^{1/2}R_{G,Vv} \sim R_{G,Vv}$ is 50% larger than the value calculated from M_w) is difficult to assess as the effects of length heterogeneity and diameter have opposite effects on the value of R_G calculated from M_w with $J^{1/2}R_{G,Vv}$.

Both $Kc/R_{Vv}\delta$ and $\partial Kc/R_{Vv}\delta/\partial \sin^2 \delta/2$ are reduced by centrifugation, suggesting that the aggregates are the dominant contribution to the scattering prior to centrifugation. If the aggregate is assumed to be a prolate ellipsoid, then comparison of $R_{G,Vv}$ and R_H obtained prior to centrifugation gives a length of 290 nm and a diameter of 6 nm for the aggregate.

1.3.15 SPBO-88/MSA

ABSOLUTE INTENSITY LIGHT SCATTERING

The Vv component of AILS of SPBO-88/MSA has a large angular dependence which is concentration dependent, as shown in fig.172 At the two highest concentrations, $dKc/R_{Vv}(\theta)/d \sin^2 \theta/2$ is 50 % greater than found at the lowest concentration. This suggests a state of aggregation that is concentration dependent. The low angle scattering exhibits a slight deviation from the linear angular dependence from the data extrapolated from high scattering angles. This is unusual behavior since most samples studied here contain aggregates which contribute to a large forward scattering intensity causing a deviation at low scattering angles from the linear angular dependence extrapolated from data at high scattering angles. The concentration dependence of $Kc/R_{Vv}(0)$ is shown in figure 173.

After centrifugation, the angular dependence of $Kc/R_{Vv}(\theta)$ is independent of concentration and a factor of two smaller. The magnitude of $Kc/R_{Vv}(\theta)$ decreases by a factor of 2. This indicates large moities removed by sedimentation. The lack of an increased low angle scattering intensity, characteristic of aggregation, indicates sedimentation was effective in removing the aggregated species. The concentration dependence of $Kc/R_{Vv}(0)$ is shown in figure 173.

The angular dependence of $Kc/R_{Hv}(\theta)$ prior to centrifugation is larger than after centrifugation as shown in figure 174. This sample has been subjected to precipitation from MSA which has been shown to increase aggregation. From the previous discussions involving the addition of salt where ordered aggregates resulted, it is possible the aggregates formed in this case are ordered and removed by sedimentation. The concentration dependence of $Kc/R_{Hv}(0)$ is shown in figure 175. The large change of $[Kc/R_{Hv}(0)]^o$ indicates the loss of higher molecular weight aggregates upon centrifugation.

DYNAMIC LIGHT SCATTERING

The dynamic light scattering was performed on a sample prepared from a stock solution that had been sonicated for 1 hour and centrifuged for 24 hours in which a portion of the solution was removed prior to the preparation of the solutions used for light scattering. The autocorrelation functions were decomposed into components. The weighting factors r_i and $\tau_i \sin^2 \theta/2$ are shown as a function of concentration in figures 176 and 177. The hydrodynamic radii of the two components is listed in table 22.

INTERPRETATION OF LIGHT SCATTERING DATA

Prior to sonication and centrifugation, the scattering data reveal large species and substantial Hv scattering. Since $J^{1/2}R_{G,Vv}$ and $f_3 R_{G,Hv}$ differ greatly, it must be assumed that the order obtained in the scattering species is not large (ie. either f_3 or $R_{G,Hv}$ must be small). A possible model would be a large overall disordered structure with localized small loci exhibiting a high degree of local orientation of the rodlike chain elements, (ie., large f_3 but small $R_{G,Hv}$ for these loci). This represents a kind of fringed micelle model. The observed $J^{1/2}R_{G,Vv}$ is 50% larger than the R_G calculated from M_w on the assumption of a rodlike conformation; this may indicate that with the uncentrifuged specimen, the sample consists of a heterodisperse collection of rodlike aggregates.

Surprisingly, after sonication, both $J^{1/2}R_{G,Vv}$ and M_w are increased. This may indicate that the original aggregate structure was partially loosened during sonication, to permit reformation of larger, more open structures after sonication. Significant Hv scattering with $f_3 R_{G,Hv}$ less than $J^{1/2}R_{G,Vv}$ appears to be consistent with a fringed micelle model. After the sonicated sample is centrifuged, both M_w and $R_{G,Vv}$ decrease , as do $\delta^2 M_{w,Hv}$ and $f_3 R_{G,Hv}$. The centrifugation apparently removed some of the larger aggregates, but did not result in a molecular dispersion (ie., Hv is still too large, indicating the presence of ordered loci of aggregated rodlike chain elements).

The value of $R_{H,2}$ for the uncentrifuged sample is 7 nm and the value of R_G for a coil-like conformer with this R_H is 12 nm. The contribution to the Vv angular dependence would be small. The aggregate can be modelled as a prolate ellipsoid using the total $R_{G,V}$ measured as an estimate of the aggregate R_G and $R_{H,1}$. The prolate ellipsoid length is 590 nm and the diameter is 4 nm. Since the $R_{H,2}$ also small after centrifugation, the total $R_{G,V}$ can also be used as an estimate for the aggregate R_G in the prolate ellipsoid model. The length of the ellipsoid is 270 nm with a diameter of 8 nm.

We conclude the aggregates formed are highly extended with a high degree of orientational correlation among rodlike segments giving rise to the large values of R_{Hv} observed.

1.4 CONCLUSIONS

The effect of introducing articulation into rodlike polymers is to reduce the overall optical anisotropy of the chain. The free rotation about bonds of the articulated comonomer reduces the correlation of the anisotropy tensor along the chain backbone. This results in a decrease in the intensity of the Hv AILS component.

The introduction of flexible joints in a rodlike molecule has not resulted in enhanced solubility--these polymers are still only soluble in strong acids. As a result, the polyelectrolyte nature of the chains plays an important role in the determination of solution properties of the protonated polymers, especially in acids with low ionic strength. The polymers studied tend to aggregate in solution, and aggregation is promoted by increasing the ionic strength of the solvent.

From the studies of solutions with added salt, it was found that the intensity of R_{Hv} is a sensitive measure of the degree of orientational correlation between rodlike segments. The addition of salt promotes orientational correlation between rodlike segments, resulting in enhanced R_{Hv} intensity as well as $J^2 M_{w,Hv}$ as extensive aggregation of the molecules into ordered supra structures. For the rodlike PBT polymers, aggregation was postulated to form parallel bundles. This can be a desirable property in the processing of films and fibers. Understanding the process of aggregation is also important in the prediction for the behavior of solutions during processing.

It was hoped that samples received directly from the reaction mixture would be aggregate free. It was somewhat disappointing to discover the presence of metastable aggregates in the non-heat treated PBT-PBO copolymers. Furthermore, these metastable aggregates could be only partially degraded when a more drastic dissolution procedure was employed. Perhaps a molecular solution could be prepared if the dissolution conditions were more severe. Since it is known that precipitation of material from PPA causes metastable aggregation, it appears the samples in PPA hold the most promise for a truly molecular characterization.

It has been reported that the use of the low ionic strength solvent CSA for the study of rodlike polymers for the purpose of studying 'molecular' properties, the method of choice appears to lead to enhanced solvation. This is offset by experimental difficulties such as weak scattering intensities due to strong intermolecular effects and low solvent viscosity, placing dynamic light scattering measurements in a less convenient instrumental range. The former experimental difficulties, due to the exceeding long range electrostatic forces in solution, are alluded to in current literature for other polymers. For the articulated copolymer studied, a molecular solution was not obtained with CSA.

Estimate of 'molecular' properties can be obtained through the decomposition of the autocorrelation function into a number of discrete contributions, and the use of weighting factors so obtained to decompose the Rayleigh ratio into contributions from components. Interpretation of these results require a constant state of aggregation with concentration and that the overall concentration of the aggregates is small. It is important to recall this representation of the data is only a quasi-binary or ternary discrete system. In fact, each component represents a distribution of molecular weight species, If the above constraints are met, parameters for the components can be obtained from the experimental results. This method is useful to extract information from these polydisperse samples. It is of course, more desirable to achieve a molecular solution for the purposes of characterization.

References

1. E. R. Pike and E. Jakeman, *Adv. Quantum Electron.* **1974,** *2,* 1.

2. J. M. Schurr, *CRC Crit. Rev. in Biochem.* **1977,** *4,* 371.

3. B. J. Berne and R. Pecora, *Dynamic Light Scattering,* Wiley-interscience, New York, 1976, chapter 8.

4. B. Chu, *Laser Light Scattering,* Academic Press, New York, (1974).

5. Y. Einega and G. C. Berry, *J.Polym.Sci.,Polym.Phys.Ed.,* in press.

6. G. C. Berry, *J.Polym.Sci.,Polym.Phys.Ed.* **1978,** *65,* 143.

7. C.-P.Wong, H. Ohnuma, G. C. Berry, *J.Polym.Sci.,Polym.Symp.* **1978,** *65,* 173.

8. H. Yamakawa and M. Fujii, *Macromolecules* **1973,** *6407;* **1974,** *7,* 128.

9. E. Jakeman and E. R. Pike, *J.Phys.A* **1969,** *2,* 115.

10. E. Jakeman and E. R. Pike, *J.Phys.A* **1968,** *1,* 128.

11. G.Bedard, J.C.Chang, L. Mandel, *Phys.Rev.,***160,**1496,(1967).

12. E. Jakeman, *Photon Correlation in "Photon Correlation and Light Beating Spectroscopy",* H.Z.Cummins and E.R.Pike, eds.,Plenum Press, New York,1974.

13. E. F. Casassa and G. C. Berry, in *Polymer Molecular Weights,Part I,*R.E. Slade, Ed., Marcel Dekker, New York, 1975.

14. J. Perrin, *J.Phys.Radium* **1936,** *6,* 1.

15. P. Metzger Cotts, G. C. Berry, *J. Polym.Sci, Polym.Phys.Ed.* **1983,** *21,* 1255.

16. P. Metzger, Ph.D. Thesis, Carnegie-Mellon University, 1979.

Table 1 Sample Preparation for PBO Copolymers

Preparation	
1. stock solution in MSA	5. emission spectra (Hv,Vv)
2. diluted	6. AILS, IFLS
3. filtered through fine	uncentrifuged,centrifuged
sintered glass filter	7. sonication 1 hr.
4. cells flame sealed	AILS
under vacuum	

Sample	Supplie's code	Hv emission spectra
SPBO-88	SPBO-292-88	514.5nm, 633nm
SPBO-80	SPBO-292-80	633nm
SPBO-39	SPBO-352-39	633nm
SPBO-4/MSA	SPBO-352-4	514.5nm
SPBO-4/CSA	SPBO-352-4	633nm

Table 2 Sample Preparation for PBT and PBT copolymers

Preparation		
1. stock solution in MSA	5. filtered through teflon filter	
2. sonicated 1 hr.	6. cells flame sealed under vacuum	
3. precentifuged 24 hrs. (7000 rpm)	8. AILS and IFLS	
4. diluted	uncentrifuged,centrifuged	

SPBT-38	SPBT-352-38	514.5nm 633nm
SPBT-36	SPBT-352-36	633nm
SPBT-7	SPBT-388-7	633nm
SPBT-12	SPBT-388-12	514nm
SPBT-38+salt(ps+s)		
+1.09N		514nm
+0.53N		514nm
SPBT-38+salt(p+ss)		
+1.53N		514nm
+0.56N		514nm
SPBT-36+salt(ps+s)		
+1.09N		514nm
PBT-7+0.7N salt	PBT-2122-72-7	514nm
PBT-8+0.7N salt	PBT-2122-72-8	514nm
PBT-30 in PPA (9.2%)	2895-30	514nm 633nm
PBT-PBO(90/10) in PPA(7.7%)	4592-13	514nm
PBT-PBO(75/25) in PPA(5.7%)	4952-5	514nm

Table 3 Experimental parameters for PBT-30 in PPA/MSA

	uncent	cent
$(1+(4/5)\delta^2)M_{w,Vv}$	2.84×10^5	2.24×10^5
$\delta^2 M_{w,Hv}$	7.8×10^3	7.0×110^3
$J^{\frac{1}{2}}R_{G,Vv}$	140^a	130
$f_3 R_{G,Hv}$	22	14
$R_{H,1}$		
$R_{H,2}$	35	50
$R_{H,3}$	6	6
$w_1(1+(4/5)\delta^2)M_1$		
$J^{1/2}R_{G,1}$		
$w_2(1+(4/5)\delta^2)M_2$	5.4×10^5	1.1×10^5
$J^{1/2}R_{G,2}$	260	120
$w_3(1+(4/5)\delta^2)M_3$	2.6×10^4	2.6×10^4
$J^{1/2}R_{G,3}$	25	23

all lengths in nm

a) only at low c, eg. Figure 6

Table 4 Molecular Parameters Calculated for a Rodlke Conformer PBT-30 in PPA/MSA

	uncent	cent
$M_{w,Vv}$	2.37×10^5	1.87×10^5
$M_{w,Hv}$	3.1×10^4	2.8×10^4
$L_{G,V}$	580	525
$L_{G,H}$	75	50
L_V	1080	850
L_H	140	130
From $R_{H,i}$		
$L_{\Xi,2}$	400	620
$L_{\Xi,3}$	24	24
From $w_i M_{w,i}$		
$w_2 L_{V,2}$ [a]	2040	420
$w_3 L_{V,3}$ [a]	100	100

calculated with $\delta = 0.5$

all lengths in nm

Table 5 Experimental parameters for PBT-PBO (90/10) in PPA/MSA

	uncent	cent
$(1+(4/5)\delta^2)M_{w,Vv}$	8.7×10^5	1.3×10^5
$\delta^2 M_{w,Hv}$	1.0×10^4	9.0×10^3
$J^{\frac{1}{2}} R_{G,Vv}$	193	60
$f_3 R_{G,Hv}$	20	20
$R_{H,1}$	390	97
$R_{H,2}$	43	38
$R_{H,3}$	11	15
$w_1(1+(4/5)\delta^2)M_1$		
$J^{1/2} R_{G,1}$		
$w_2(1+(4/5)\delta^2)M_2$	7.4×10^5	4.9×10^5
$J^{1/2} R_{G,2}$	190	190
$w_3(1+(4/5)\delta^2)M_3$	4.4×10^4	4.4×1^4
$J^{1/2} R_{G,3}$	27	21

all lengths in nm

Table 6   Molecular Parameters Calculated for a Rodlke Conformer PBT-PBO (90/10) in PPA/MSA

	uncent	cent
$M_{w,Vv}$	7.2×10^5	1.3×10^5
$M_{w,Hv}$	4.1×10^4	3.6×10^4
$L_{G,V}$	900	280
$L_{G,H}$	70	60
L_V	3300	600
L_H	185	165
From $R_{H,i}$		
$L_{\Xi,1}$	7600	1350
$L_{\Xi,2}$	2200	420
$L_{\Xi,3}$	90	110
From $w_i M_{w,i}$		
$w_2 L_{V,2}$[a]	2800	1850
$w_3 L_{V,3}$[a]	170	170
From $R_{G,i}$		
$L_{2,V}$	900	900
$L_{3,V}$	100	115

calculated with $\delta = 0.5$

all lengths in nm

Table 7 Experimental parameters for PBT-PBO (75/25) in PPA/MSA

	uncent	cent
$(1+(4/5)\delta^2)M_{w,Vv}$	5.9×10^5	3.9×10^5
$\delta^2 M_{w,Hv}$		3.3×10^3
$J^{1/2}R_{G,Vv}$	110	105
$f_3 R_{G,Hv}{}^a$	8	8
$R_{H,1}$		
$R_{H,2}$	73	55
$R_{H,3}$	4	4.4
$w_1(1+(4/5)\delta^2)M_1$		
$J^{1/2}R_{G,1}$		
$w_2(1+(4/5)\delta^2)M_2$	1.9×10^6	6.2×10^4
$J^{1/2}R_{G,2}$	490	54
$w_3(1+(4/5)\delta^2)M_3$	6.7×10^4	3.4×10^4
$J^{1/2}R_{G,3}$	44	23

all lengths in nm

a) as $c \rightarrow 0$

Table 8 Experimental parameters for PBT-8 + salt at 514.5 nm and 25.0°

	uncent	cent	without salt
$(1+(4/5)\delta^2)M_{w,Vv}$	9.5×10^5	1.2×10^5	0.36×10^5
$\delta^2 M_{w,Hv}$	$3.3 \times 10^{4*}$	$1.1 \times 10^{4*}$	0.33×10^4
$J^{1/2}R_{G,Vv}$	185	60	43
$f_3 R_{G,Hv}$	22	14	24
$R_{H,1}$	89	89	
$R_{H,2}$	22	9	
$R_{H,3}$	3	2	
$w_1(1+(4/5)\delta^2)M_1$	6.3×10^7	7.5×10^5	
$J^{1/2}R_{G,1}$	8000		
$w_2(1+(4/5)\delta^2)M_2$	5.7×10^4	7.3×10^4	
$J^{1/2}R_{G,2}$	40	30	
$w_3(1+(4/5)\delta^2)M_3$		1.9×10^4	
$J^{1/2}R_{G,3}$		10	

all lengths in nm

* values as $c \rightarrow 0$

Table 9   Experimental parameters for PBT-7 + salt at 514.5 nm and 25.0°

	uncent	cent	without salt
$(1+(4/5)\delta^2)M_{w,Vv}$	4.7×10^5	5.8×10^5	0.42×10^5
$\delta^2 M_{w,Hv}$	$6.1 \times 10^{4*}$	$6.1 \times 10^{4*}$	0.35×10^4
$J^{\frac{1}{2}} R_{G,Vv}$	85^*	20^*	50
$f_3 R_{G,Hv}$	20	25	
δ	0.34	0.38	0.3
$R_{H,1}$	130	130	
$R_{H,2}$	30	30	
$R_{H,3}$	6	3	
$w_1(1+(4/5)\delta^2)M_1$	2.3×10^9	1.3×10^9	
$J^{1/2} R_{G,1}$	5000	140^*	
$w_2(1+(4/5)\delta^2)M_2$	1.1×10^7	6.3×10^5	
$J^{1/2} R_{G,2}$	1300	85	
$w_3(1+(4/5)\delta^2)M_3$	2.5×10^4		
$J^{1/2} R_{G,3}$	6		

all lengths in nm

* values at $c \to 0$

85

Table 10 Experimental parameters for SPBT-38/MSA at 514.5 nm and 25.0°

	uncent	cent
$(1+(4/5)\delta^2)M_{w,Vv}$	1.04×10^5	0.79×10^5
$J^{1/2}R_{G,Vv}$	30	25
$R_{H,2}$	80	8*
$R_{H,3}$	5	2*
$w_2(1+(4/5)\delta^2)M_2$	1.5×10^5	8.4×10^4
$J^{1/2}R_{G,2}$	40	14
$w_3(1+(4/5)\delta^2)M_3$	8.3×10^3	

all lengths in nm

* experiments performed at 15.0° C

Table 11 Experimental parameters for SPBT-36/MSA at 632.8 nm and 25.0° C

	uncent	cent
$(1+(4/5)\delta^2)M_{w,Vv}$	1.6×10^5	3.1×10^4
$\delta^2 M_{w,Hv}$	0.27×10^4	0.40×10^4
$J^{1/2}R_{G,Vv}$	150	50
$f_3 R_{G,Hv}$	70	18
$R_{H,2}$	97	34
$R_{H,3}$	12	

all lengths in nm

dynamic light scattering performed at 514.5 nm and 25.0°C

Table 12 Experimental parameters for SPBT-7/MSA

	uncent	cent
$(1+(4/5)\delta^2)M_{w,Vv}$	5.1×10^5	4.3×10^4
$\delta^2 M_{w,Hv}$		
$J^{1/2}R_{G,Vv}$	500	110
$f_3 R_{G,Hv}$		
$R_{H,2}$	130	60
$R_{H,3}$	7.3	6.3
$w_2(1+(4/5)\delta^2)M_2$	1.3×10^5	7.6×10^2
$J^{1/2}R_{G,2}$	190	
$w_3(1+(4/5)\delta^2)M_3$	8.2×10^3	

all lengths in nm

Dynamic light scattering performed at 514.5 nm and 25.0° C

Table 13 Experimental parameters for SPBT-12/MSA at 514.5 nm and 25.0°C

	uncent	cent
$M_{w,Vv}$	1.4×10^5	7.8×10^4
$R_{G,Vv}$	60	30

all lengths in nm

Table 14 Experimental parameters for SPBT-38 (ps+s) solutions at 514.5 nm and 25.0°

	uncent	cent	uncent	cent
$(1+(4/5)\delta^2)M_{w,Vv}$	1.4×10^{5}	4.5×10^{4}	3.5×10^{5}	4.6×10^{4}
$\delta^2 M_{w,Hv}$	1.15×10^{4}	0.35×10^{4}		
$J^{1/2}R_{G,Vv}$	71	32	115	35
$f_3 R_{G,Hv}$	32	8–13	22–40	12–17
$R_{H,1}$		285	300	250
$R_{H,2}$	22	22	30	13
$R_{H,3}$	3	6.5	4	1
$L_{p,2}$	310	140	510	160

all lengths in nm

Table 15   Experimental parameters for SPBT-38 (p+ss solutions at 514.5 nm and 25.0°)

	uncent	cent	uncent	cent	
$(1+(4/5)\delta^2)M_{w,Vv}$		2.6×10^5	8.65×10^4	2.4×10^5	1.8×10^5
$\delta^2 M_{w,Hv}$	0.42×10^4	0.42×10^4	0.85×10^4		
$J^{1/2}R_{G,Vv}$	80-90	35	50-100	30-50	
$f_3 R_{G,Hv}$	10-25	17	25-32	10-27	
$R_{H,1}$	90	135		210	
$R_{H,2}$		22	17	17	
$R_{H,3}$	1	3	4	4	
$L_{p,2}$	160	350	180		

all lengths in nm

Table 16 Experimental parameters for SPBT-36 + salt at 514.5 nm and 25.0°C

	uncent	cent
$(1+(4/5)\delta^2)M_{w,Vv}$	8.2×10^4	4.4×10^4
$\delta^2 M_{w,Hv}$	3.1×10^3	2.3×10^3
$J^{\frac{1}{2}}R_{G,Vv}$	36*	30
$f_3 R_{G,Hv}$	30	15
$R_{H,2}$	20	16
$R_{H,3}$	4	4
$w_2(1+(4/5)\delta^2)M_2$	5.7×10^4	4.2×10^4
$J^{1/2}R_{G,2}$		
$w_3(1+(4/5)\delta^2)M_3$		
$J^{1/2}R_{G,3}$		

all lengths in nm

* value as $c \to 0$

Table 17 Experimental parameters for SPBO-4/CSA at 632.8 nm and 25.0°C

	uncent	cent
$(1+(4/5)\delta^2)M_{w,Vv}$		
$\delta^2 M_{w,Hv}$	7.4×10^3	
$J^{1/2} R_{G,Vv}$		
$f_3 R_{G,Hv}$	35[*]	
$R_{H,2}$	87	
$R_{H,3}$	2	

all lengths in nm

[*] value as c→0

dynamic light scattering performed at 514.5 nm and 25.0°C

Table 18 Experimental parameters for SPBO-4/MSA

	uncent	cent
$M_{w,Vv}$	1.0×10^5	9.2×10^5
$R_{G,Vv}$	20	20
$R_{H,2}$	24	
$R_{H,3}$	2.4	
$w_2 M_2$	9.8×1^4	
$R_{G,2}$	32	
$w_3 M_3$	6.4×10^3	
$R_{G,3}$		

all lengths in nm

Table 19 Experimental parameters for SPBO-96/MSA at 514.5 nm and 25.0°C

	uncent	cent	sonicated	cent
$M_{w,Vv}$	5.7×10^5	4.0×10^5	2.1×10^5	1.9×10^5
$R_{G,Vv}$	64	45	48	30
$R_{H,2}$				
$R_{H,3}$				
$w_2 M_2$	7.2×10^5	7.2×10^5		
$R_{G,2}$	100	40		
$w_3 M_3$	1.5×10^5	1.5×10^5		
$R_{G,3}$				

all lengths in nm

Table 20 Experimental parameters for SPBT-39/MSA at 632.8 nm and 25.0°C

	uncent	cent
$(1+(4/5)\delta^2)M_{w,Vv}$	1.3×10^5	1.3×10^5
$\delta^2 M_{w,Hv}$	4.2×10^3	4.2×10^3
$J^{\frac{1}{2}}R_{G,Vv}$	77	80
$f_3 R_{G,Hv}$		
$R_{H,2}$		
$R_{H,3}$	2.4	
$w_2(1+(4/5)\delta^2)M_2$	$1. \times 10^5$	1.4×10^5
$J^{1/2}R_{G,2}$		73
$w_3(1+(4/5)\delta^2)M_3$		
$J^{1/2}R_{G,3}$	5	

all lengths in nm

dynamic light scatteringg performed at 514.5 nm and 25.0°C

Table 21 Experimental parameters for SPBO-80/MSA at 632.8 nm and 25.0°C

	uncent	sonicated	cent
$(1+(4/5)\delta^2)M_{w,Vv}$	2.9×10^4	6.2×10^4	1.8×10^4
$\delta^2 M_{w,Hv}$	2.2×10^3	2.7×10^3	1.5×10^3
$J^{\frac{1}{2}}R_{G,Vv}$	65\200	45	
$f_3 R_{G,Hv}$	6	25	10
R_H	32	25	

all lengths in nm

dynamic light scattering performed at 514.5 nm and 25.0°C

Table 22 Experimental parameters for SPBO-88/MSA at 632.8 nm and 25.0°C

	uncent	cent
$(1+(4/5)\delta^2)M_{w,Vv}$	6.9×10^4	2.7×10^4
$\delta^2 M_{w,Hv}$	6.3×10^3	3.8×10^3
$J^{1/2}R_{G,Vv}$	110	60
$f_3 R_{G,Hv}$	20	23
$R_{H,2}$	45	32
$R_{H,3}$	7	
all lengths in nm		

dynamic light scattering performed at 514.5 nm and 25.0°C
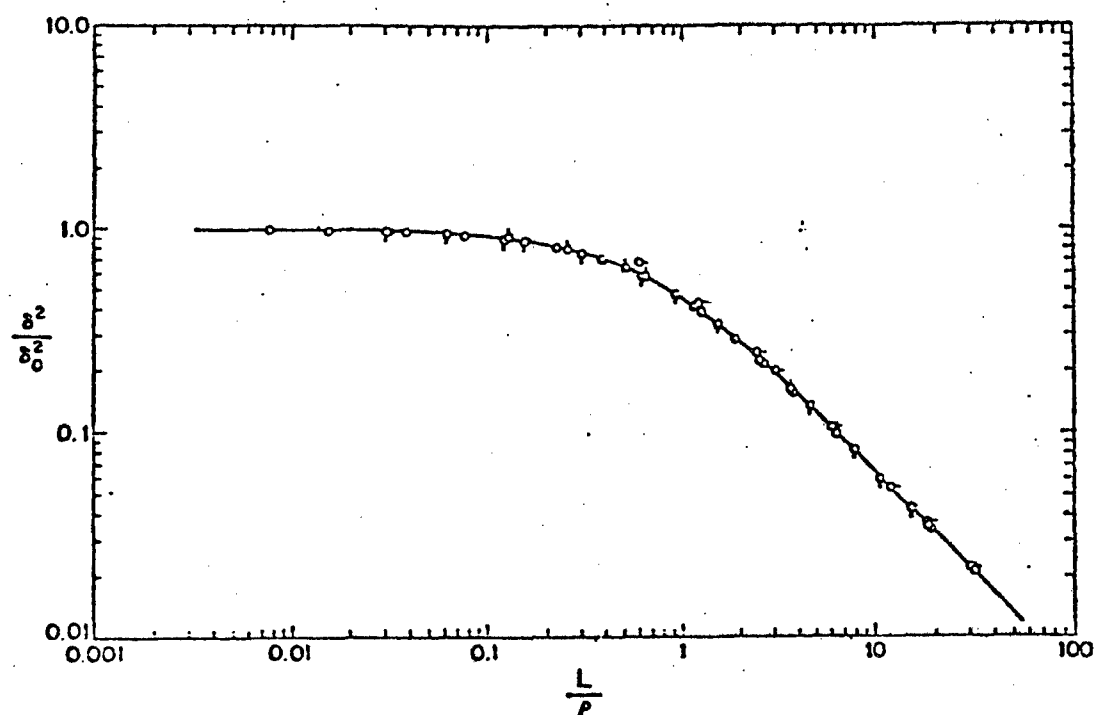
Figure 1: Overall anisotropy δ^2 for a polymer chain with free
rotation about bonds with valence angles $(\pi - \alpha)$ with a=cos
α and N the number of bonds. The points are calculated with
$\alpha=5°$, O; $10°$, O; $20°$, Q; and $40°$, O. The solid
curve gives δ^2/δ_o versus L/ρ according to equation
14

99
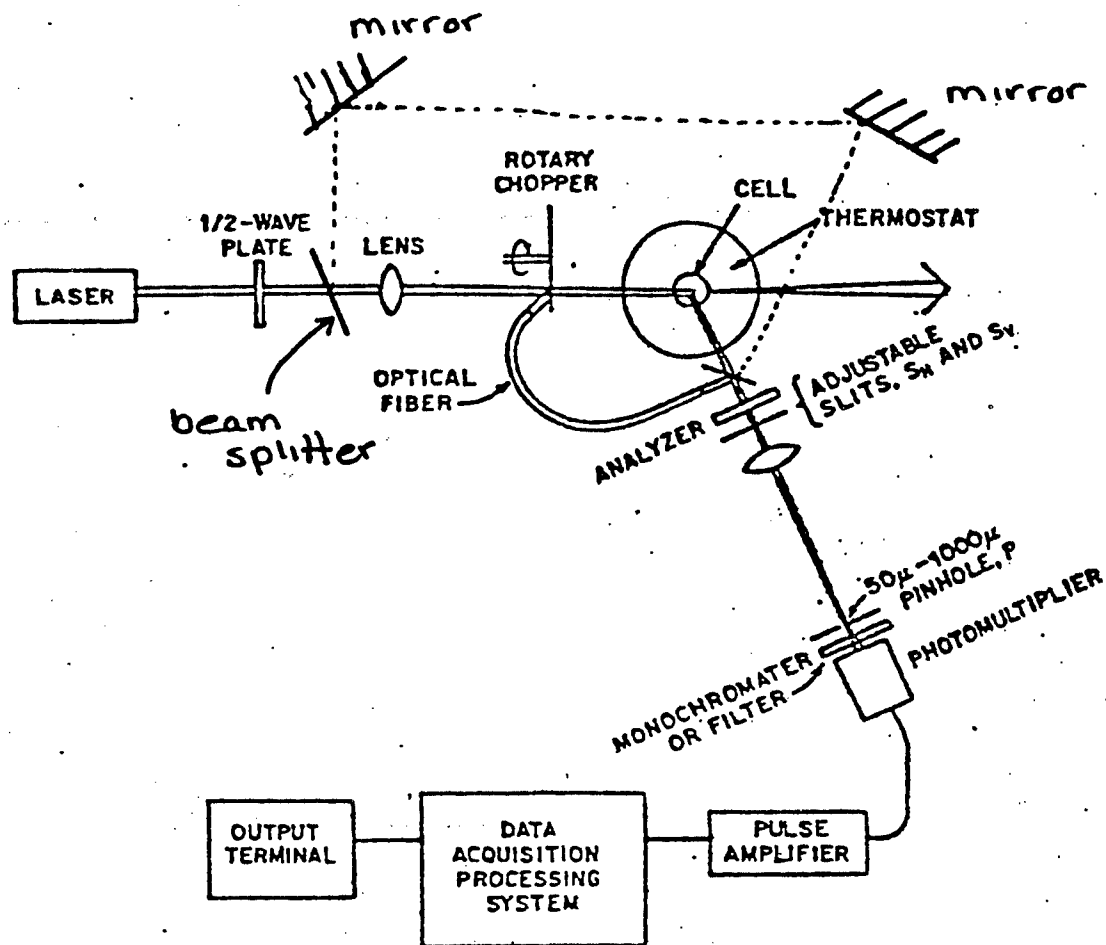
Figure 2: Schematic diagram of light scattering apparatus showing the principal components discussed in the text.
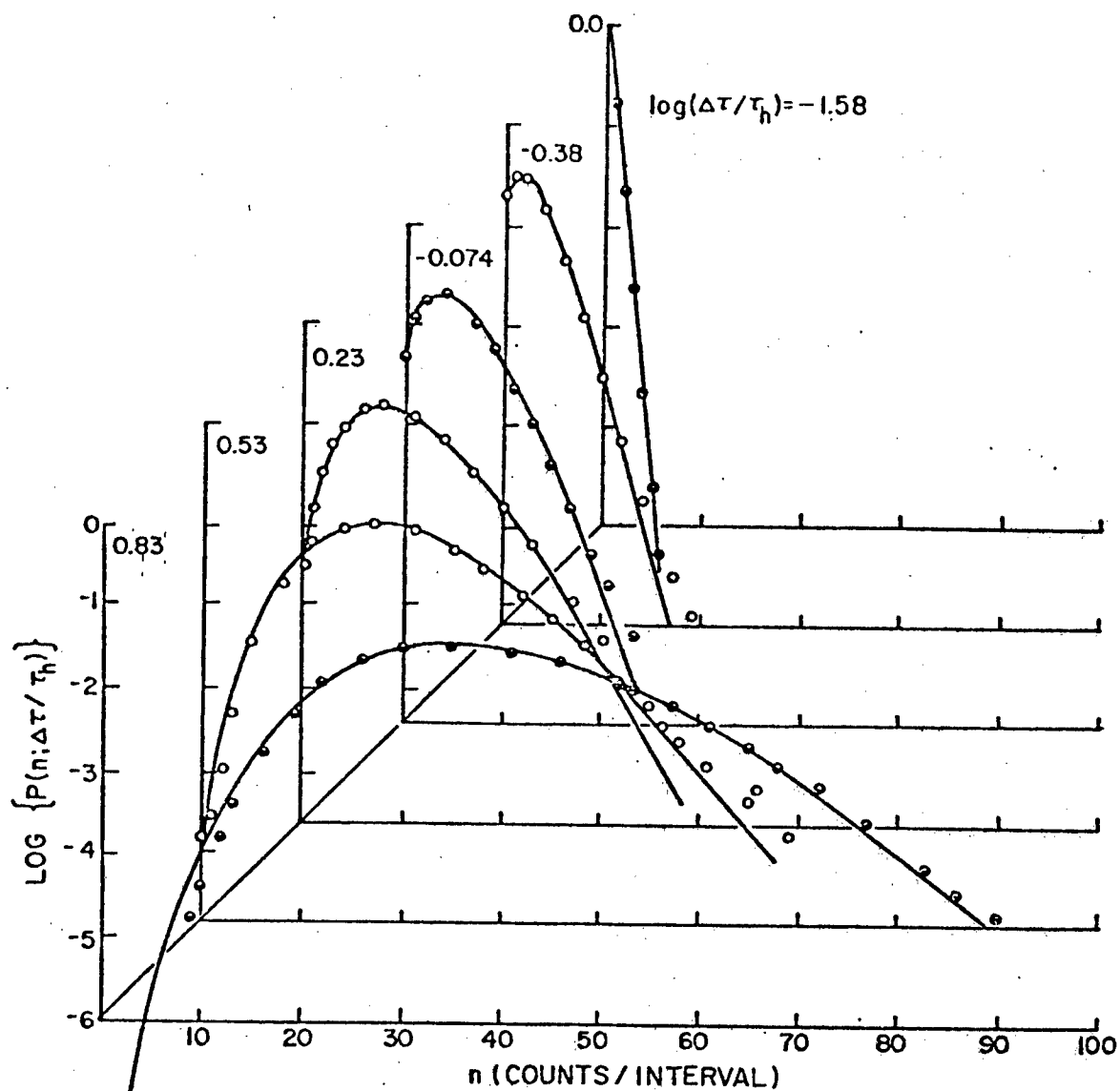
Figure 3: The distribution $P(n, \gamma)$ determined for a polystyrene solution for several values of $\Delta\tau$. Numbers on each curve give $\log \Delta\tau/\tau_h$. The solid curves were constructed with Eqn.34 using the experimental $n^{(2)}$ to compute $m^{-1} = n^{(2)} - 1$.
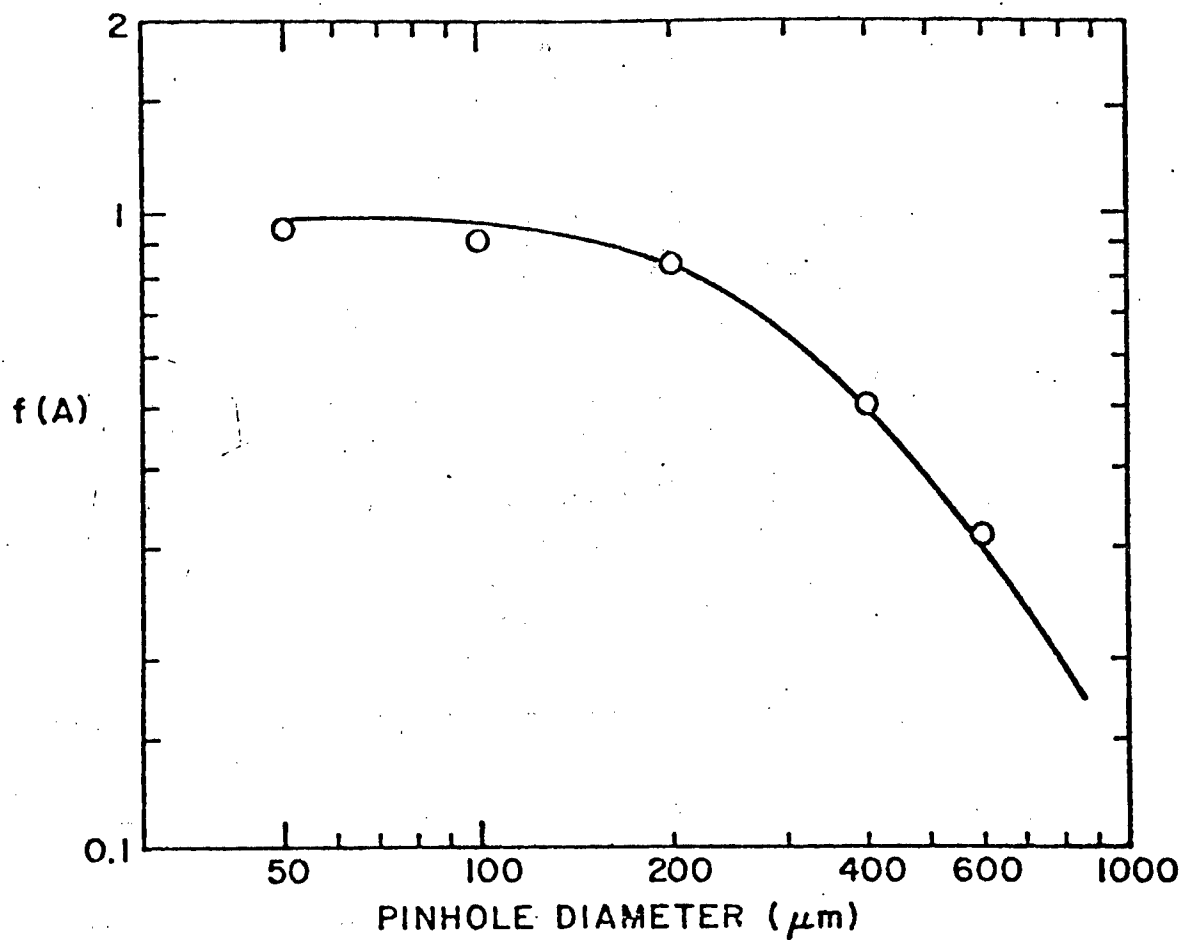
Figure 4: The coherence factor f(A) determined for several values of the pinhole diameter D. The curve is a theoretical estimate, fitted to the data by use of an arbitrary proportionality between D^2 and the coherence area A.
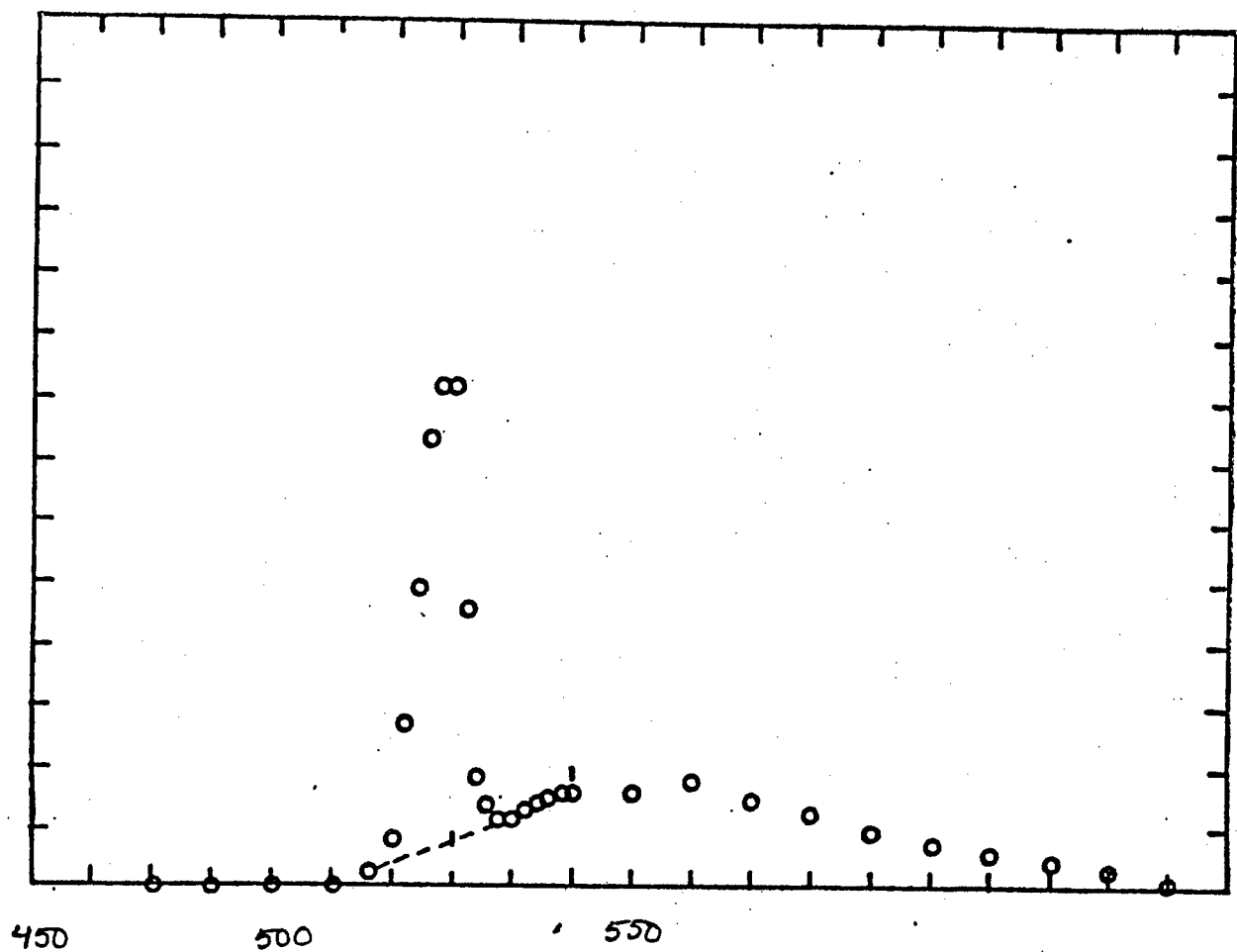
Figure 5:   The Vv emission spectra of SPBT 38+0.53 N salt excited with a 514.5 nm source at 25.0 ° C. 0.0506 g/dl
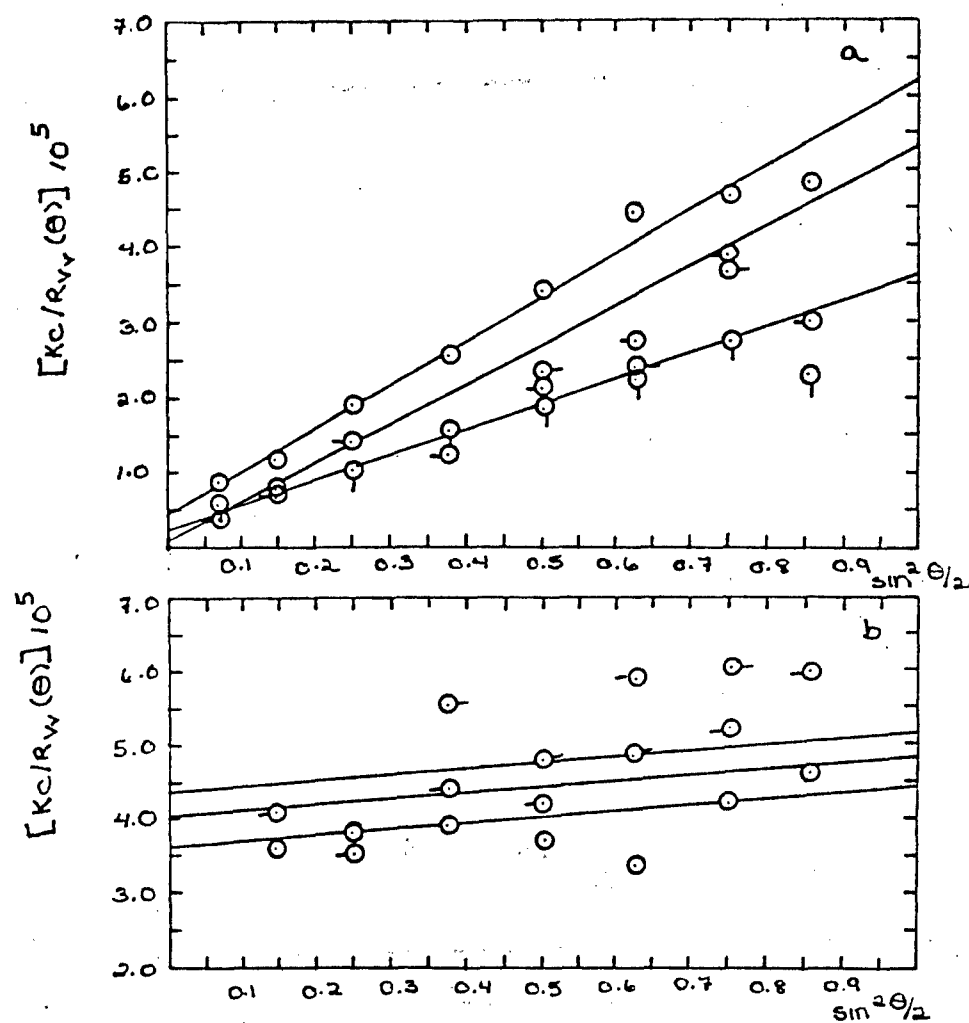
Figure 6: The a)uncentrifuged and b)centrifuged Vv components of the integrated intensity light scattering of PBT IN PPA/MSA at 514.5 nm and 25.0°C. O 0.0491 g/dl O–0.0349 g/dl Q 0.0249 g/dl –O 0.096 g/dl
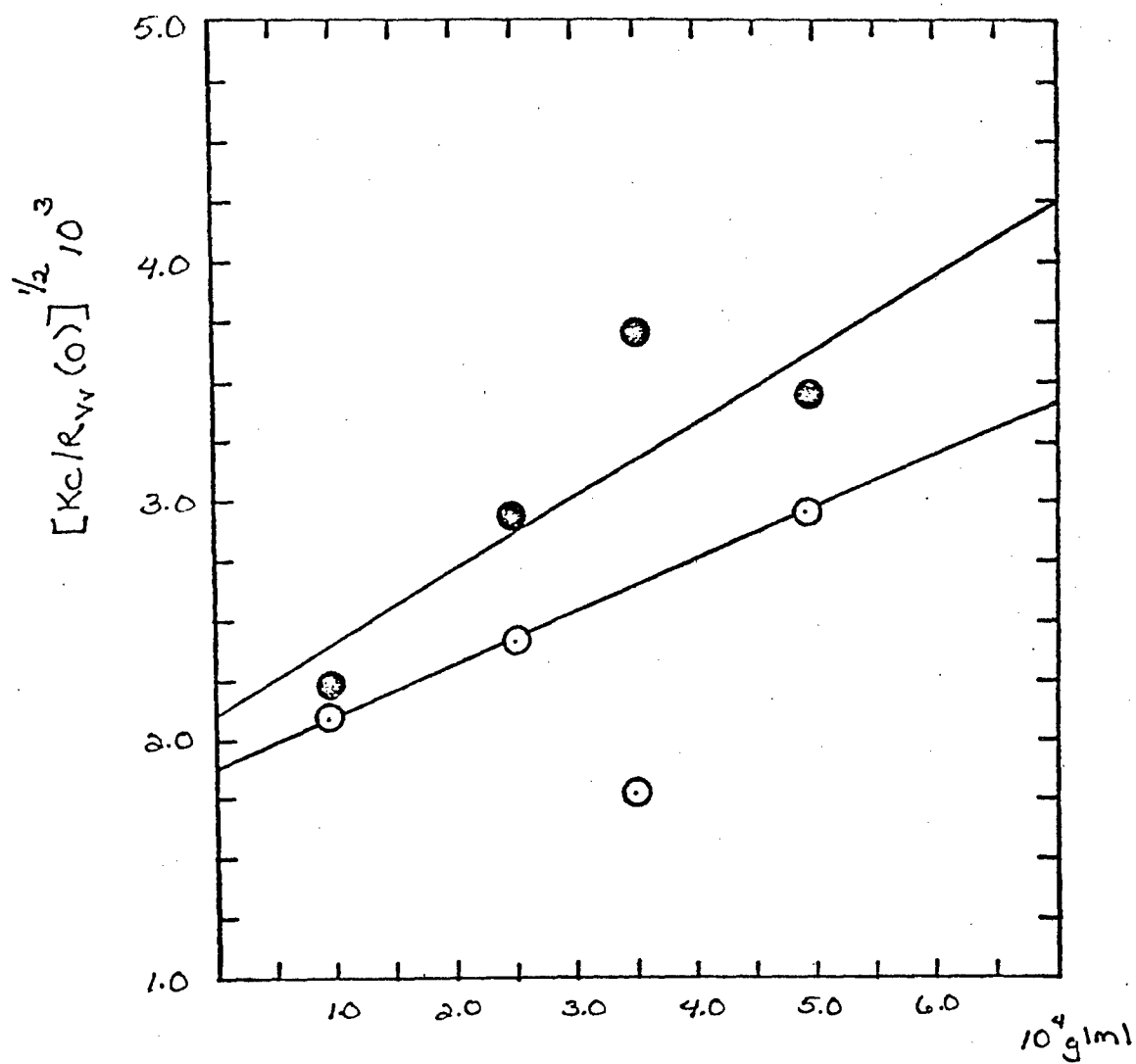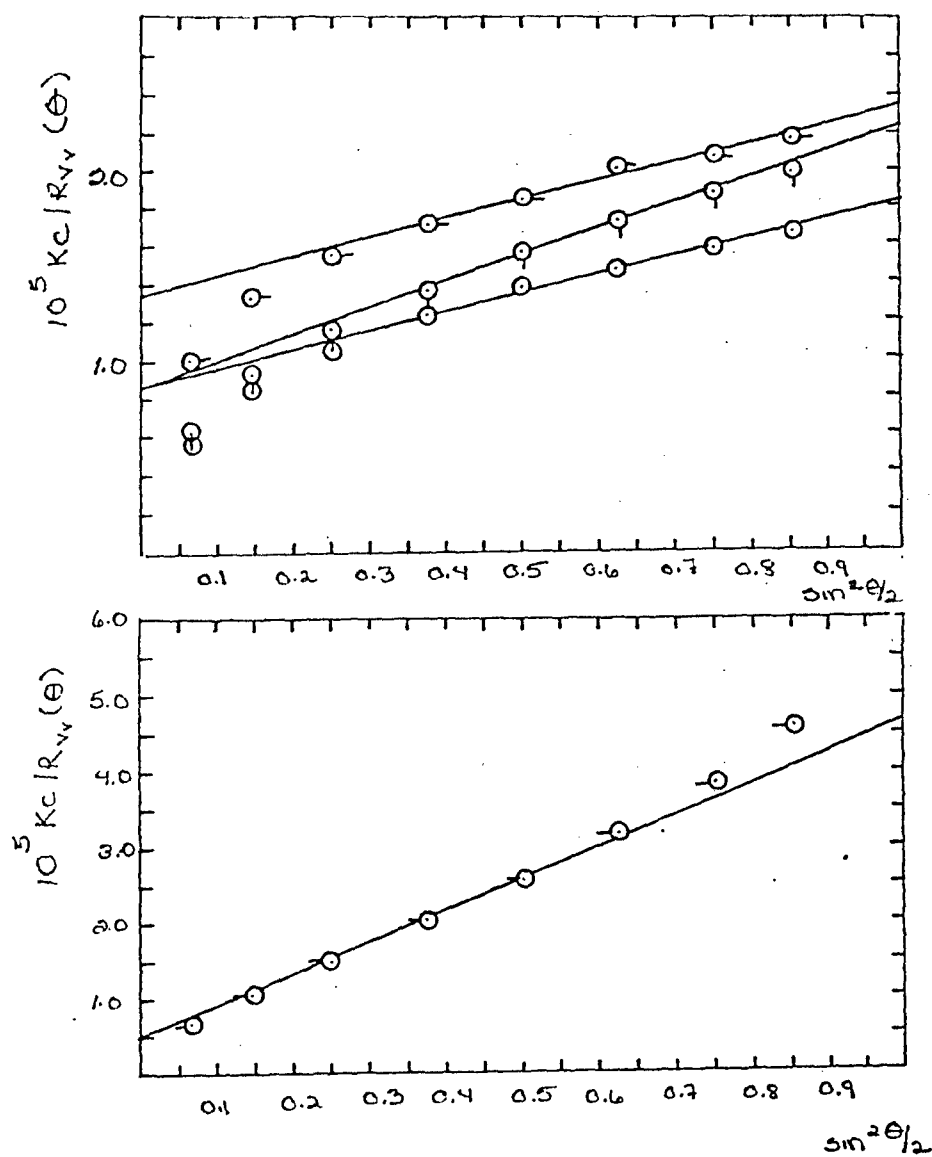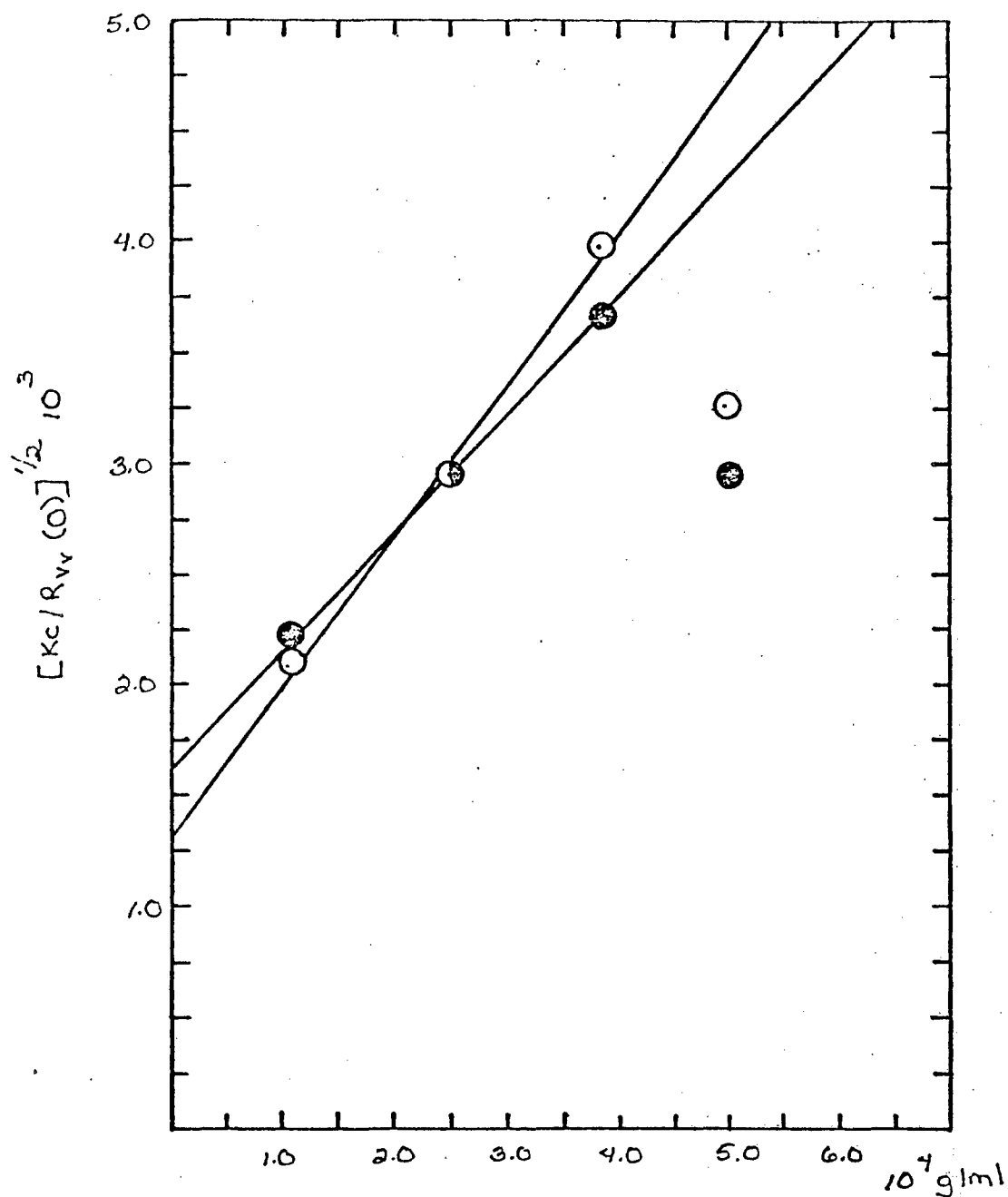
Figure 7: The concentration dependence of the Vv components of the integrated intensity light scattering of PBT IN PPA/MSA.   O uncentrifuged
O centrifuged
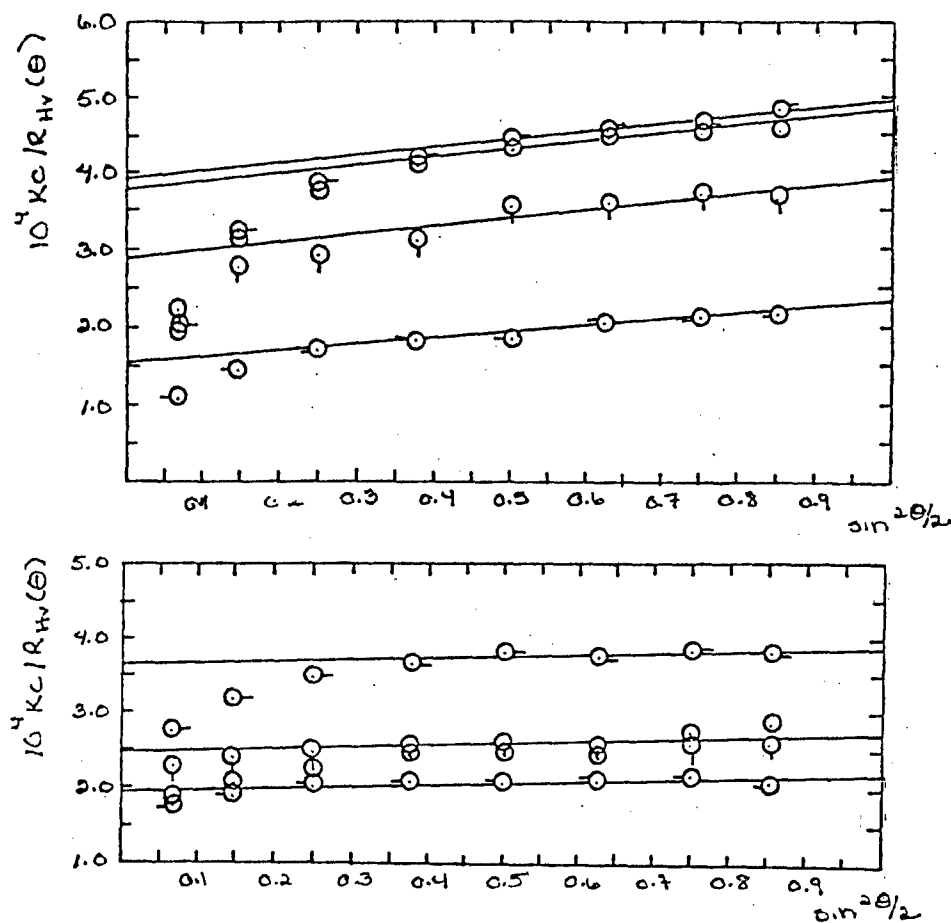
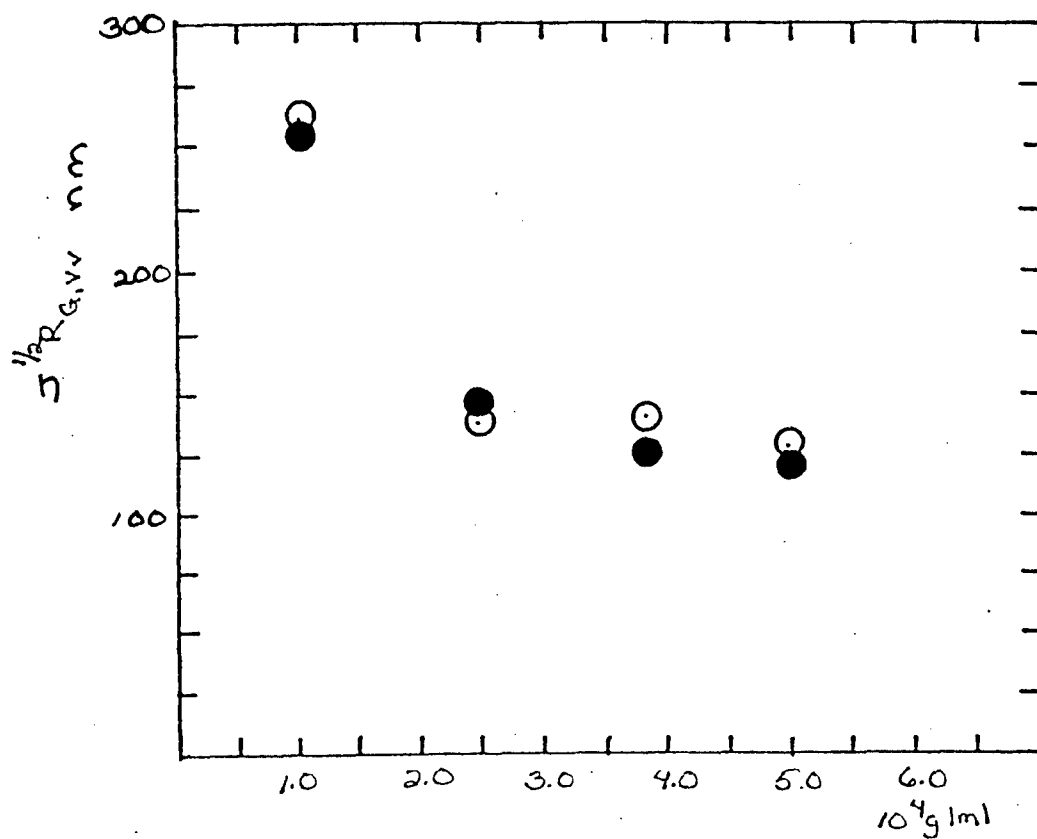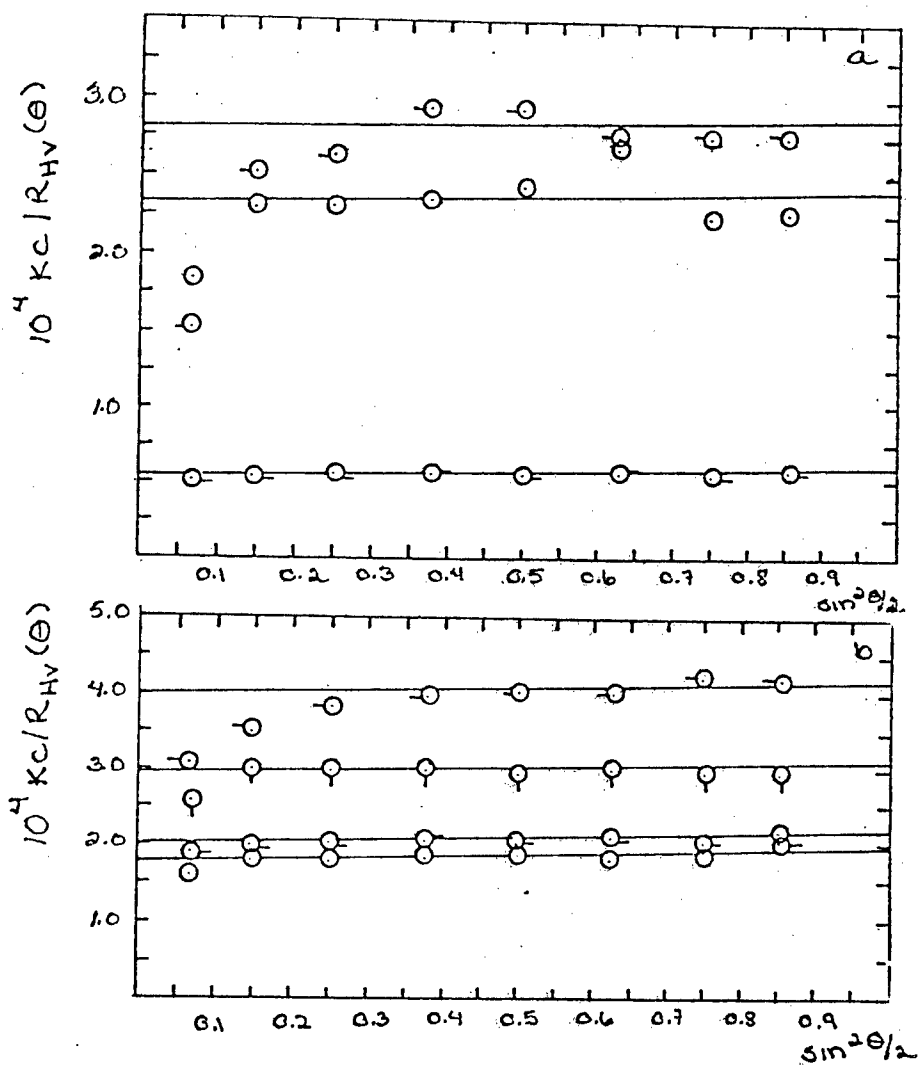Figure 8: The a)uncentrifuged and b)centrifuged Hv component of the integrated intensity light scattering of PBT IN PPA/MSA at 514.5 nm and 25.0 °C. O 0.0491 g/dl O-0.0349 g/dl Q 0.0249 g/dl-O 0.0096 g/dl
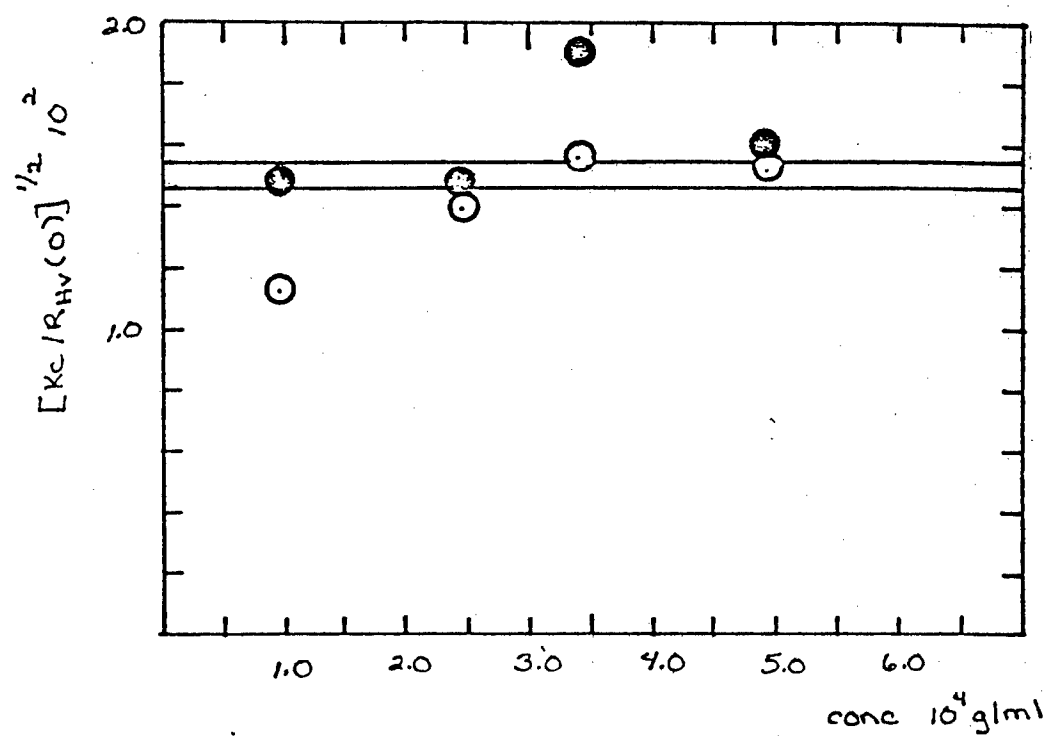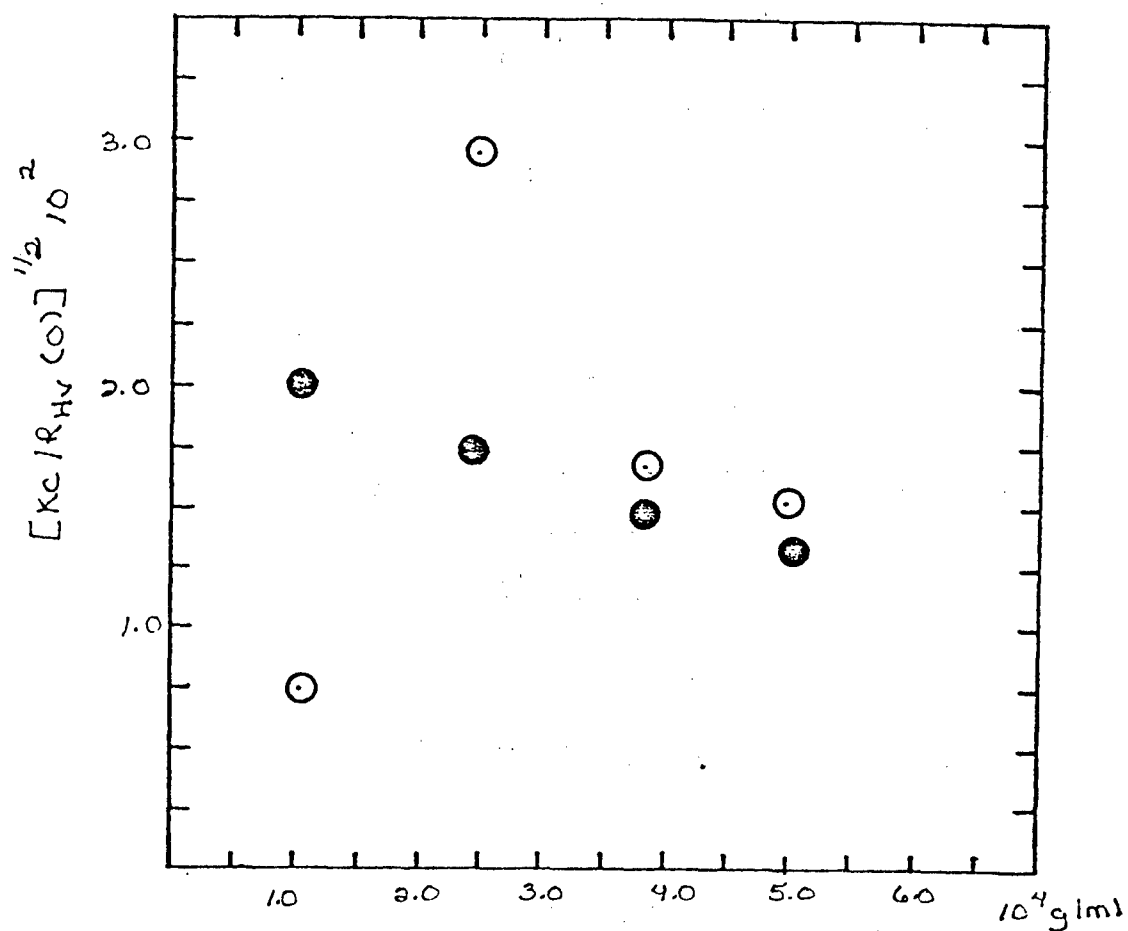
Figure 9: The concentration dependence of the Hv component of the integrated intensity light scattering of PBT in PPA/MSA. O uncentrifuged and ● centrifuged
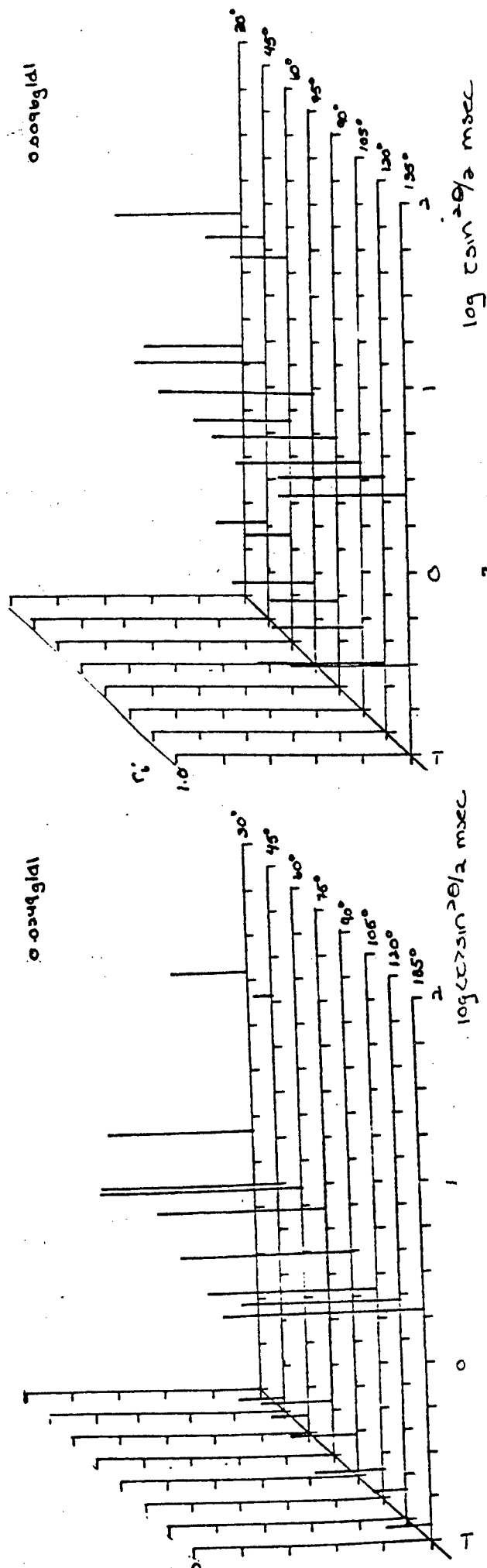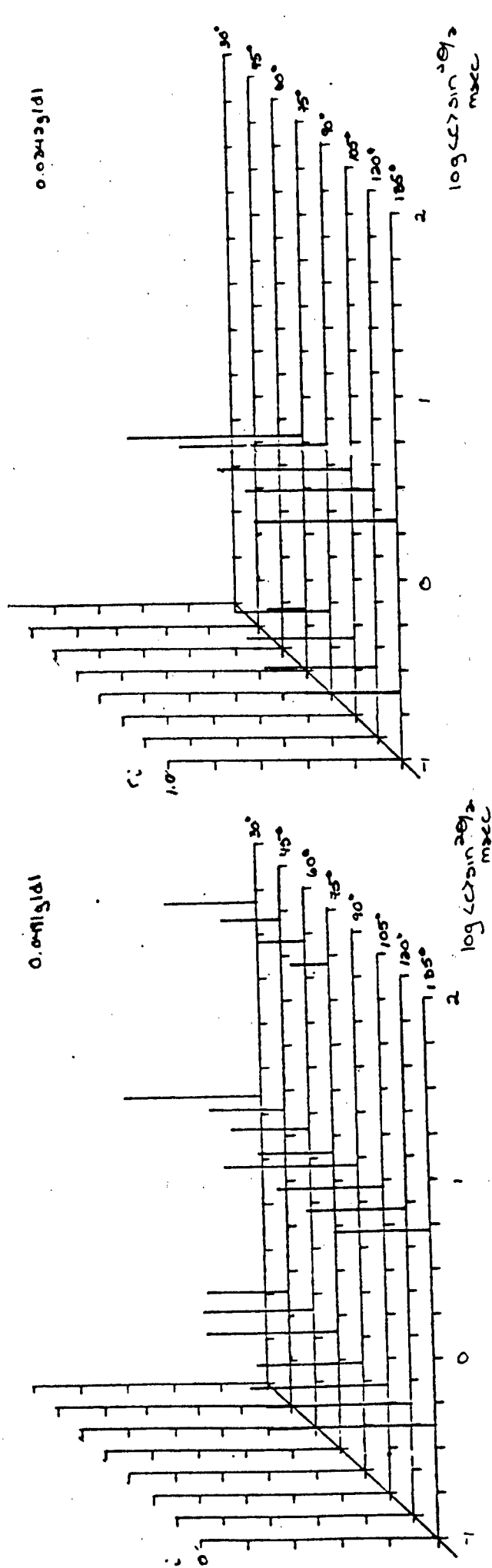
Figure 10: a) The concentration dependence of $\tau_i \sin^2 \theta/2$ of uncentrifuged PBT in PPA/MSA
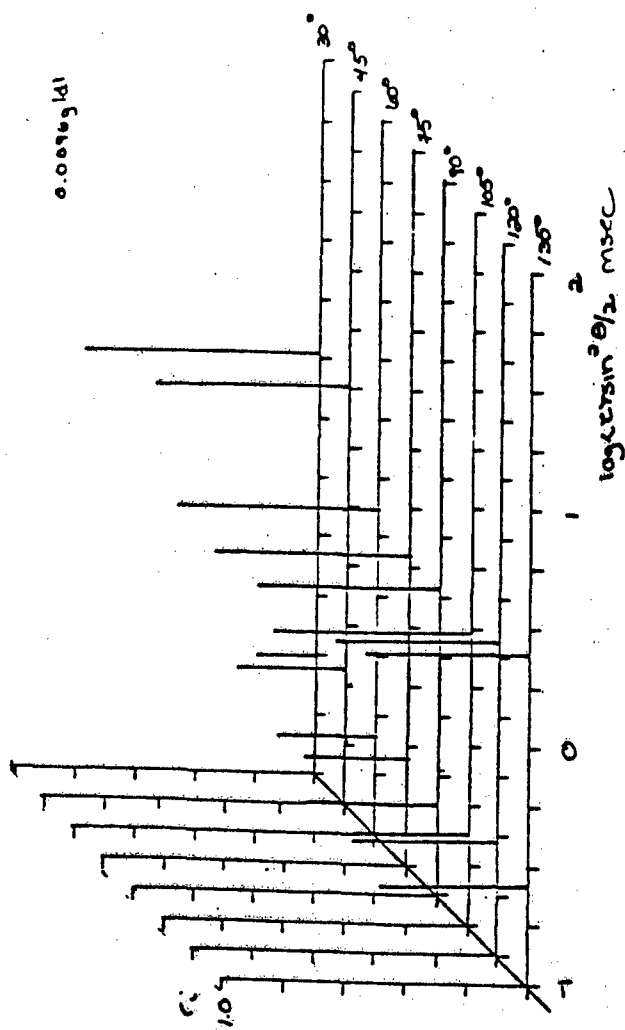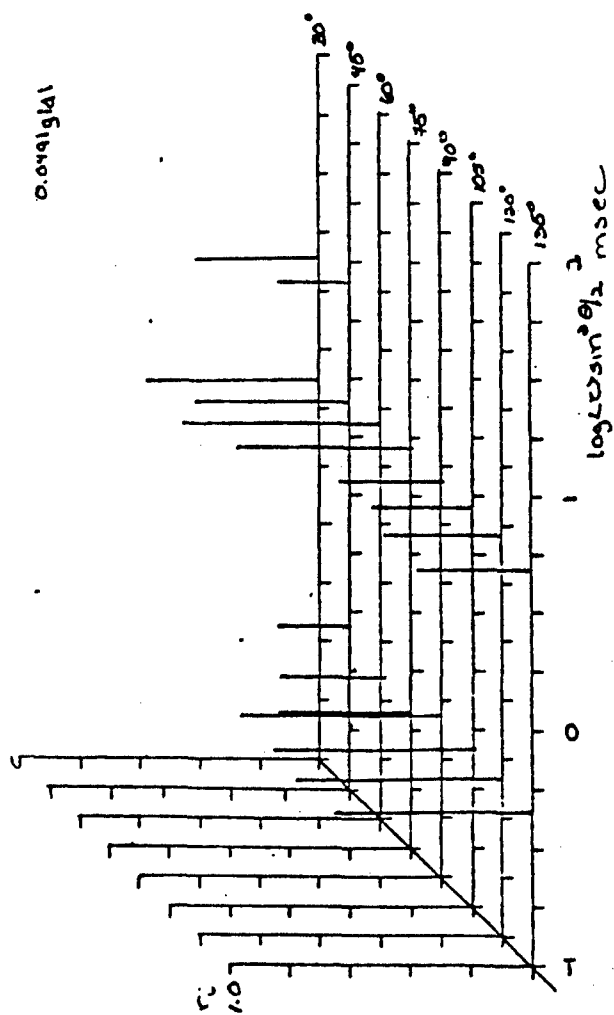
Figure 11: a) The concentration dependence of $\tau_1 \sin^2 \theta/2$ of centrifuged PBT in PPA/MSA
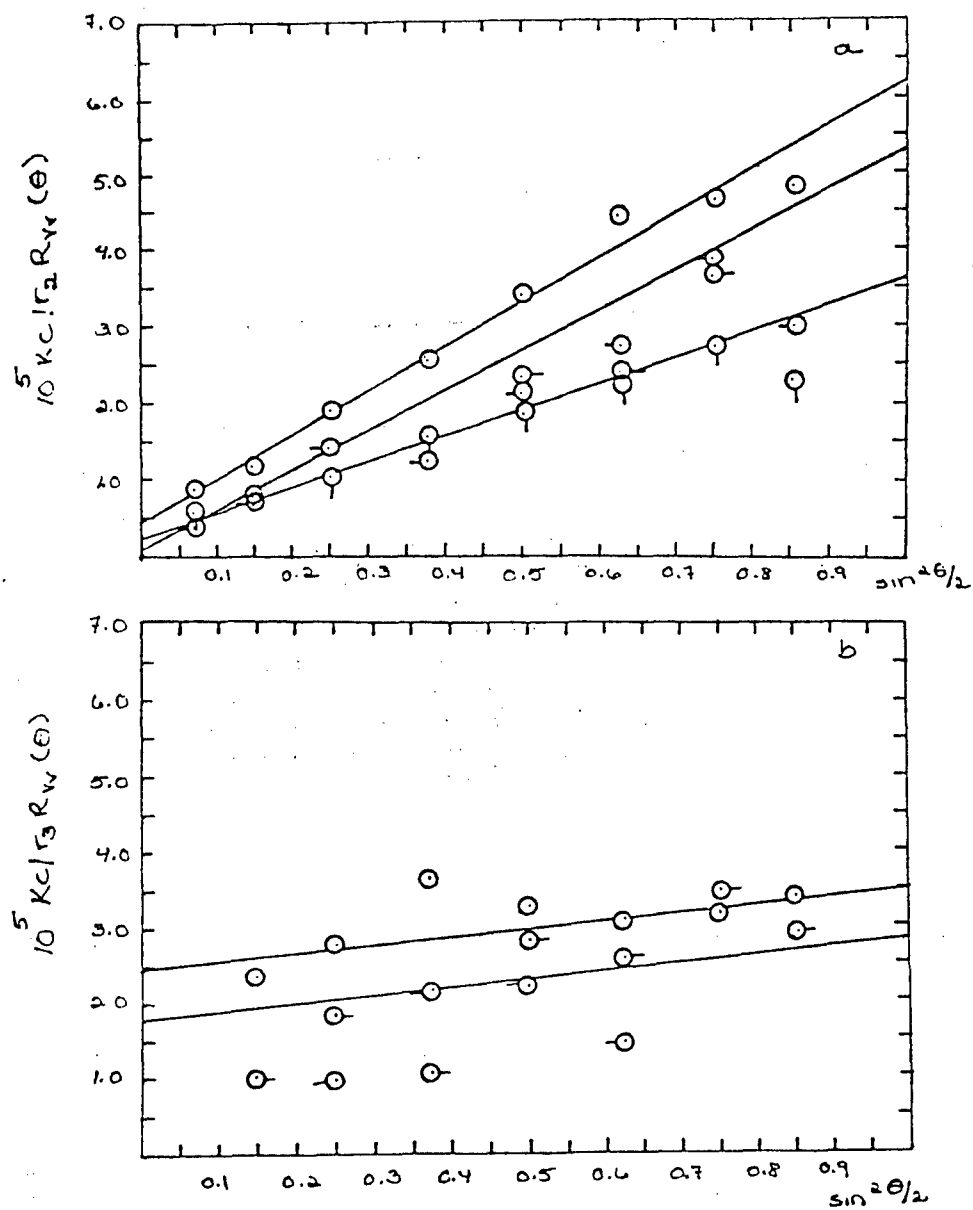
Figure 12: The uncentrifuged Kc/R$_{vv}$ of PBT in PPA/MSA at 514 nm and 25.0°C. O 0.0491g/dl O 0.0349 g/dl Q 0.0249 g/dl O 0.096g/dl
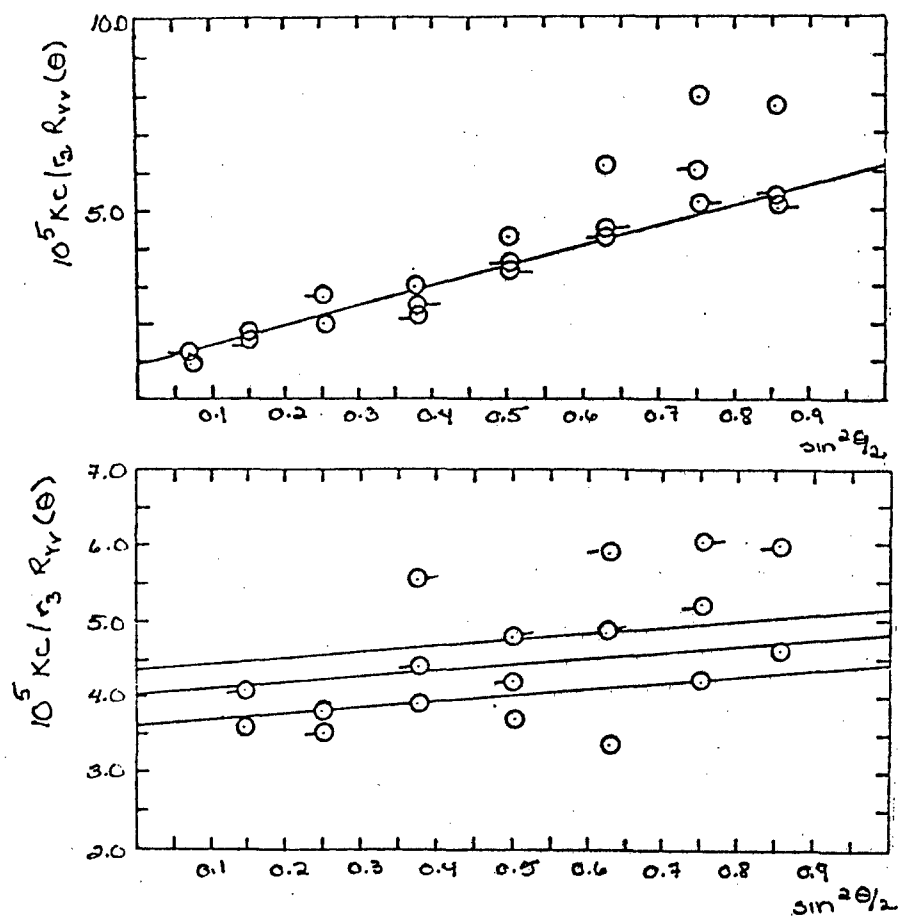
Figure 13: The centrifuged Kc/R$_{Vv}$ of PBT in PPA/MSA at 514 nm and 25.0°C. O 0.0491g/dl O 0.0349 g/dl Q 0.0249 g/dl ⊸O 0.096g/dl
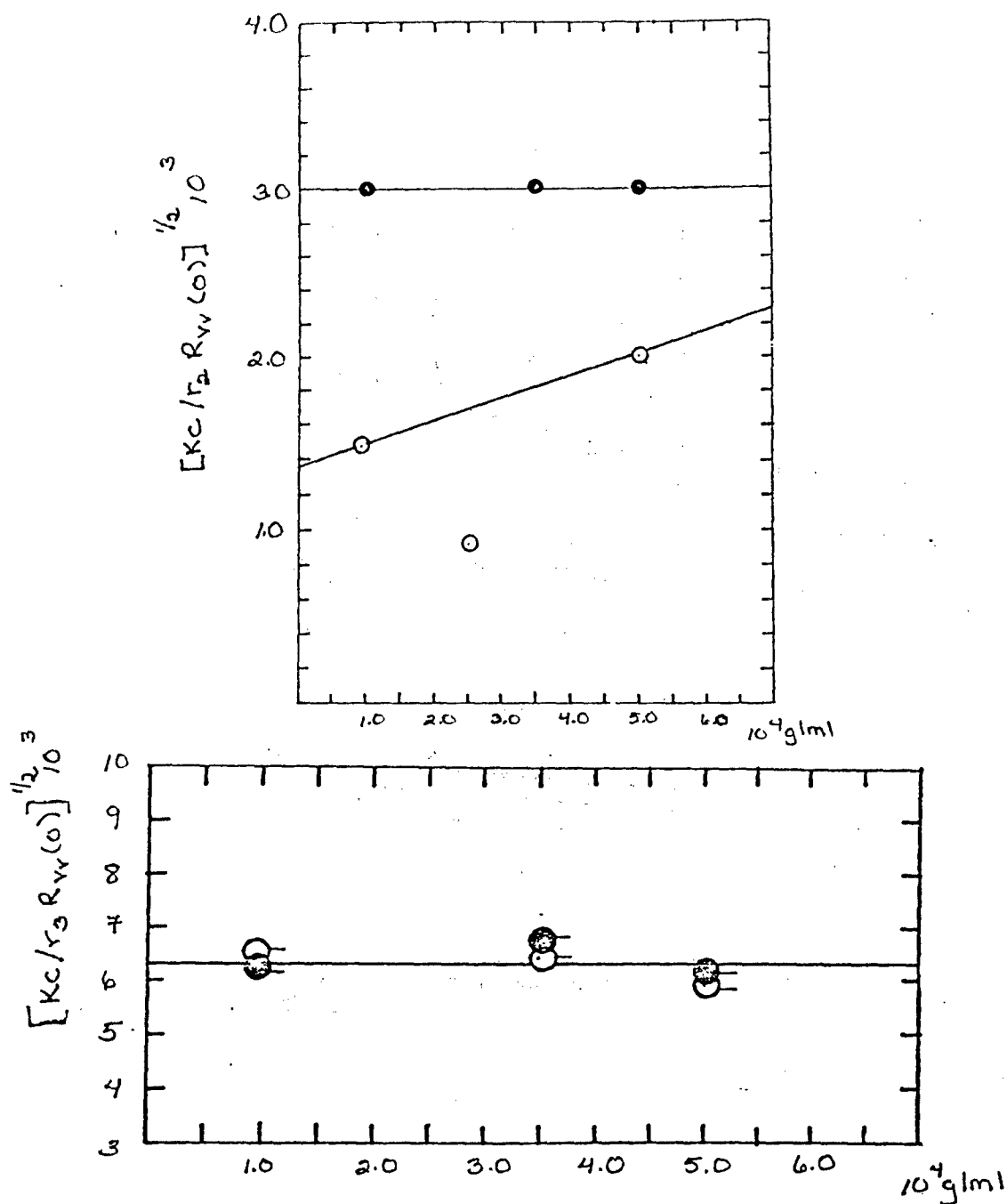
Figure 14: The concentration dependence of the Vv components of the integrated intensity light scattering of PBT in PPA/MSA. O r_2 uncentrifuged ● $r_2$centrifuged O-r_3 uncentrifuged ●-r_3 centrifuged

112
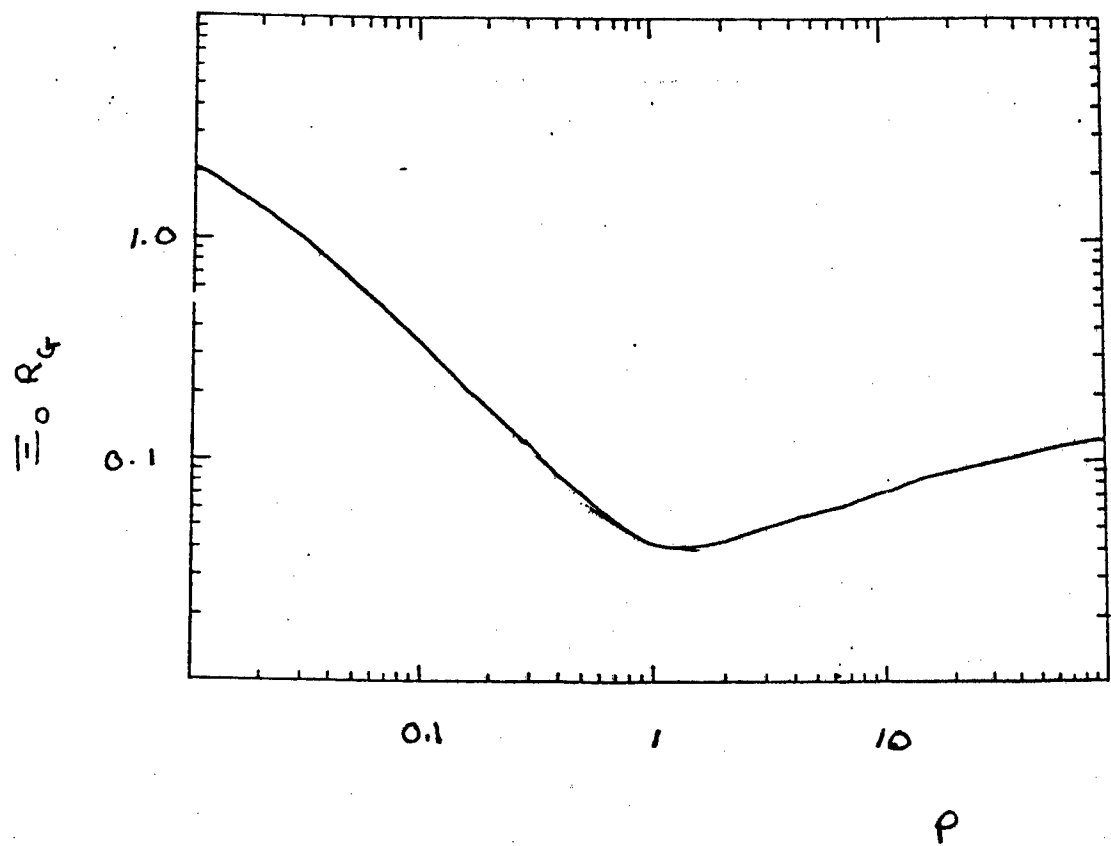
Figure 15: $\Xi_o R_G$ versus p
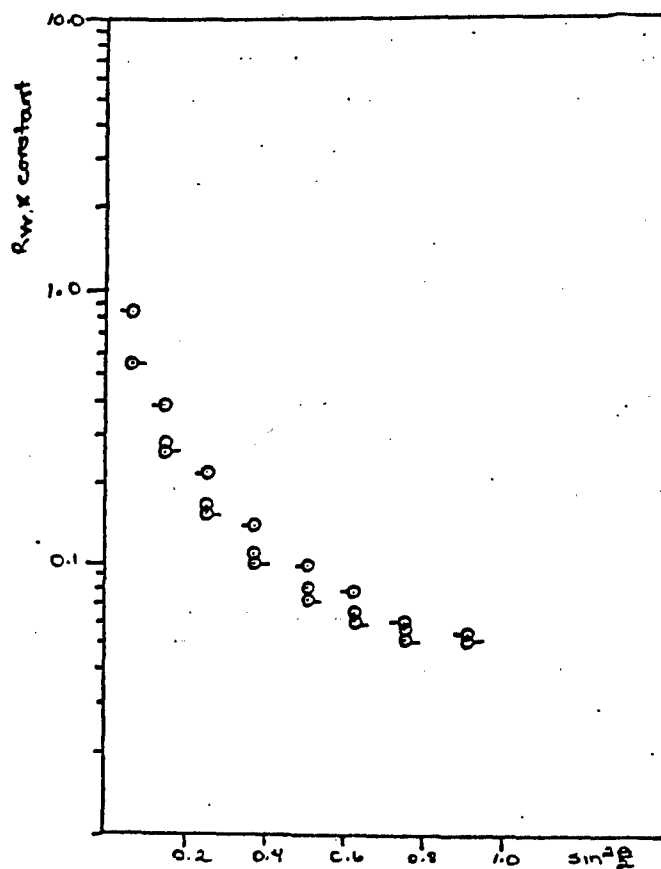
Figure 16: The uncentrifuged component of the Vv
AILS of non heat treated PBT-PBO (90/10) in PPA/MSA at 633 nm and 25.0°C
. O 0.0499 g/dl O-0.0388 g/dl-O 0.0145 g/dl
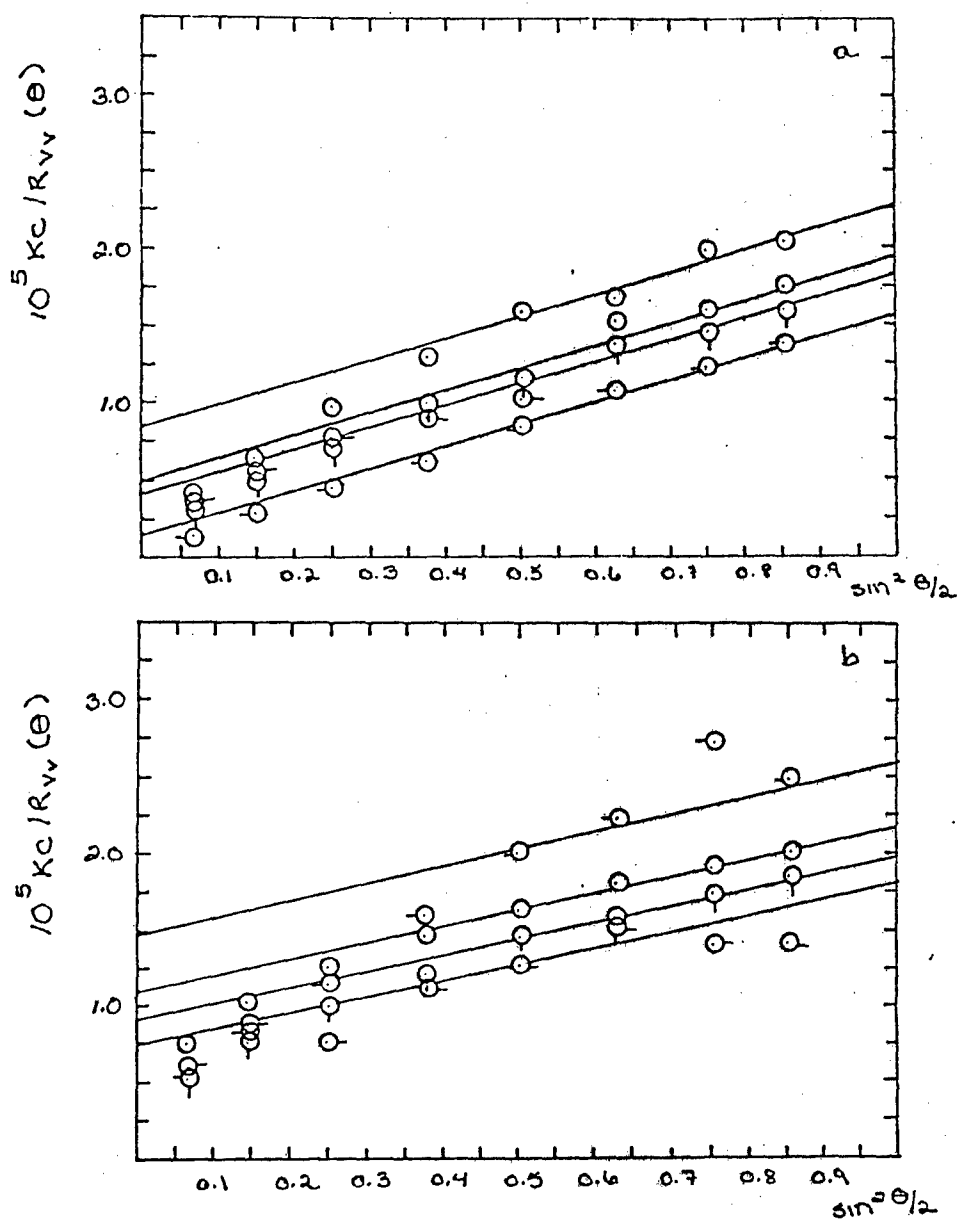
Figure 17: The a)uncentrifuged and b)centrifuged Vv components of the integrated intensity light scattering of PBT–PBO (90/10) in PPA/MSA at 514.5 nm and 25.0°C. O 0.0491 g/dl O–0.0385 g/dl Q 0.0232 g/dl–O 0.0102 g/dl
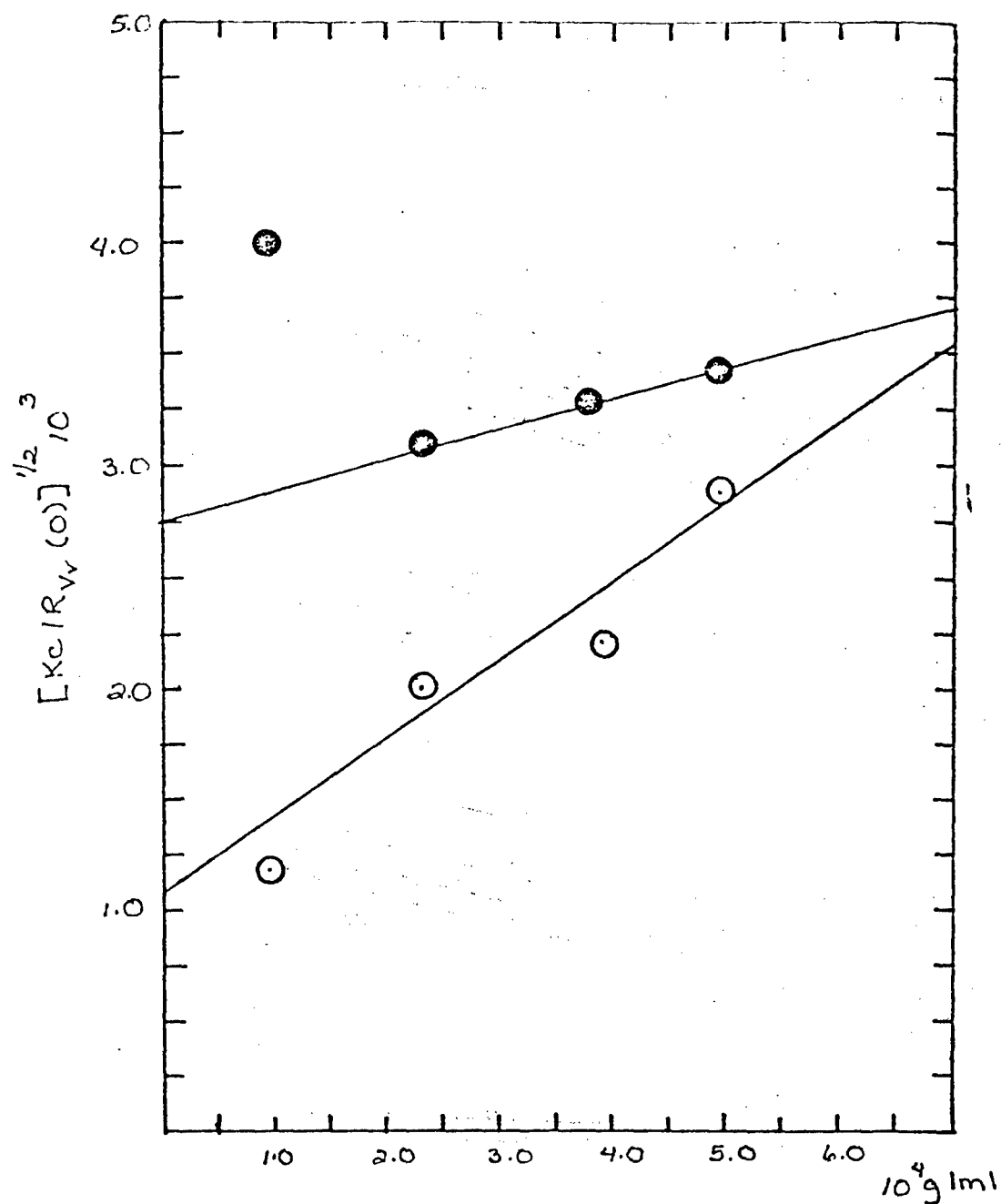
Figure 18: The concentration dependence of the Vv components of the integrated intensity light scattering of PBT-PBO (90/10) in PPA/MSA. O uncentrifuged ● centrifuged
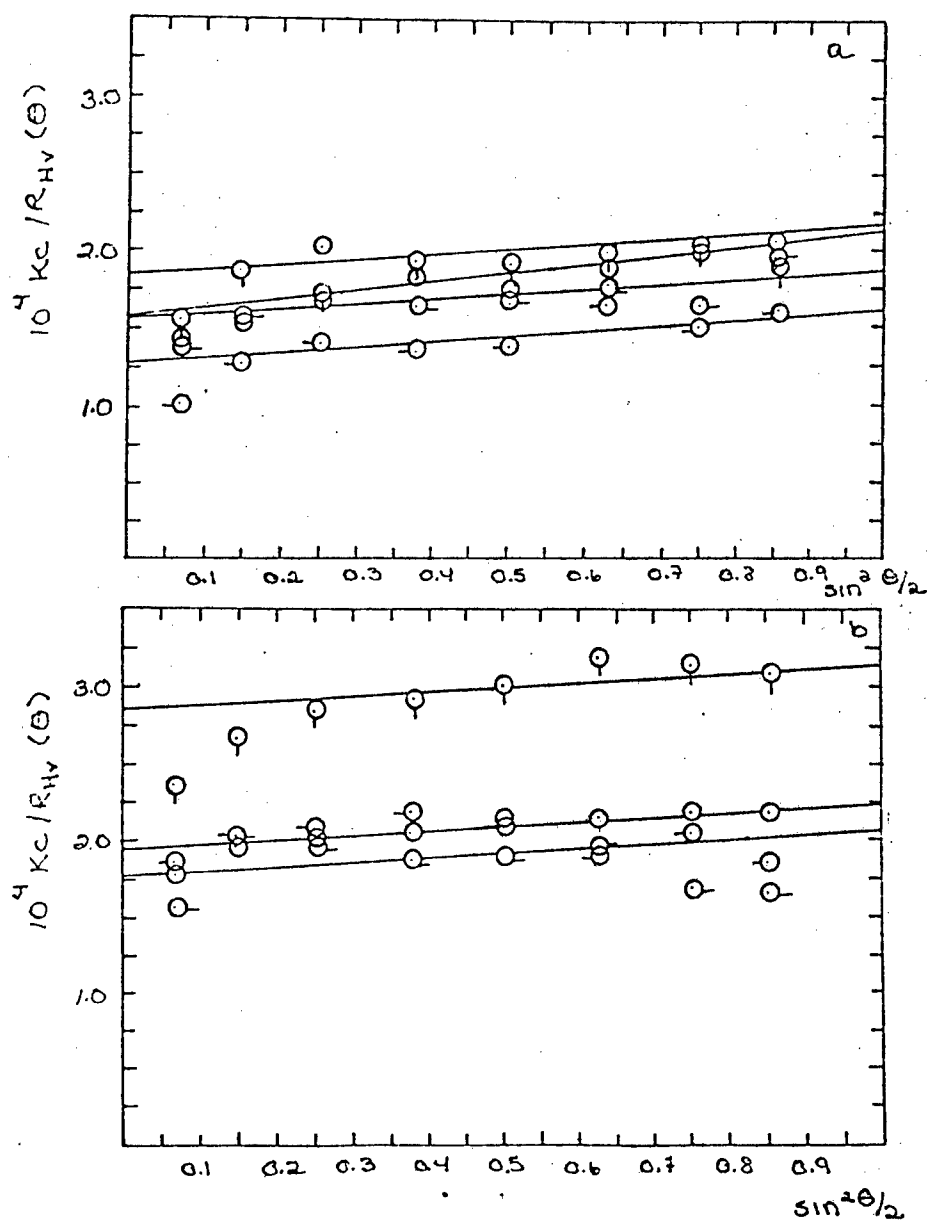
Figure 19: The a)uncentrifuged and b)centrifuged Hv component of the integrated intensity light scattering of PBT–PBO (90/10) in PPA/MSA at 514.5 nm and 25.0 °C. O 0.0491 g/dl O-0.0385 g/dl Q 0.0232 g/dl-O 0.0102 g/dl

117
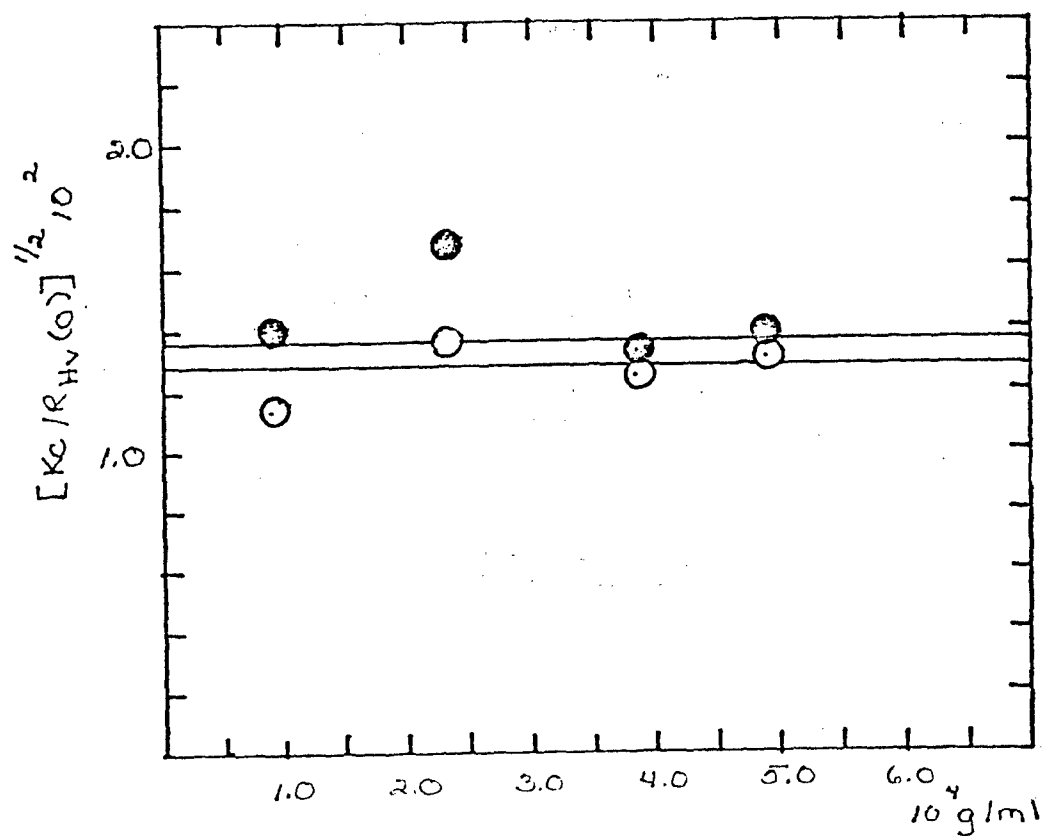
Figure 20: The concentration dependence of the Hv component of the integrated intensity light scattering of PBT-PBO (90/10) in PPA/MSA. O uncentrifuged and ● centrifuged
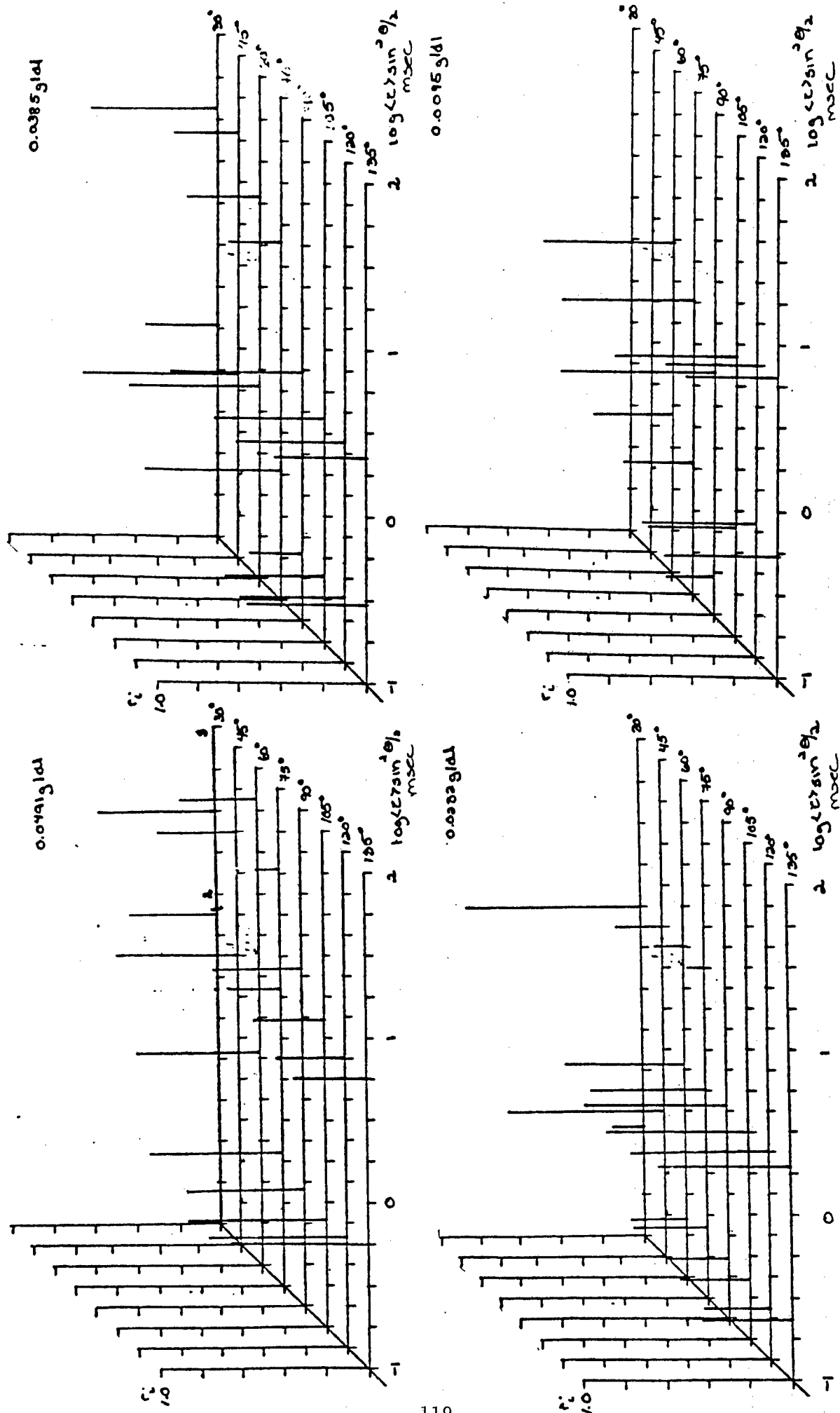
Figure 21: a)The concentration dependence of $r \sin^2 \theta/2$ of uncentrifuged PBT–PBO (90/10) in PPA/MSA.

119
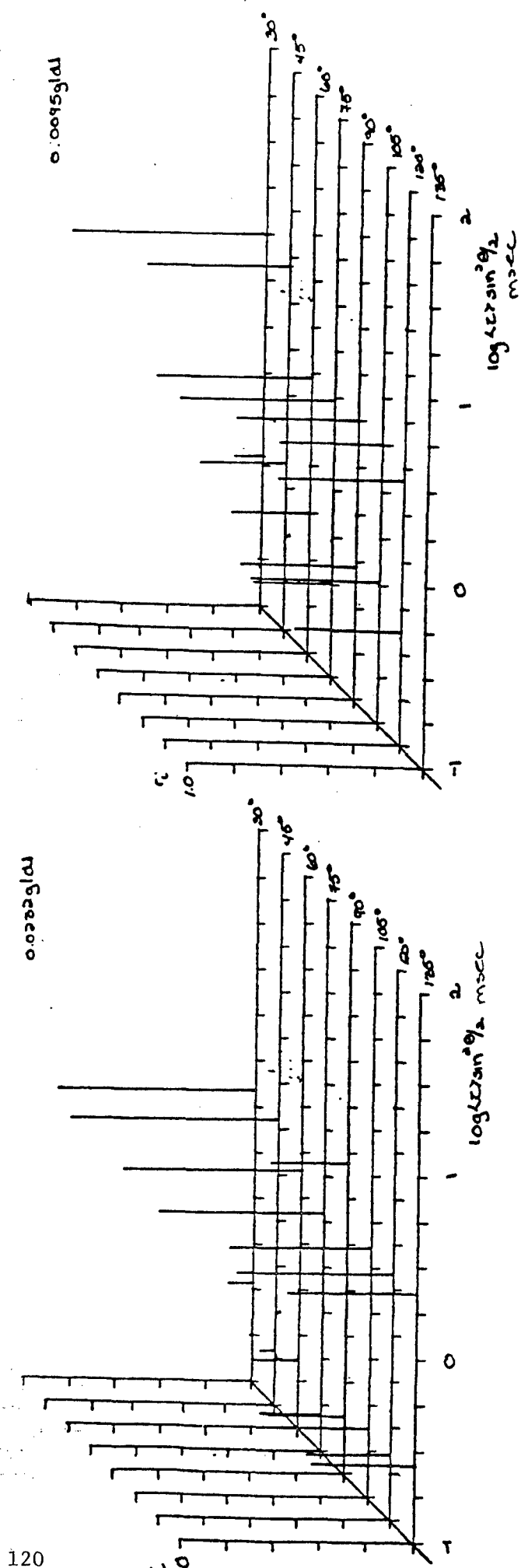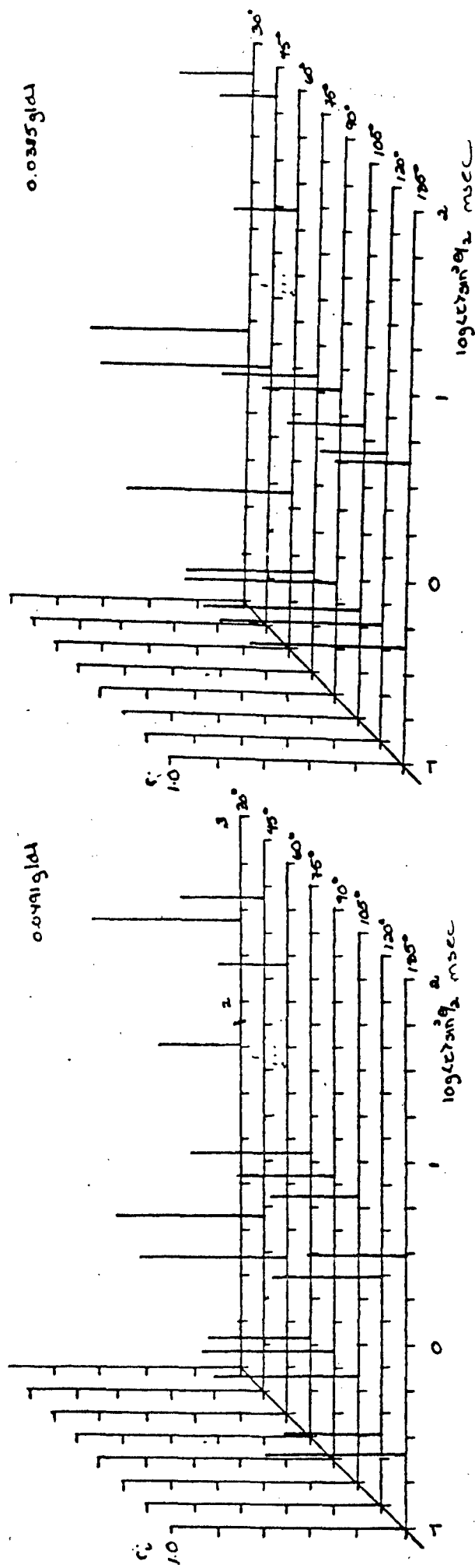
Figure 22: a)The concentration dependence of $\tau \sin^2 \theta/2$ of centrifuged PBT-PBO (90/10) in PPA/MSA

120
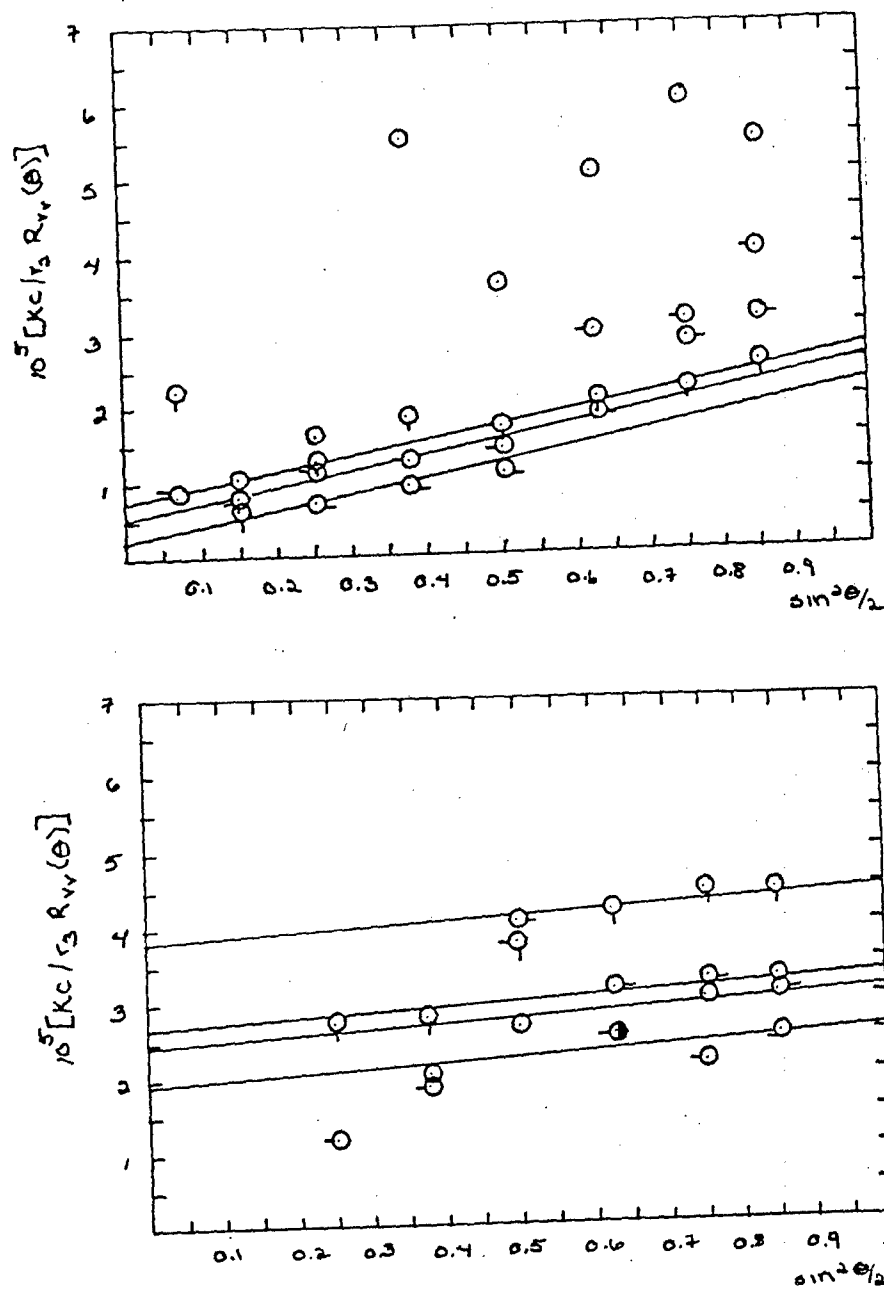
Figure 23: The uncentrifuged Kc/R$_{vv}$ of PBT-PBO (90/10) in PPA/MSA at 514 nm and 25.0°C. O 0.0491 g/dl O–0.0385 g/dl O 0.0232 g/dl –O 0.0102 g/dl

121
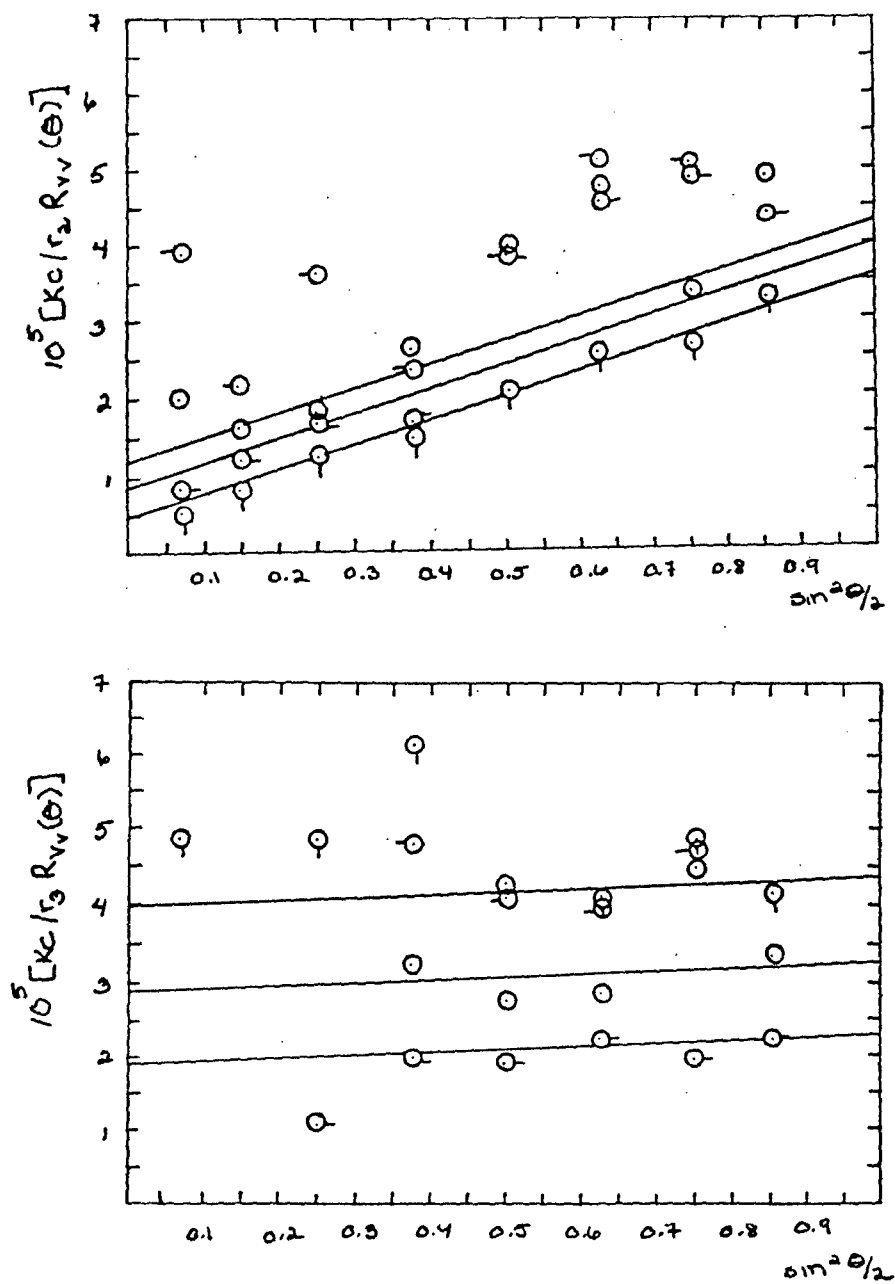
Figure 24: The centrifuged Kc/R_{Vv} of PBT-PBO(90/10) in PPA/MSA at 514 nm and 25.0°C. O 0.0491 g/dl O-0.0385 g/dl Q 0.0232 g/dl -O 0.0102 g/dl

122
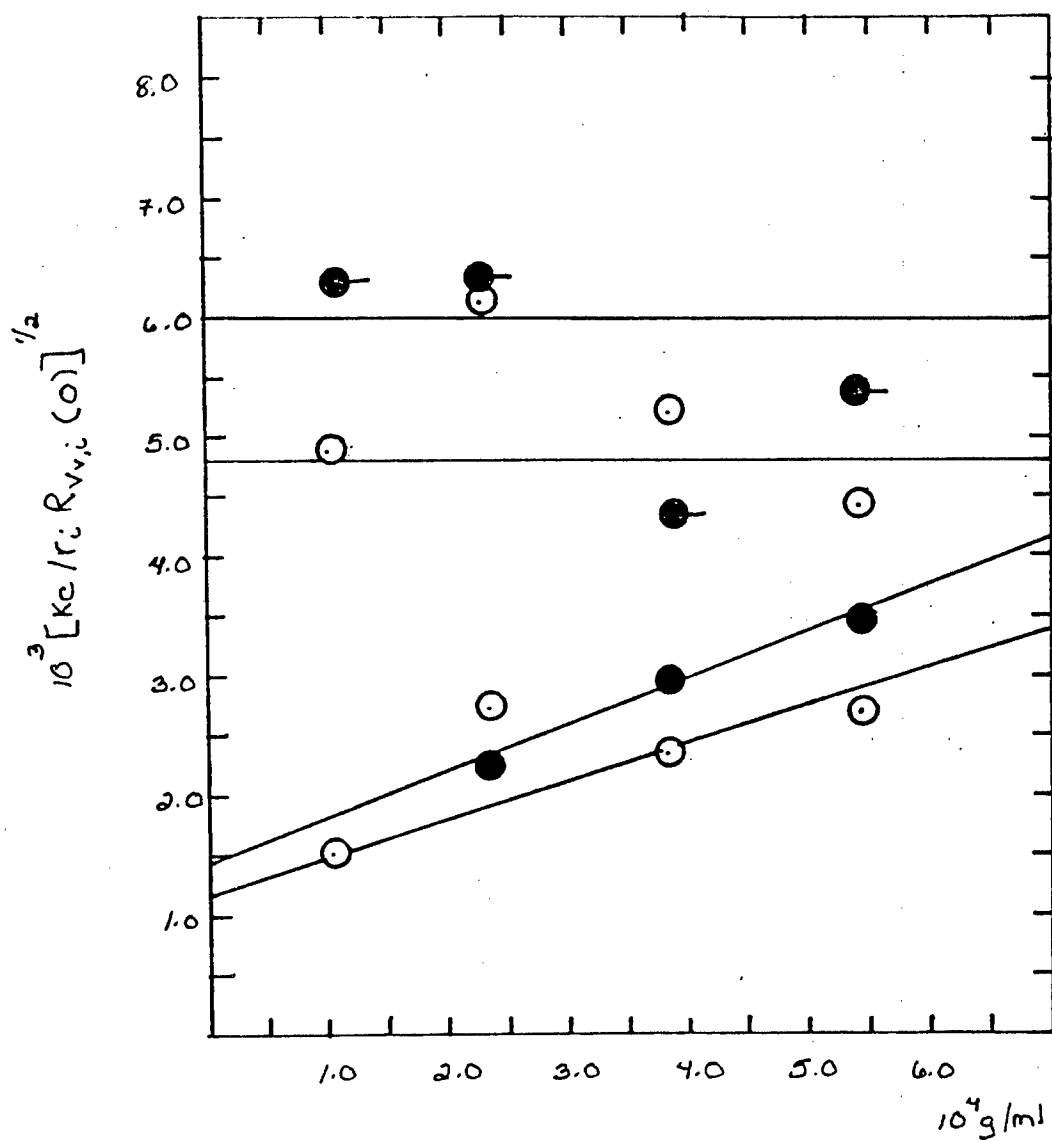
Figure 25: The concentration dependence of the Vv components of the integrated intensity light scattering of PBT–PBO(90/10) in PPA/MSA. O r_2 uncentrifuged ● r_2 centrifuged O r_3 uncentrifuged ●–r_3 centrifuged

123
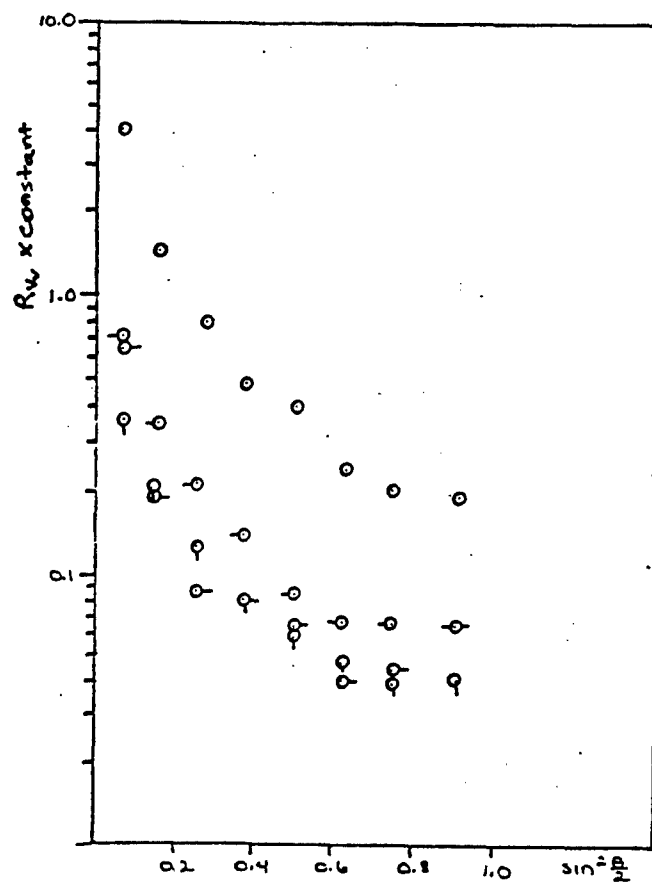
Figure 26: Absolute intensity light scattering for PBT-PBO (75/25) without heat treatment in PPA/MSA at 633 nm and 25.0°. O 0.529 g/dl O-0.327 g/dl Q 0.268 g/dl-O 0.138 g/dl
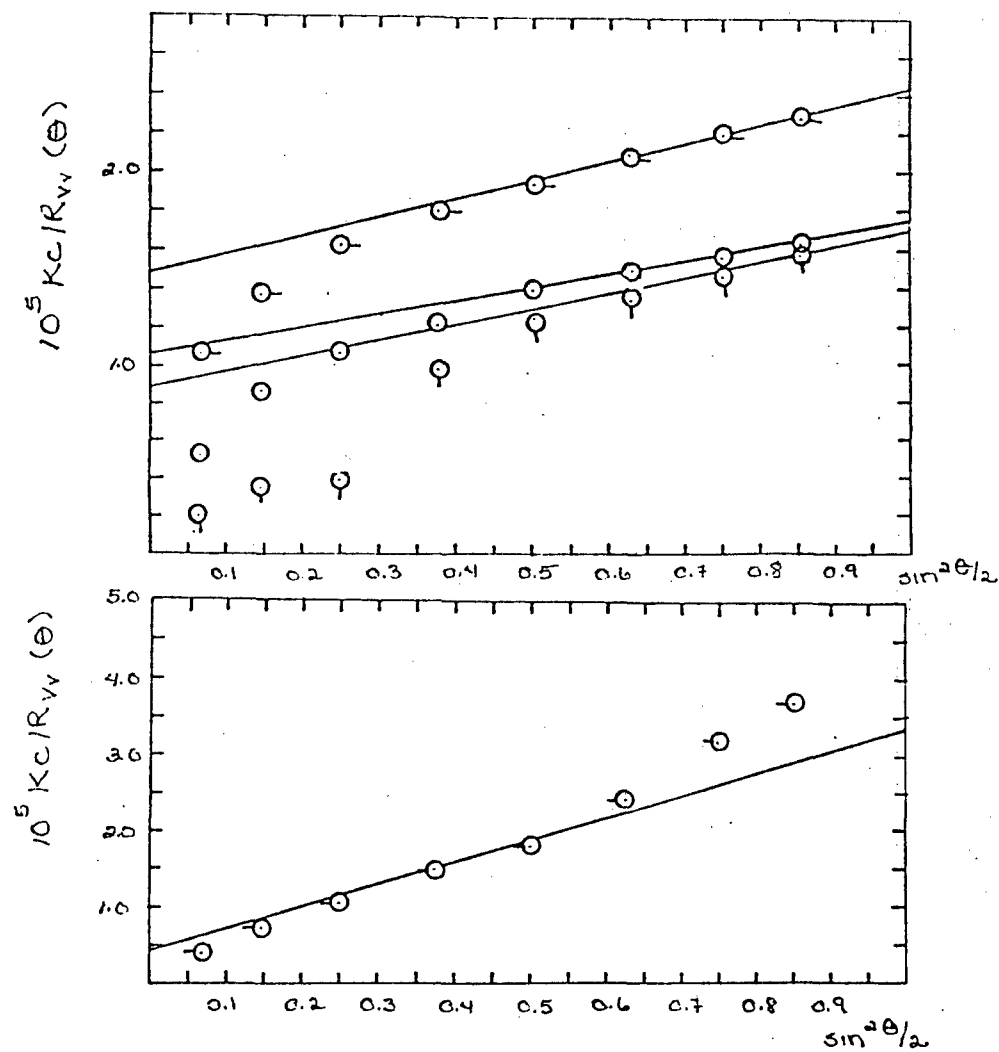
Figure 27: The uncentrifuged Vv component of the integrated intensity light scattering of PBT–PBO (75/25) in PPA/MSA at 514.5 nm and 25.0°C. O 0.0499 g/dl O-0.0381 g/dl Q 0.0247 g/dl-O 0.0102 g/dl

Figure 28: The centrifuged Vv component of the integrated intensity light scattering of PBT–PBO (75/25) in PPA/MSA at 514.5 nm and 25.0°C. O 0.0499 g/dl O–0.0381 g/dl Q 0.0247 g/dl–O 0.0102 g/dl

Figure 29: The concentration dependence of the Vv components of the integrated intensity light scattering of PBT-PBO (75/25) in PPA/MSA. O uncentrifuged ● centrifuged

Figure 30: The concentration dependence of $J^{1/2}R_{G,Vv}$ of PBT–PBO(75/25) in PPA/MSA. $JR^2_{G,Vv}$ calculated as $3(Kc/R_{Vv}(0))_o^{-1}$ $\partial(Kc/R_{Vv})/\partial q^2$

O uncentrifuged and ● centrifuged

Figure 31: The a)uncentrifuged and b)centrifuged Hv component of the integrated intensity light scattering of PBT–PBO (75/25) in PPA/MSA at 514.5 nm and 25.0 ° C. O 0.0499 g/dl O–0.0381 g/dl Q 0.0247 g/dl–O 0.0102 g/dl

Figure 32: The concentration dependence of the Hv component of the integrated intensity light scattering of PBT-PBO in PPA/MSA. O uncentrifuged and ● centrifuged
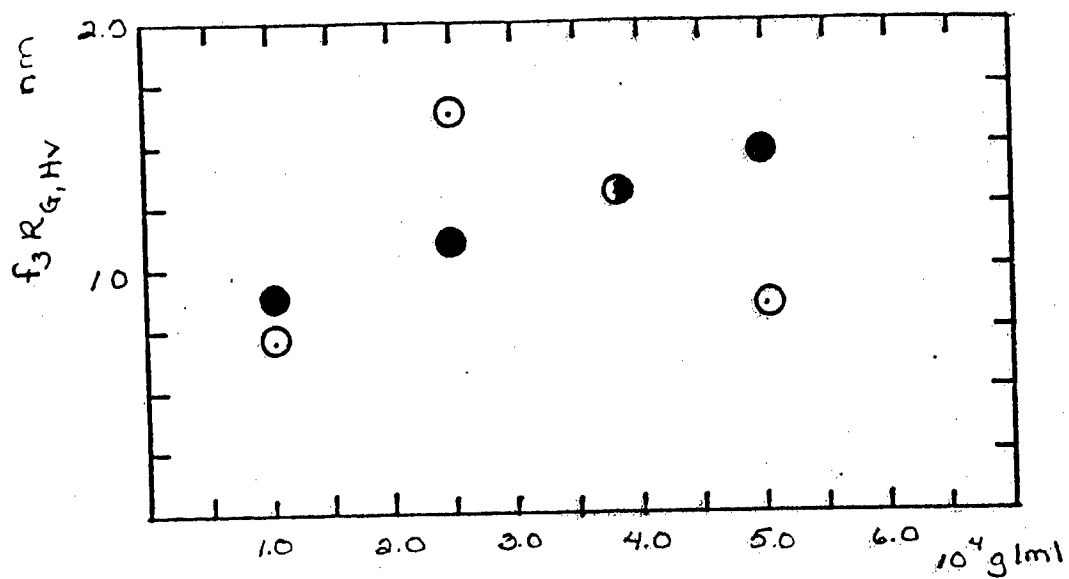
Figure 33: The concentration dependence of $f_3 R_{G,H}$ of PBT–PBO(75/25) in PPA/MSA $f_3 R_{G,Hv}$ calculated as $(7/3)[Kc/R_{Hv}(0)]^{-1} \partial (Kc/R_{Hv})/\partial q^2$. $\odot$ uncentrifuged and $\bullet$ centrifuged
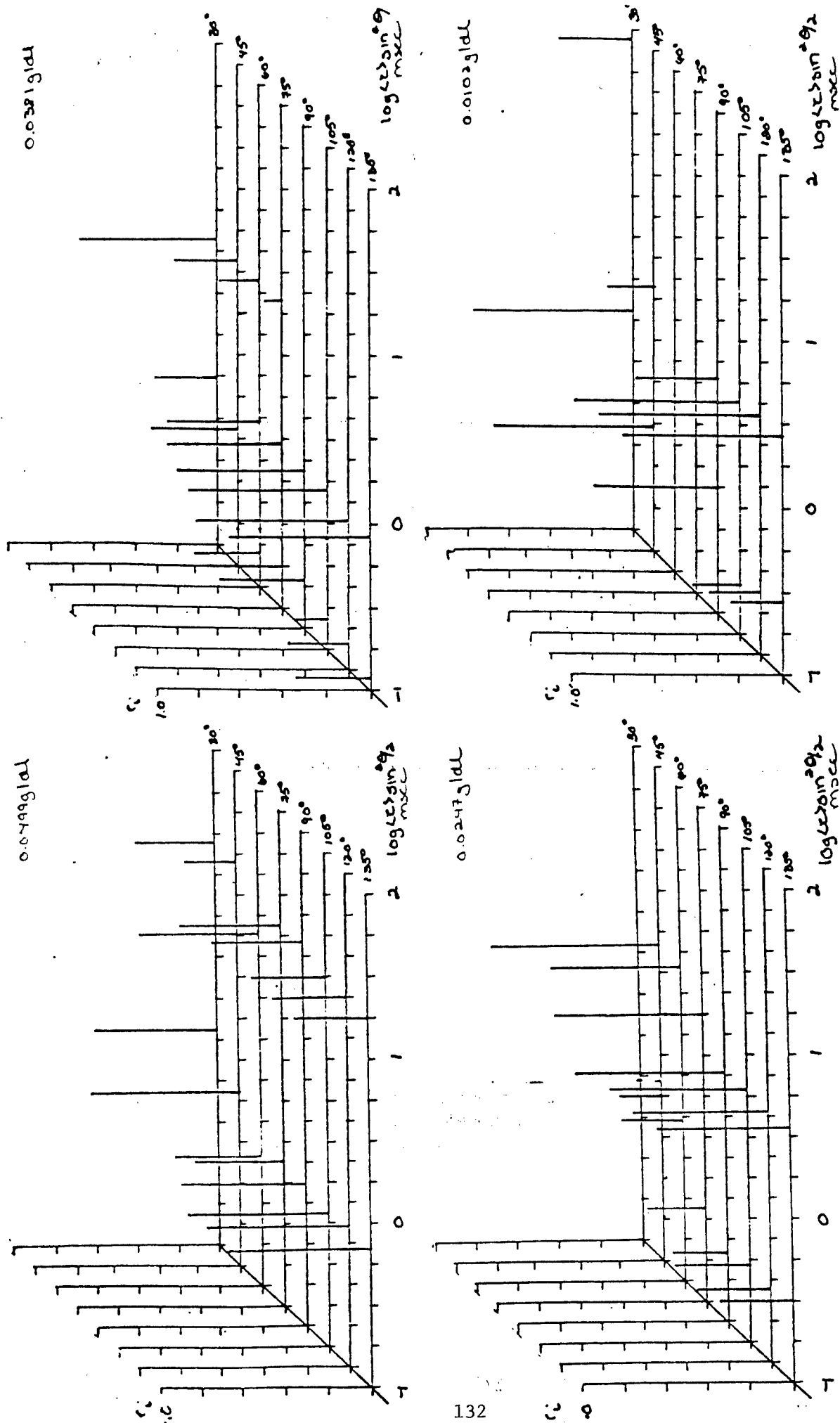
Figure 34: a)The concentration dependence of $\tau \sin^2 \theta/2$ of uncentrifuged PBT–PBO (75/25) in PPA/MSA

132
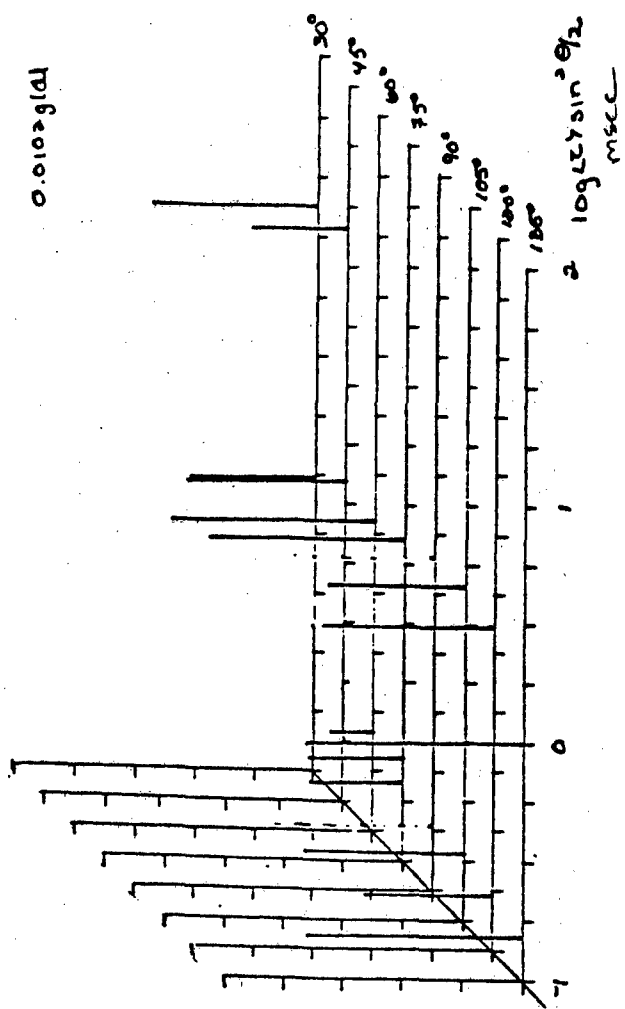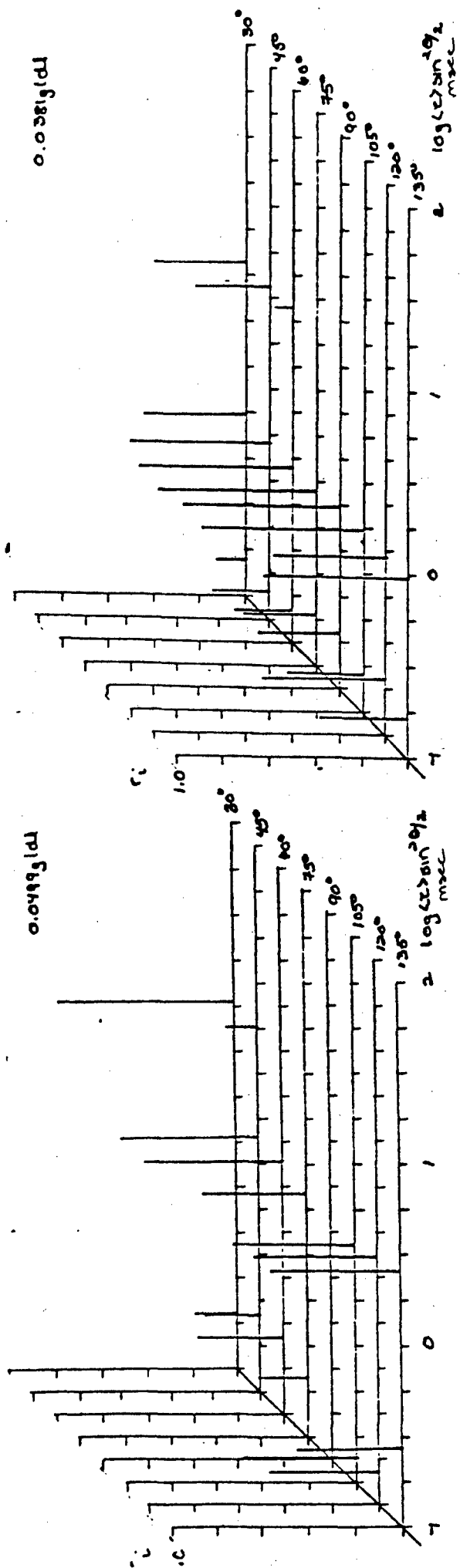
Figure 35: a) The concentration dependence of $\tau_i \sin^2 \theta/2$ of centrifuged PBT-PBO (75/25) in PPA/MSA.
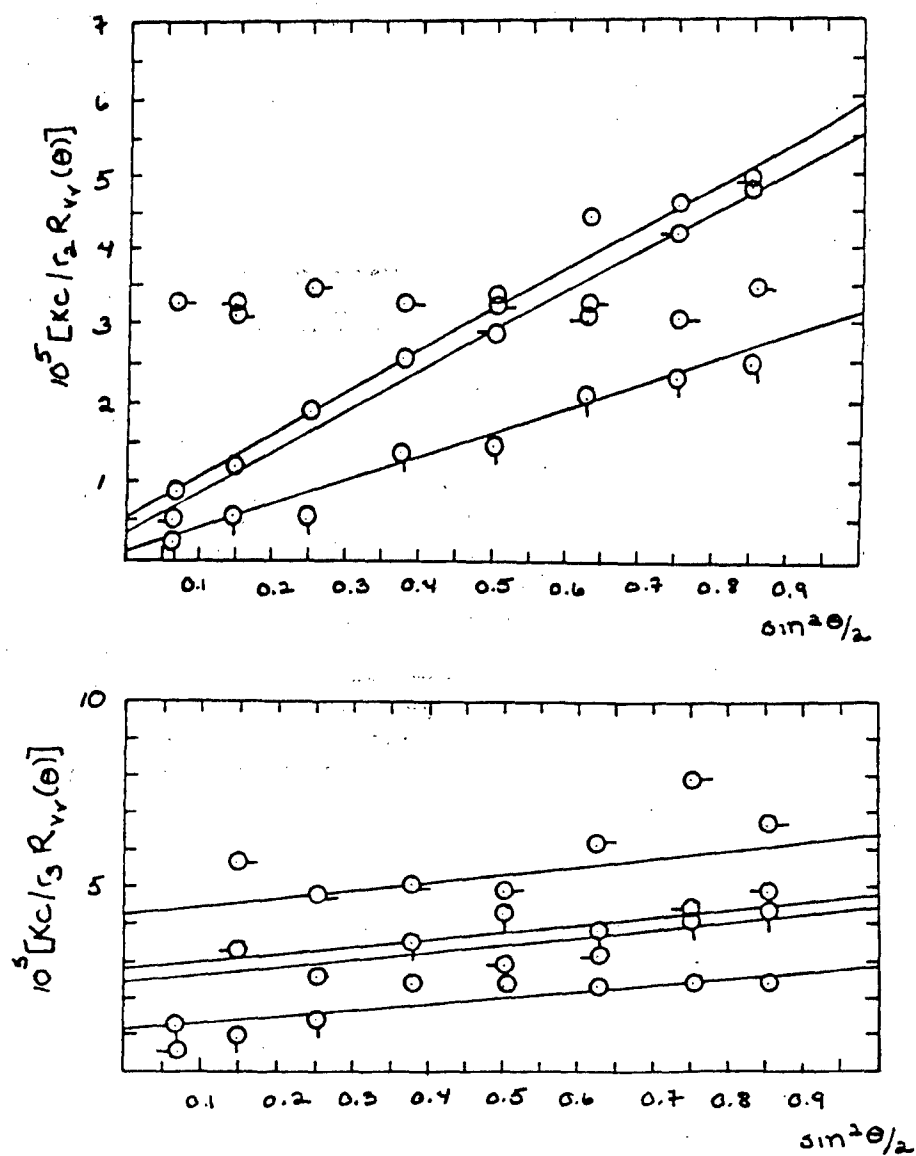
Figure 36:   The a)uncentrifuged   Kc/R$_{Vv}$, of PBT-PBO(75/25)
in PPA/MSA at 514 nm and 25.0°C. O   0.0499g/dl,i O— 0.0381 g/dl
Q 0.0247 g/dl —O 0.0102g/dl
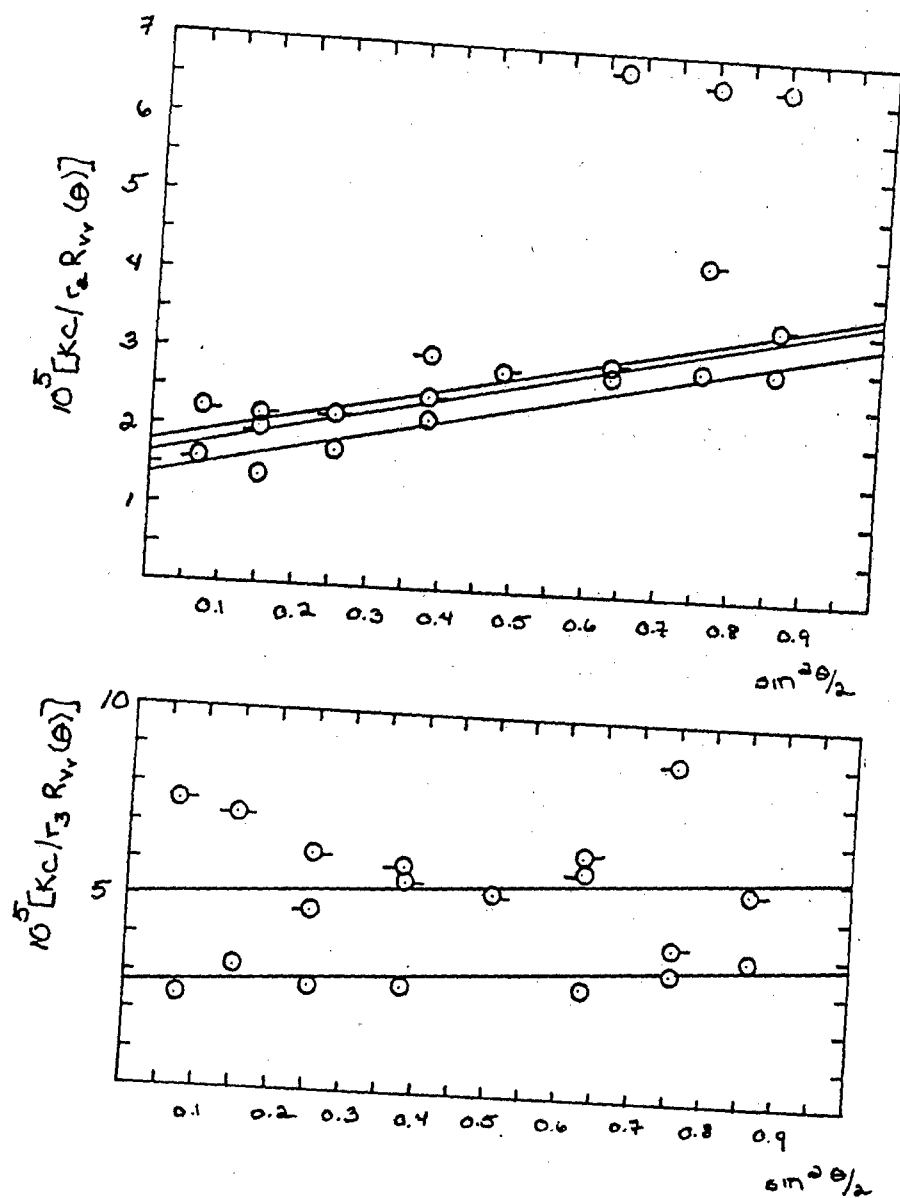
Figure 37: The centrifuged Kc/R_{vvi} of PBT-PBO(75/25) in PPA/MSA at 514 nm and 25.0°C. O 0.0499g/dl O- 0.0381 g/dl Q 0.0247 g/dl -O 0.0102g/dl

135
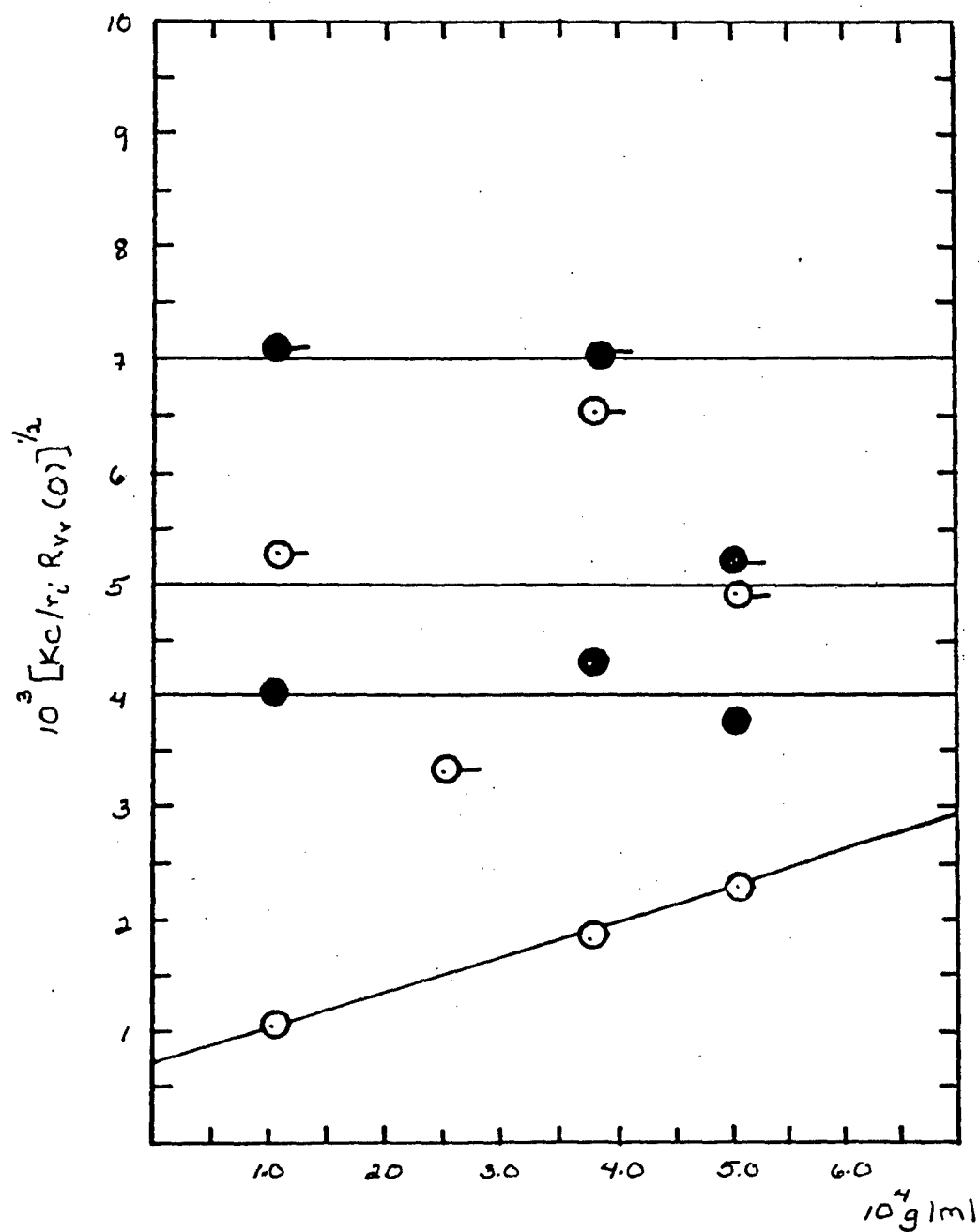
Figure 38: The concentration dependence of the Vv components of the integrated intensity light scattering of PBT-PBO (75/25) in PPA/MSA. O r_2 uncentrifuged ● r_2 centrifuged O r_3 uncentrifuged ●-r_3 centrifuged
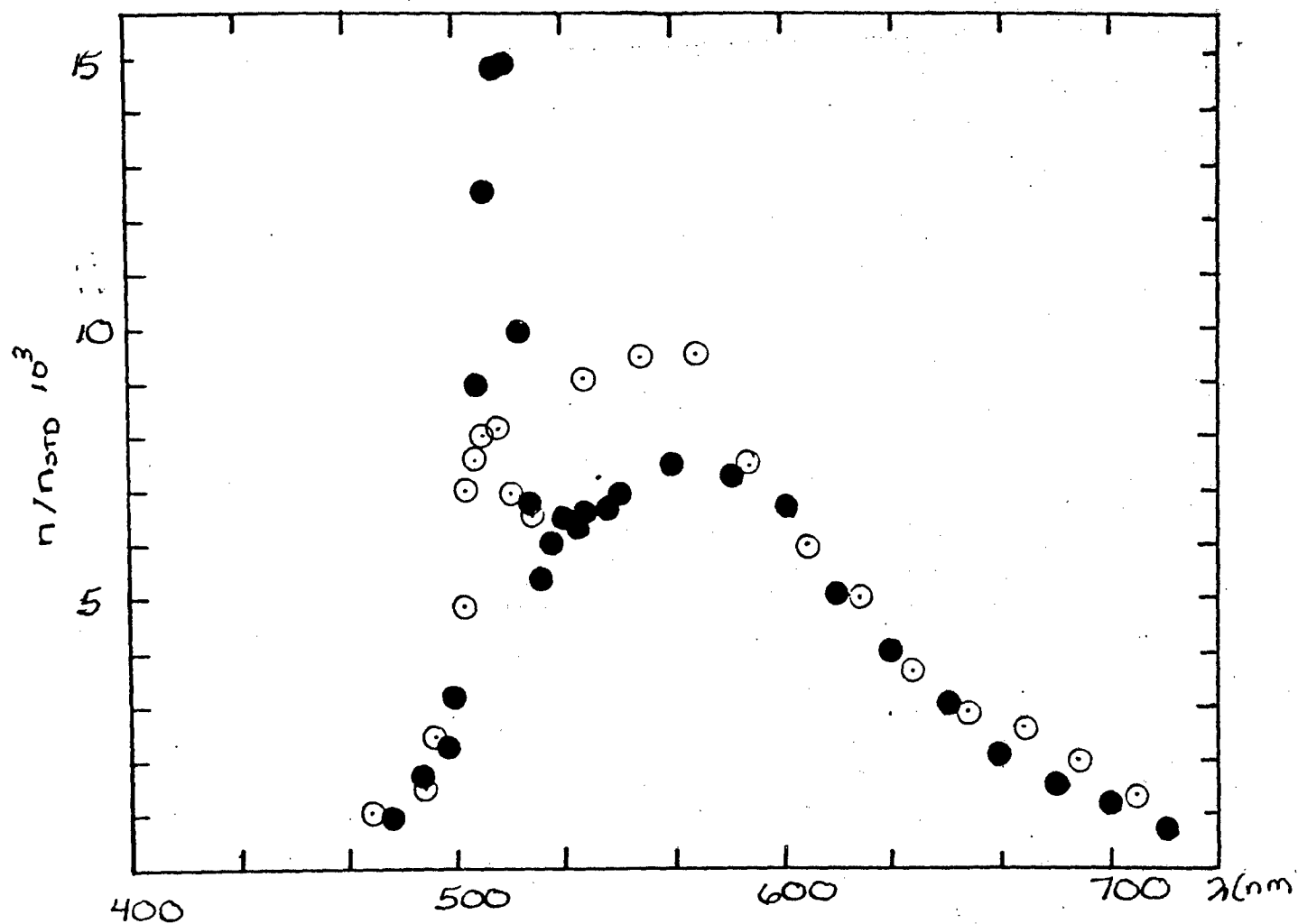
Figure 39: Hv scattering and Hv emission spectra for PBT 8 excited at 514 nm and 25.0°C. ● 0.0483 g/dl + 0.30 N salt   O 0.0658 g/dl, no salt
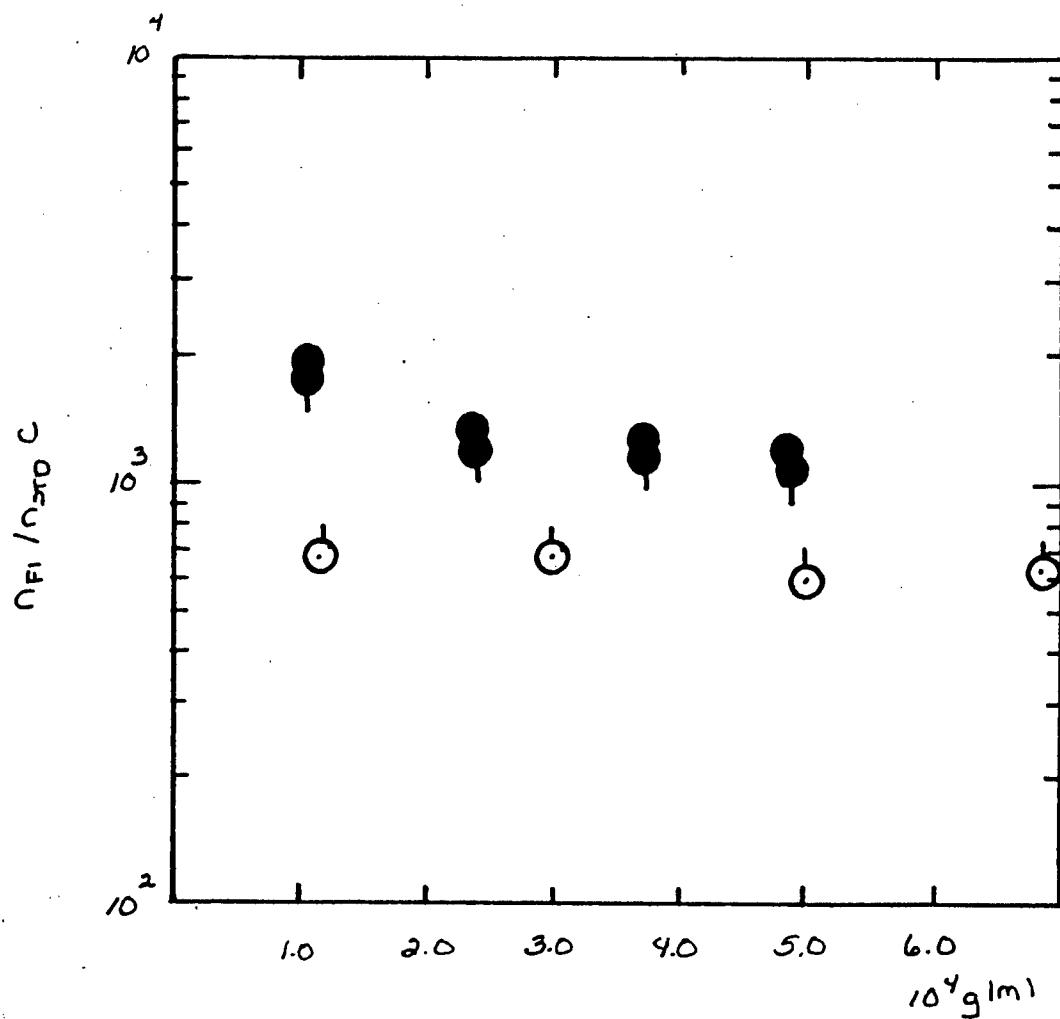
Figure 40: Vv fluorescence intensity for PBT 8 at 25.0° C versus concentration ● uncentrifuged, ● centrifuged + 0.3N salt , O centrifuged without salt excited at 514.5nm and 25.0° C
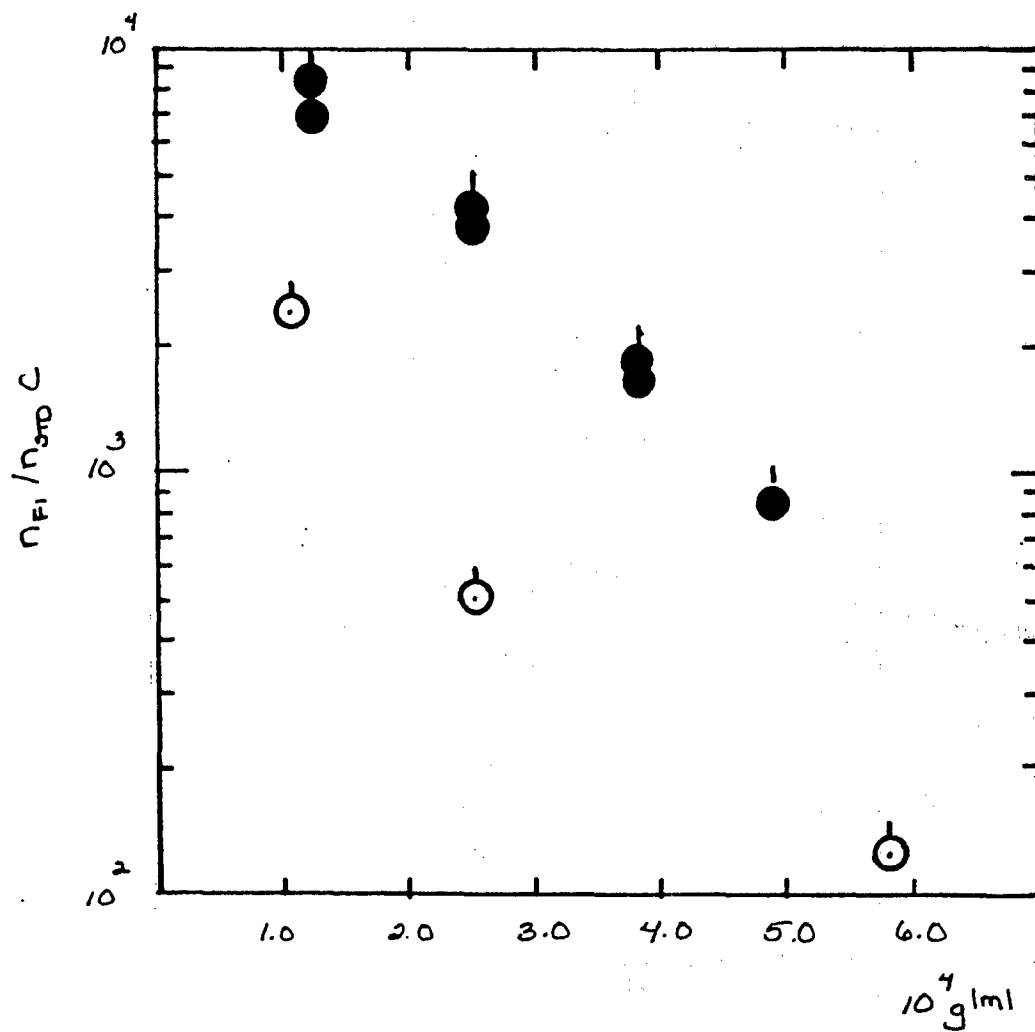
Figure 41:   Vv fluorescence intensity for PBT 7 at 25.0°
C versus concentration. ● uncentrifuged, ◖ centrifuged +0.361 N salt,
○ centrifuged without salt excited at 514.5nm and 25.0°C
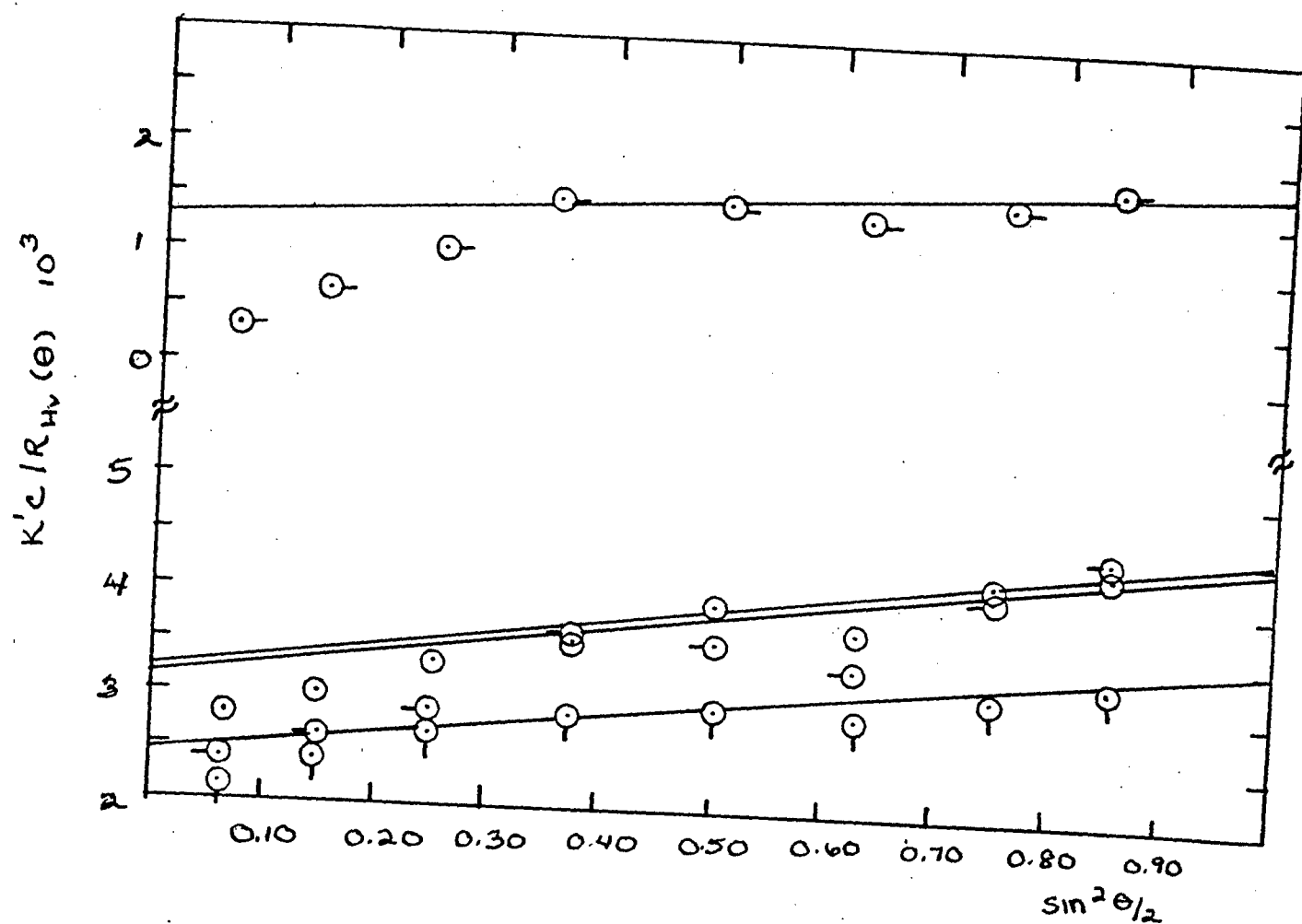
Figure 42: The Hv component of the integrated intensity light scattering of PBT 8. +0.30 N salt, O 0.0483 g/dl, ⊸O 0.0383 g/dl, ⊙ 0.0236 g/dl, ◐–0.0106 g/dl, at 514.5nm and 25.0° C
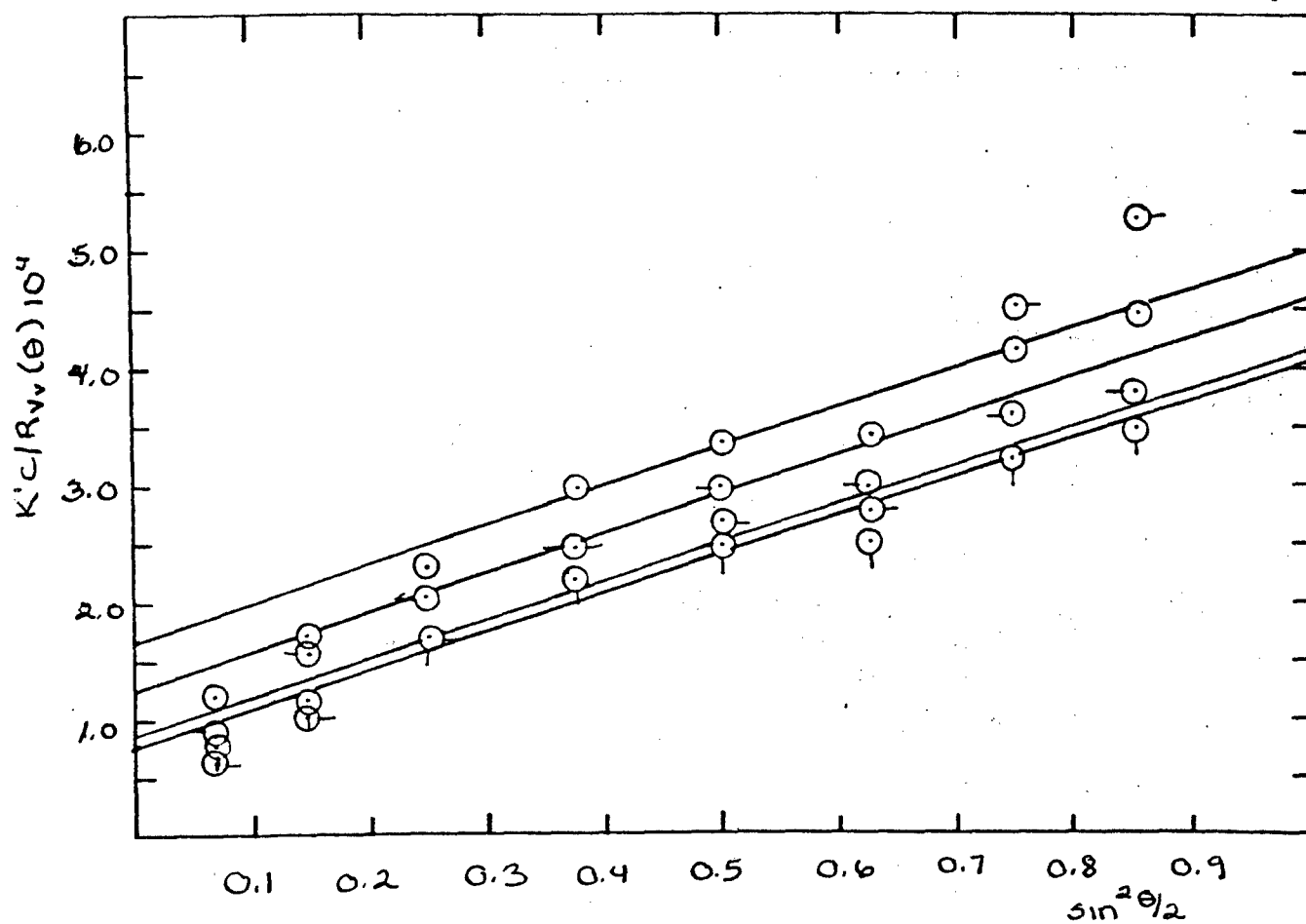
Figure 43: The Vv component of the integrated intensity light scattering of PBT 8. + 0.30N salt O 0.0483 g/dl,—O 0.0383 g/dl, Q 0.0236 g/dl, O—0.0106 g/dl 0.25 g/dl at 514.5 nm and 25.0°
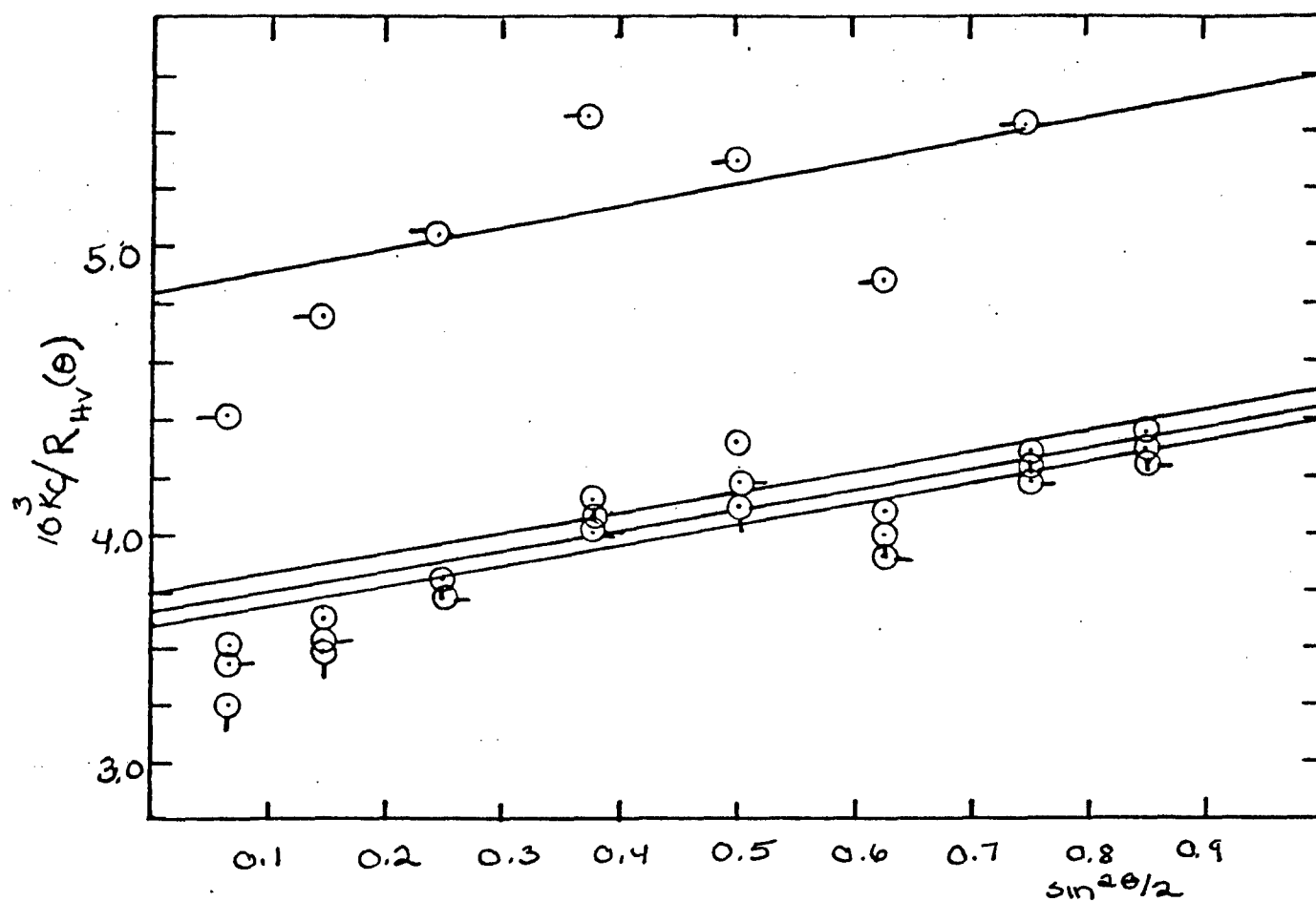
Figure 44: The centrifuged Hv component of the integrated intensity light scattering for PBT-8 + 0.3N salt. O 0.0483 g/dl, O—0.0383 g/dl, ○ 0.0236 g/dl,—O 0.0106 g/dl, at 514.5nm and 25.0°
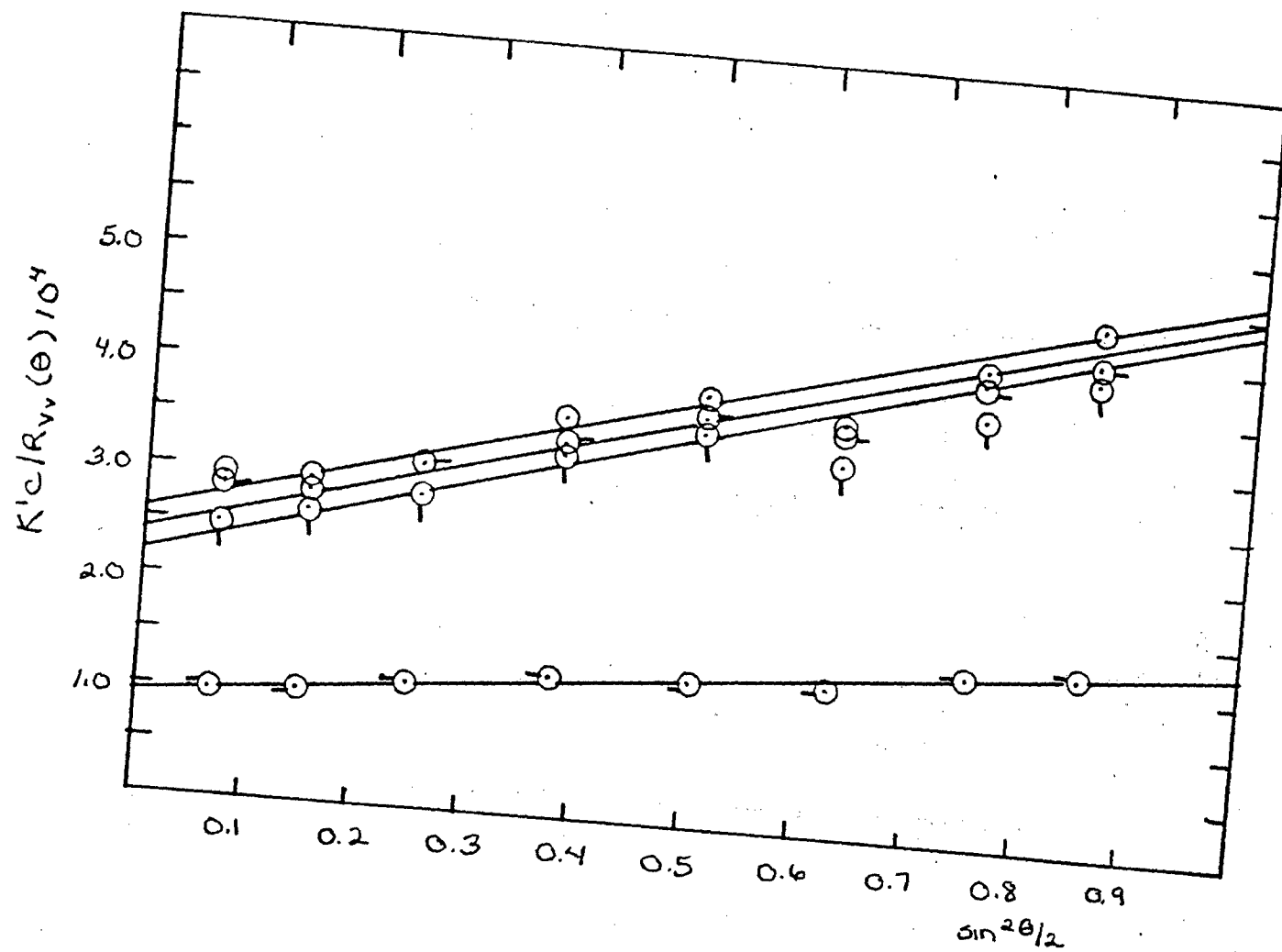
Figure 45: The centrifuged Vv component of the integrated intensity light scattering PBT-8 + 0.3N salt O 0.0483 g/dl, O–0.0383 g/dl, Q 0.0236 g/dl,–O 0.0106 g/dl, at 514.5nm and 25.0°

Figure 46: The concentration dependence of the Hv component for PBT $\mathbf{8}$, O uncentrifuged, ● centrifuged + salt at 514.5nm and φ centrifuged without salt at 633 nm and 25.0° C.

Figure 47: The concentration dependence of the Vv component for PBT 8 + 0.3N salt at 514.5 nm and 25.0° ● uncentrifuged and ● centrifuged, PBT-8 without salt ○ centrifuged at 633 nm and 25.0°C

145
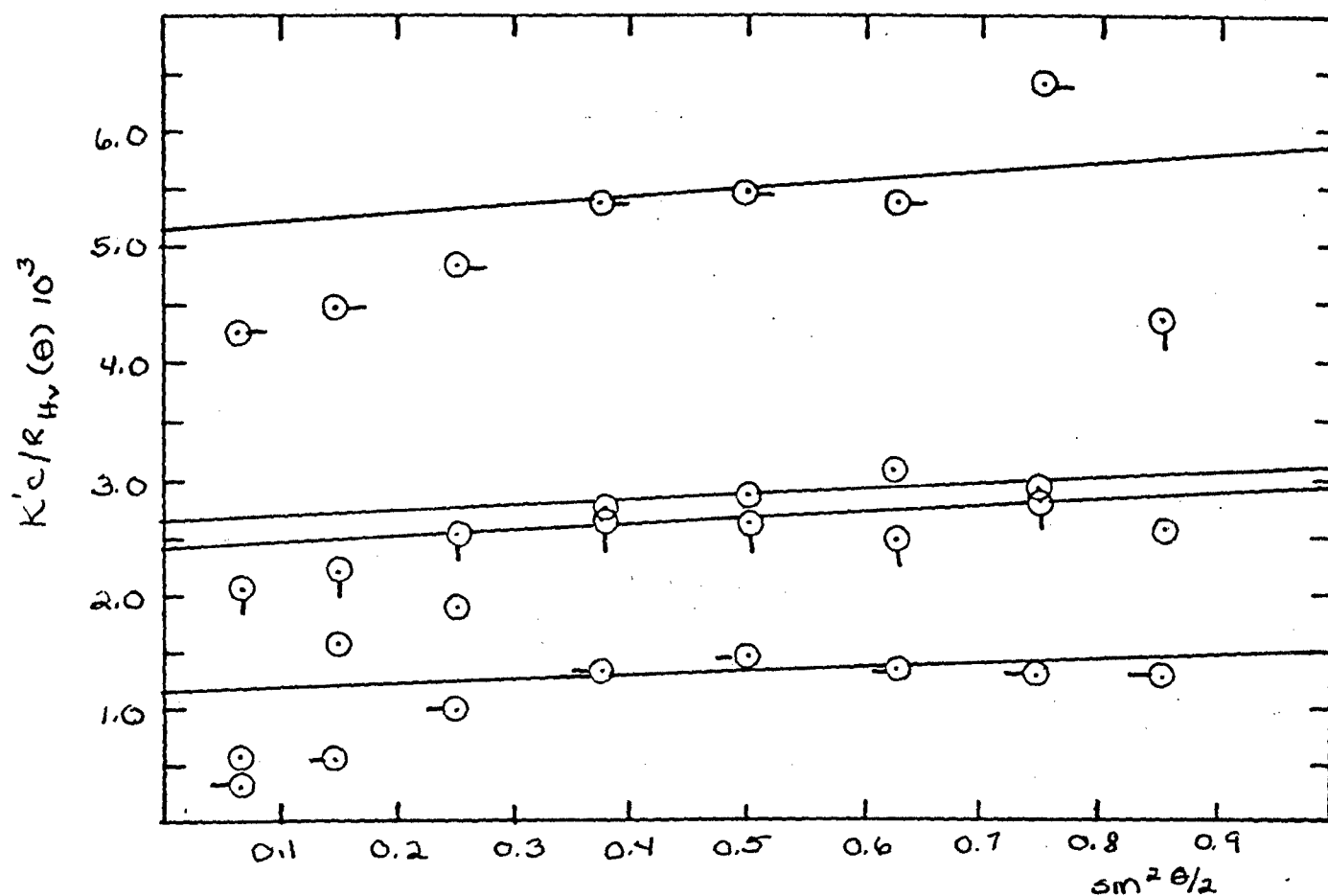
Figure 48: The Hv component of the integrated intensity light scattering for PBT 7 + 0.3 N salt at 514.5nm and 25.0°C. O 0.0492 g/dl, O– 0.0392 g/dl, Q 0.0250 g/dl,–O 0.0121 g/dl.
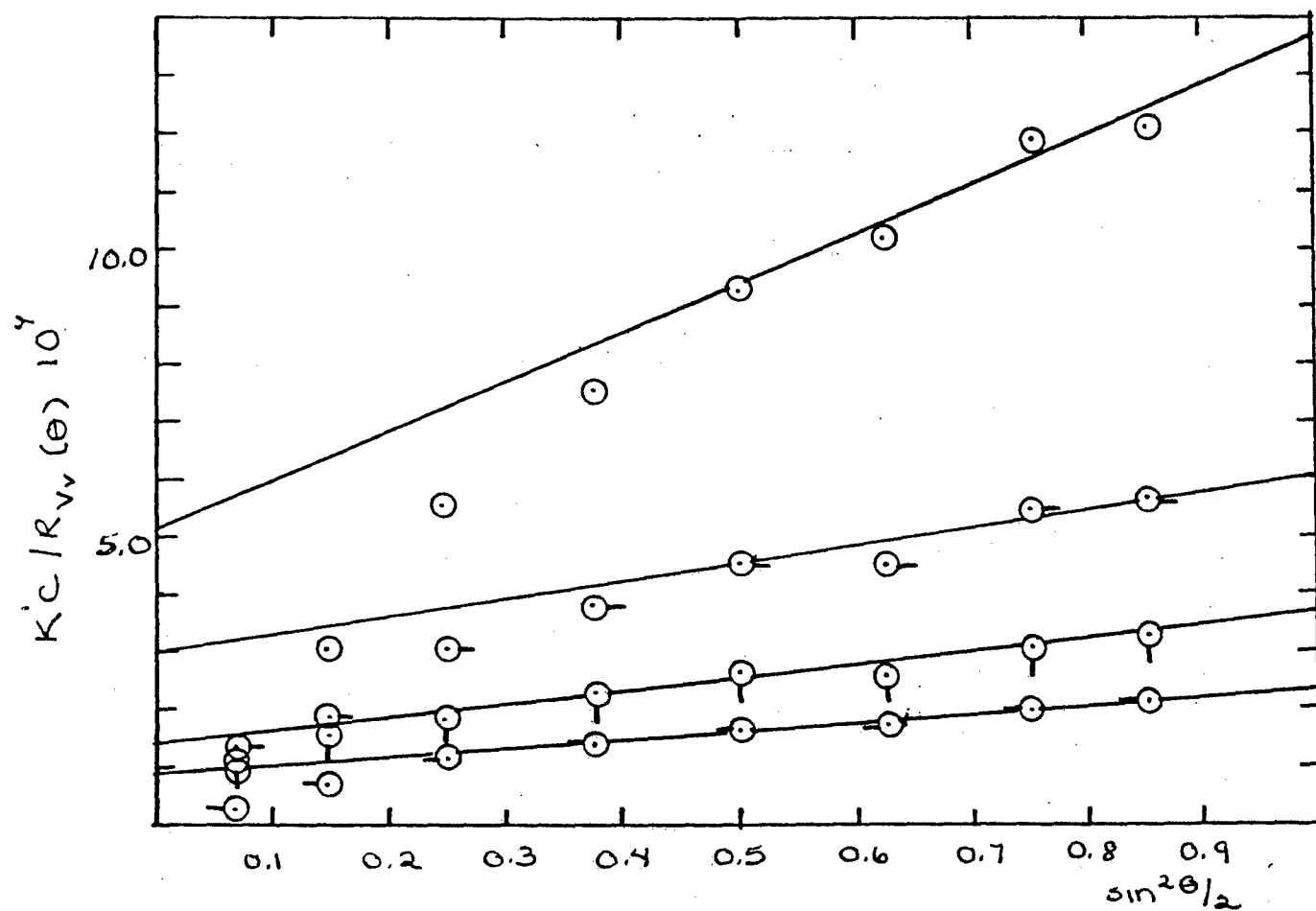
Figure 49: The Vv component of the integrated intensity light scattering for PBT 7 + 0.3N salt at 514.5 nm and 25.0°C. O 0.0492 g/dl, O–0.0392 g/dl, Q 0.0250 g/dl, –O 0.0121 g/dl

147
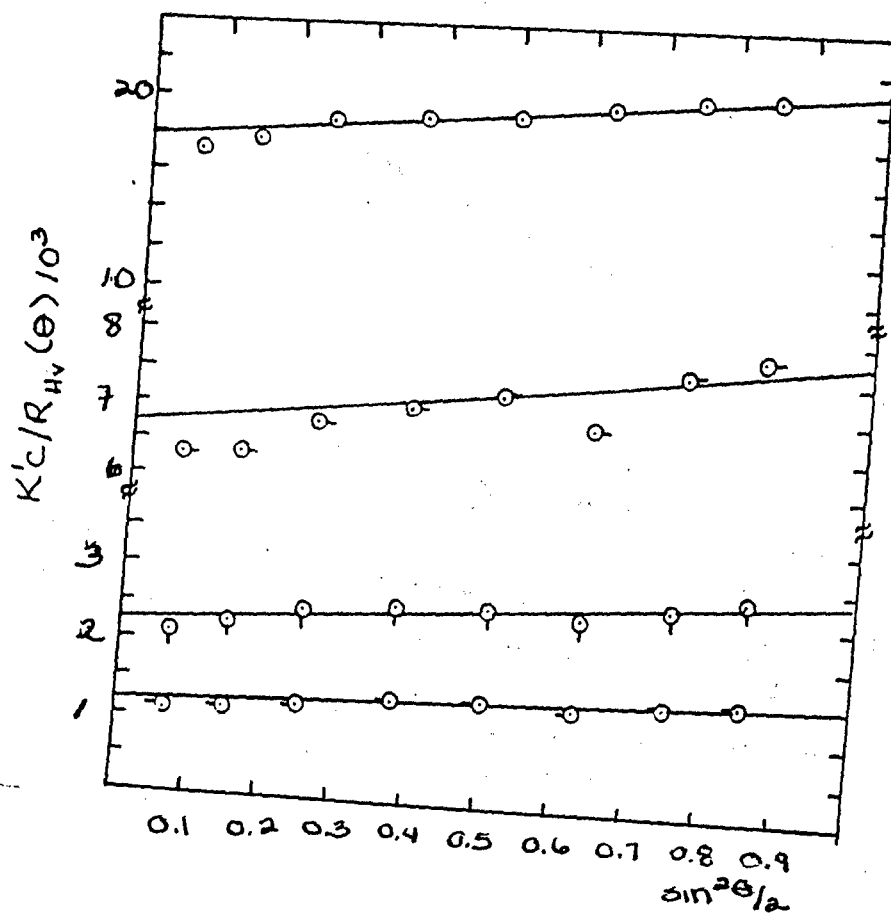
Figure 50: The Hv component of the integrated intensity light scattering for centrifuged PBT 7 + 0.3 N salt at 514.5nm and 25.0°C. O 0.0492 g/dl, O 0.0392 g/dl, Q 0.0250 g/dl, O 0.0121 g/dl.
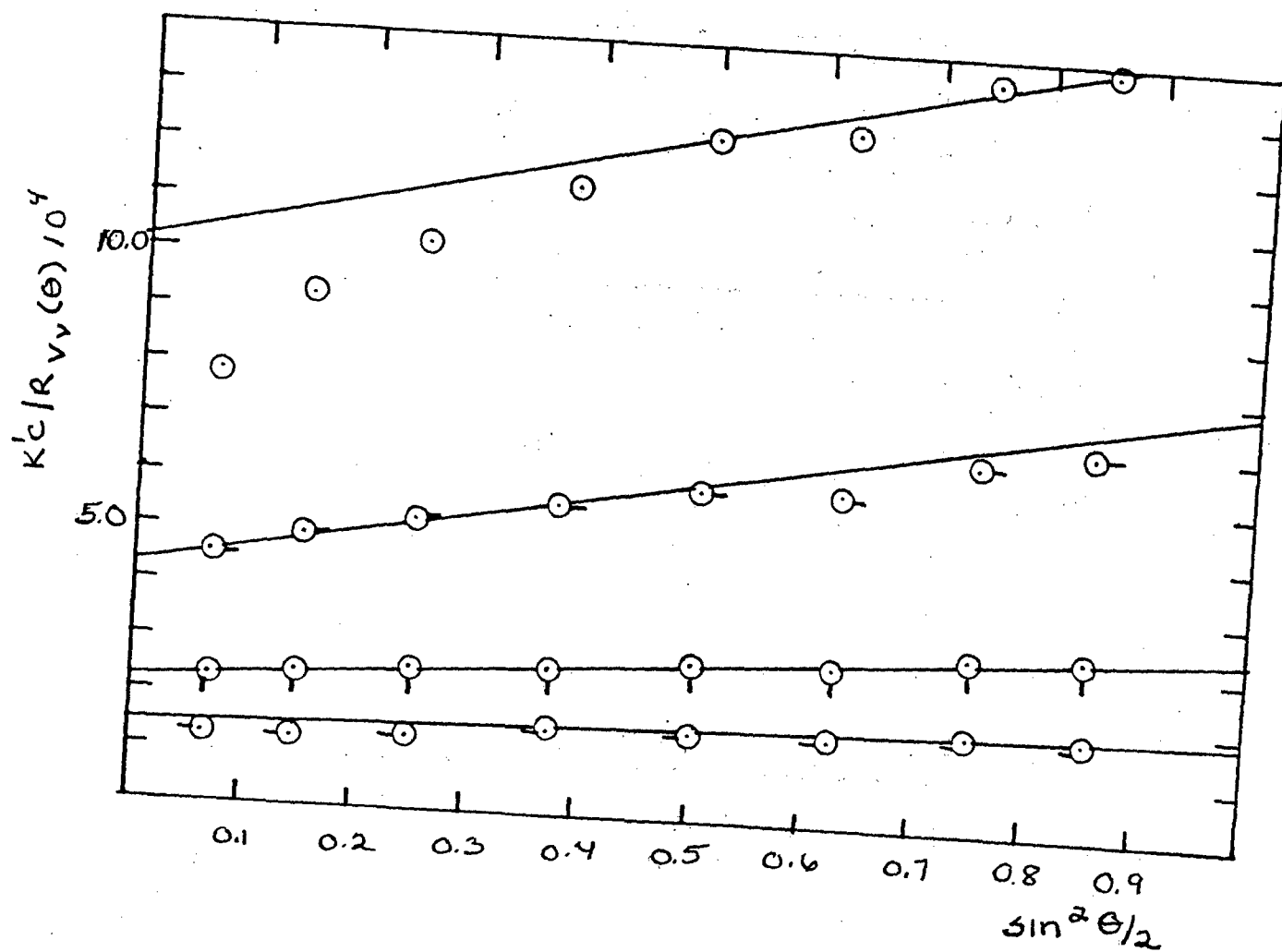
Figure 51: The Vv component of the integrated intensity light scattering for centrifuged PBT 7 + 0.3 N salt at 514.5nm and 25.0°C. O 0.0492 g/dl, O- 0.0392 g/dl, ⦶ 0.0250 g/dl, –O 0.0121 g/dl.
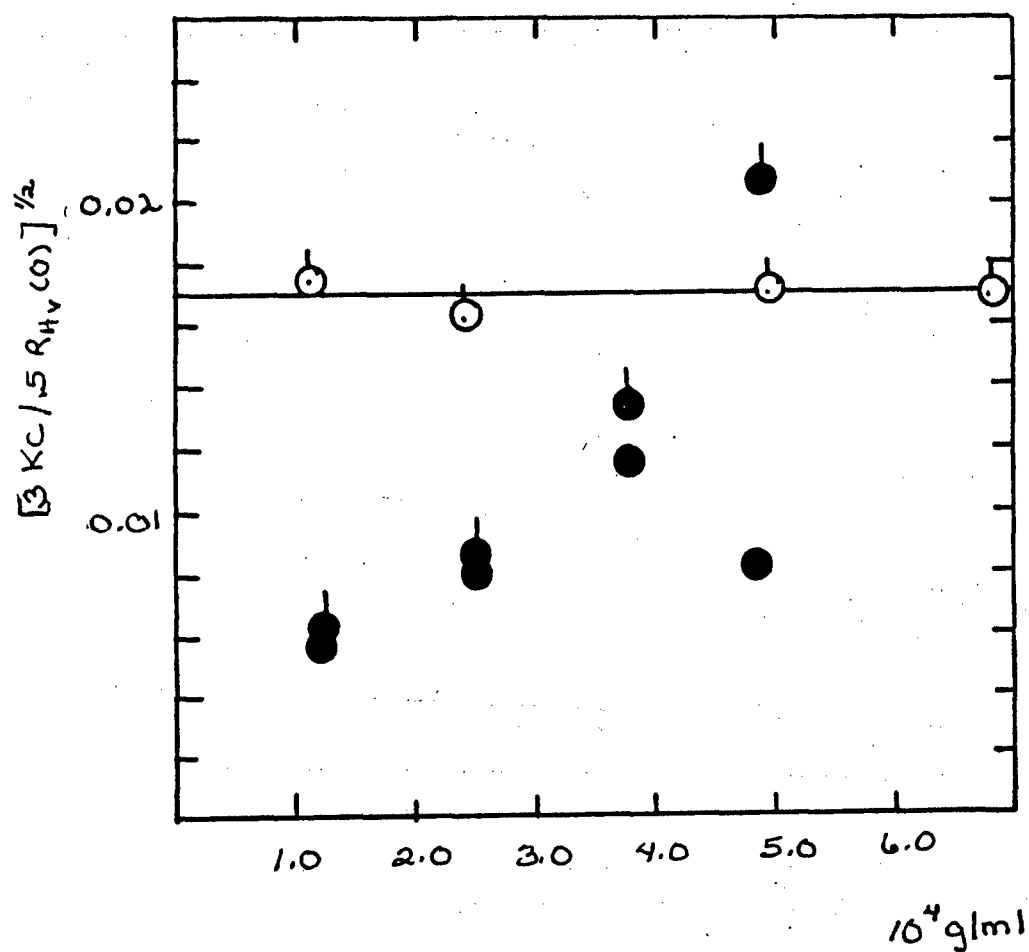
Figure 52 :   The concentration dependence of the Hv component for PBT 7 , ● uncentrifuged, ● centrifuged + salt at 514.5nm and O centrifuged without salt at 633 nm and 25.0° C.

Figure 53: The concentration dependence of the Vv component for PBT 7 , ● uncentrifuged, ● centrifuged + salt at 514.5 nm and ○ centrifuged without salt at 633 nm and 25.0°C.
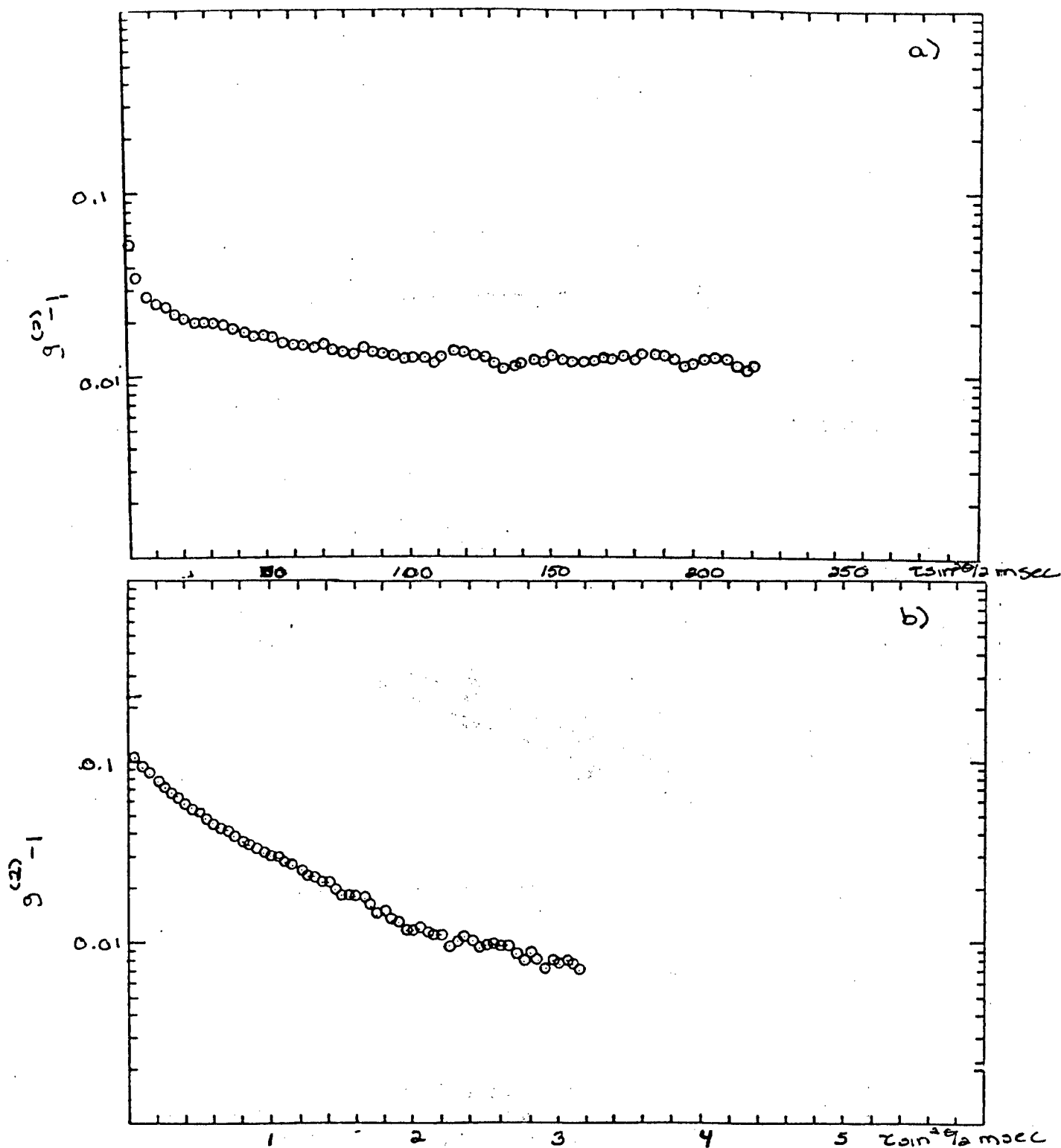
Figure 54: Intensity fluctuation light scattering $g^{(2)}(\Delta\tau,\tau)$ versus $\tau\sin^2\theta/2$ for PBT 8 + salt 0.0106 g/dl at 514.5 nm and 25.0°C. a) 30° b)90°
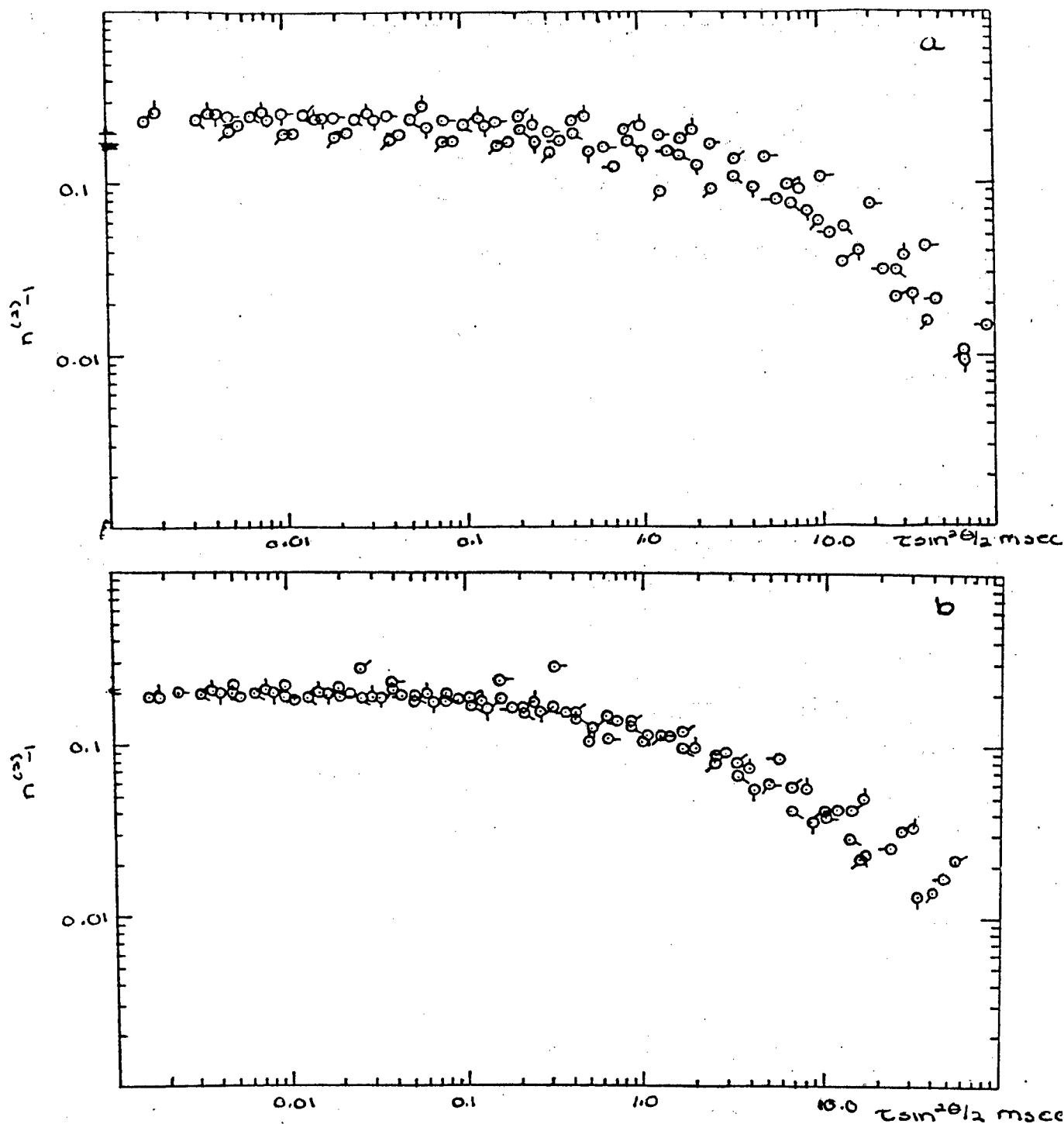
Figure 55: Intensity fluctuation light scattering $n^{(2)}-1$ versus $\tau \sin^2 \theta/2$ for PBT 8 + salt at 514.5 nm and 25.0°C. a) 0.0106 g/dl b) 0.0483 g/dl Ⓞ 45° with pips clockwise to 135° in 15° increments.
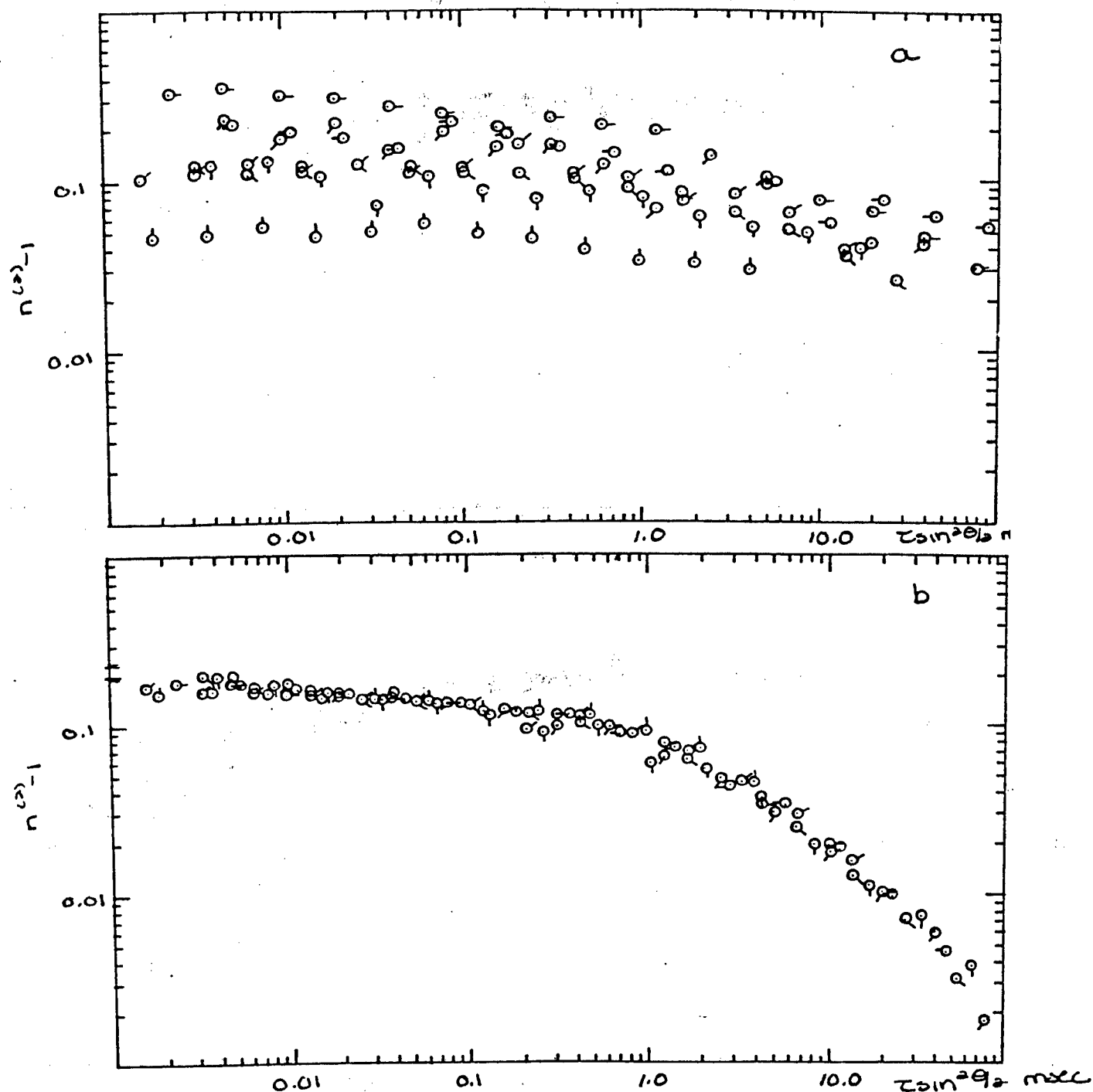
Figure 56: Intensity fluctuation light scattering n^2-1
versus $\tau \sin^2 \theta/2$ for centrifuged PBT 8 + salt at 514.5 nm
and 25.0°C a) 0.0106 g/dl b) 0.0483 g/dl ◯ 45° with pips clockwise
to 135° in 15° increments.
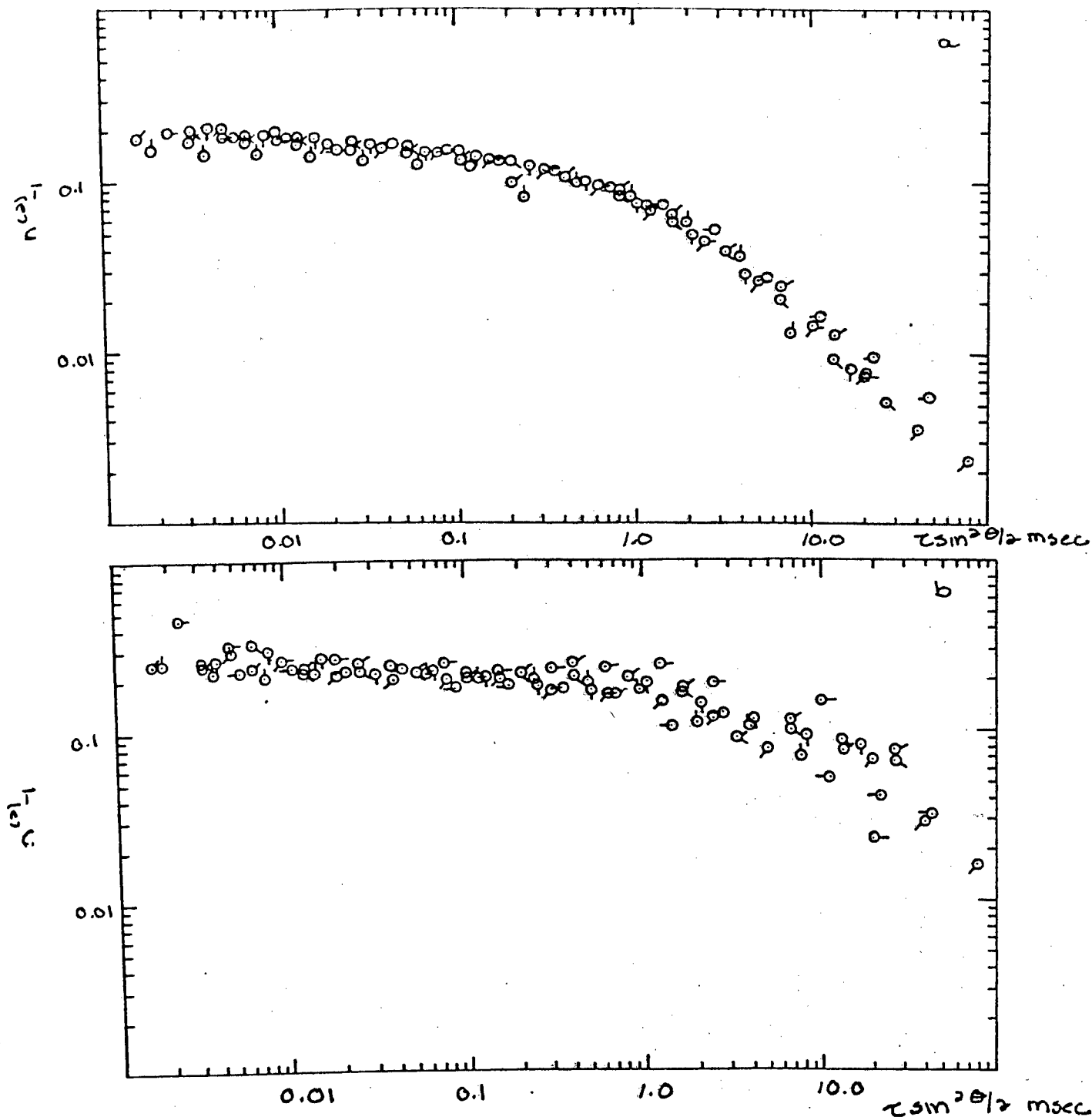
Figure 57: Intensity fluctuation light scattering
n^2-1 versus $\tau\sin^2 \theta/2$ for PBT 7 + salt at 514.5 nm and
and 25.0°C a)0.0121 g/dl b)0.0492 g/dl. ○ 45° with pips clockwise
to 135° in 15° increments.
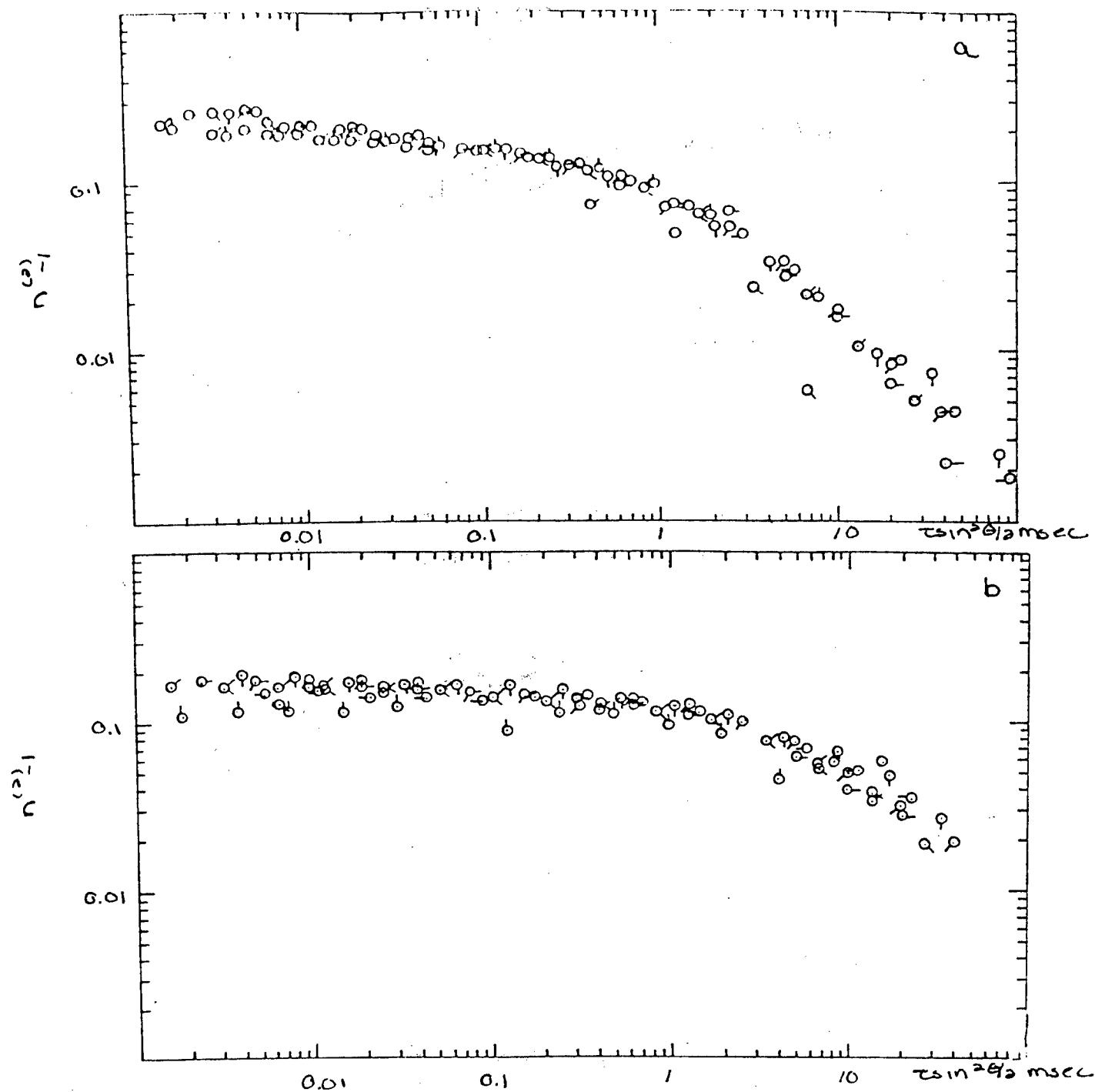
Figure 58: Intensity fluctuation light scattering n^2-1 versus τ $\sin^2 \theta/2$ for centrifuged PBT 7 + salt at 514.5 nm and and 25.0°C a)0.0121 g/dl b)0.0492 g/dl. ○ 45° with pips clockwise to 135° in 15° increments.
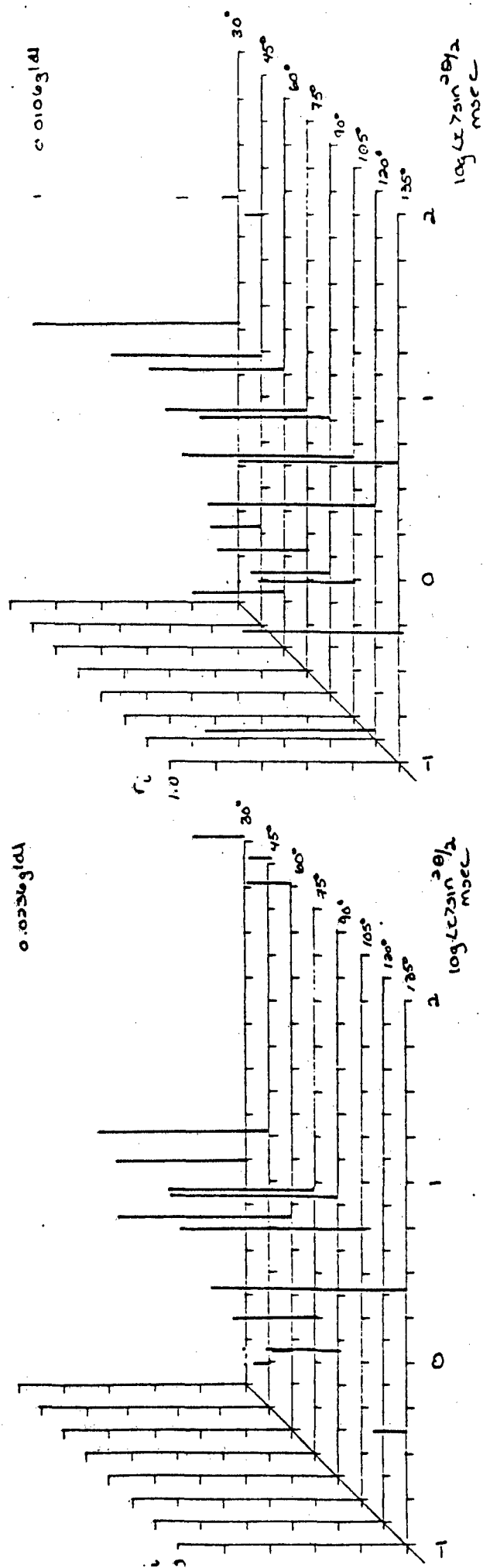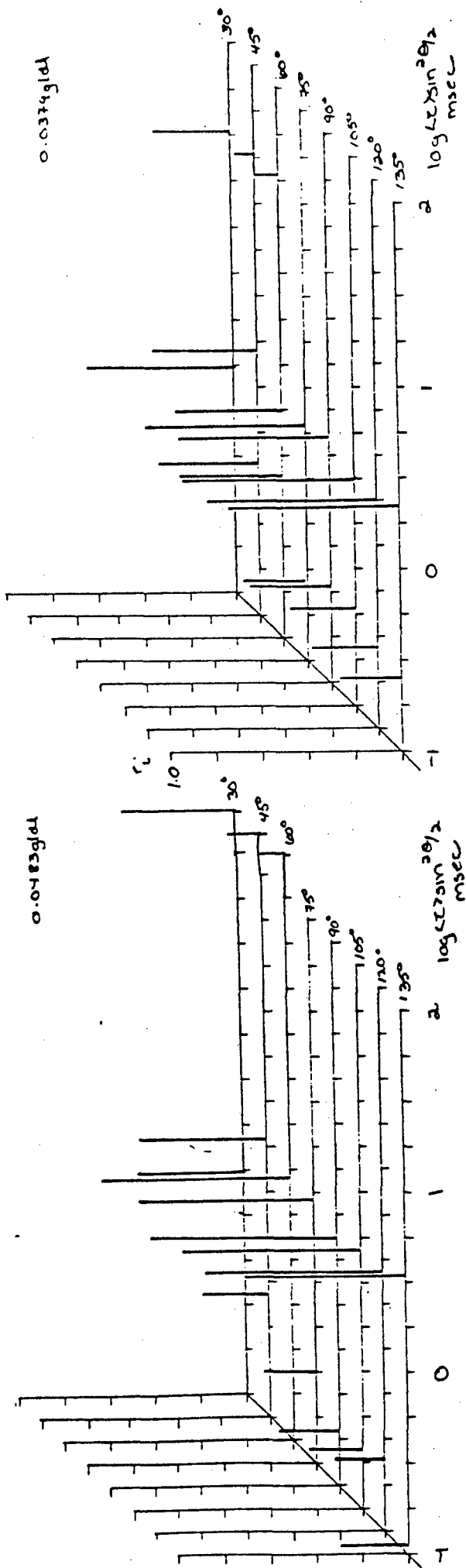
Figure 59: a)The concentration dependence of $\tau_i \sin^2 \theta/2$ of uncentrifuged PBT-8 + salt
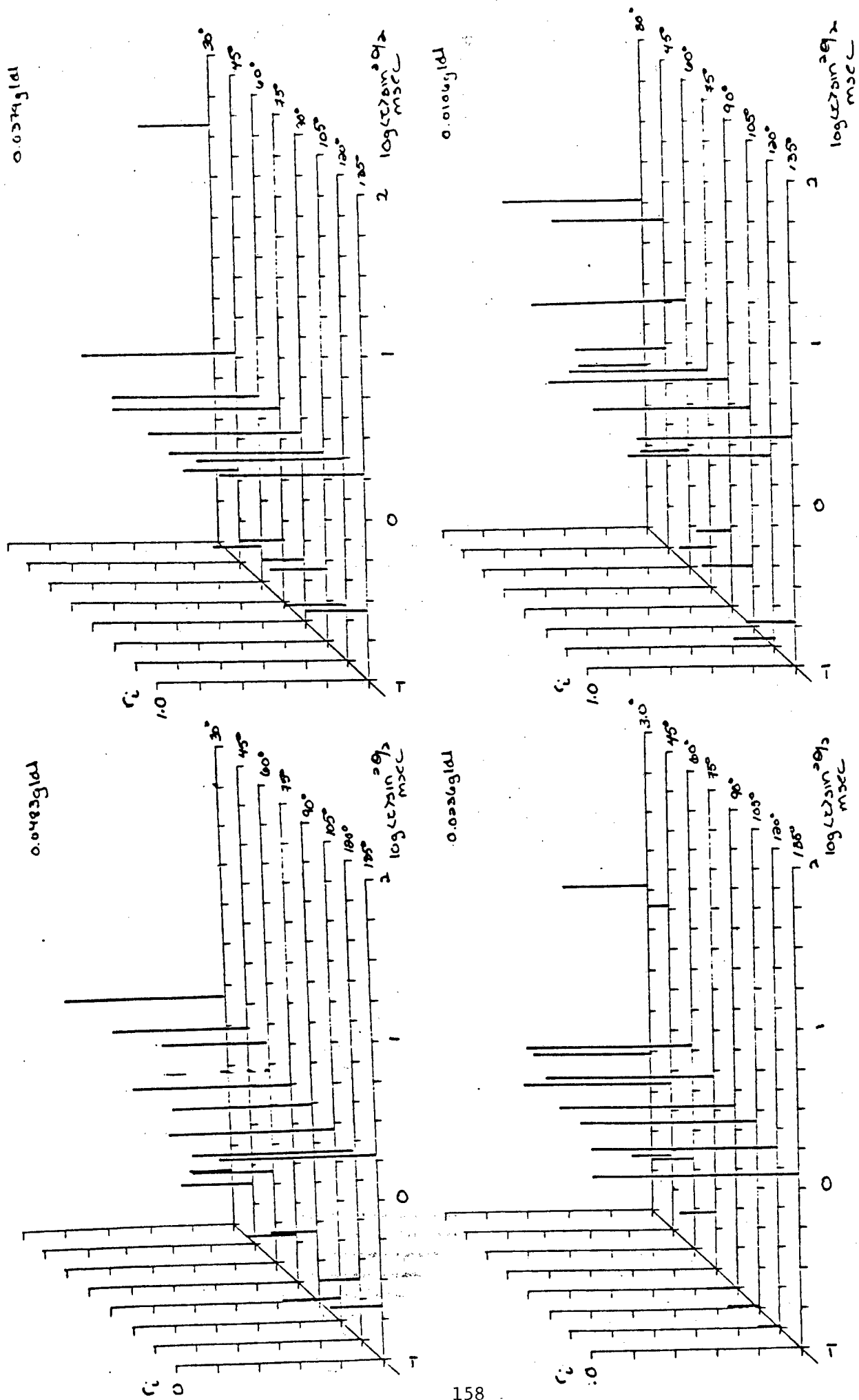
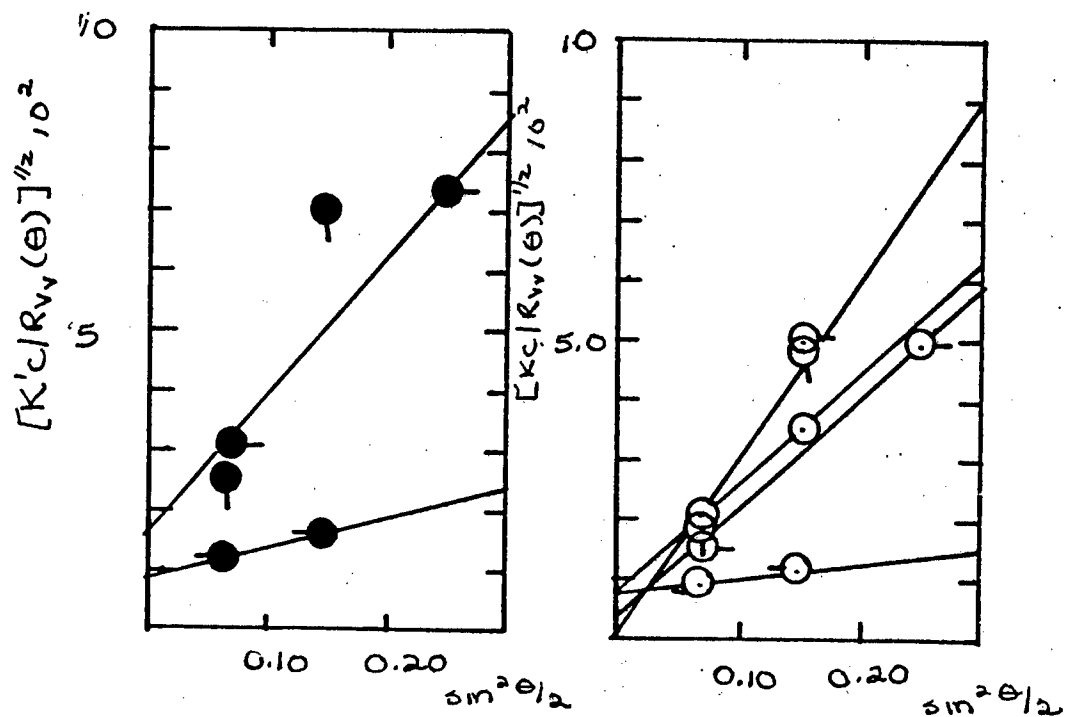Figure 60: a)The concentration dependence of $\tau_i \sin^2 \theta/2$ of centrifuged PBT-8 + salt

158

Figure 61: a)The concentration dependence of $\tau \sin^2 \theta/2$ of uncentrifuged PBT-7+ salt
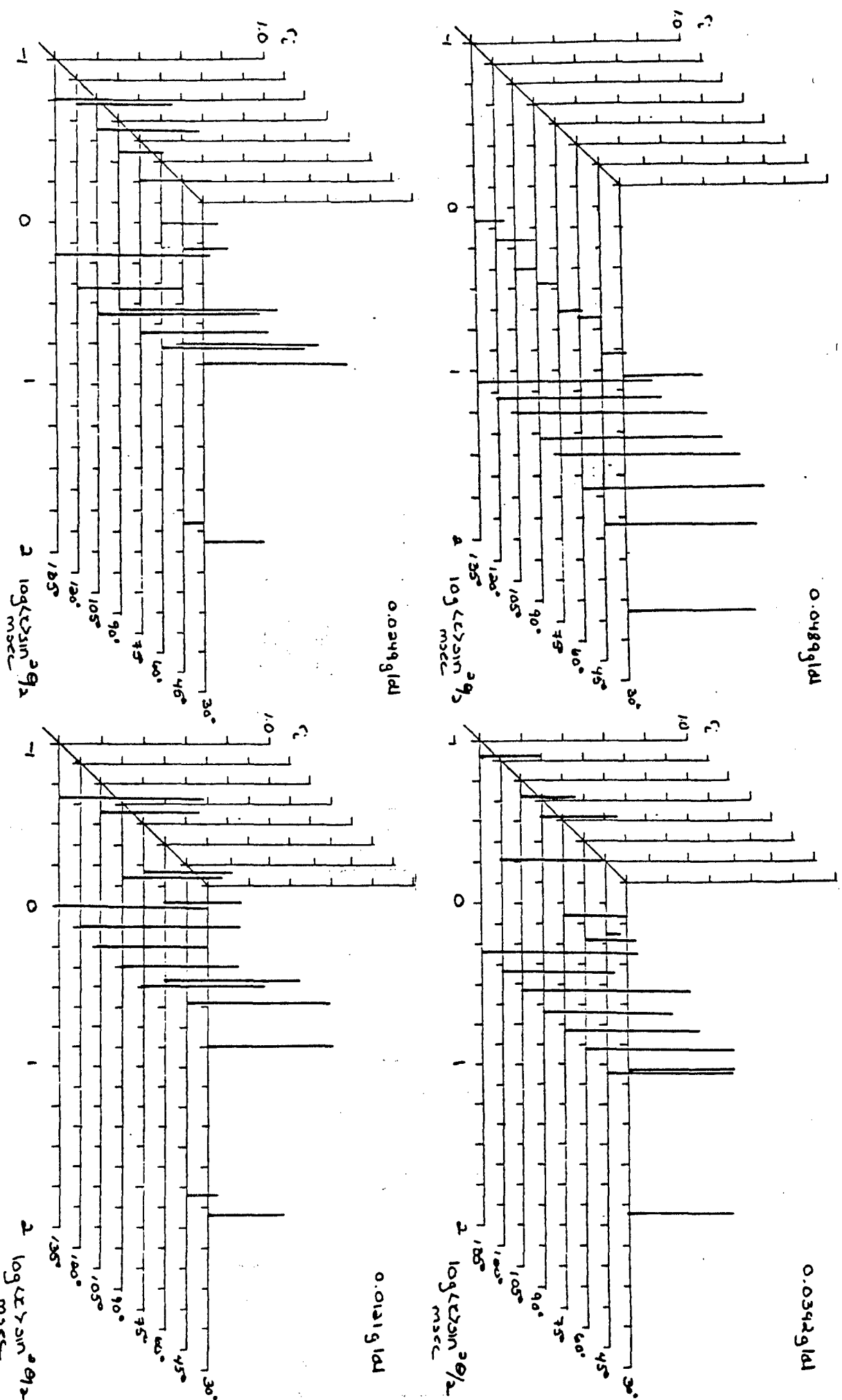
Figure 62: a) The concentration dependence of $\tau_i \sin^2 \theta/2$ of centrifuged PBT-7 + salt

160

Figure 63: $[Kc/R_{Vv_1}]^{1/2}$ versus $\sin^2 \theta/2$ for solutions of PBT 8 + salt. O uncentrifuged ● centrifuged, O 0.0483 g/dl, O–0.0383 g/dl, φ 0.0236 g/dl,–O 0.0106 g/dl, at 514.5nm and 25.0°
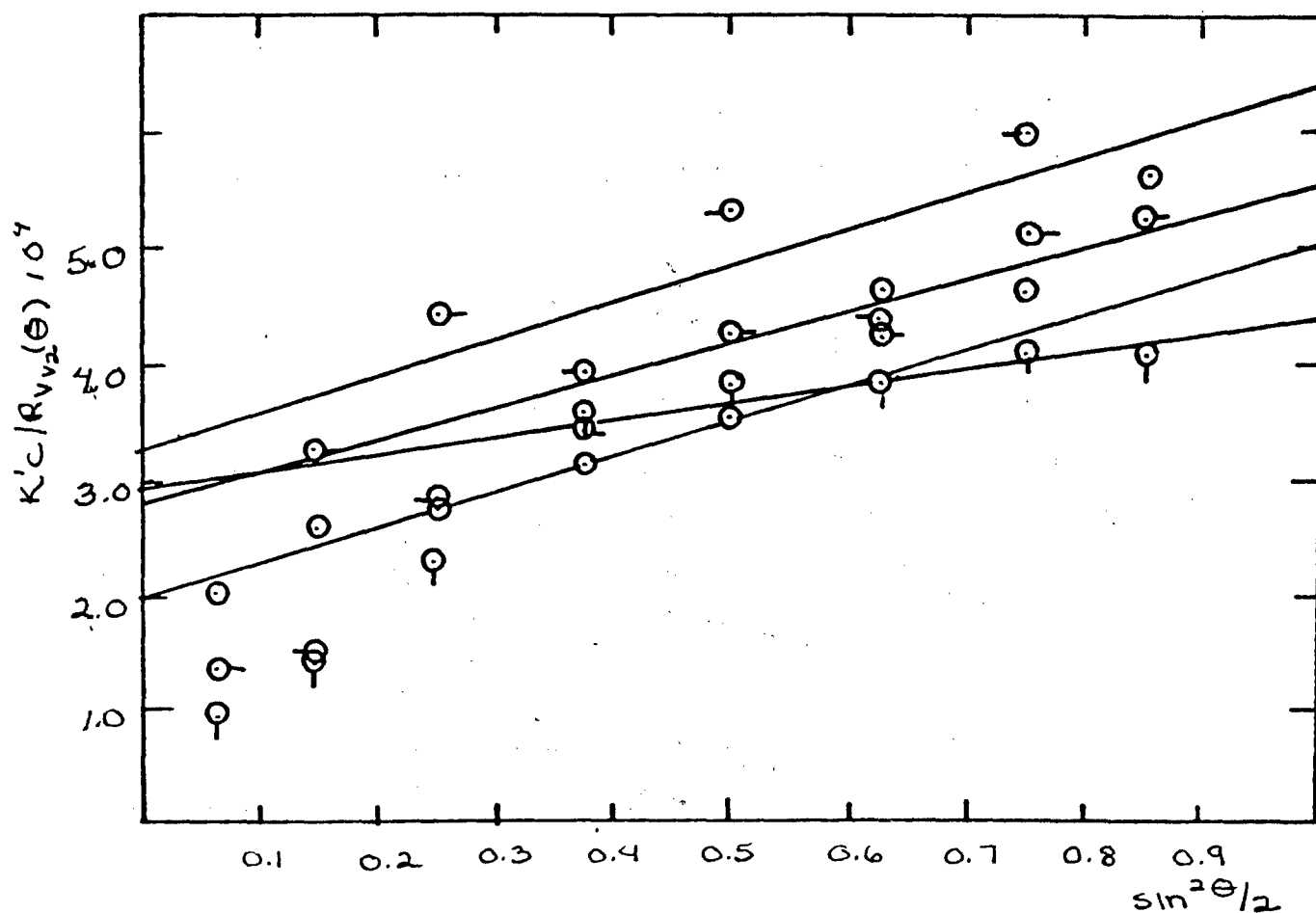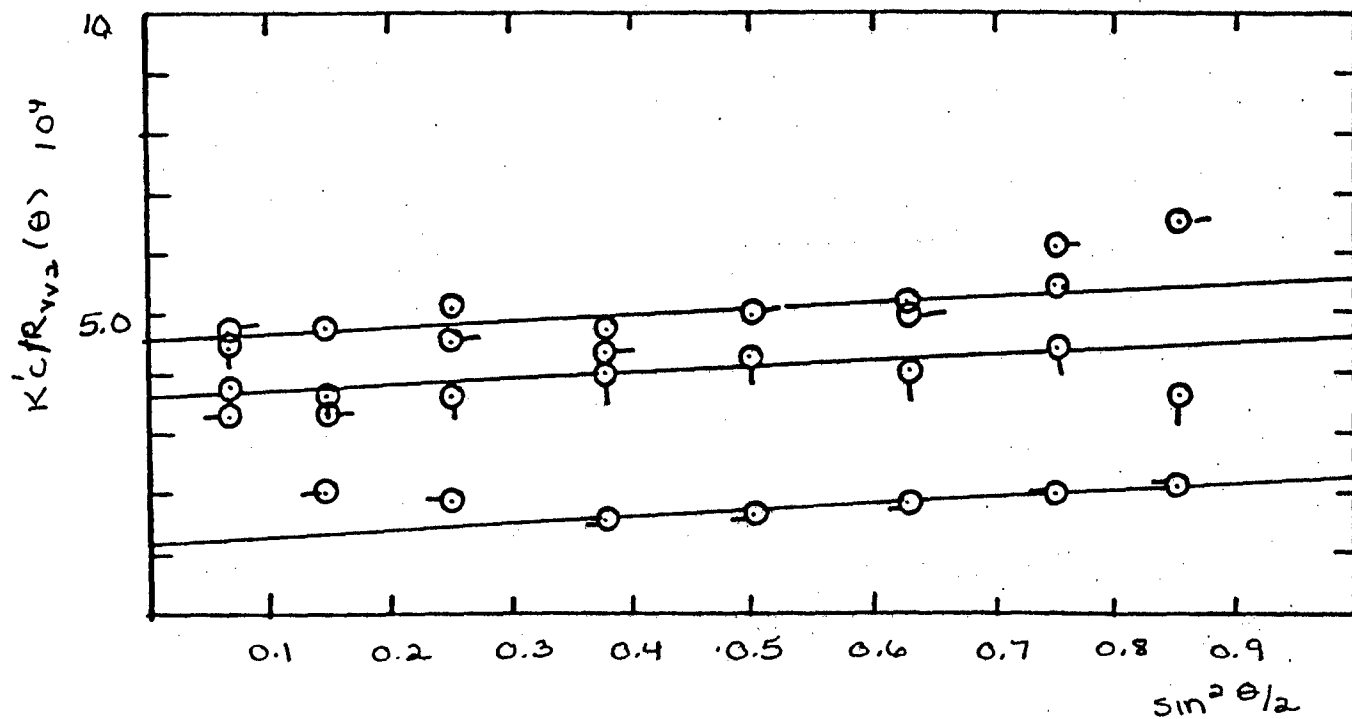
Figure 64 : $K_c/R_{Vv,2}$ versus $\sin^2 \theta/2$ for
solutions of PBT 8 + salt uncentrifuged,   O 0.0483 g/dl, O−0.0383 g/dl,
Q 0.0236 g/dl,−O 0.0106 g/dl, at 514.5nm and 25.0°

Figure 65:   Kc/R$_{vv2}$ versus sin^2 θ/2 for
solutions of PBT 8 + salt at 25.0°C centrifuged, O 0.0483 g/dl,
O 0.0383 g/dl, Q 0.0236 g/dl, -O 0.0106 g/dl, at 514.5nm and 25.0°
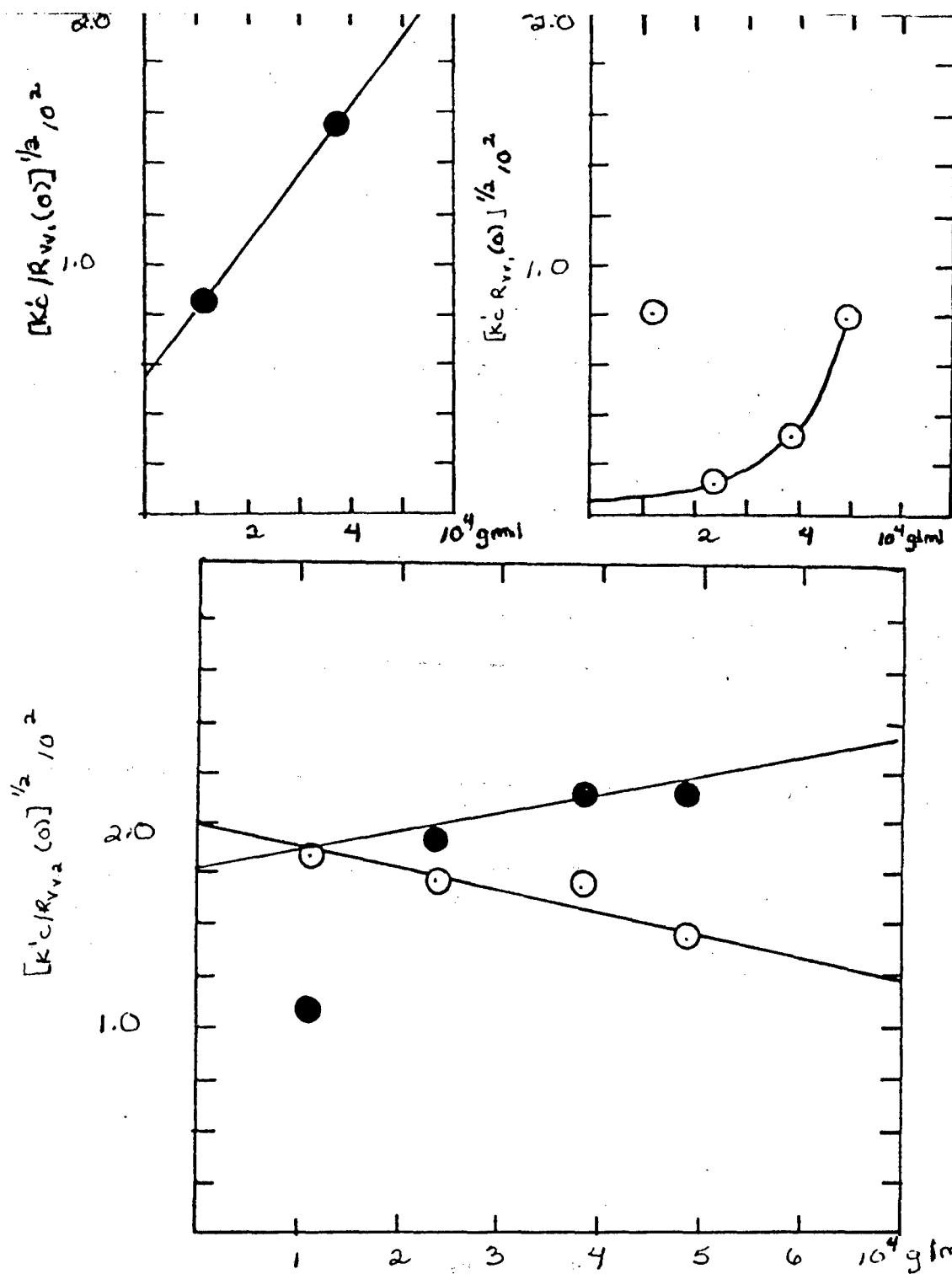
163

Figure 66: Concentration dependence of $R_{Vv,1}$ and $R_{Vv,2}$, O uncentrifuged and ● centrifuged for solutions of PBT 8 + salt at 25.0°C
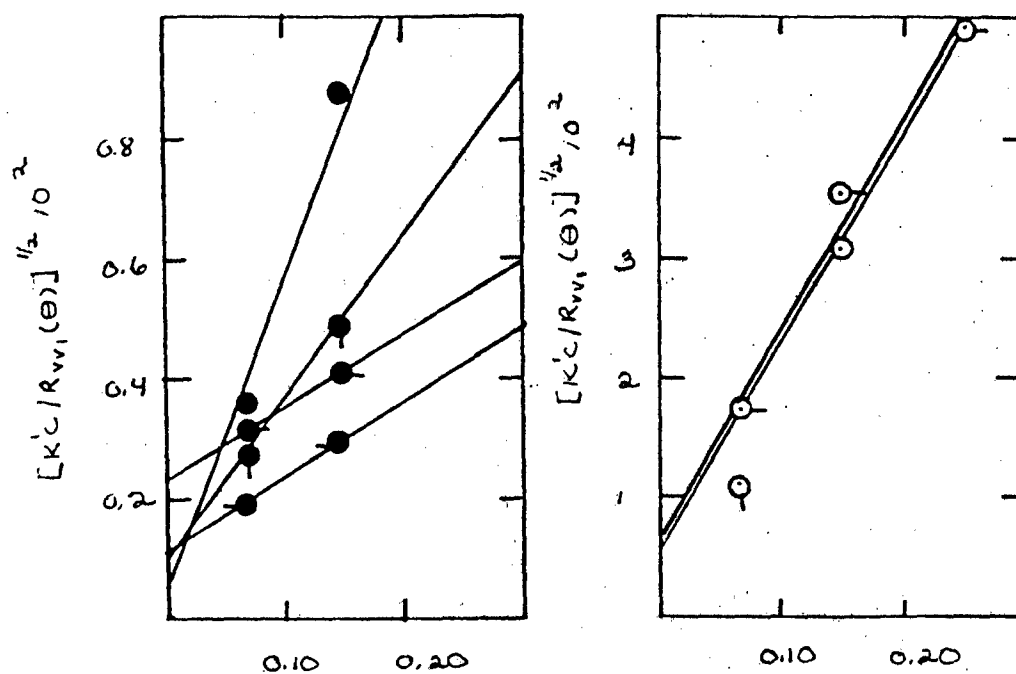
Figure 67: $[Kc/R_{Vv_1}]^{1/2}$ versus $\sin^2 \theta/2$ for solutions of PBT 7 + salt. O uncentrifuged ● centrifuged ,at 514.5 nm and 25.0°C. O 0.0492 g/dl, O-0.0392 g/dl, Q 0.0250 g/dl,-O 0.0121 g/dl.
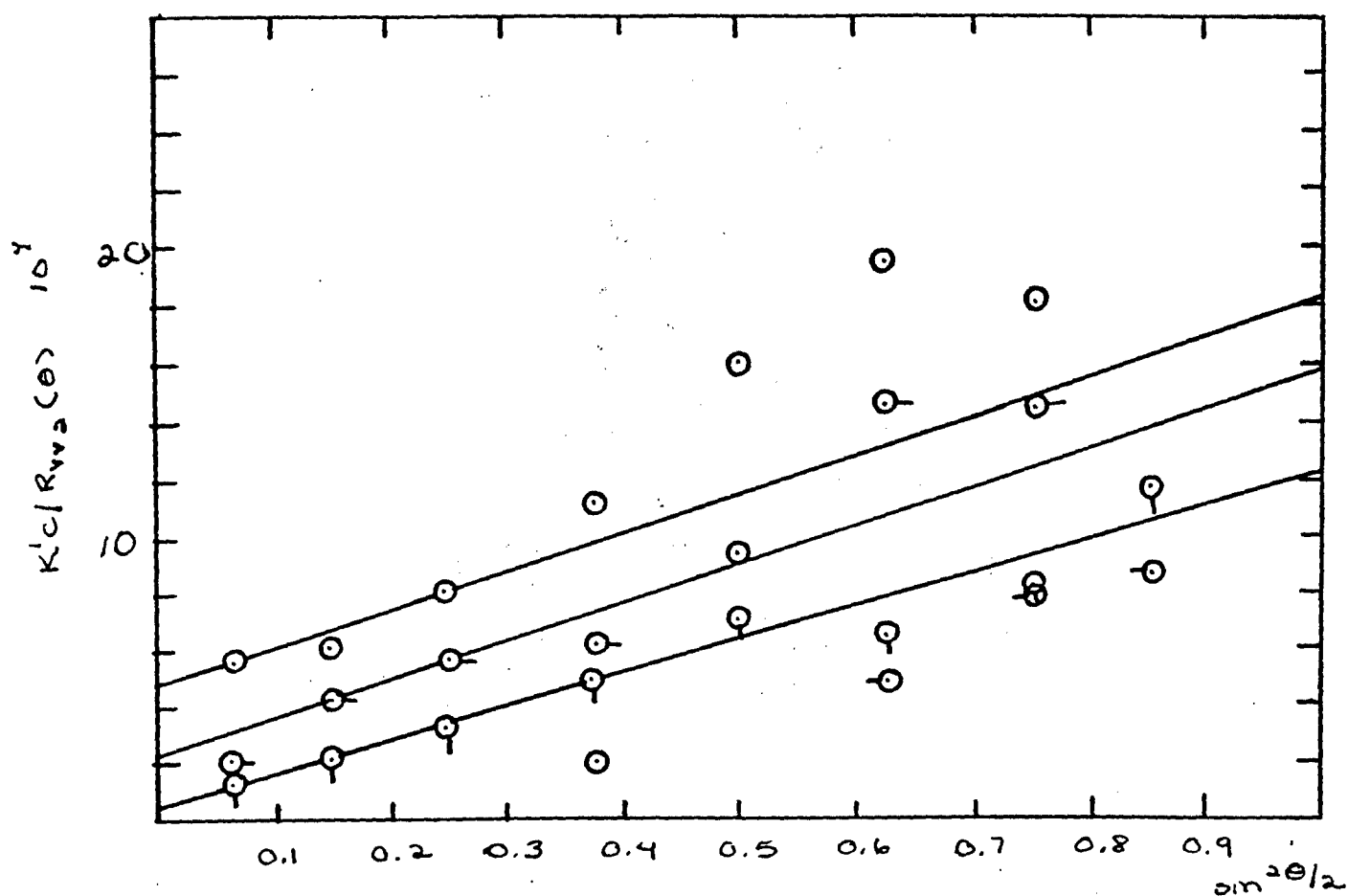
Figure 68 Kc/R_{vv2} versus $\sin^2 \theta/2$ for solutions of PBT 7 + salt at 514.5 nm and 25.0°C. O 0.0492 g/dl. O—0.0392 g/dl. Q 0.0250 g/dl. —O 0.0121 g/dl.
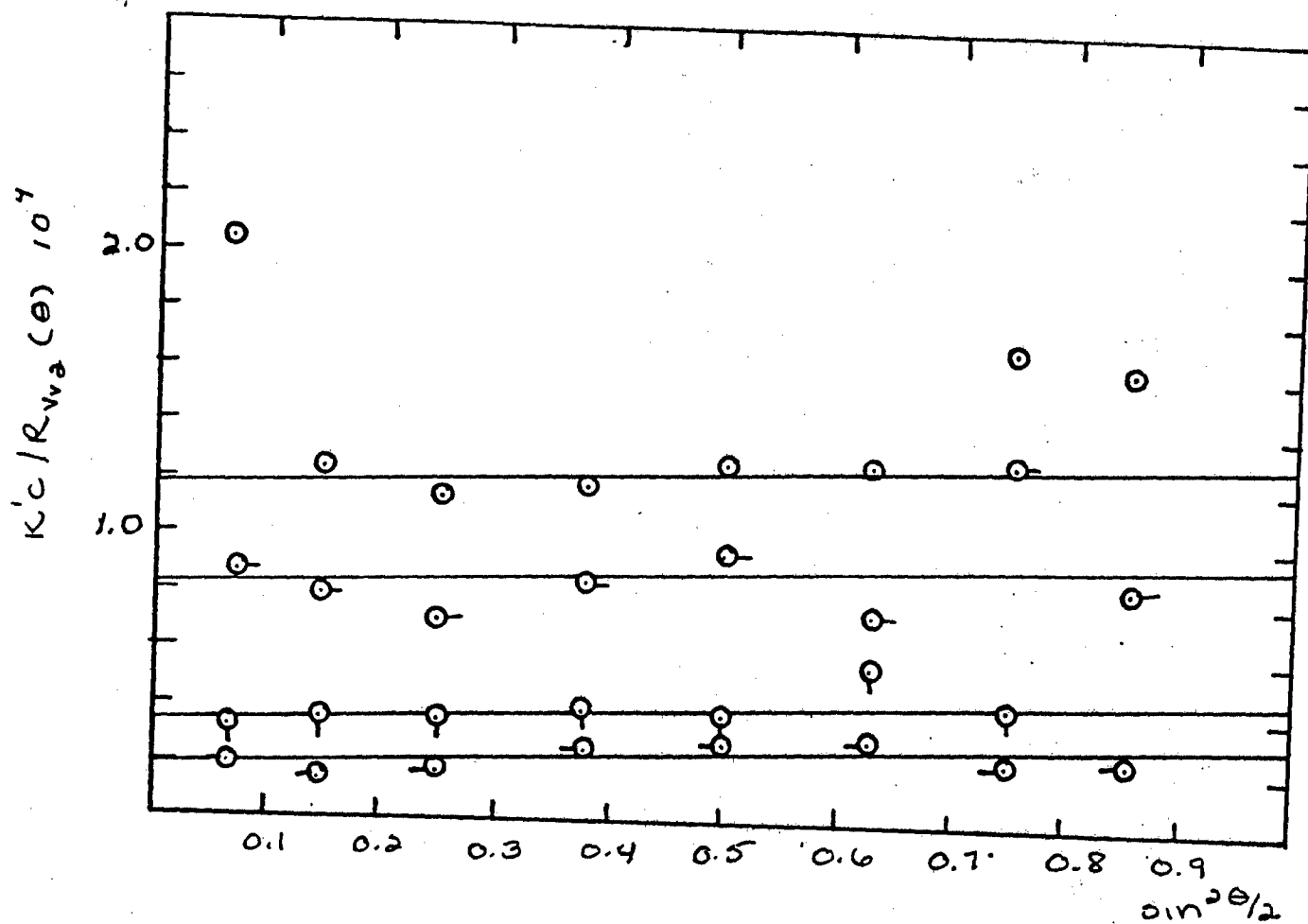
Figure 69: Kc/R_{Vv_2} versus $\sin^2 \theta/2$ for centrifuged solutions of PBT 7^{V+2} salt at 514.5 nm and 25.0°C. O 0.0492 g/dl, O-0.0392 g/dl, Q 0.0250 g/dl,-O 0.0121 g/dl.
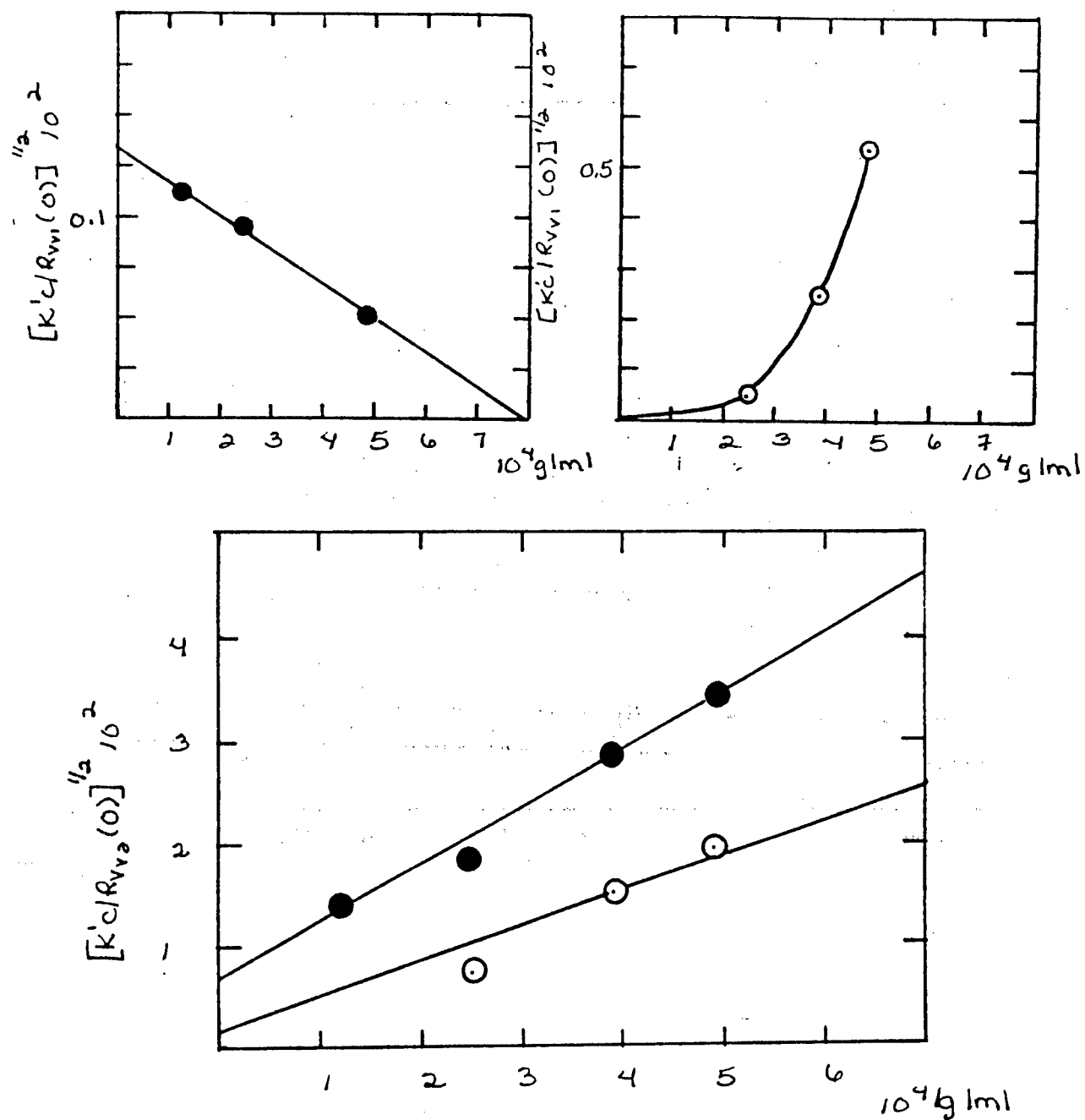
167

Figure 70: Concentration dependence of $R_{Vv,1}$ and $R_{Vv,2}$, O uncentrifuged and ● centrifuged for solution of PBT 7 + salt at 25.0°C
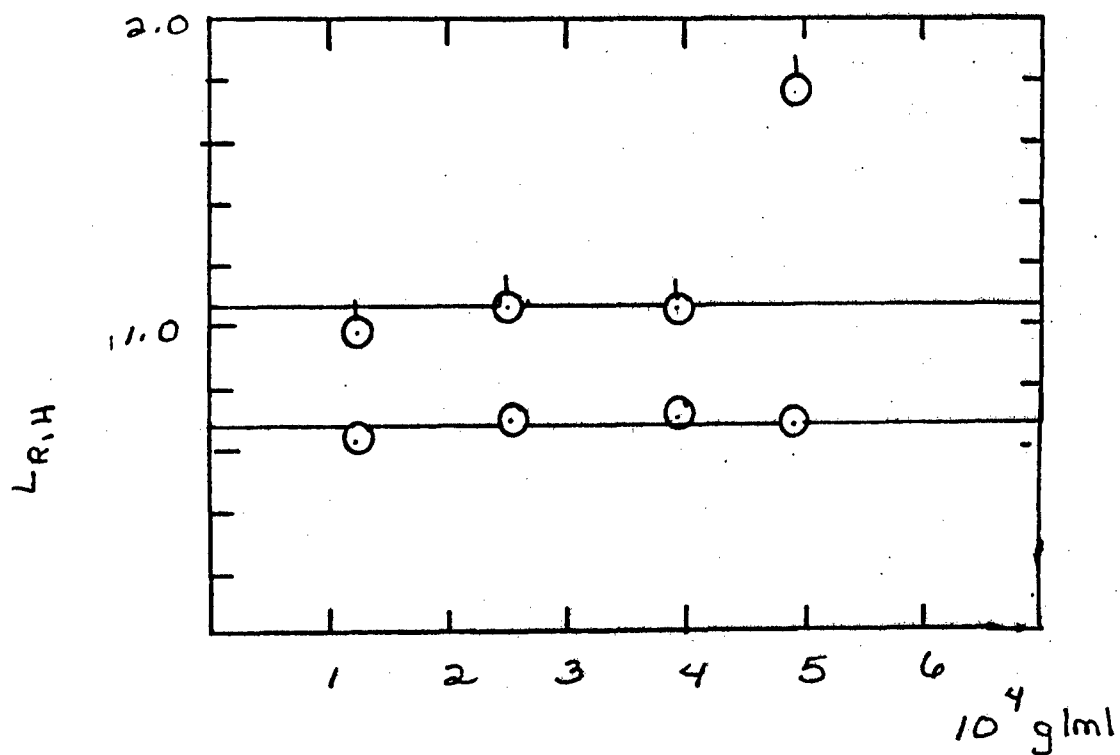
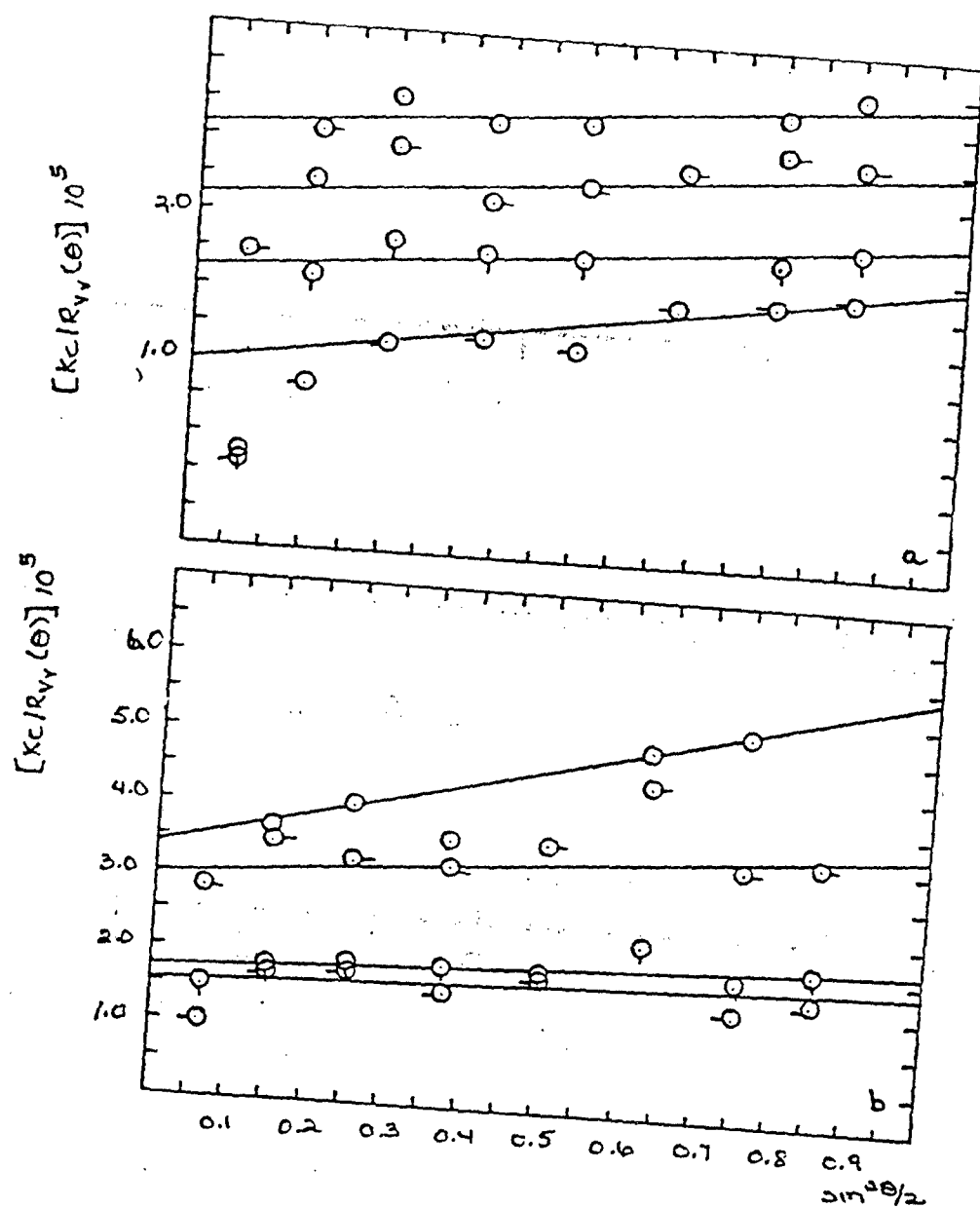Figure 71: $L_{R,H}$ for centrifuged solution of PBT 7 + salt

Figure 72: The a)uncentrifuged and b) centrifuged Vv component of the integrated intensity light scattering of SPBT 38 in MSA at 514.5 nm and 25.0° C.
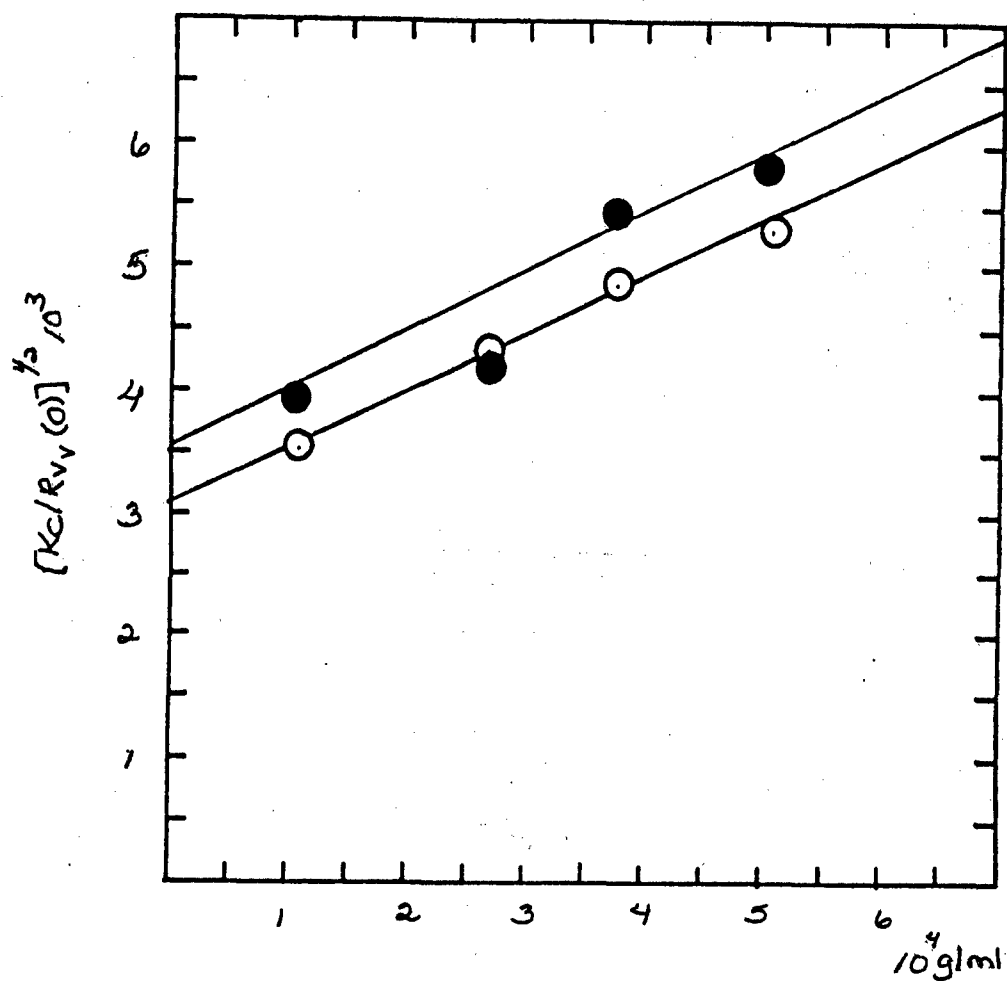0 0.0506 g/dl O-0.0375 g/dl Q 0.025 g/dl-O 0.0108 g/dl

Figure 73: The concentration dependence of the Vv component of the integrated intensity light scattering of SPBT 38 in MSA O uncentrifuged and ● centrifuged
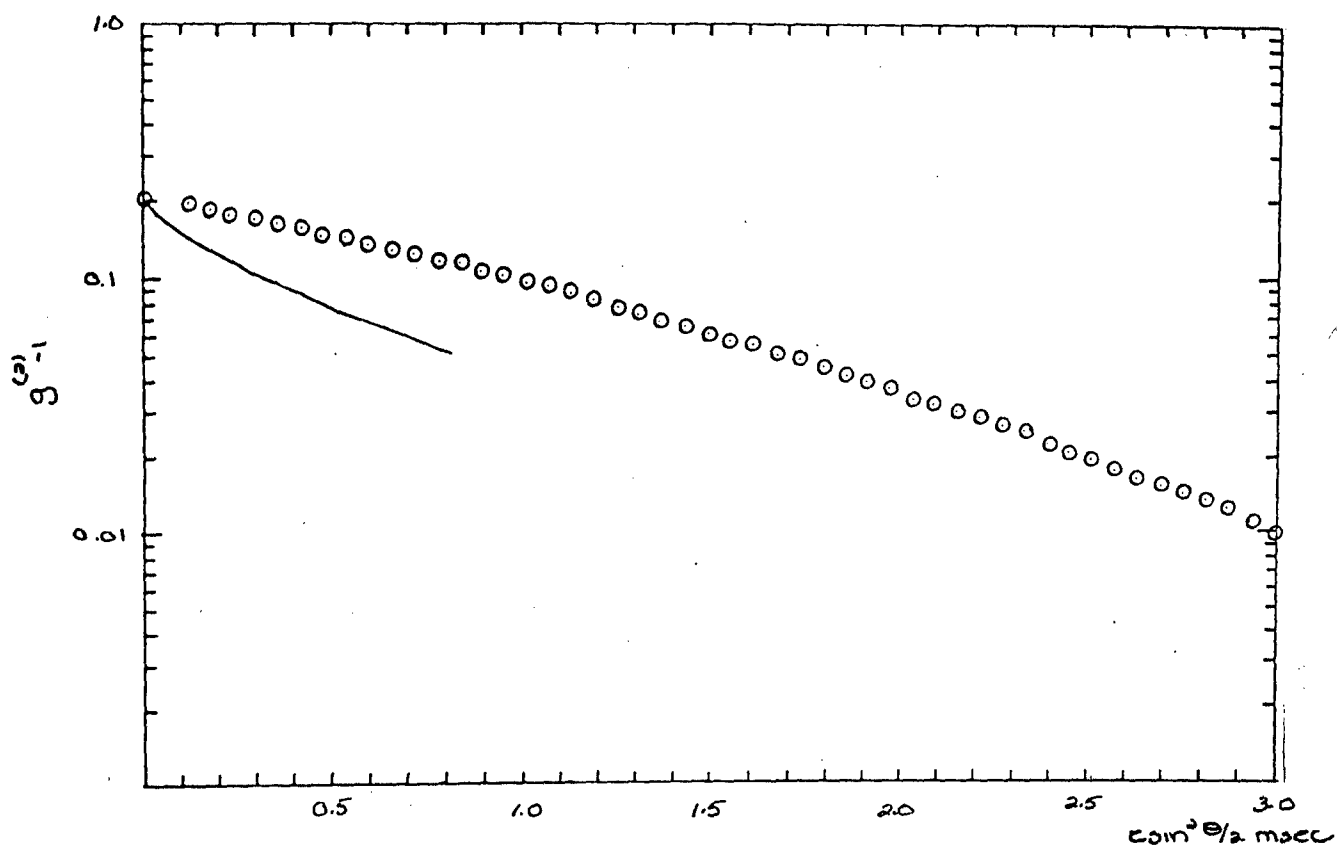
Figure 74: Intensity fluctuation light scattering $g^{(2)}(\Delta\tau,\tau)$ versus $\tau\sin^{-2}\theta/2$ for SPBT-38, 0.0106 g/dl at 514.5 nm and 25.0°C. ○ 45° → 90°
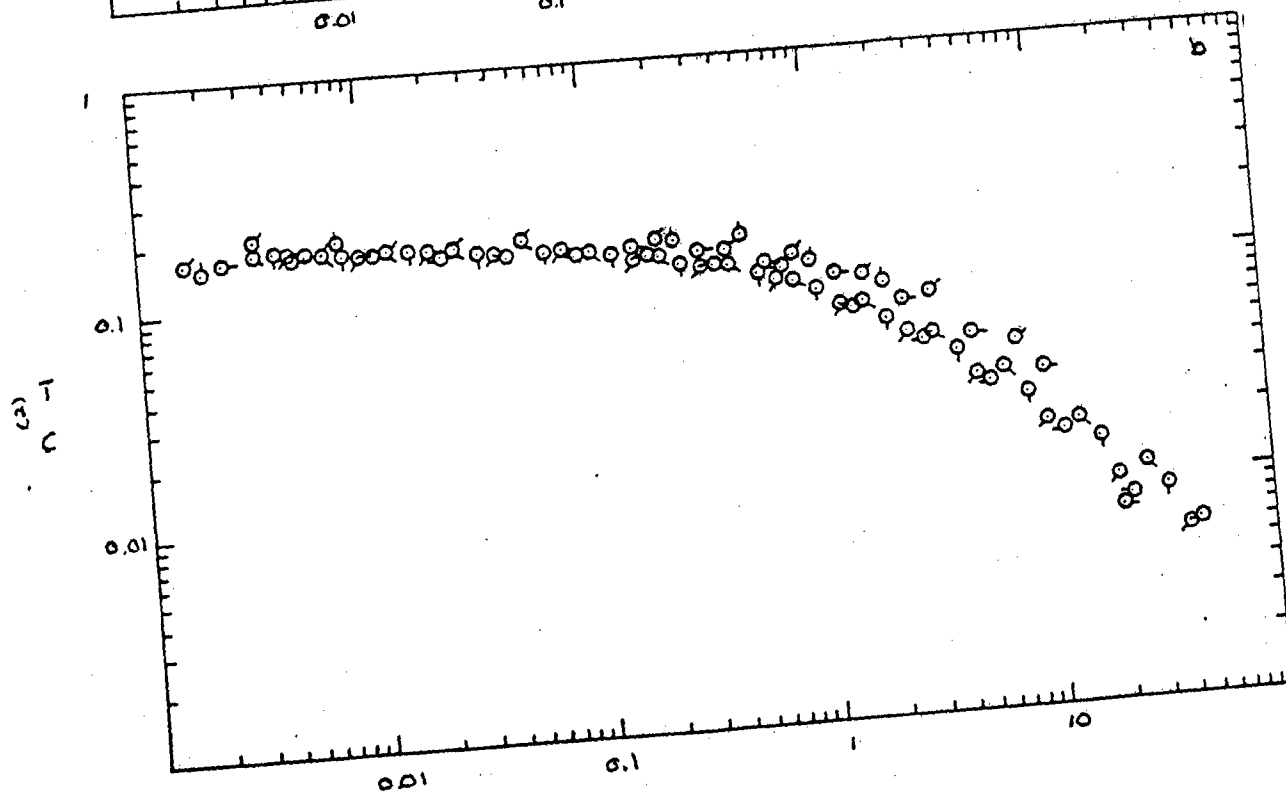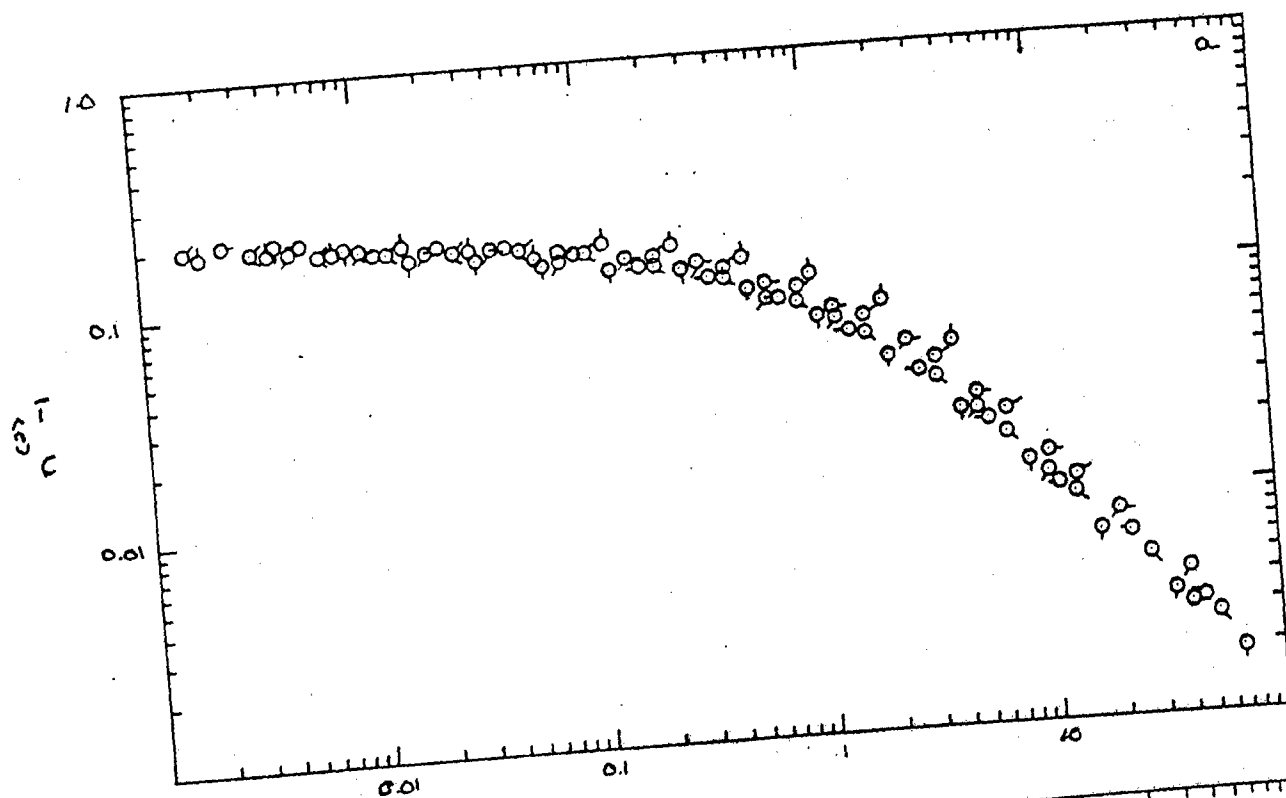
Figure 75: Photon correlation spectroscopy of SPBT 38 at 514.5 nm and 25.0° a)0.0129 g/dl b)0.0465 g/dl ○ 45° ○ 60° O–75° ○ 90° ○ 105° ○ 120°–○ 135°
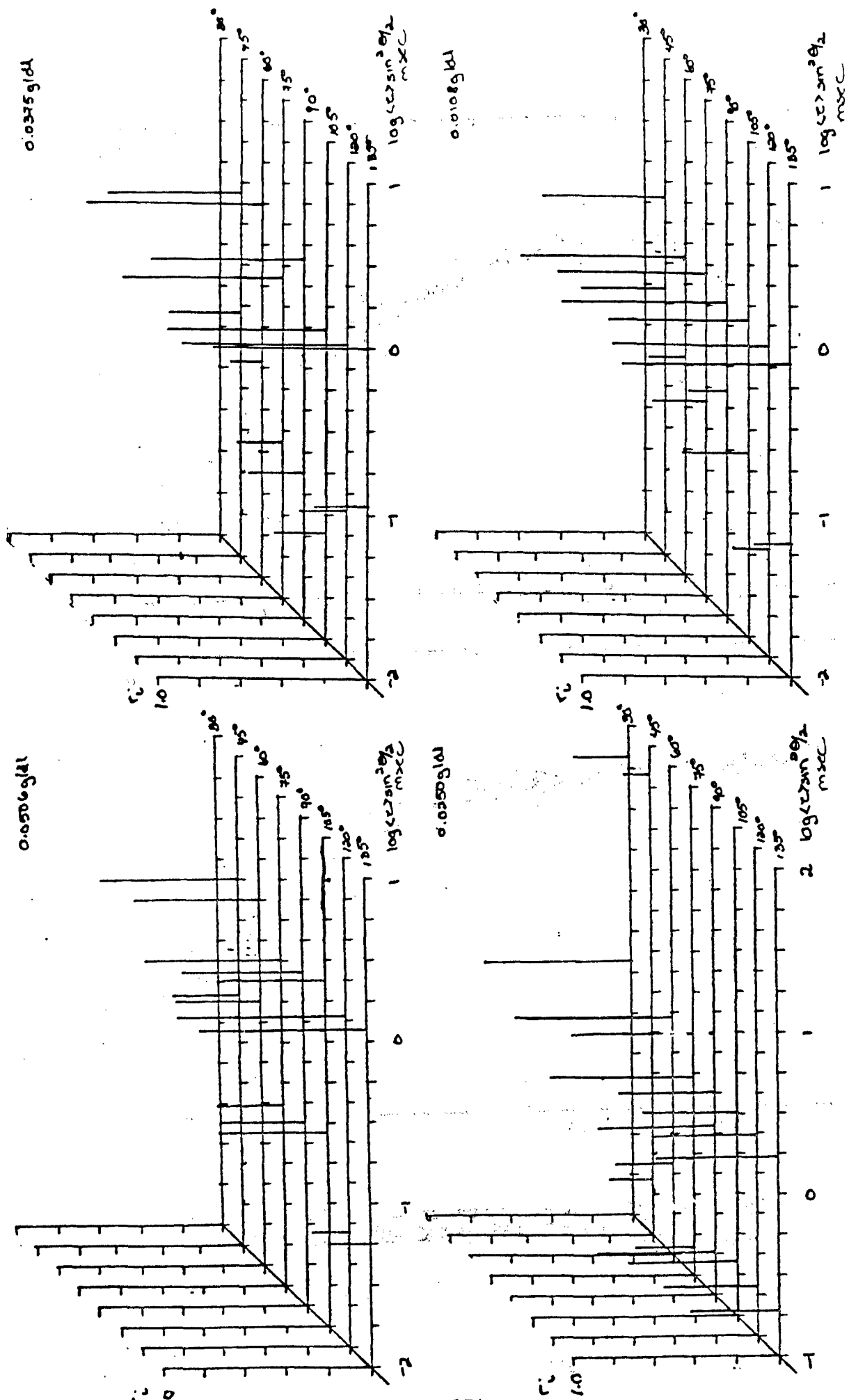
Figure 76: a)The concentration dependence of $r_i \sin^2 \theta/2$ of uncentrifuged SPBT-38
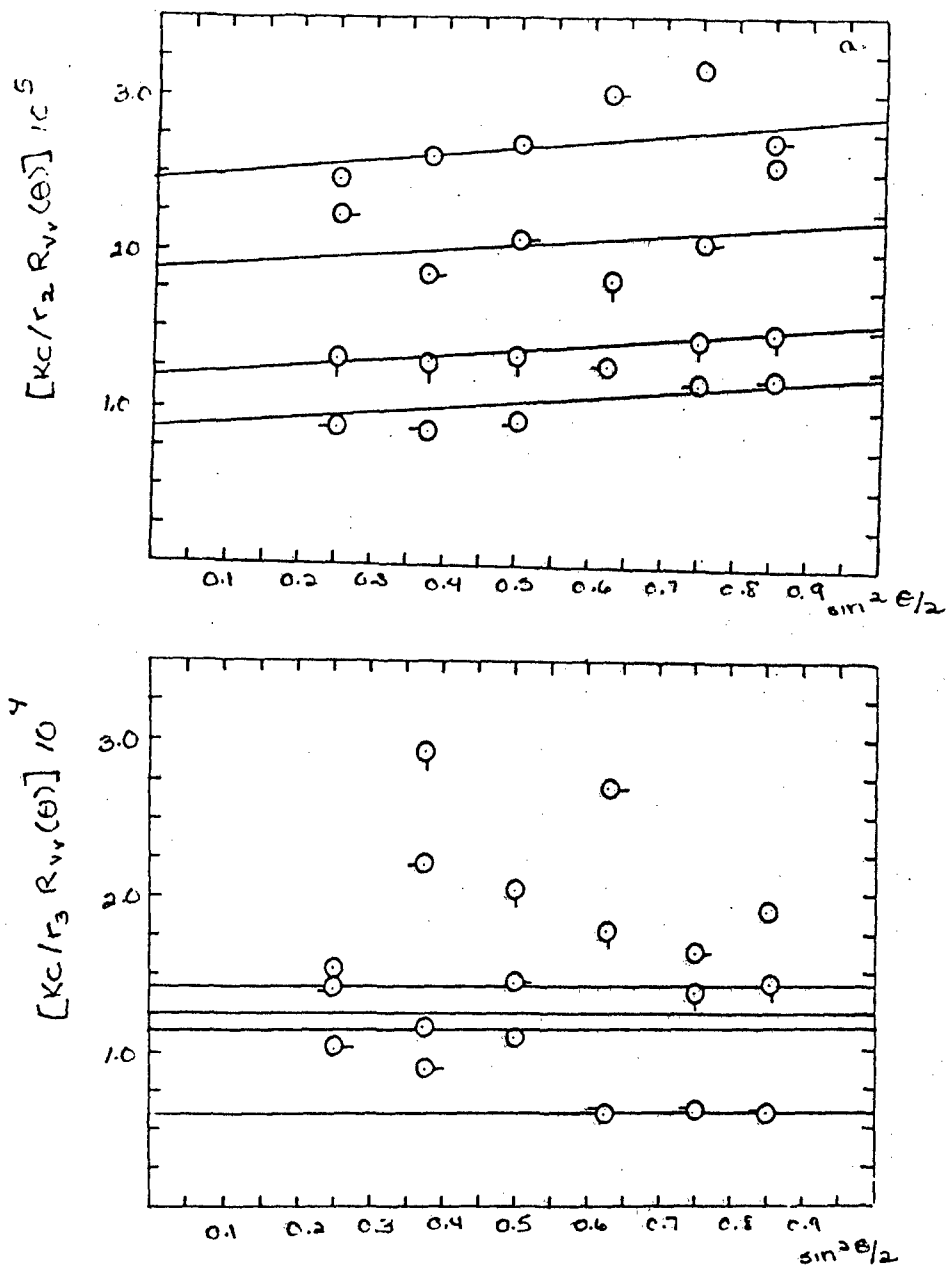
Figure 77: Kc/R_{Vv2} versus $\sin^2 \theta/2$ for solutions of SPBT-38 at 25.0°C uncentrifuged, at 514.5 nm and 25.0°C. ○ 0.0508 g/dl, ○-0.0375 g/dl ○ 0.0250 g/dl ○ 0.0108 g/dl
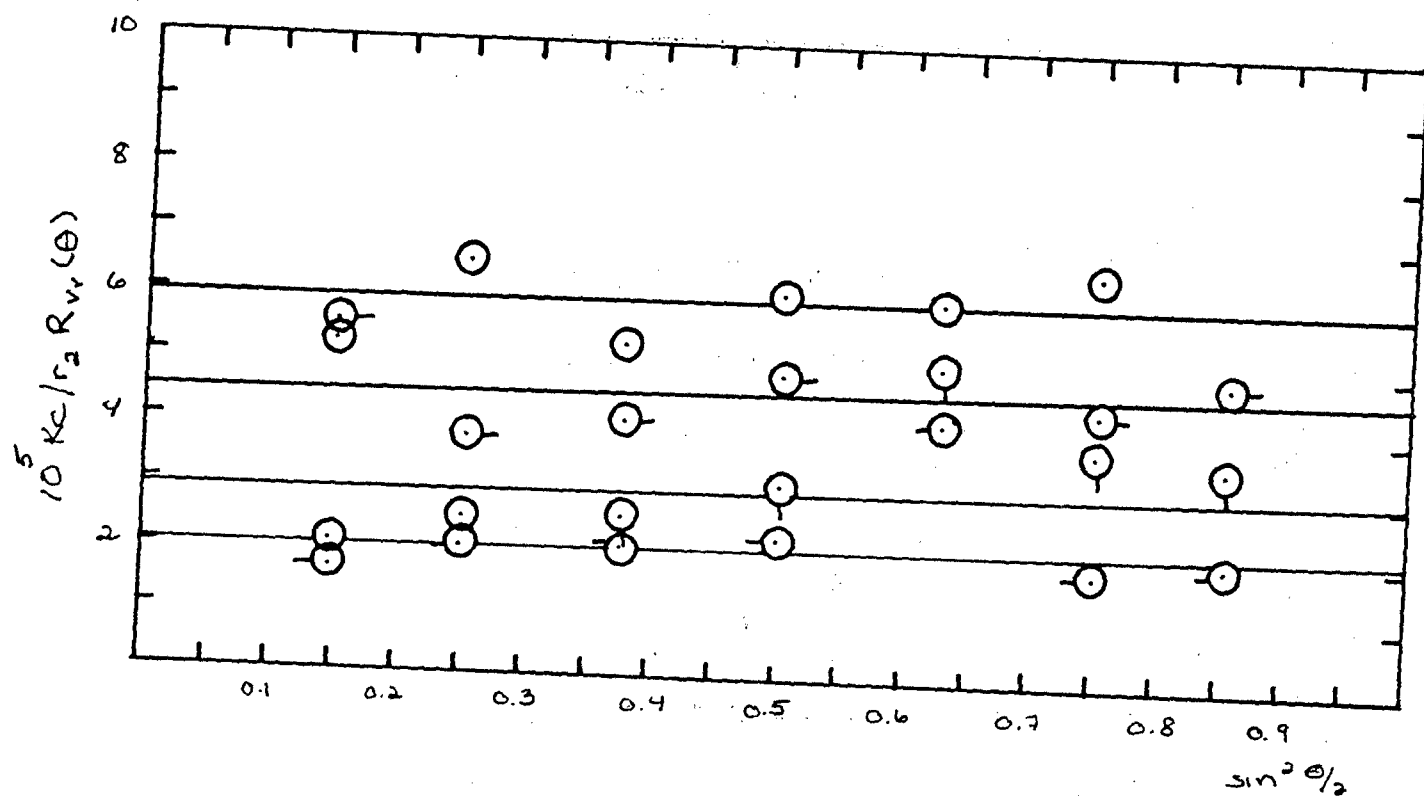
Figure 78: $Kc/R_{Vv,2}$ versus $\sin^2 \theta/2$ for solutions of SPBT-38 at 25.0°C centrifuged, O 0.0508 g/dl, O- 0.0375 g/dl φ 0.0250 g/dl -O 0.0108 g/dl
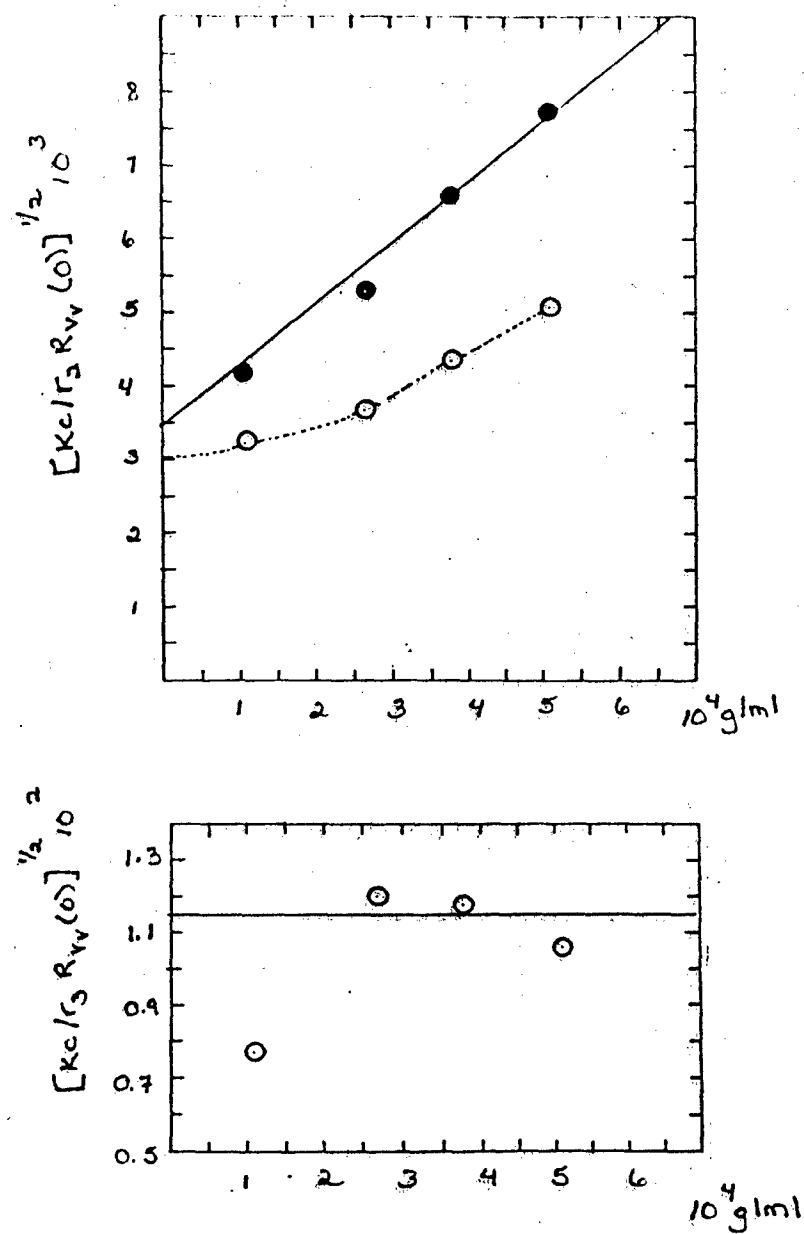
Figure 79: Concentration dependence of $Kc/R_{Vv,1}(\theta)$ and $Kc/R_{Vv,2}(\theta)$, O uncentrifuged for solutions of SPBT-38 at 25.0°C

Figure 80: The a)uncentrifuged and b)centrifuged Vv components of the integrated intensity light scattering of SPBT 36/MSA at 633 nm and 25.0°C. O 0.0516 g/dl O–0.0378 g/dl Q 0.0204 g/dl–O 0.0099 g/dl

Figure 81: The concentration dependence of the Vv components of the integrated intensity light scattering of SPBT 36/MSA. O uncentrifuged ● centrifuged

Figure 82: The a)uncentrifuged and b)centrifuged Hv component of the integrated intensity light scattering of SPBT 36/MSA at 633 nm and 25.0 ° C. O 0.0516 g/dl O–0.0378 g/dl Q 0.0204 g/dl–O 0.0099 g/dl

Figure 83: The concentration dependence of the Hv component of the integrated intensity light scattering of SPBT 36/MSA O uncentrifuged and ● centrifuged
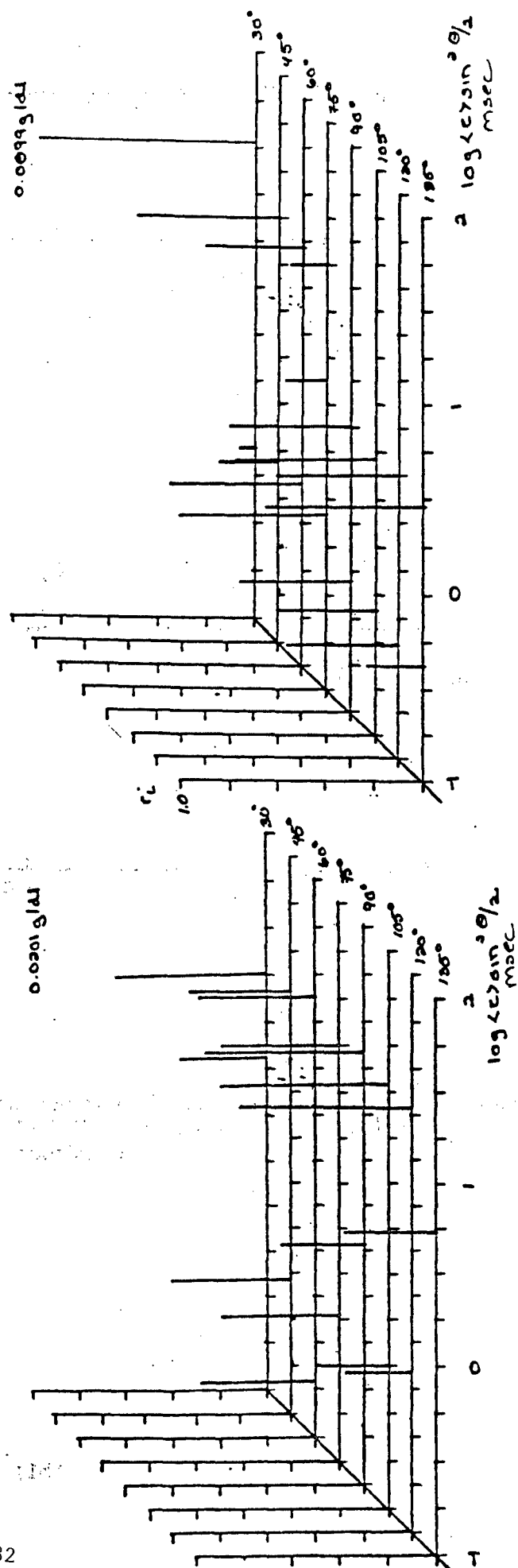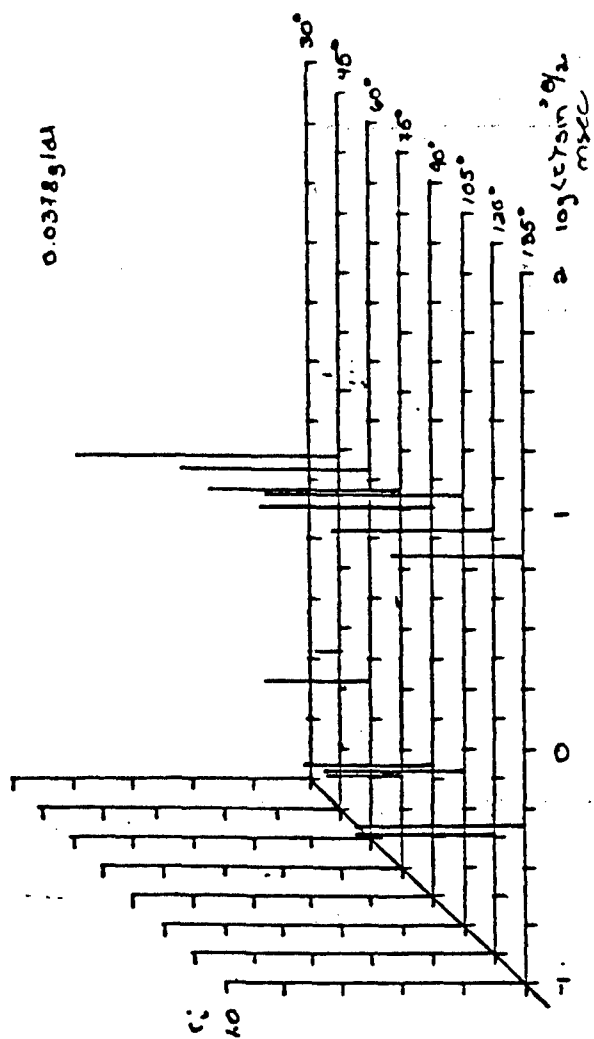
Figure 84: a)The concentration dependence of $\tau_1 \sin^2 \theta/2$ of uncentrifuged SPBT 36/MSA.
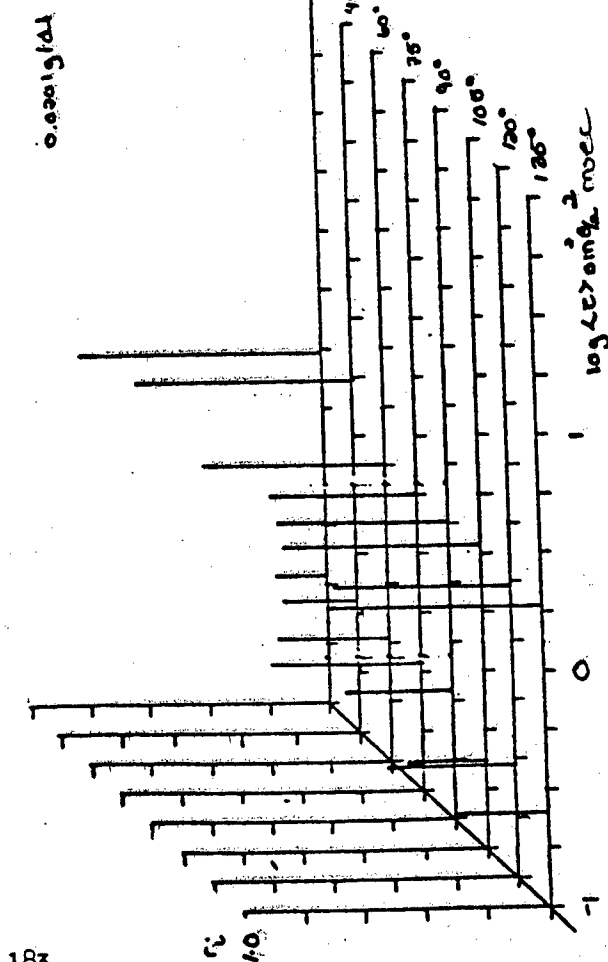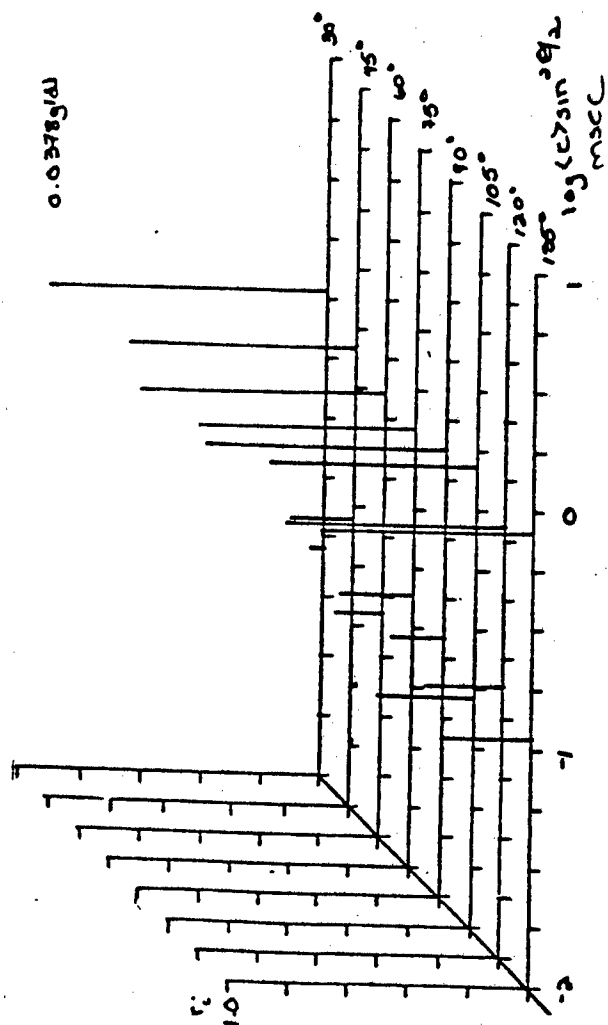
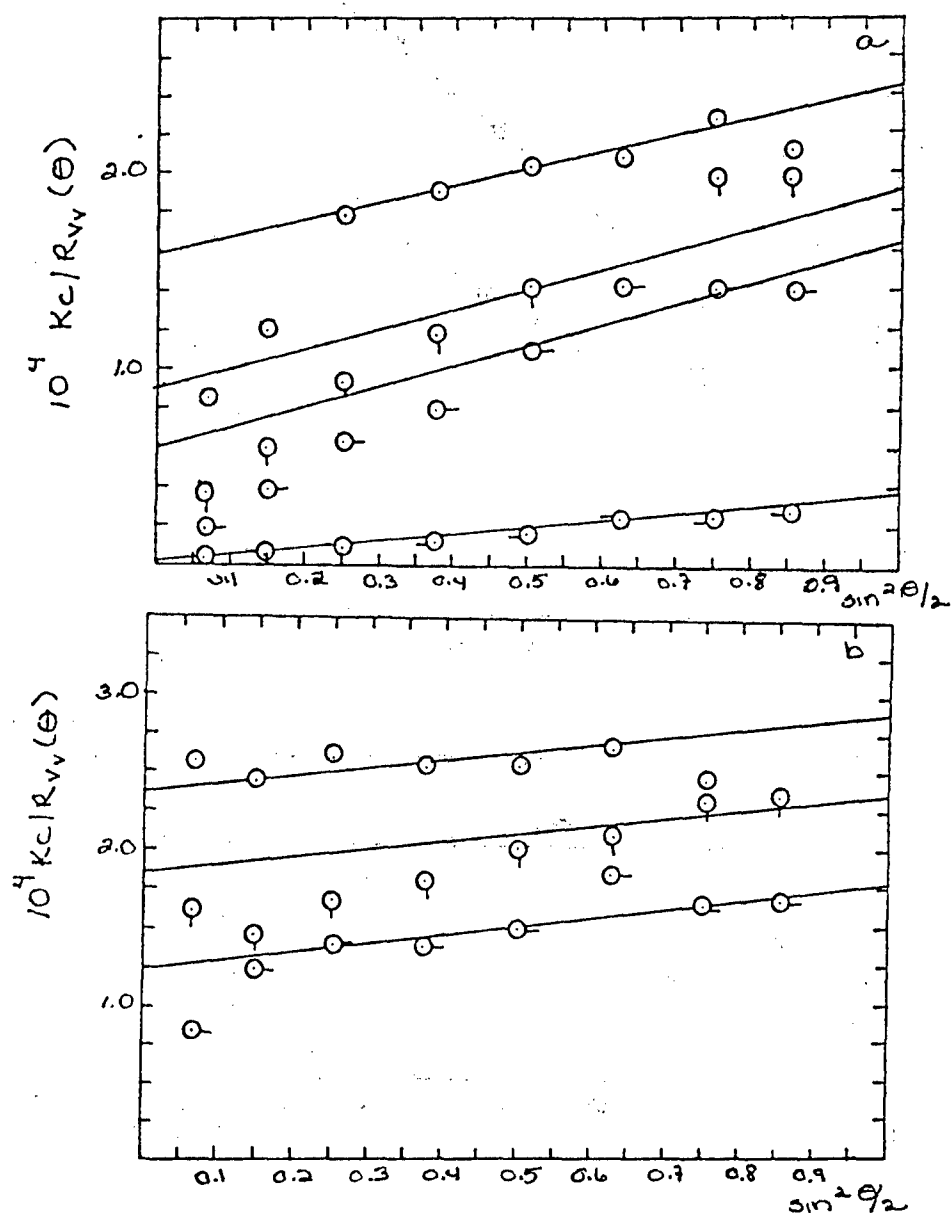Figure 85: a)The concentration dependence of $r_i \sin^2 \theta/2$ of centrifuged SPBT 36/MSA.
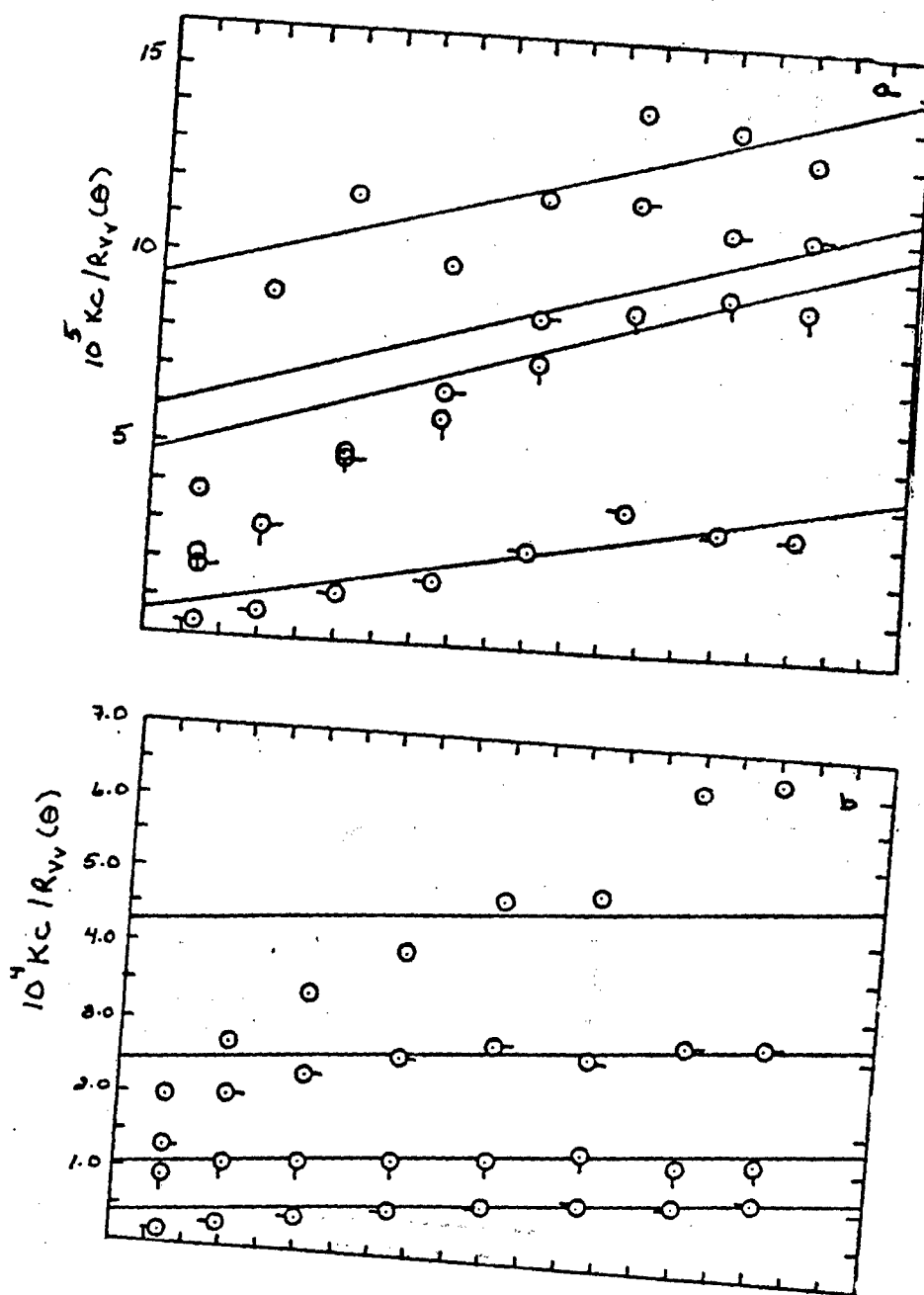
Figure 86: The a)uncentrifuged and b)centrifuged Vv components of the integrated intensity light scattering of SPBT-7/MSA at 633 nm and 25.0°C. O 0.0516 g/dl O-0.0378 g/dl Q 0.0204 g/dl-O 0.0099 g/dl
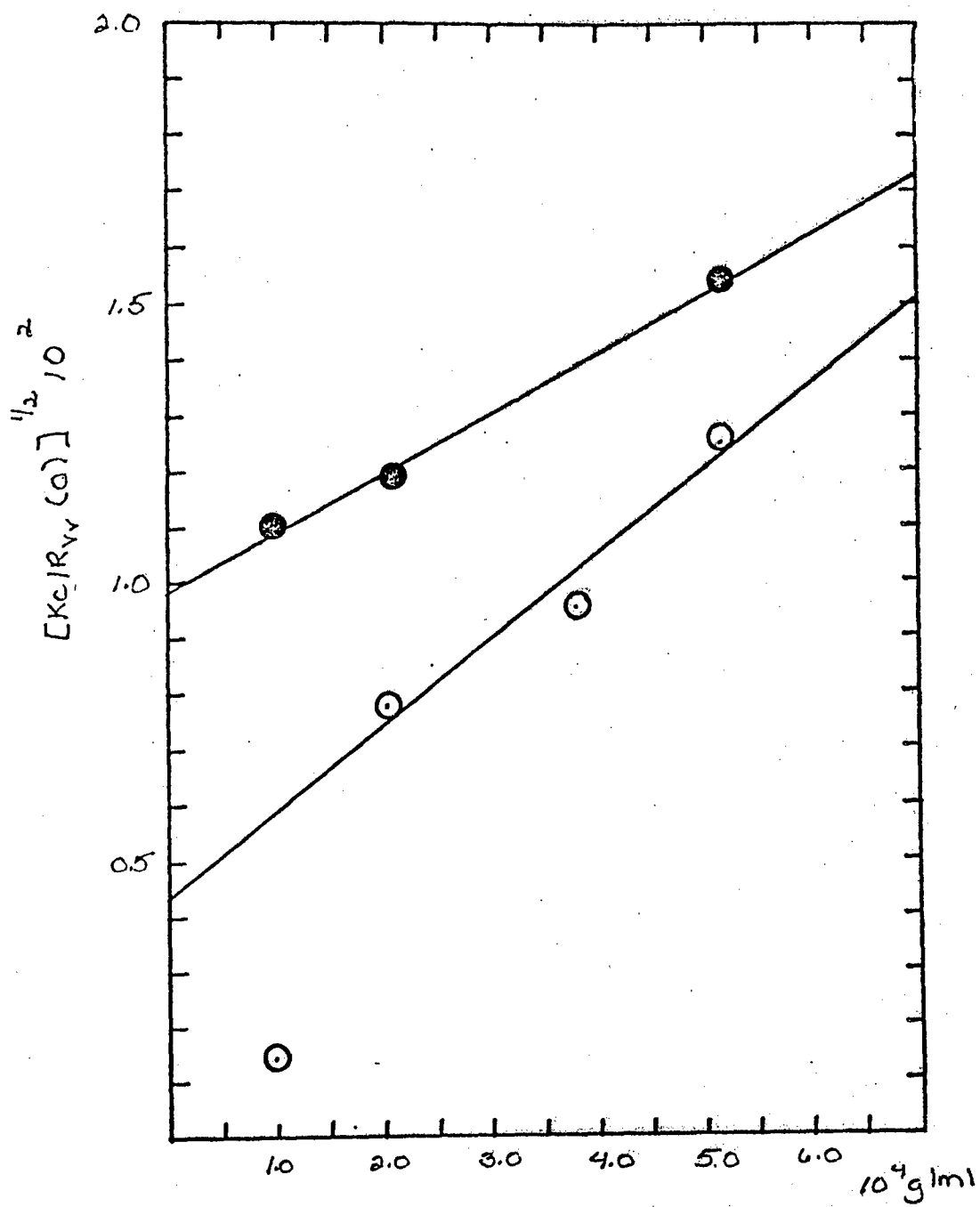
Figure 87 : The concentration dependence of the Vv components of the integrated intensity light scattering of SPBT-7/MSA O uncentrifuged
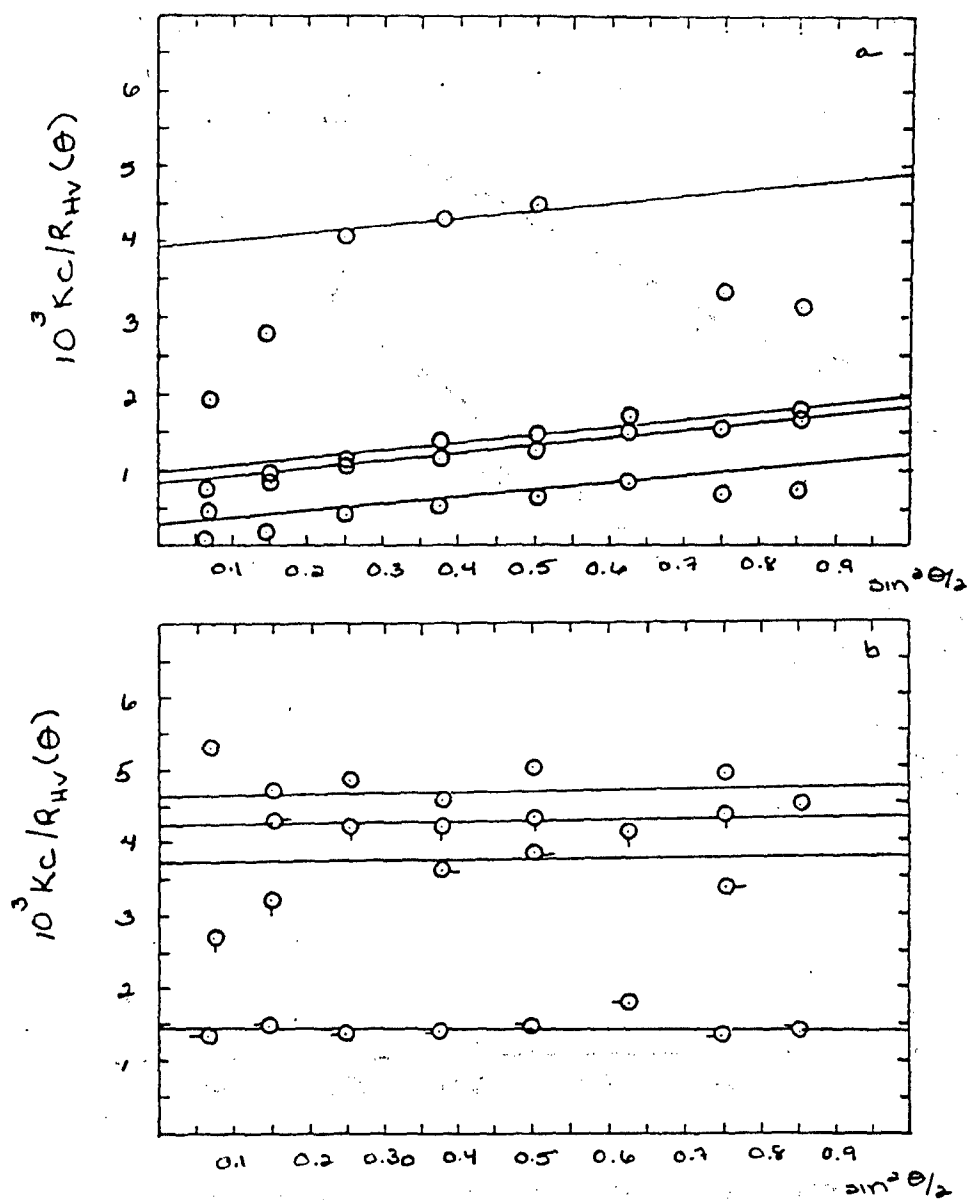● centrifuged

Figure 88: The concentration dependence of $\tau_i \sin^2 \theta/2$ of uncentrifuged SPBT-7
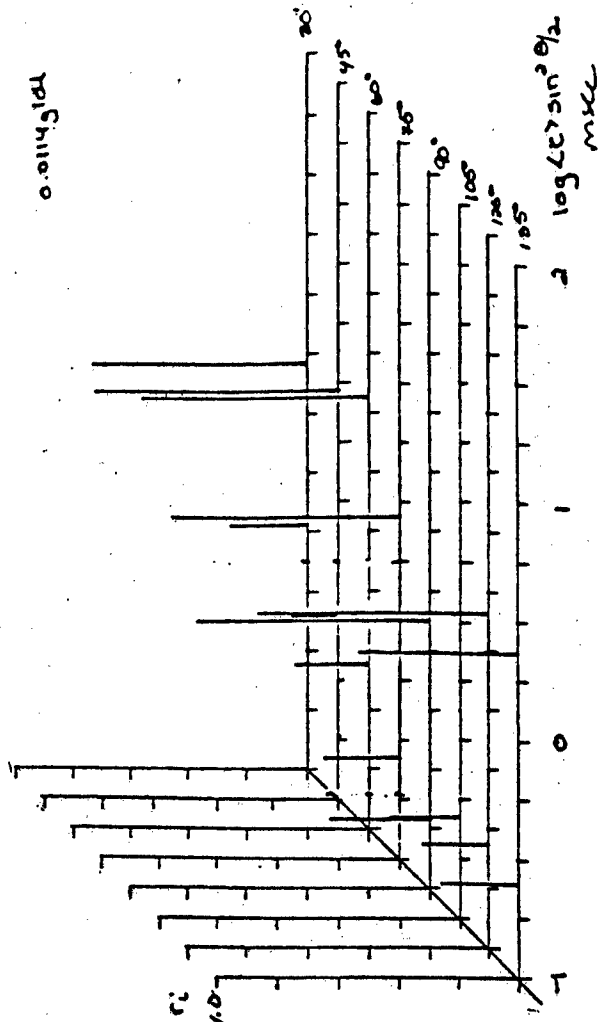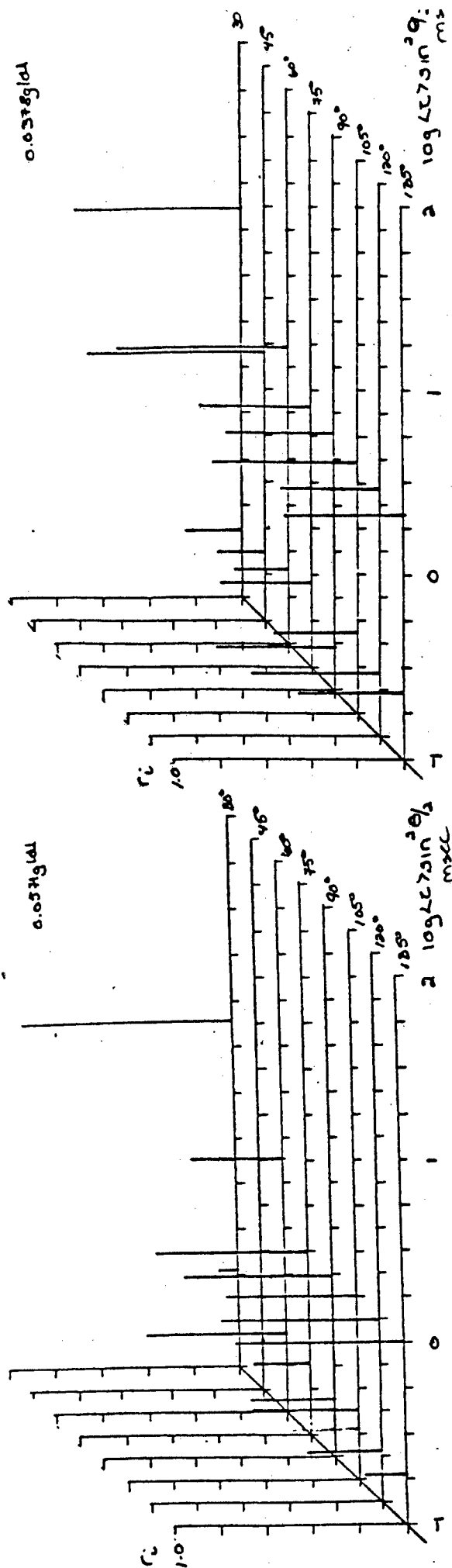
Figure 89: The concentration dependence of $r_i \sin^2 \theta/2$ of centrifuged SPBT-7
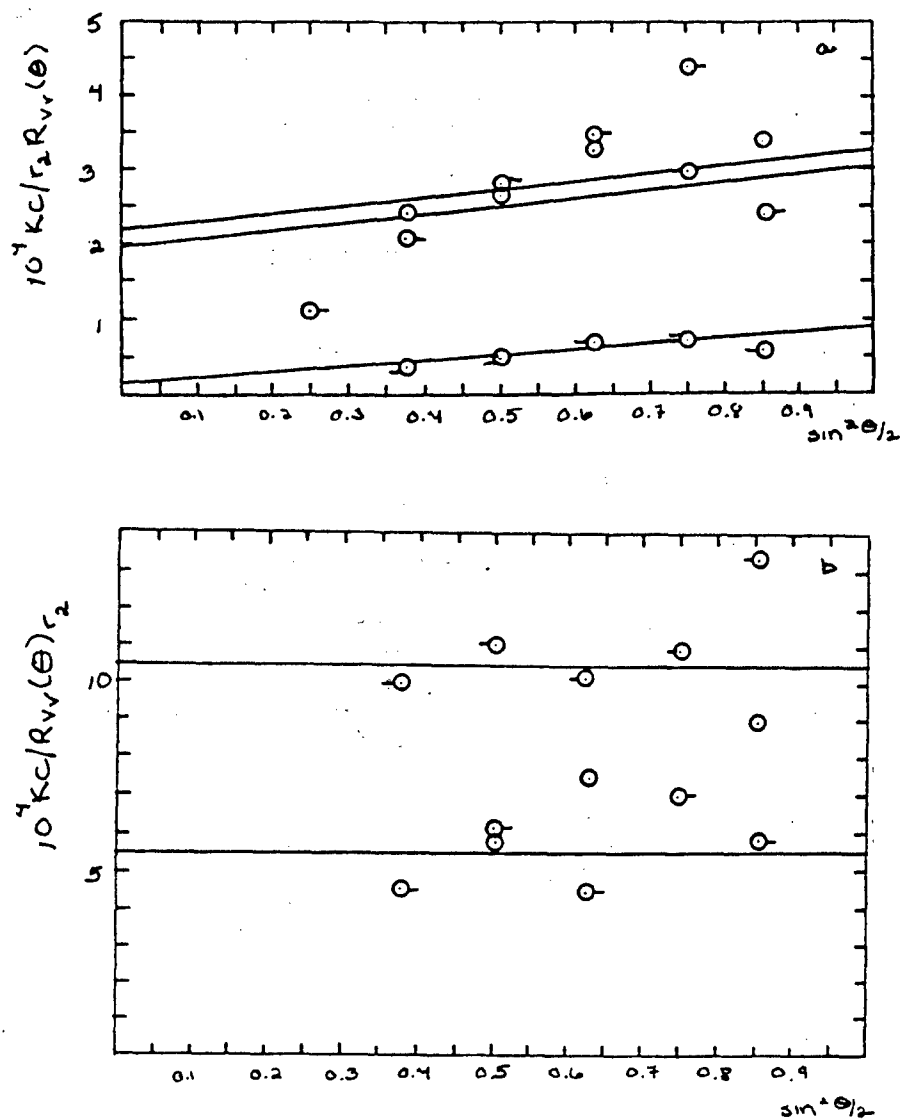
Figure 90: Kc/R$_{Vv,2}$ versus sin^2 $\theta/2$ for solutions of SPBT-7 at 25.0°C uncentrifuged and centrifuged. O 0.0516 g/dl O–0.0378 g/dl Q 0.0204 g/dl –O 0.0099 g/dl

188
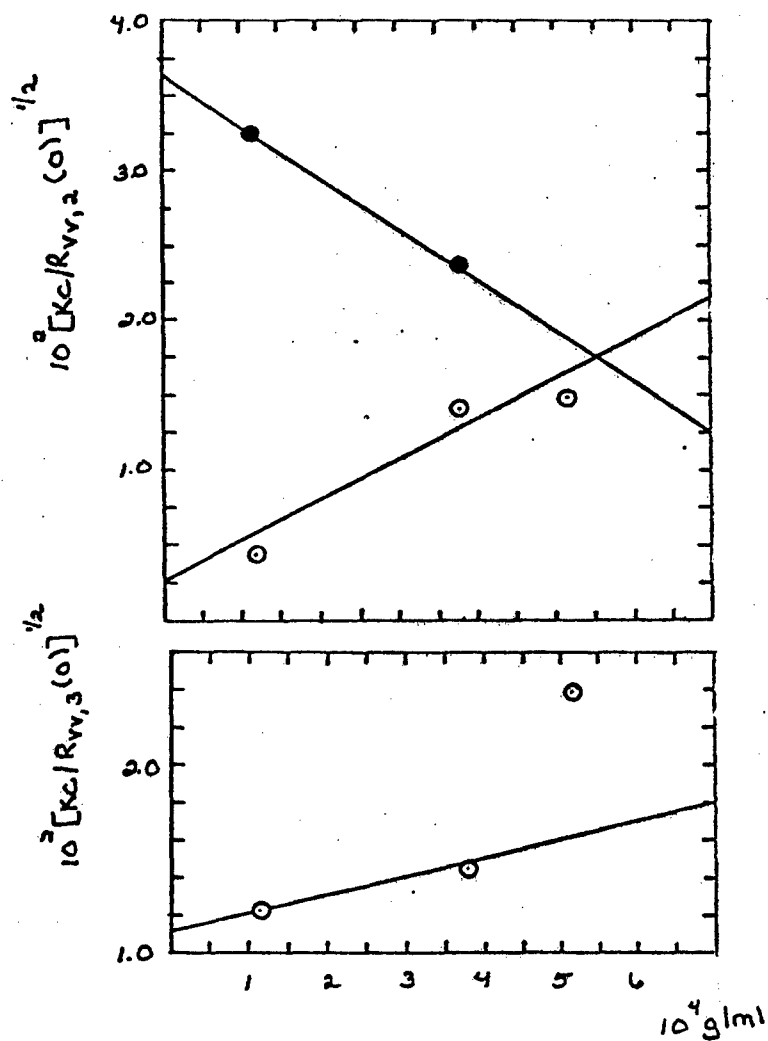
Figure 91: Concentration dependence of $Kc/R_{Vv,1}(\theta)$ and $Kc/R_{Vv,2}(\theta)$, O uncentrifuged and ● centrifuged for solutions of SPBT-7 at 25.0°C
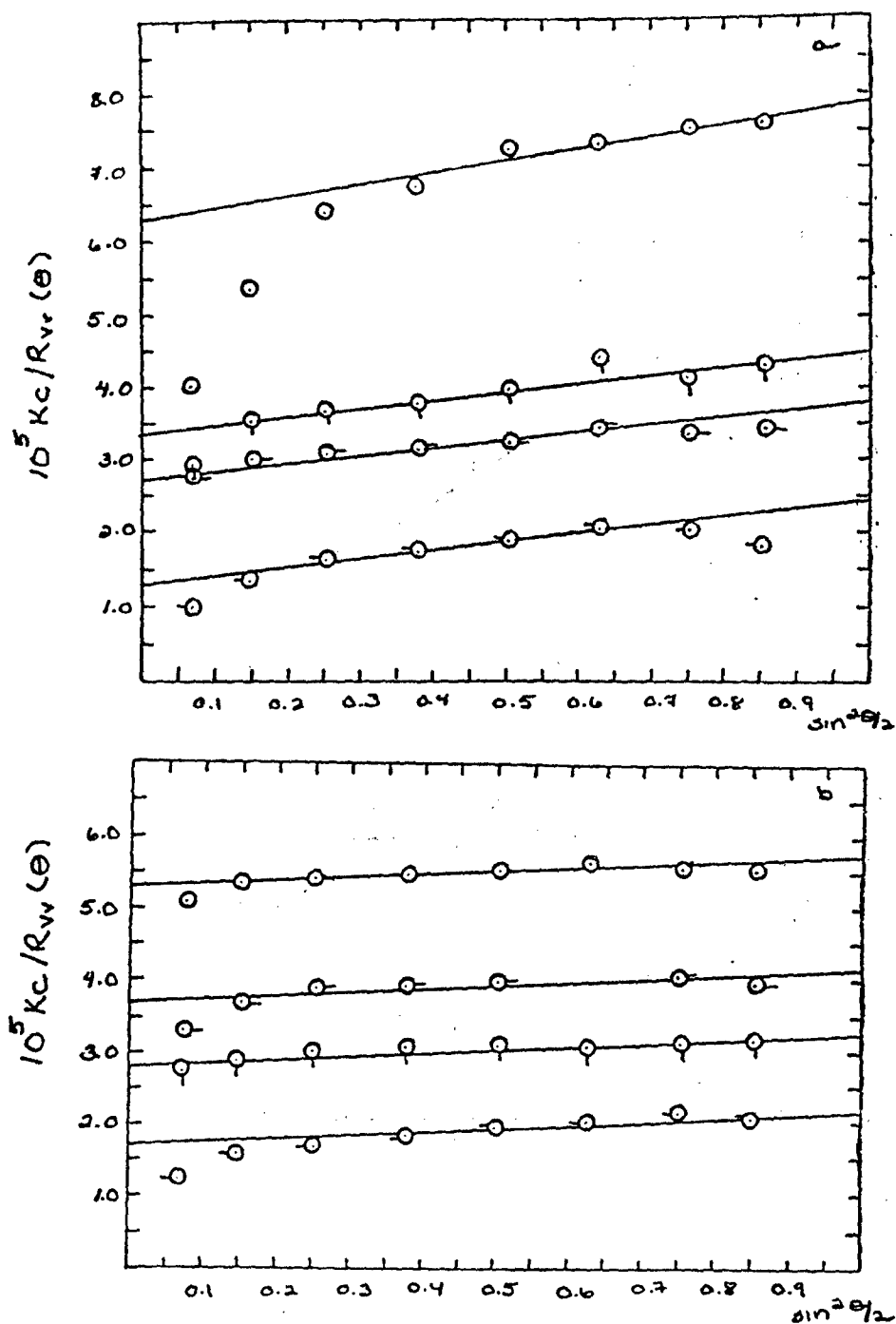
Figure 92: The a)uncentrifuged and b)centrifuged Vv components of the integrated intensity light scattering of SPBT-12/MSA at 514.5 nm and 25.0°C. O 0.0516 g/dl O 0.0378 g/dl O 0.0204 g/dl-O 0.0099 g/dl
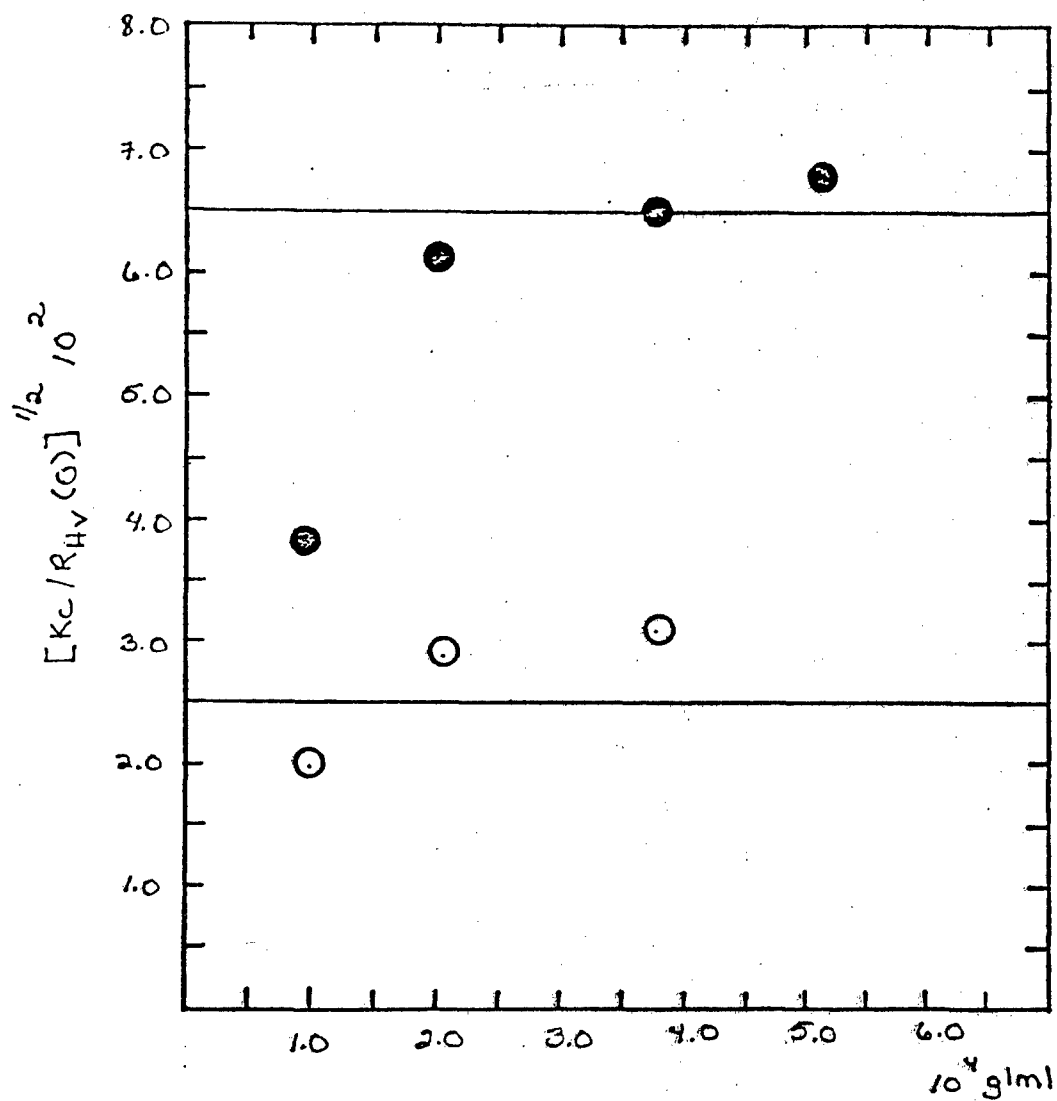
Figure 93: The concentration dependence of the Vv components of the integrated intensity light scattering of SPBT-12/MSA. O uncentrifuged ● centrifuged

191

Figure 94: The Hv emission spectra of SPBT 38 excited with a 514.5 nm source at 25.0 ° C.—— 0.0512 g/dl + 0.561 N salt (p+ss); − − 0.0506 g/dl without added salt

Figure 95: The a)uncentrifuged and b)centrifuged Vv components of the integrated intensity light scattering of SPBT 38 + 1.05N salt (ps+s) at 514.5 nm and 25.0°C. O 0.0500 g/dl O—0.0371 g/dl Q 0.0254 g/dl -O 0.0129 g/dl

Figure 96: The concentration dependence of the Vv components of the integrated intensity light scattering of SPBT 38 + 1.05N salt. O uncentrifuged ● centrifuged
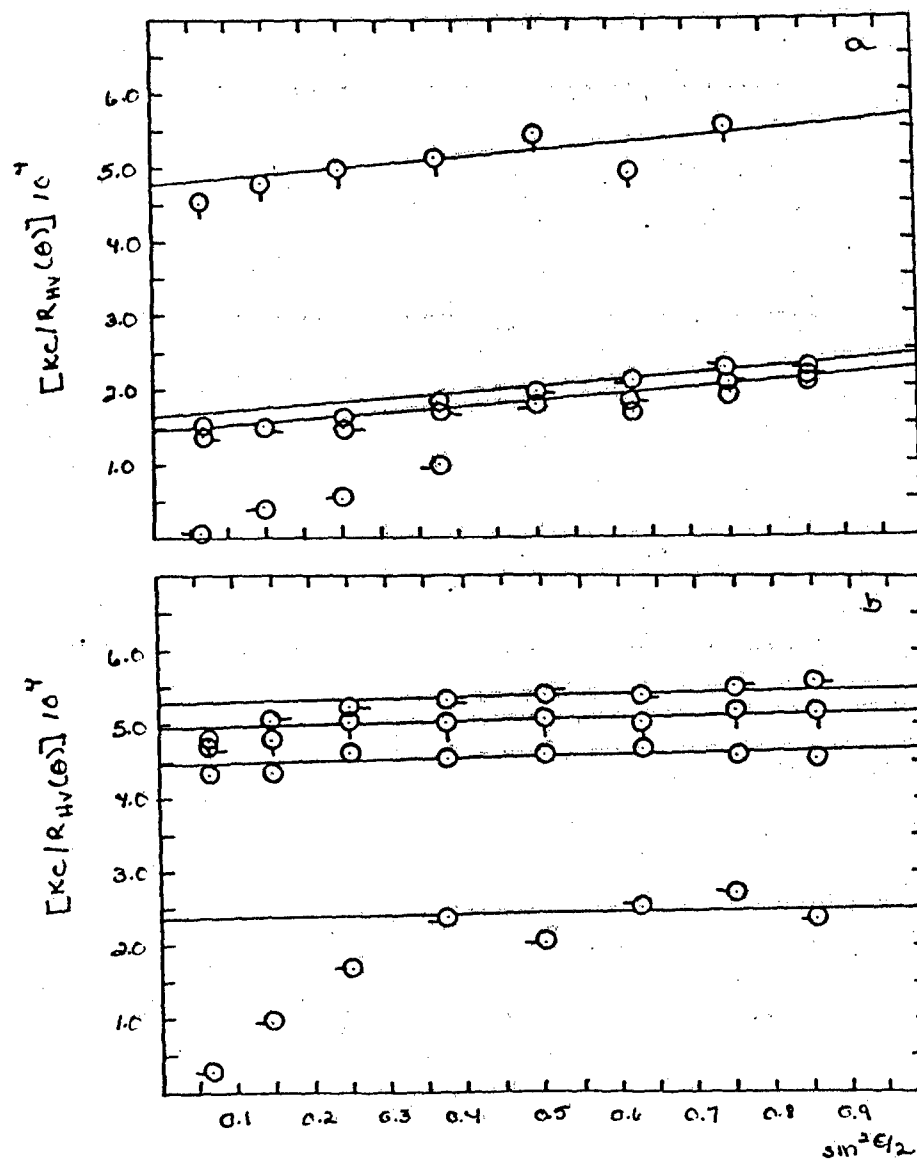
Figure 97: The a)uncentrifuged and b)centrifuged Hv component of the integrated intensity light scattering of SPBT 38+ 1.05N salt (ps+s) at 514.5 nm and 25.0 ° C. O 0.0466 g/dl O–0.0359 g/dl Q 0.0240 g/dl–O 0.0129 g/dl
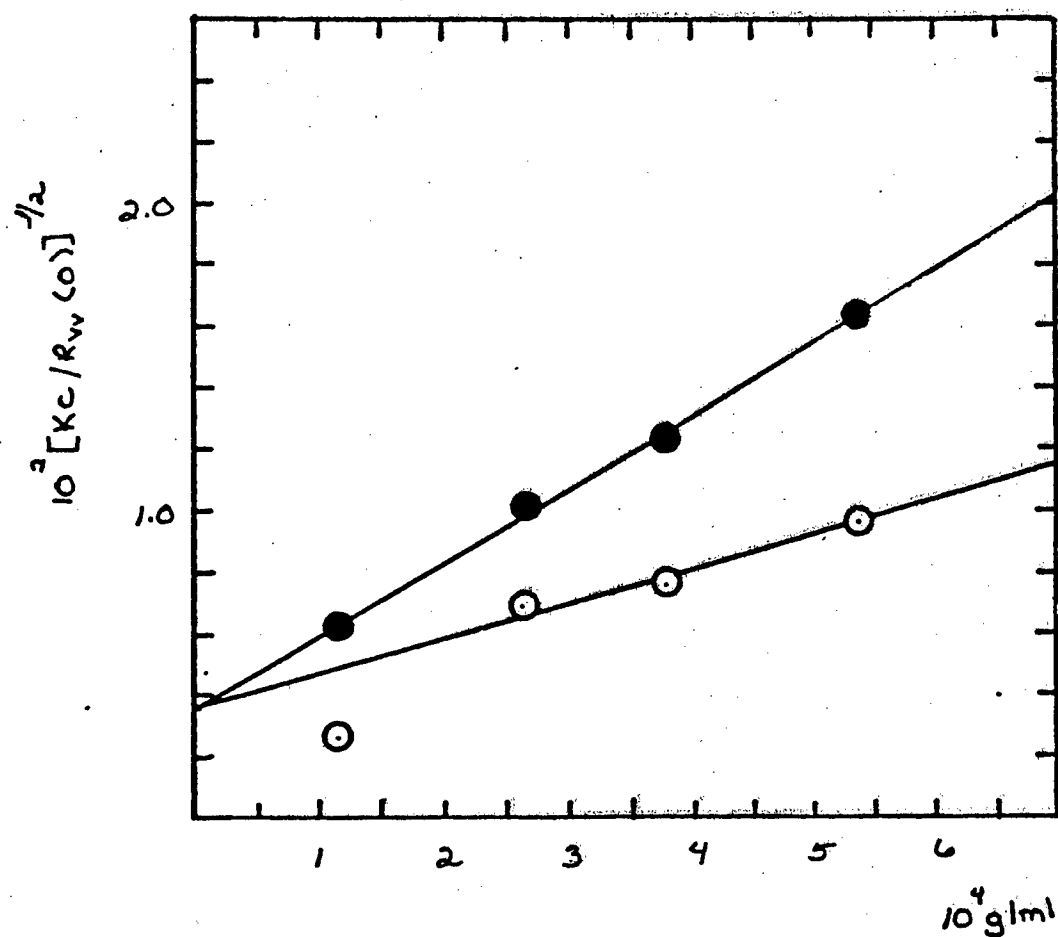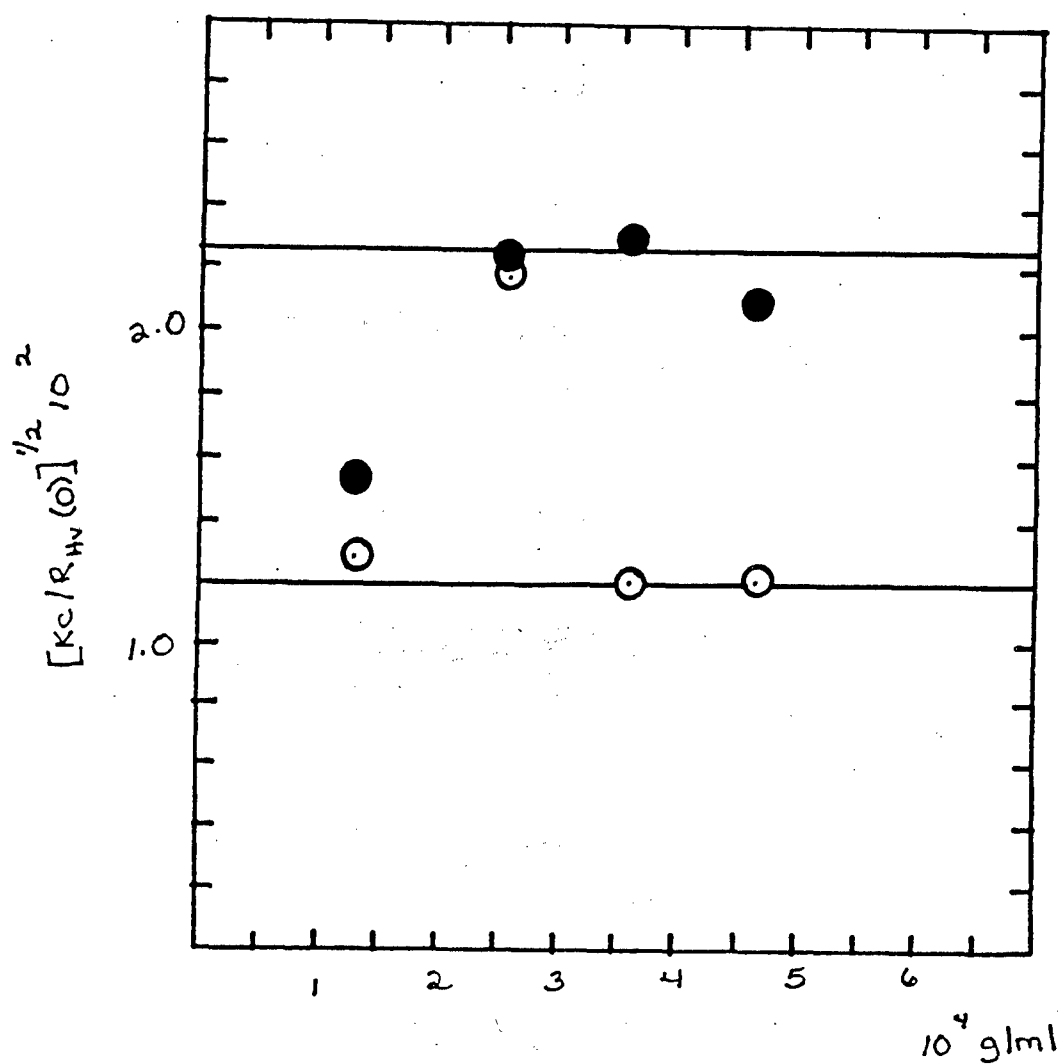
Figure 98: The concentration dependence of the Hv component of the integrated intensity light scattering of SPBT 38+ 1.05 N salt O uncentrifuged and ● centrifuged
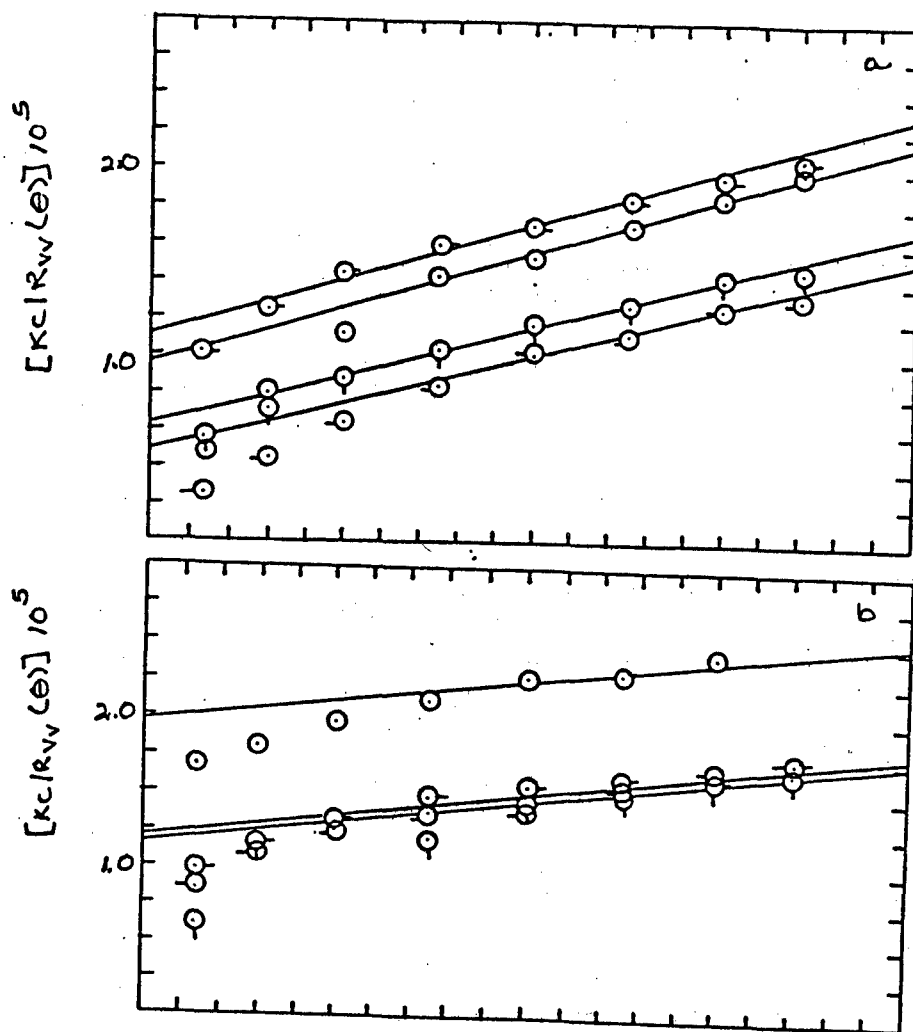
Figure 99: The a)uncentrifuged and b)centrifuged Vv component of the integrated intensity light scattering of SPBT 38 +1.5 N salt (p+ss) at 514.5 nm and 25.0° C. O 0.0512 g/dl O-0.0327 g/dl Q 0.0207 g/dl-O 0.0101 g/dl

Figure 100: The concentration dependence of the Vv component of the integrated intensity light scattering of SPBT 38 + 1.5 N salt. O uncentrifuged ● centrifuged
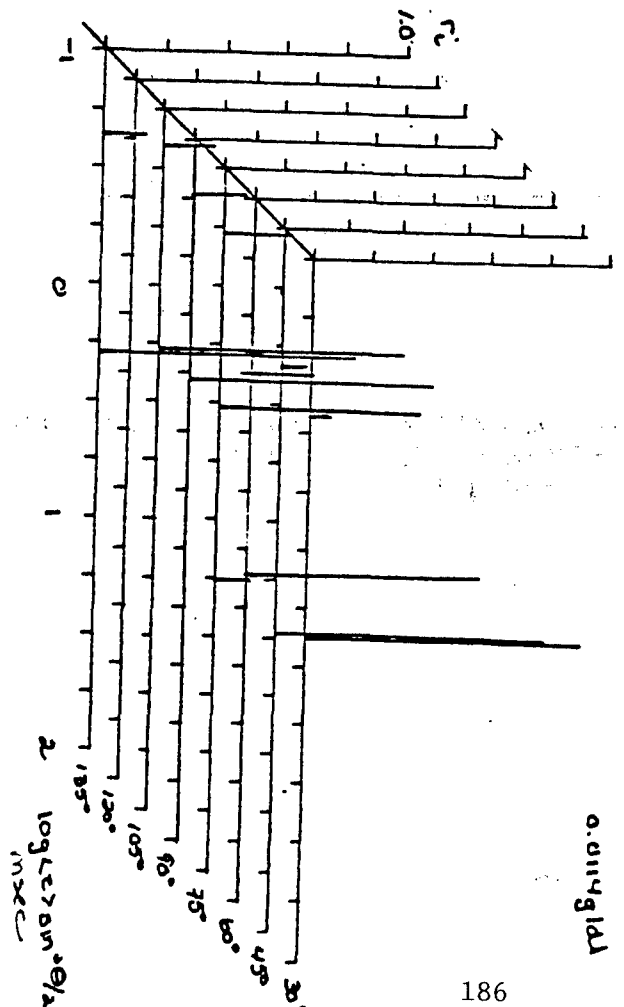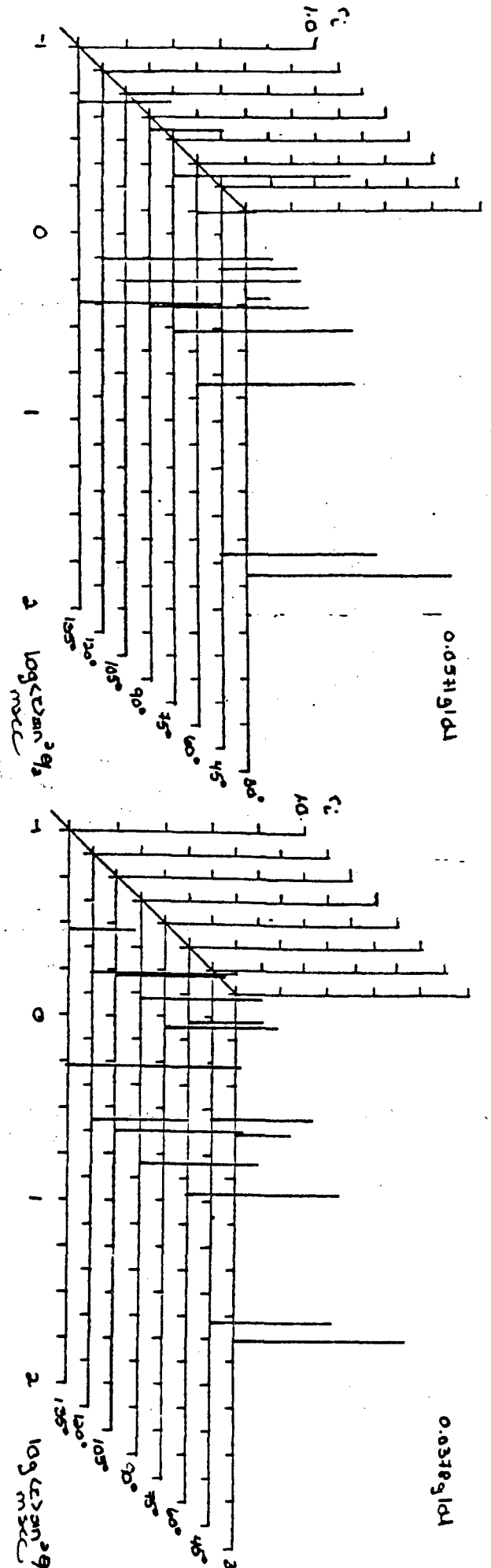
Figure 101: The a)uncentrifuged and b) centrifuged H v component of the integrated intensity light scattering of SPBT 38+ 1.5N salt (p+ss) at 514.5 nm and 25.0 °C. O 0.0512 g/dl O- 0.0327 g/dl Q 0.0207 g/dl -O 0.0101 g/dl

Figure 102: The concentration dependence of the Hv component of the integrated intensity light scattering of SPBT 38+ 1.5N salt . O uncentrifuged and ● centrifuged

Figure 103: The a)uncentrifuged and b) centrifuged Vv component of the integrated intensity light scattering of SPBT 38+ 0.561 N salt (p+ss) at 514.5 nm and 25.0°C. O 0.0465 g/dl O-0.0359 g/dl Q 0.0207 g/dl -O 0.0101 g/dl
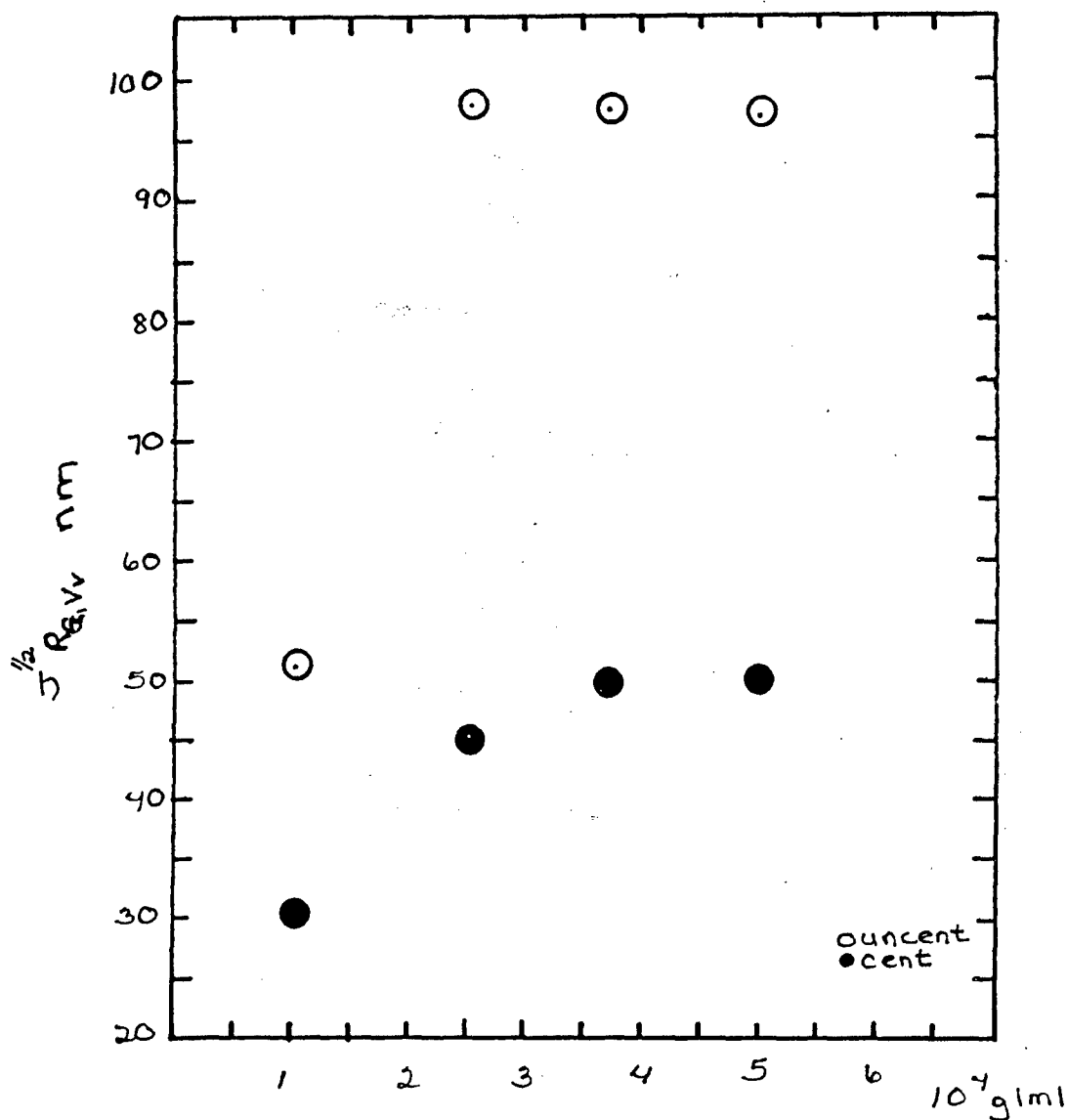
Figure 104: The concentration dependence of $J^{1/2}R_{G,V_v}$ of SPBT 38 + 0.561N salt (p+ss). $J^{1/2}R^2_{G,V_v}$ as calculated from $3[Kc/R_{V_v}(0)]_o^{-1} \partial Kc/R_{V_v}/\partial q^2$

202

Figure 105: The concentration dependence of the Vv component of the integrated intensity light scattering of SPBT 38+ 0.561N salt. O uncentrifuged ● centrifuged
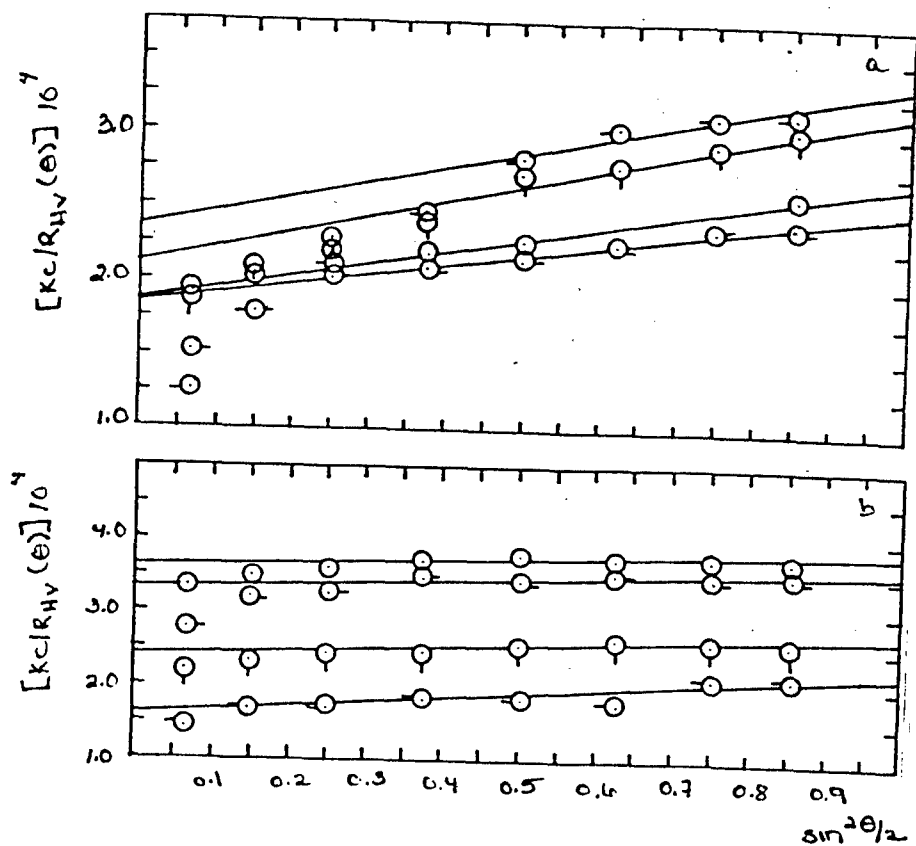
Figure 106: The a) uncentrifuged and b) centrifuged Hv component of the integrated intensity light scattering of SPBT 38 + 0.561 N salt (p+ss) at 514.5 nm and 25.0° C. O 0.0465 g/dl O-0.0359 g/dl Q 0.024 g/dl-O 0.0101 g/dl
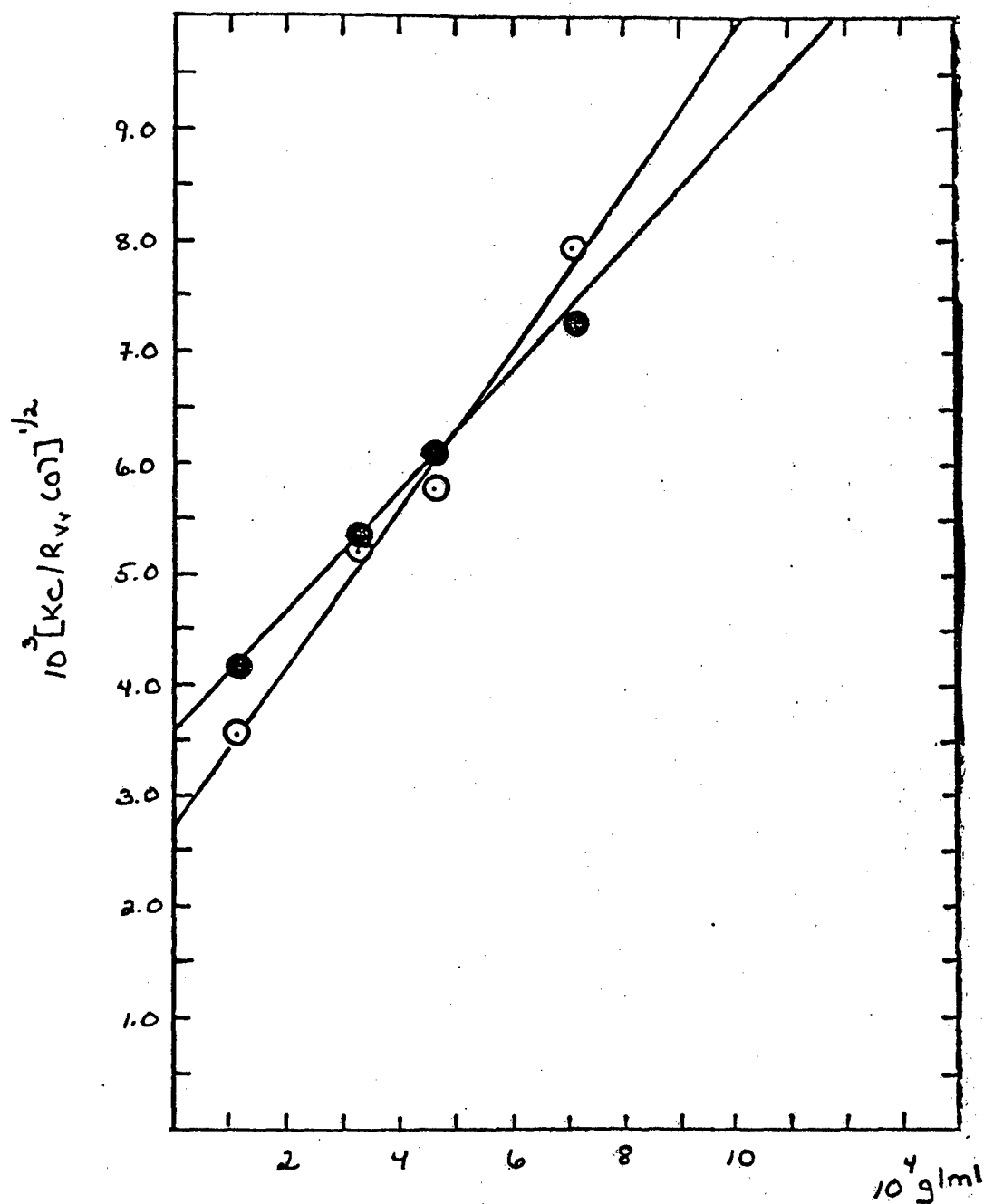
Figure 107: The concentration dependence of the Hv component of the integrated intensity light scattering of SPBT 38+ 0.0561N salt. O uncentrifuged ● centrifuged.

Figure 108: The a) uncentrifuged and b) centrifuged Vv component of the integrated intensity light scattering of SPBT 38 +0.53N salt (ps+s) at 514.5 nm and 25.0°C . O 0.055 g/dl O-0.0377 g/dl Q 0.0242 g/dl –O 0.0102 g/dl

Figure 109: The concentration dependence of the Vv component of the integrated intensity light scattering of SPBT 38 + 0.53N salt . O uncentrifuged ● centrifuged
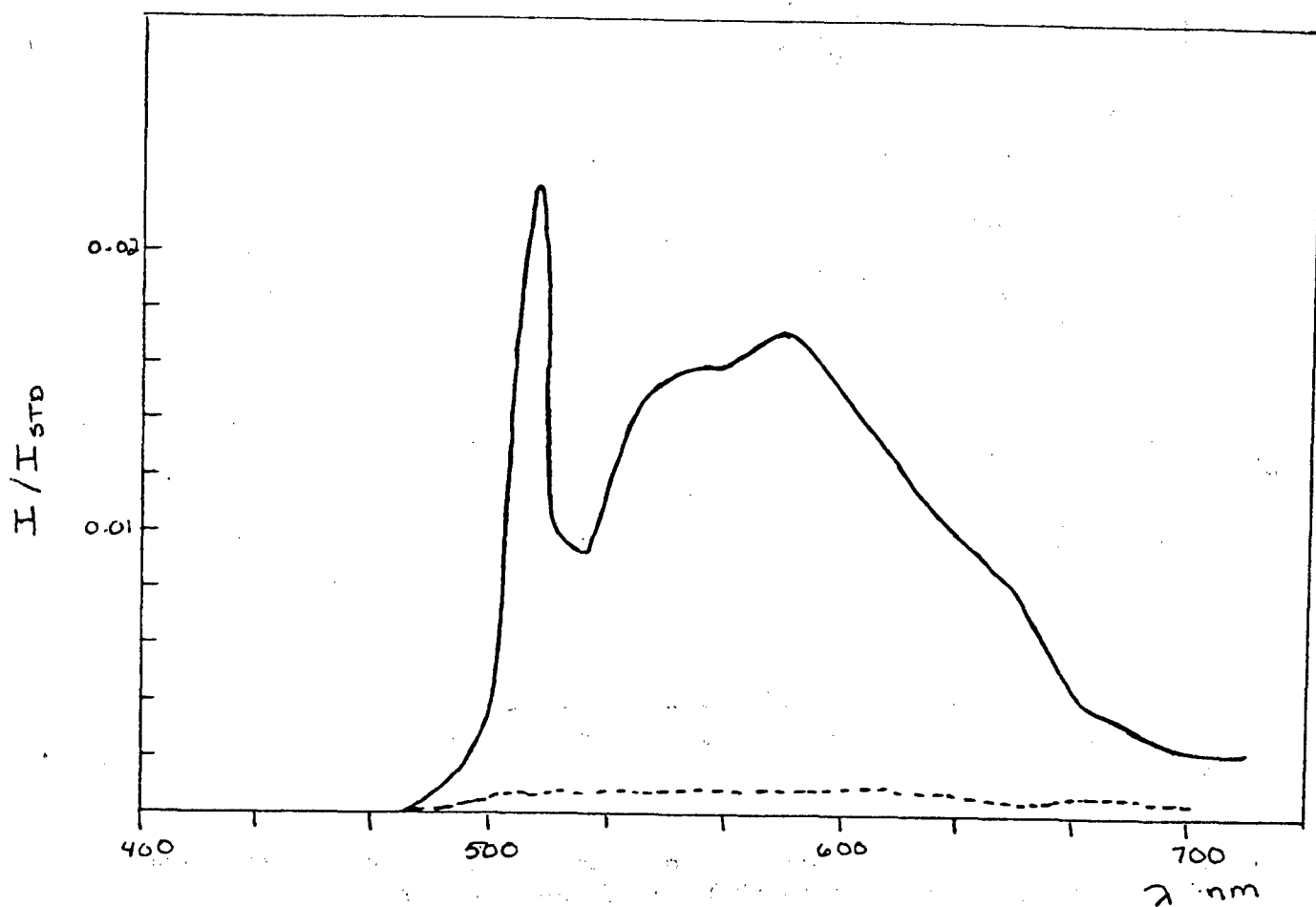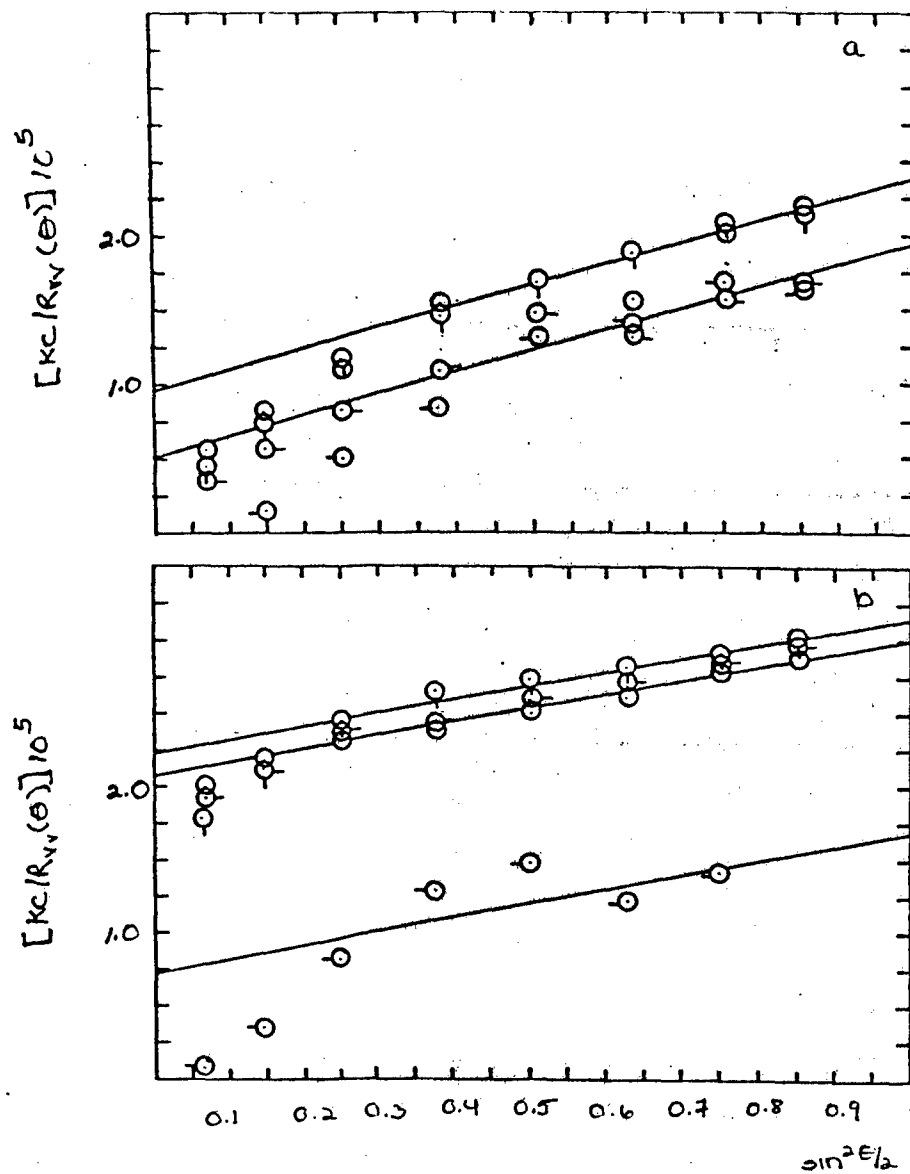
Figure 110: The a) uncentrifuged and b) centrifuged Hv component of the integrated intensity light scattering of SPBT 38+ 0.53N salt (ps+s) at 514.5nm and 25.0 °C. O 0.055 g/dl ⊖ 0.377 g/dl ○ 0.0242 g/dl –O 0.0102 g/dl
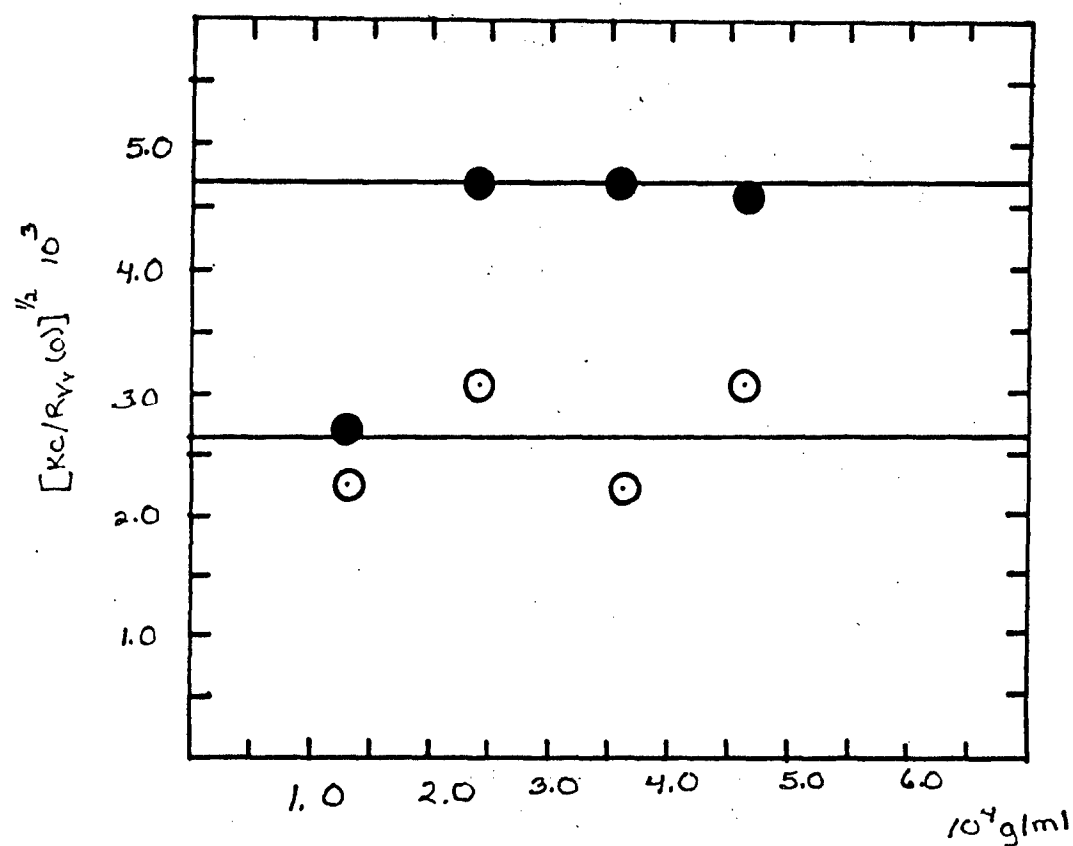
Figure 111: The concentration dependence of the Hv component of the integrated intensity light scattering of SPBT 38 + 0.53N salt. O uncentrifuged ● centrifuged
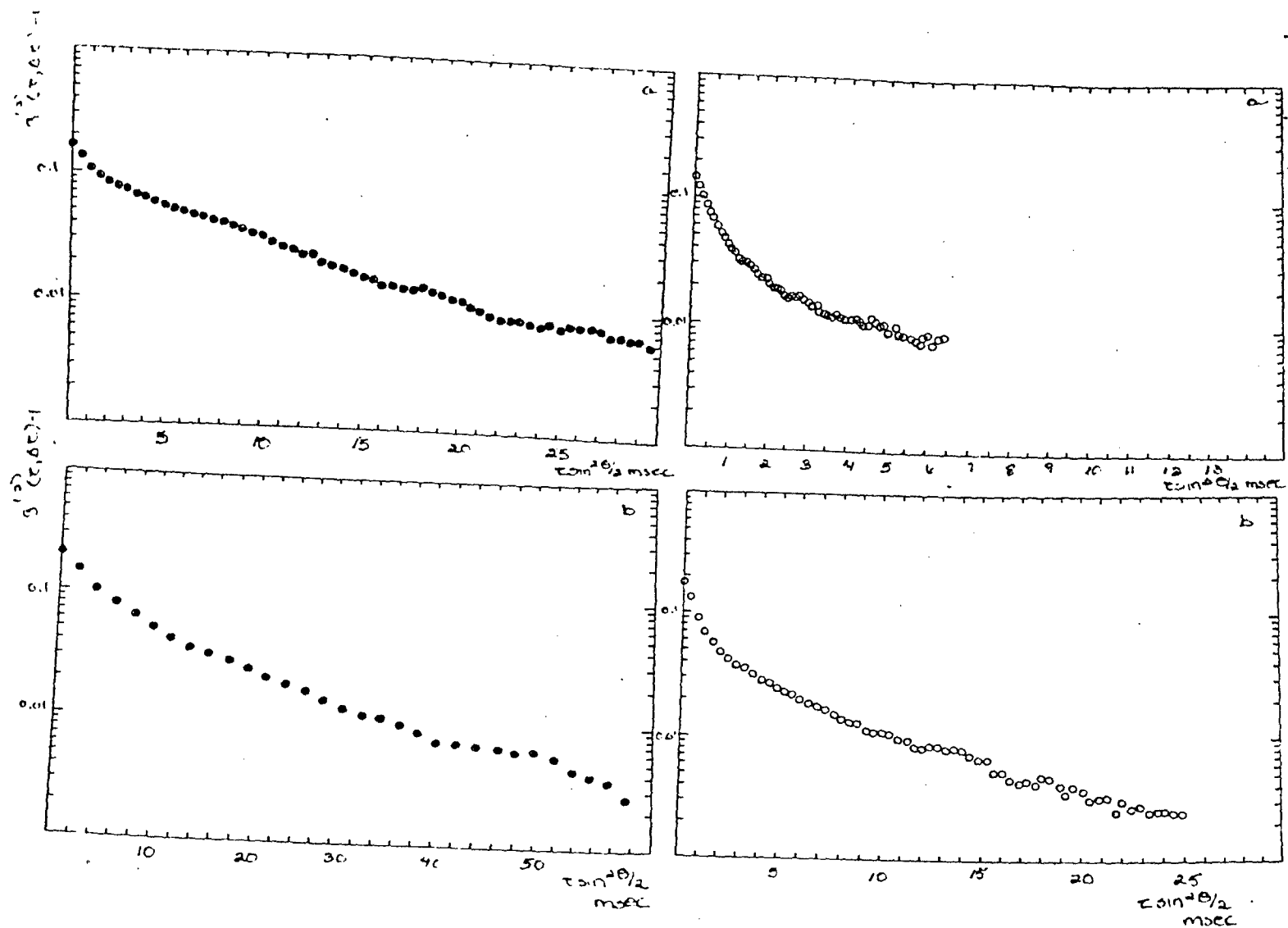
Figure 112: $g^2(\tau, \Delta\tau) - 1$ versus $\tau \sin^2 \theta/2$ of
SPBT 38+0.5N salt (ps+s) at 514.5 nm and 25.0°C ● 45° O 90°
a)0.0102 g/dl b)0.05 g/dl
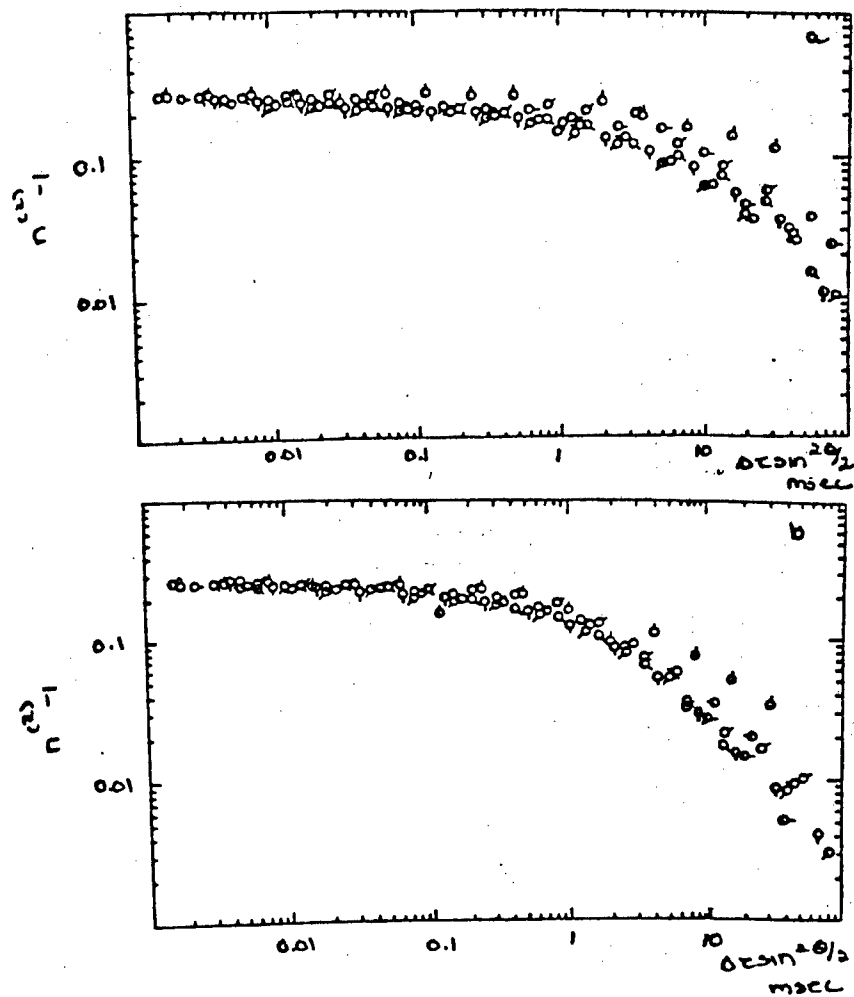
Figure 113: Photon correlation spectroscopy of SPBT 38 + 0.561N salt at 514.5 nm and 25.0° a)0.0129 g/dl b)0.0465 g/dl Ȯ 45° ơ 60° O- 75° Ọ 90° Q 105° Ọ 120°-O 135°
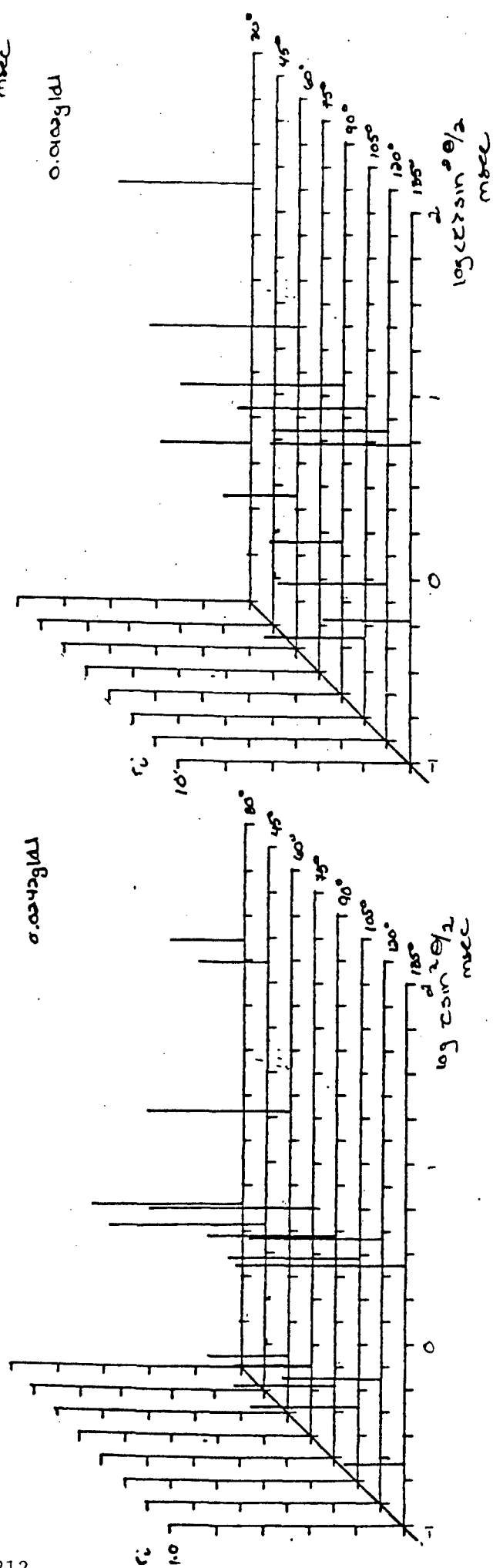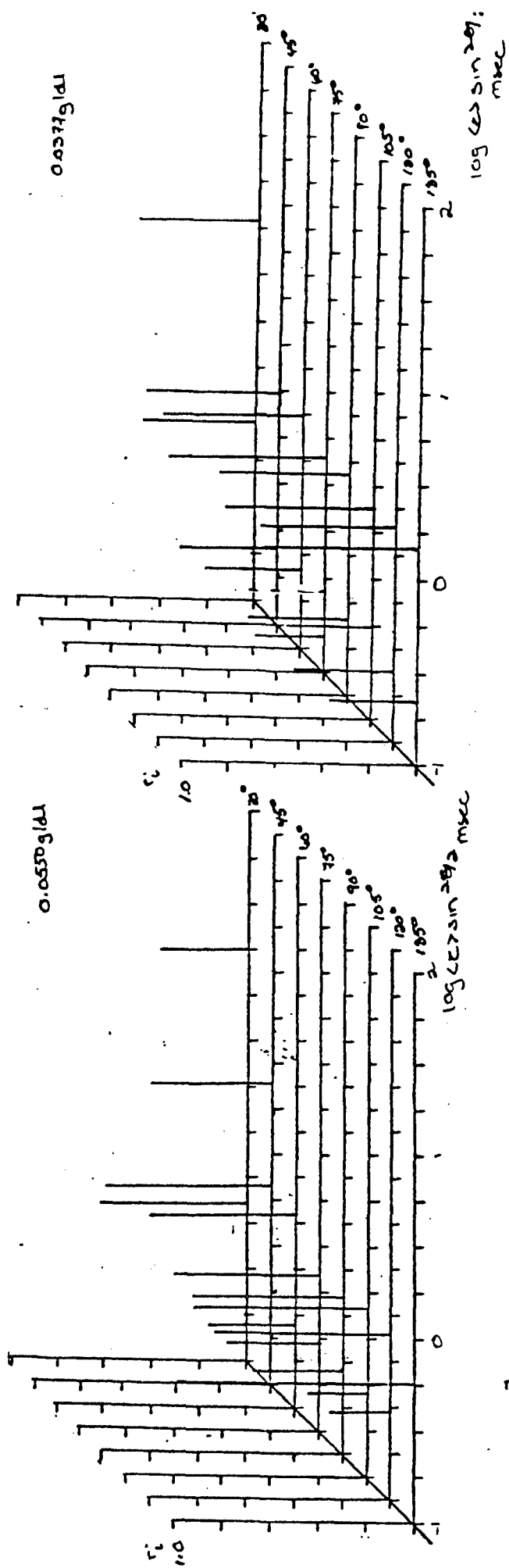
Figure 114: The concentration dependence of $\tau_i \sin^2 \theta/2$ of SPBT 38 + 0.53 N salt (ps+s)

Figure 115: The concentration dependence of $\tau_i \sin^2 \theta/2$ of SPBT 38 + 0.53 N salt (ps+s) uncentrifuged

213

Figure 116: The concentration dependence of $r_i \sin^2 \theta/2$ of SPBT 38
+ 0.561N salt (p+ss)   uncentrifuged

214
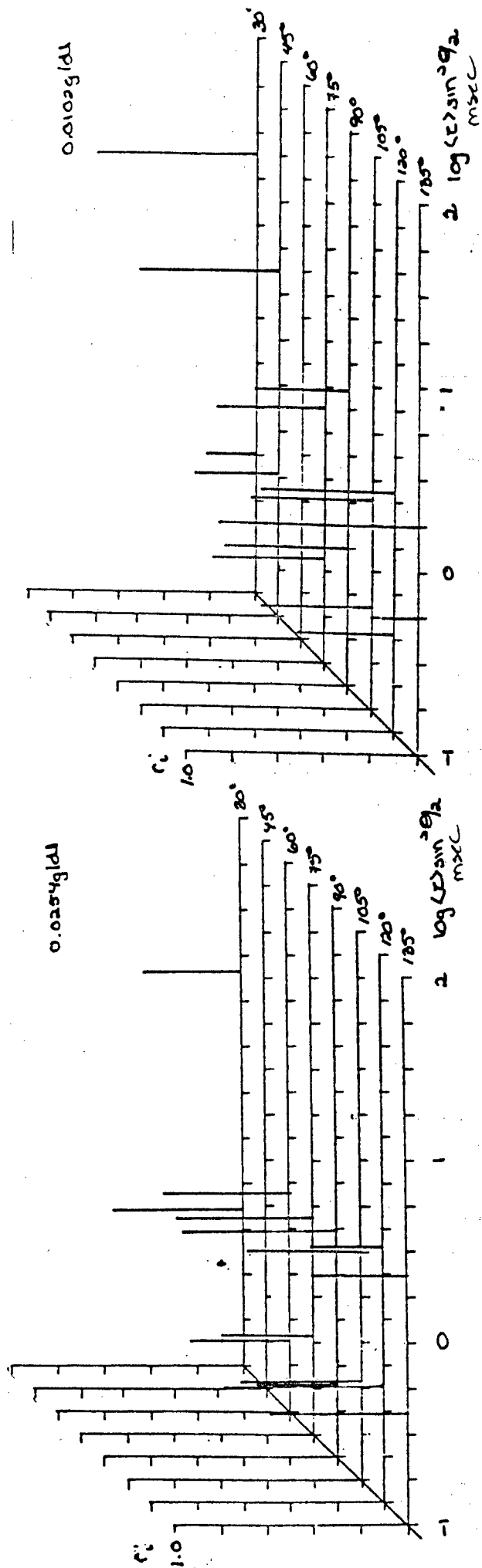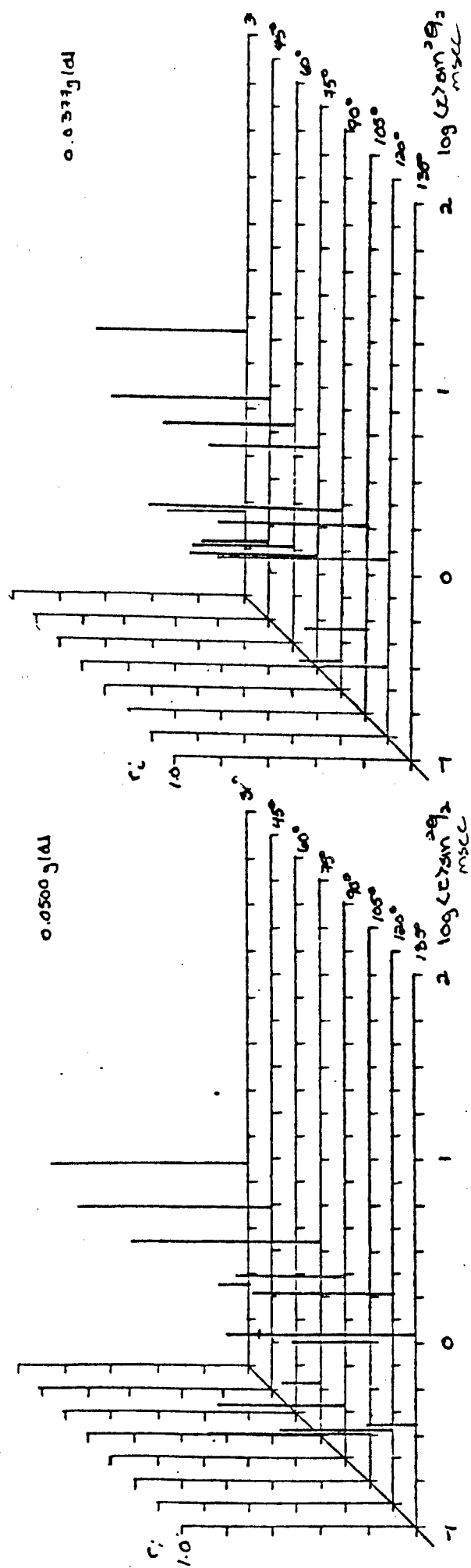
Figure 117: The concentration dependence of $\tau \sin^2 \theta/2$ of SPBT 38 + 0.56 1N salt (p+ss)

O centrifuged

215
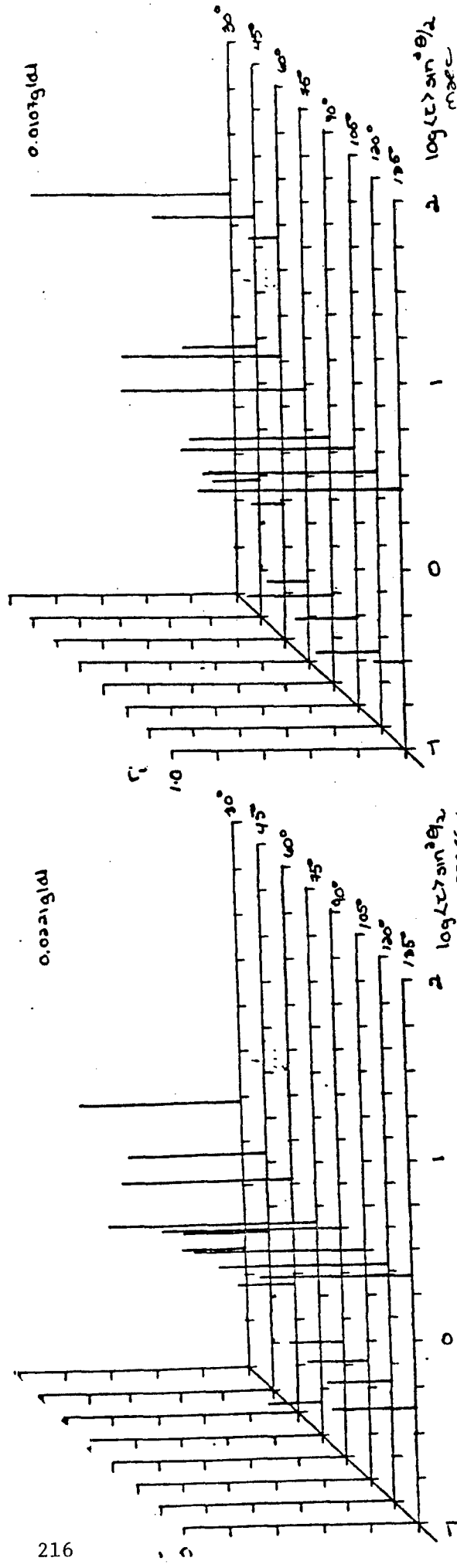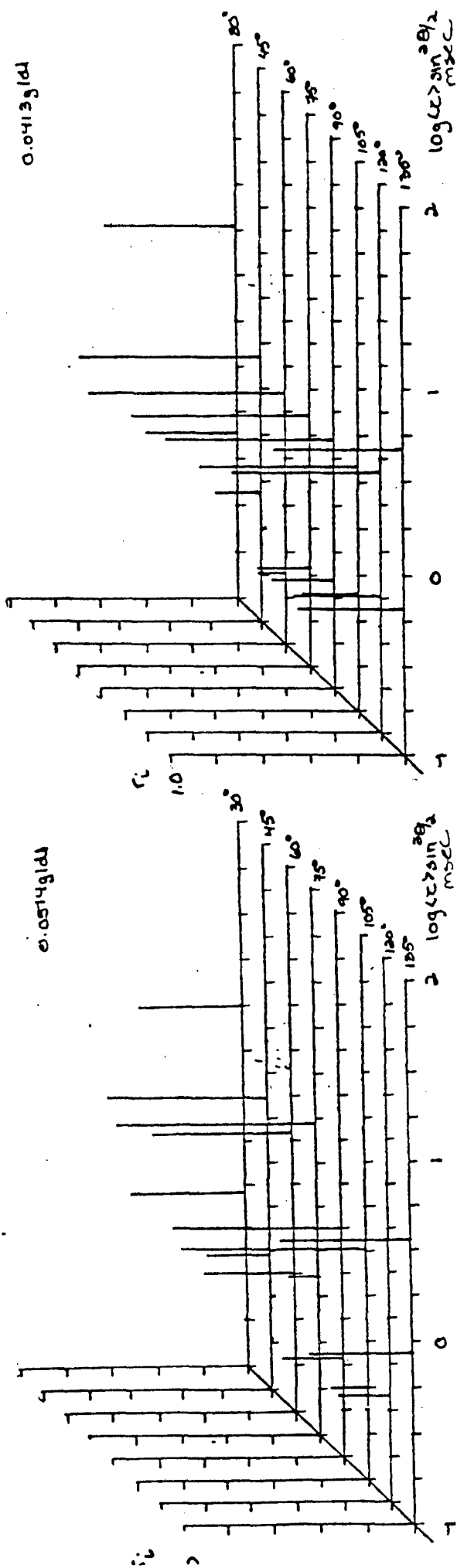
Figure 118: a)The concentration dependence of $\tau_i \sin^2 \theta/2$ of uncentrifuged SPBT+1.09N salt

216
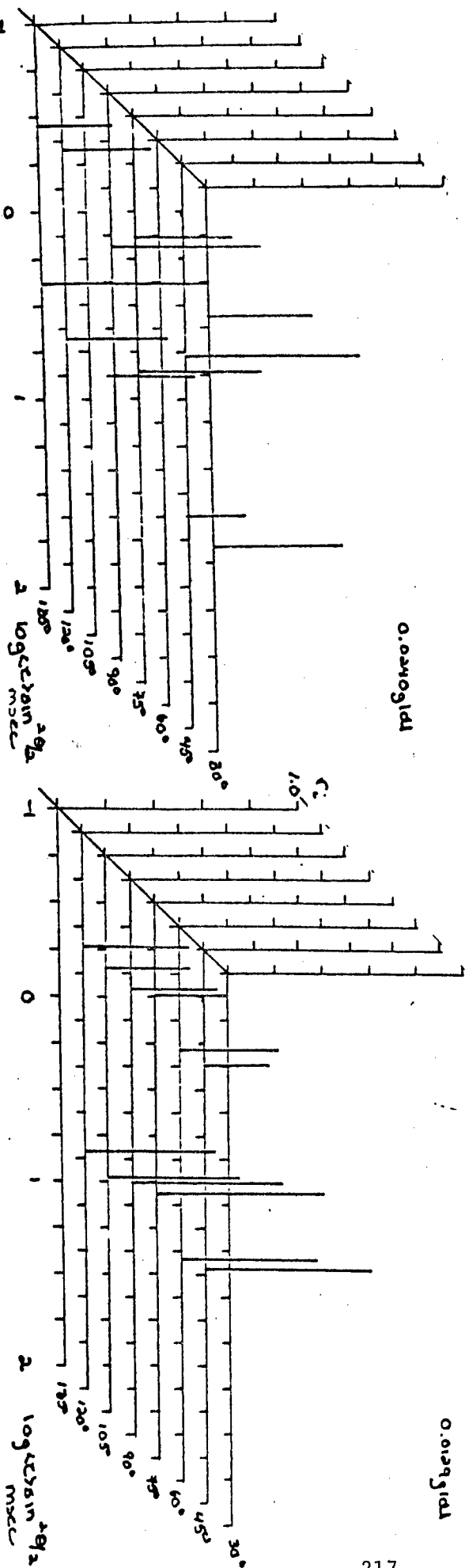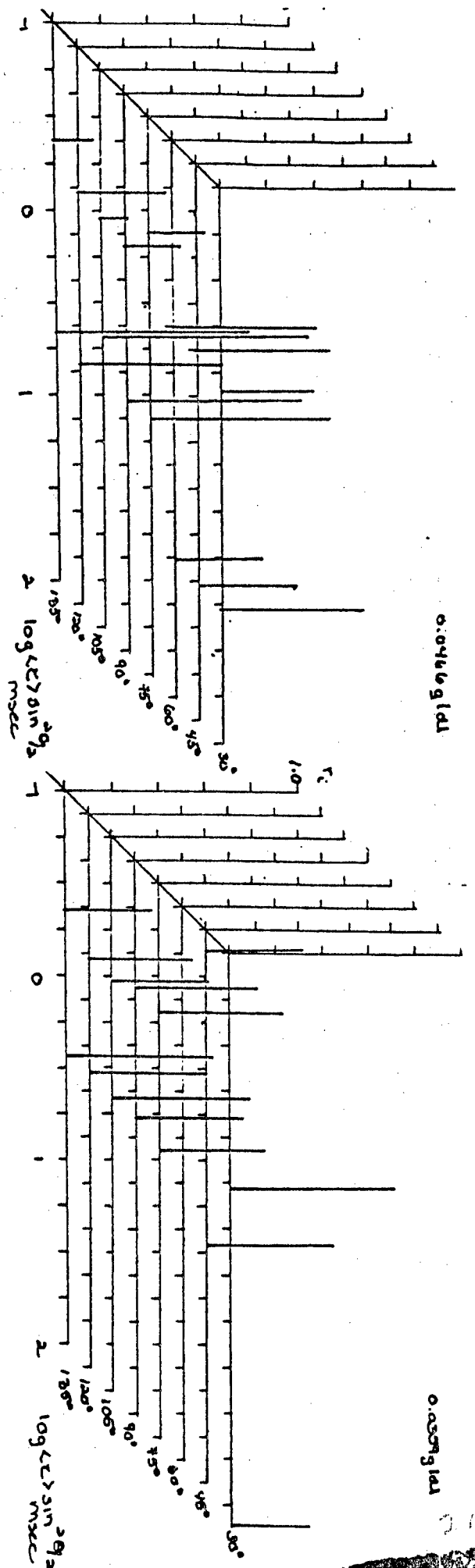
Figure 119: The concentration dependence of $\tau_i \sin^2 \theta/2$ of SPBT 38 +1.05N salt ps+s centrifuged

217
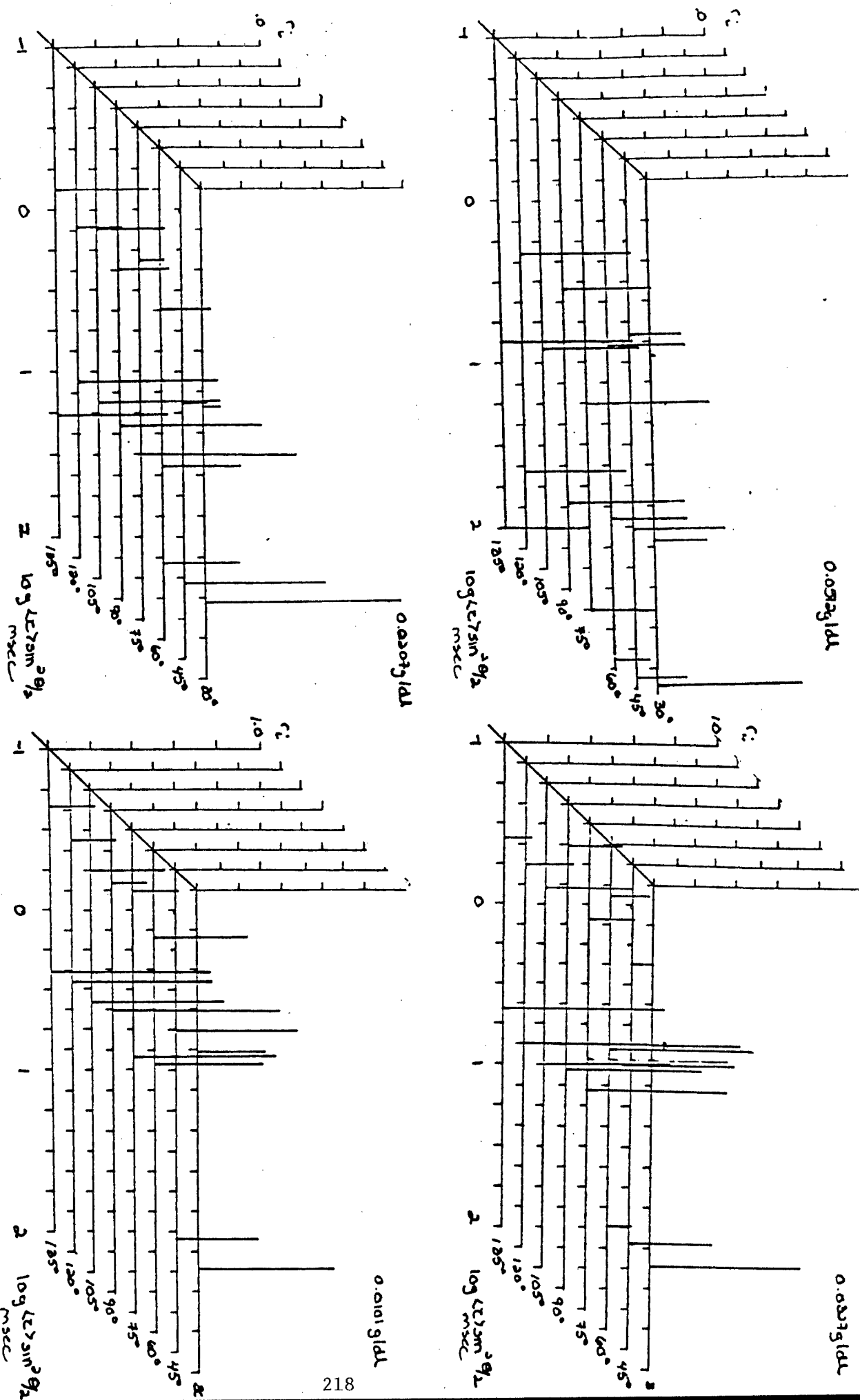
Figure 120: The concentration dependence of $\tau_i \sin^2 \theta/2$ of
SPBT 38 + 1.50 N salt p+ss   Uncentrifuged
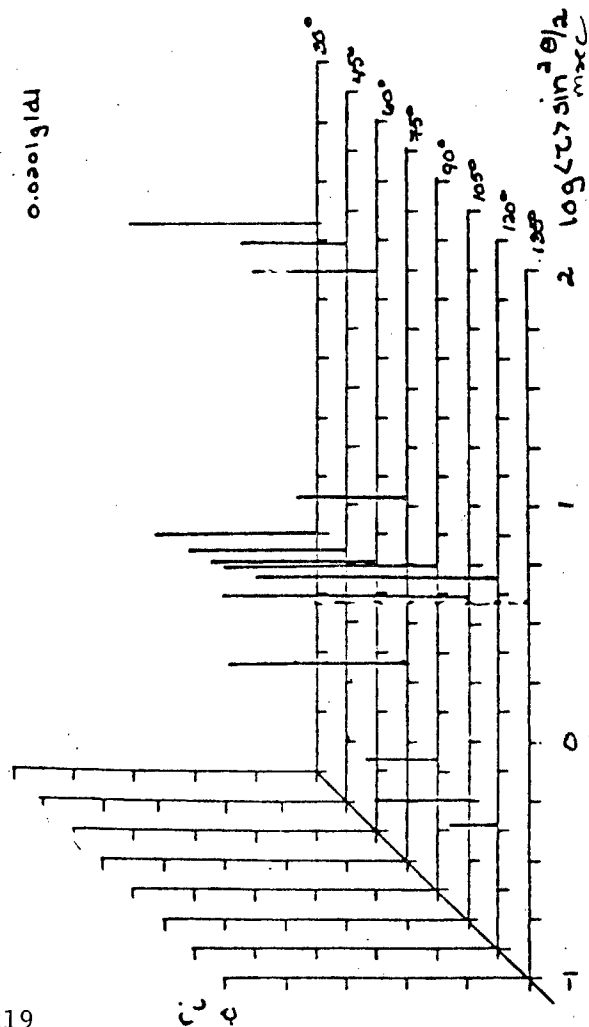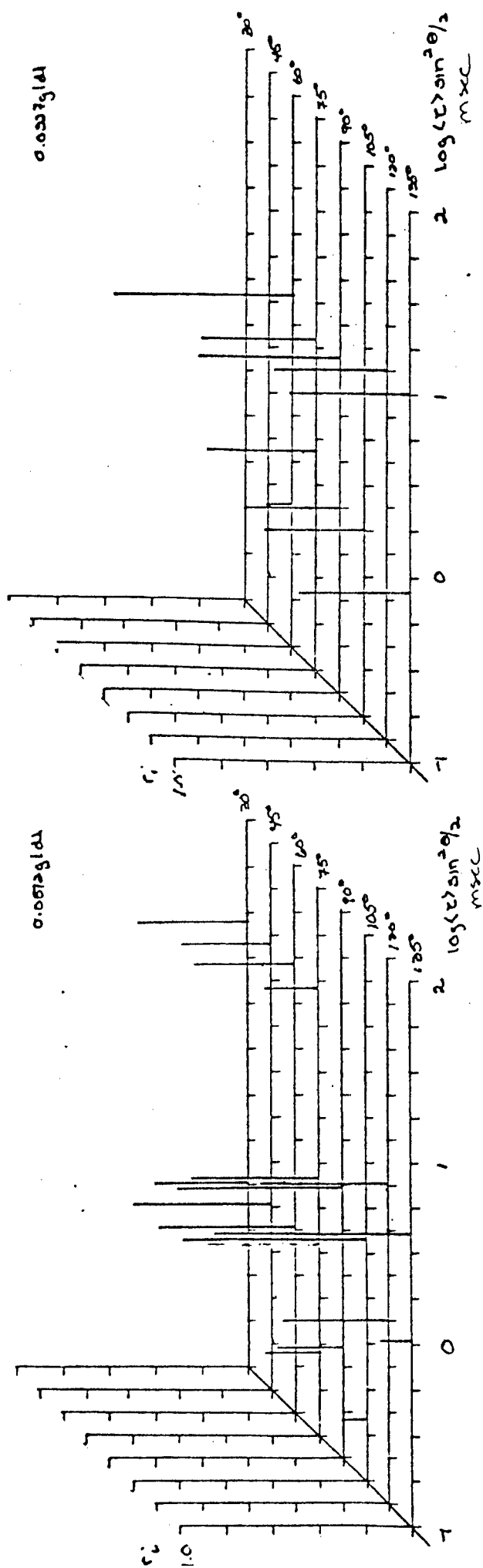
Figure 121: The concentration dependence of $r_i \sin^2 \theta/2$ of SPBT 38 + 1.50 N salt p+ss centrifuged.
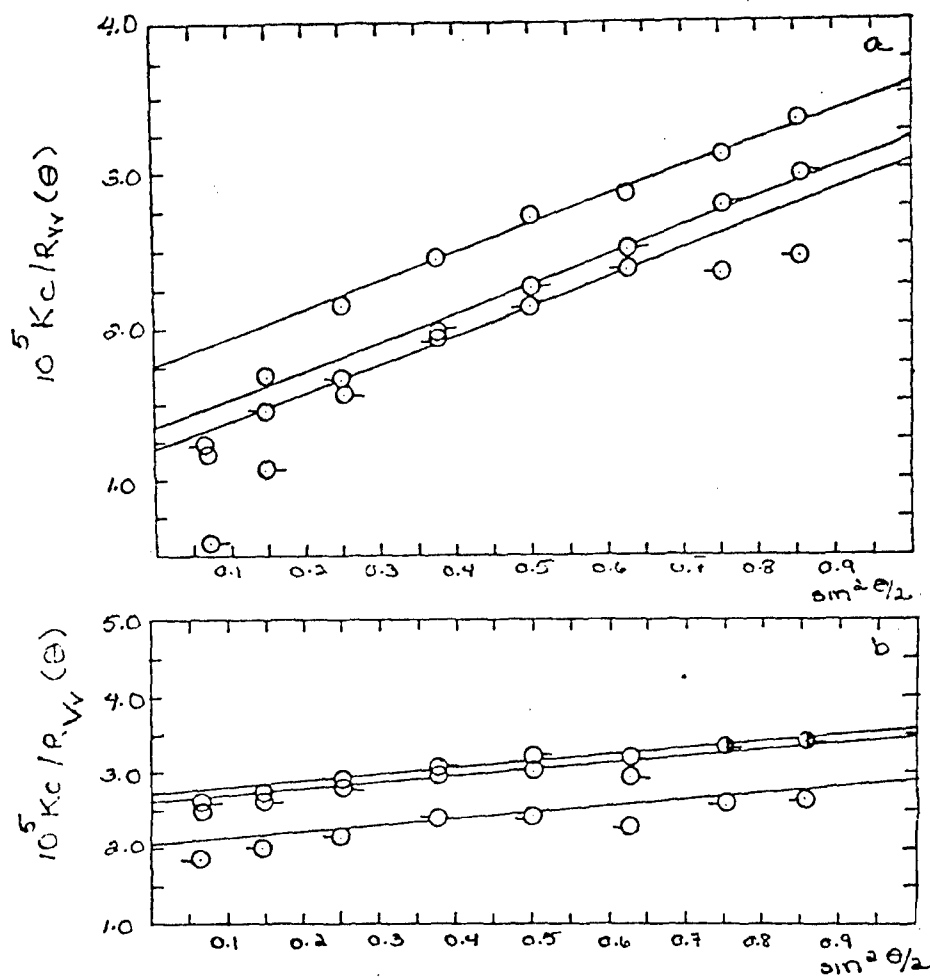
Figure 122: The a)uncentrifuged and b)centrifuged Vv components of the integrated intensity light scattering of SPBT 36 + 1.09N salt (ps+s) at 514.5 nm and 25.0°C. O 0.0544 g/dl O-0.0413 g/dl Q 0.0221 g/dl-O 0.0099 g/dl
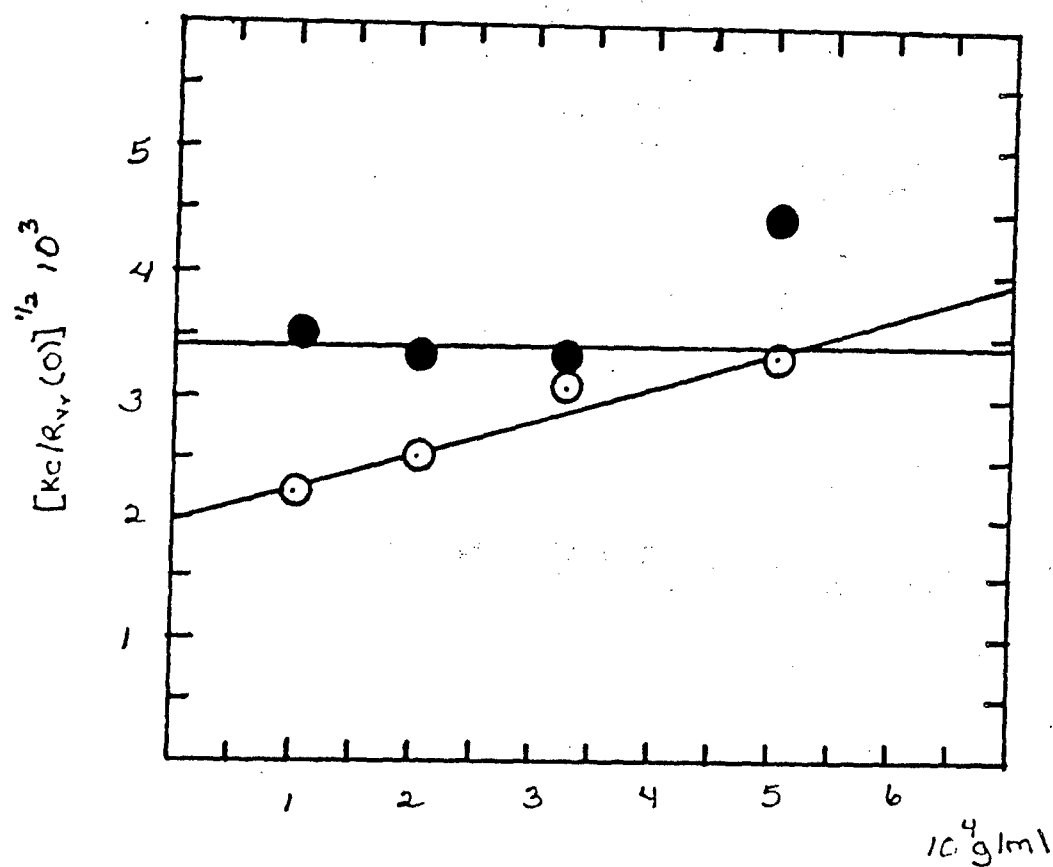
Figure 123: The concentration dependence of the Vv components of the integrated intensity light scattering of SPBT 36 + 1.09N salt. O uncentrifuged ● centrifuged
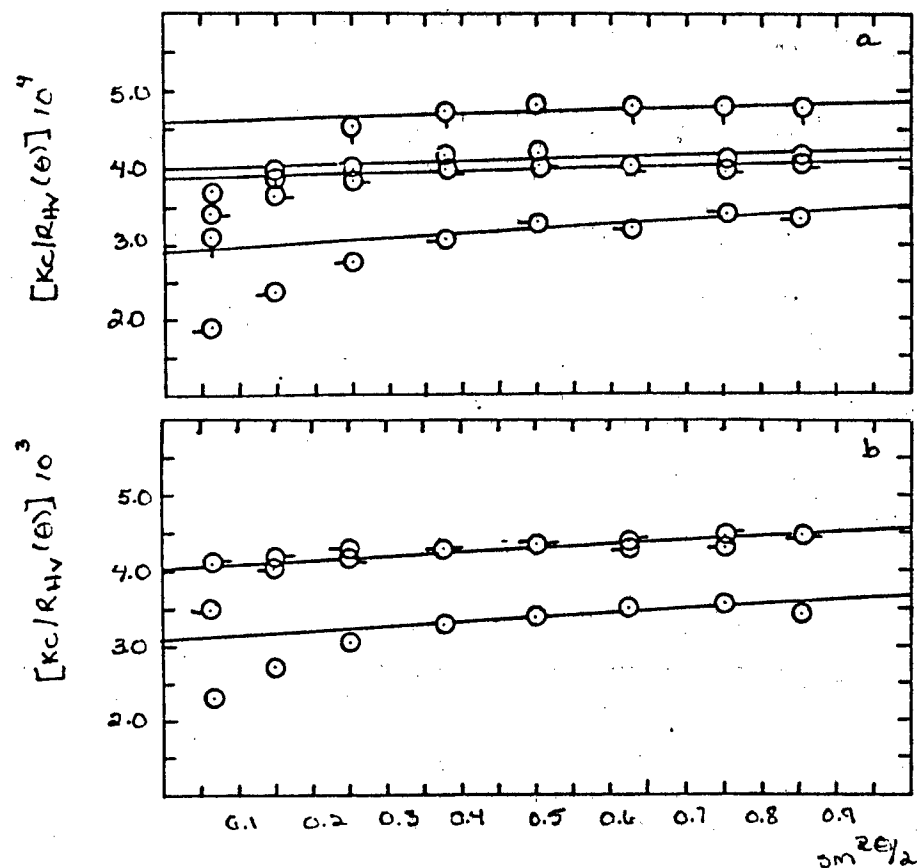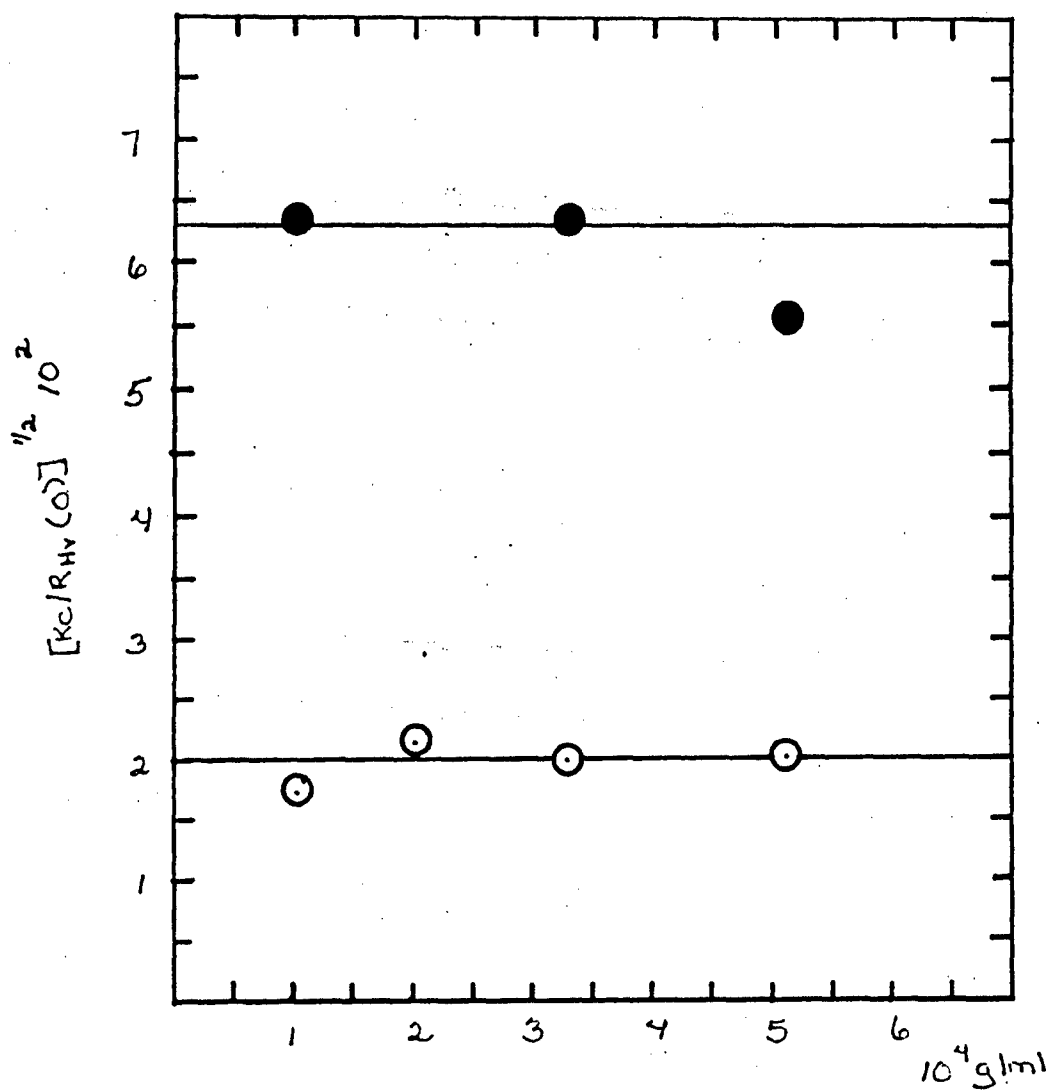
Figure 124: The a)uncentrifuged and b)centrifuged Hv component of the integrated intensity light scattering of SPBT 36+ 1.09N salt (ps+s) at 514.5 nm and 25.0 °C. O 0.0544 g/dl O-0.0413 g/dl Q 0.0221 g/dl-O 0.0107 g/dl

Figure 125: The concentration dependence of the Hv component of the integrated intensity light scattering of SPBT 36+ 1.09 N salt O uncentrifuged and ● centrifuged
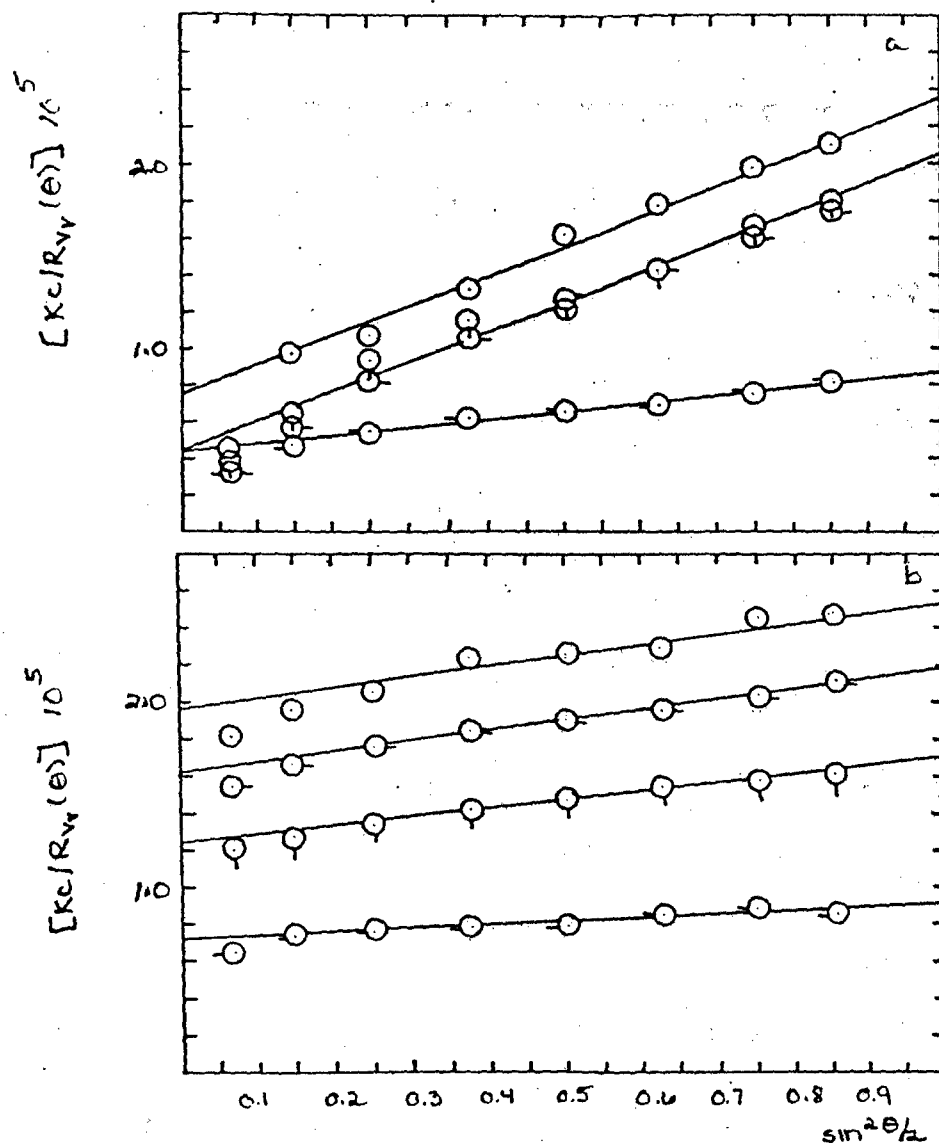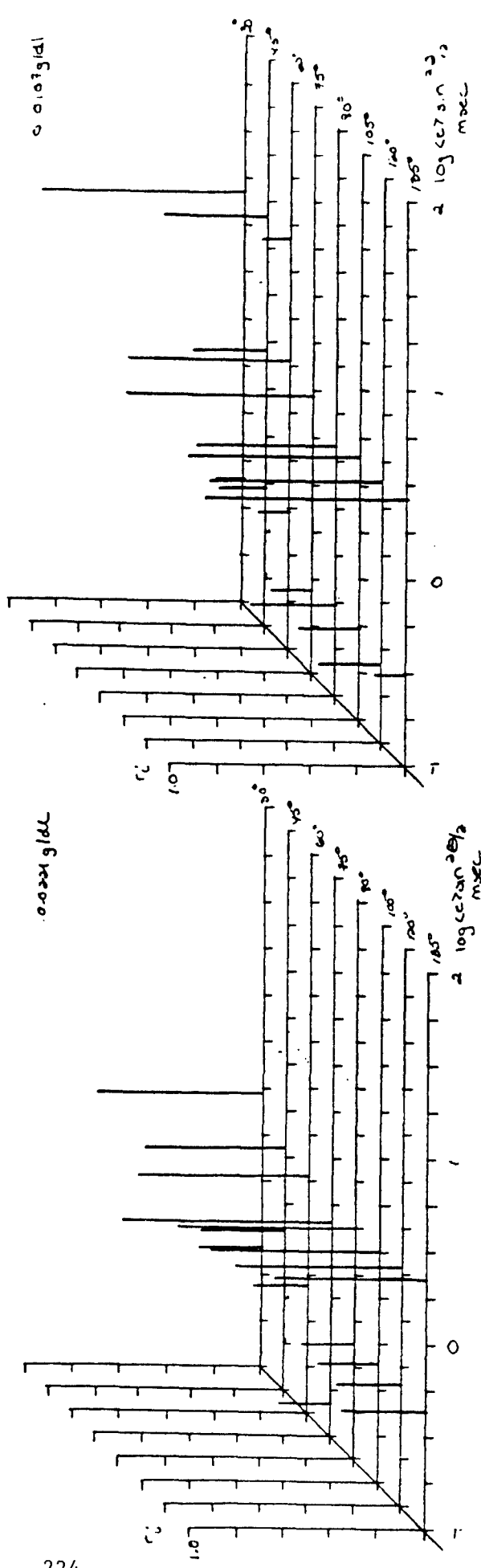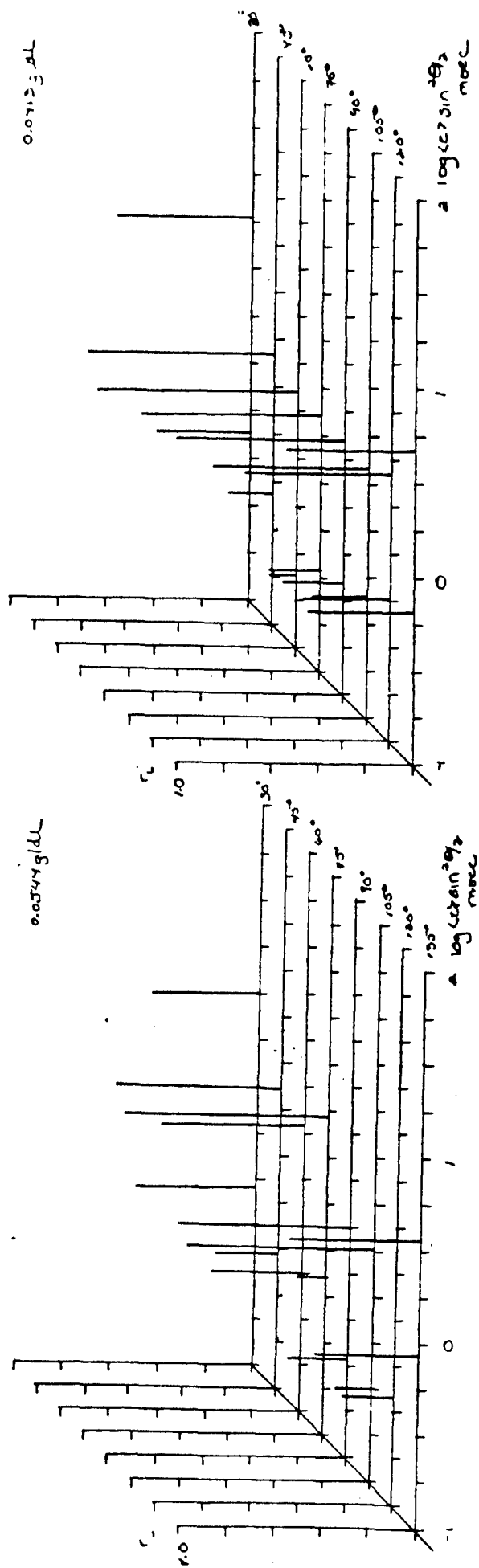
Figure 126: a]The concentration dependence of $\tau \sin^2 \theta/2$ of uncentrifuged SPBT-36+ 1.09N salt at 514.5 nm and 25.0°C
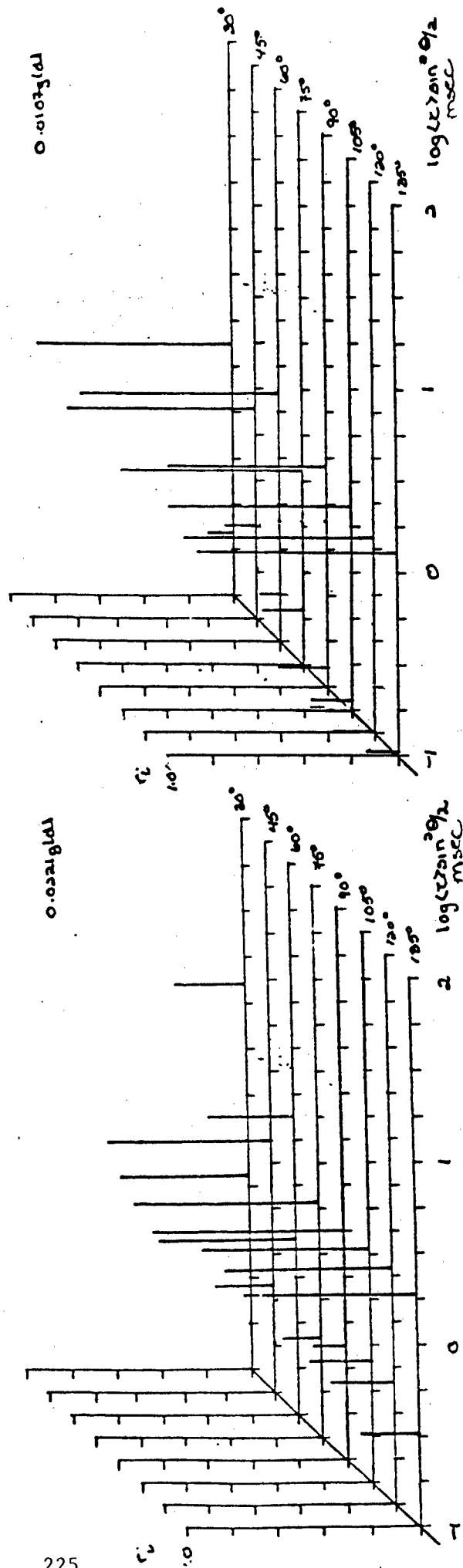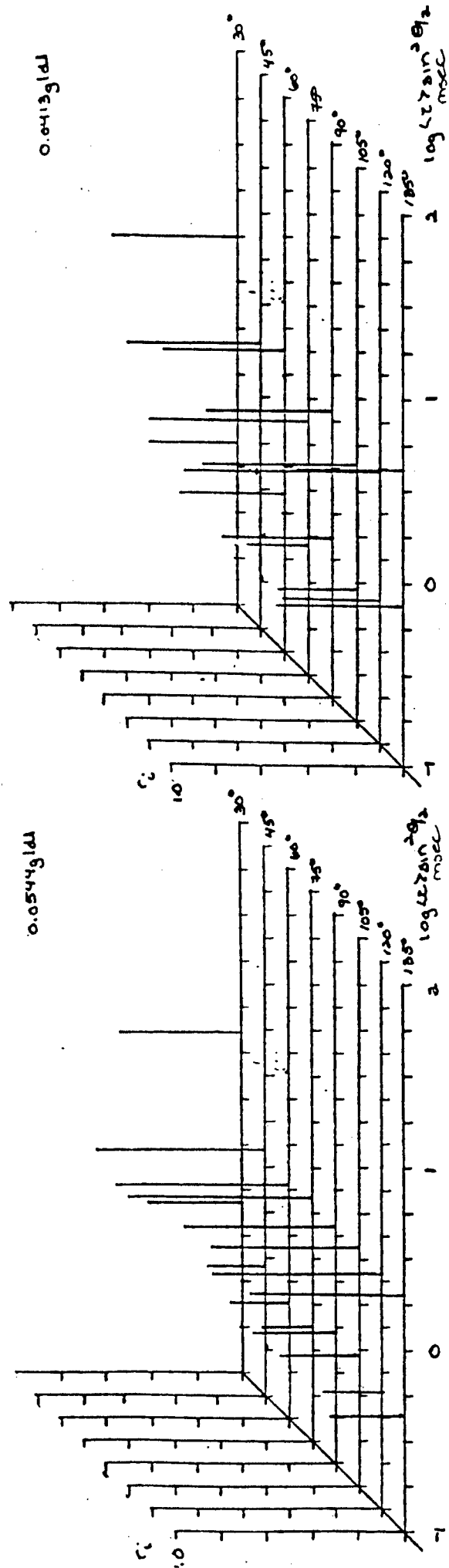
Figure 127: a)The concentration dependence of $r_i \sin^2 \theta/2$ of centrifuged SPBT-36 + 1.09N salt
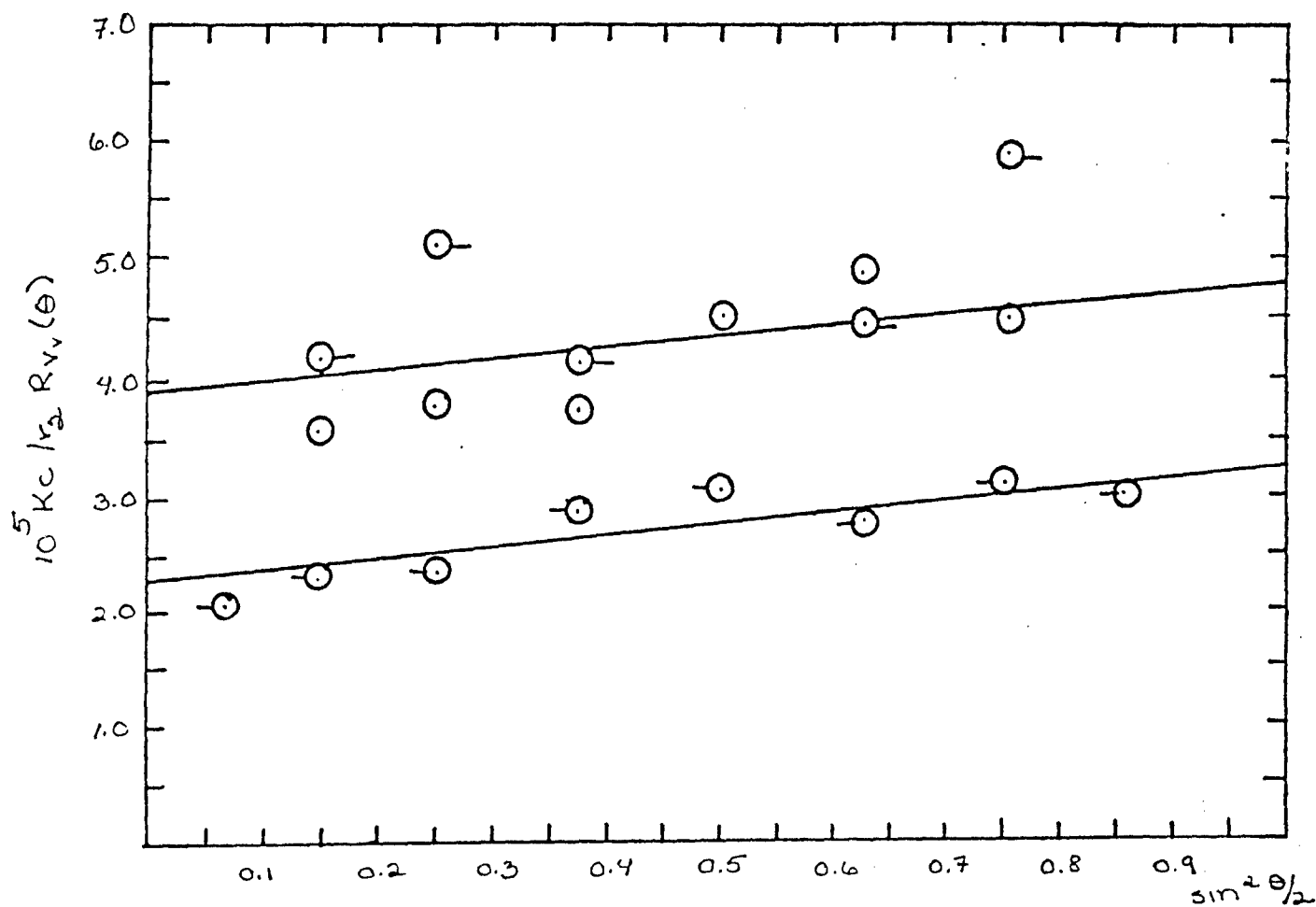
Figure 128: The angular dependence for the uncentrifuged components of the Vv AILS of SPBT-36 + 1.09 N salt. O 0.0544g/dl O- 0.0413 g/dl Q 0.0221 g/dl
-O 0.0102g/dl
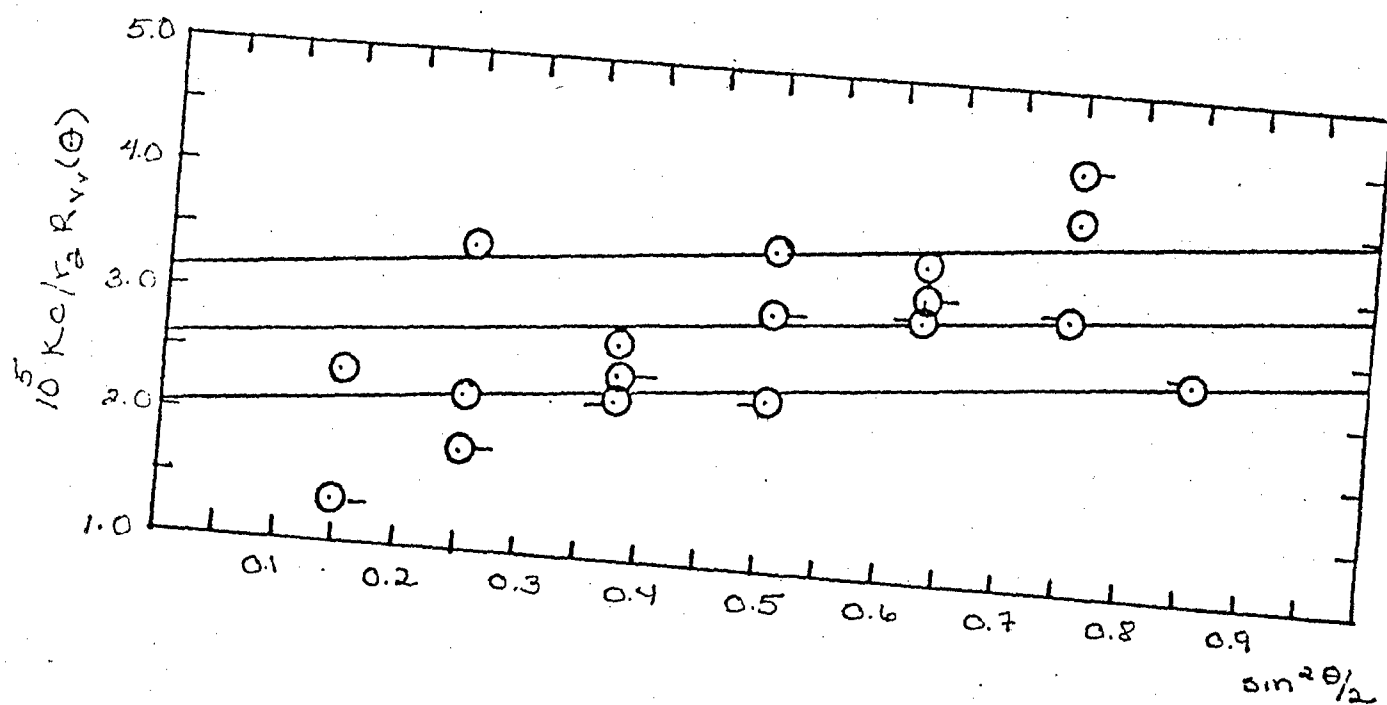
Figure 129: The angular dependence for the centrifuged components of the Vv AILS of SPBT–36 + 1.09N . O 0.0544g/dl O– 0.0413 g/dl ○ 0.0221 g/dl –O 0.0102g/dl
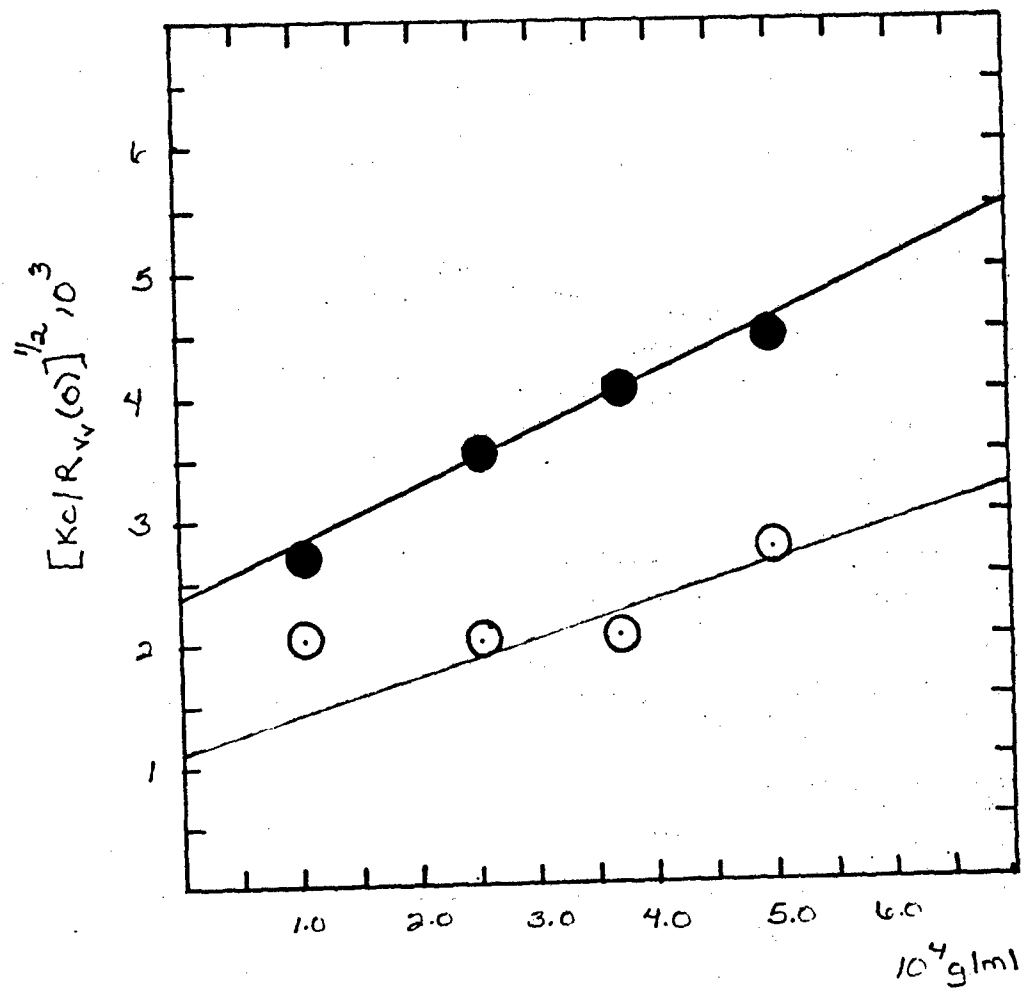
Figure 130: The concentration dependence of the Vv components of the integrated intensity light scattering of SPBT 36 + 1.09N salt. O r_2 uncentrifuged ● r_2 centrifuged
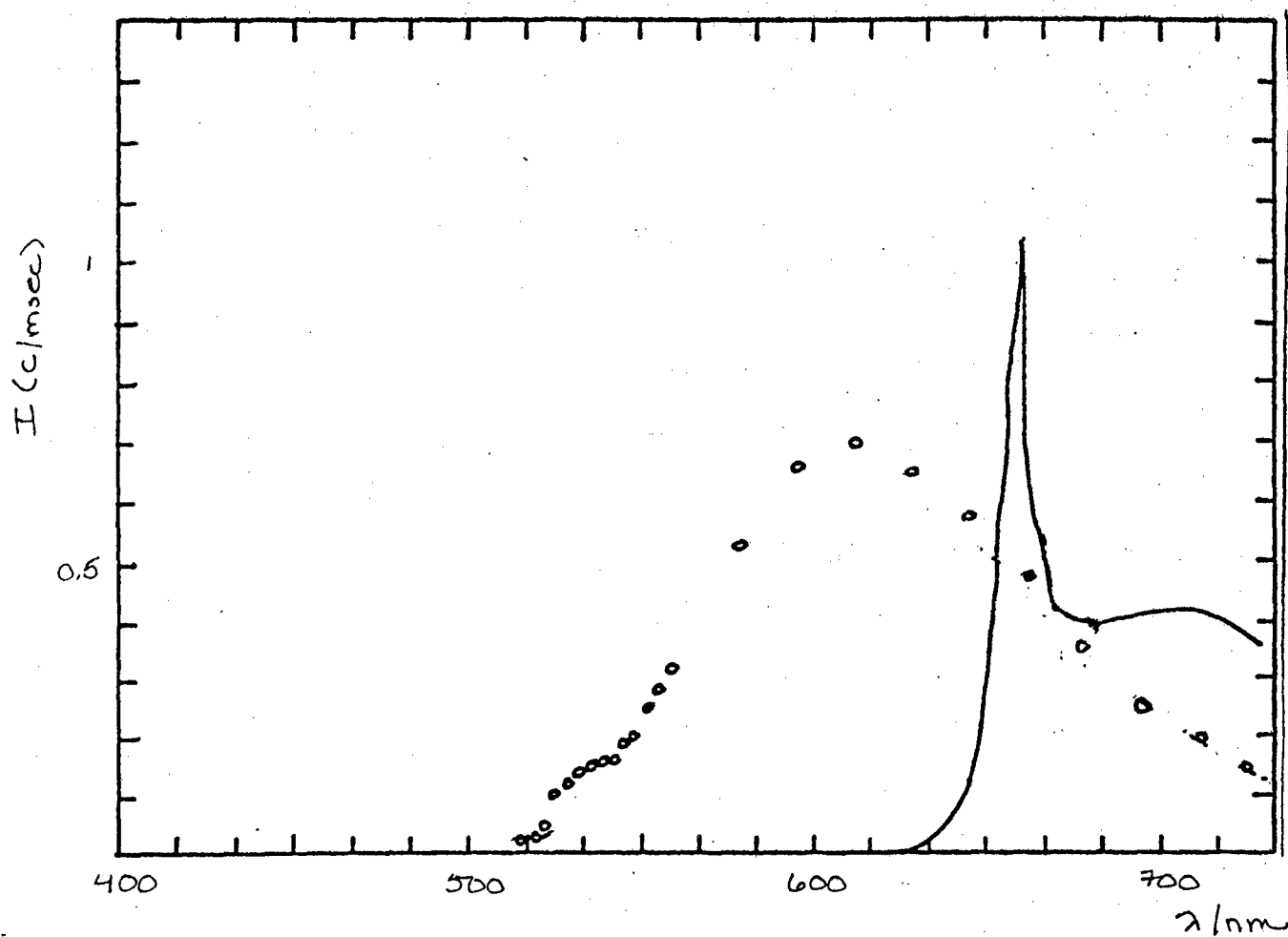
Figure 131: Hv emission spectra for SPBO-4 in MSA and CSA excited at 514 nm and 633 nm respectively at 25.0°C.
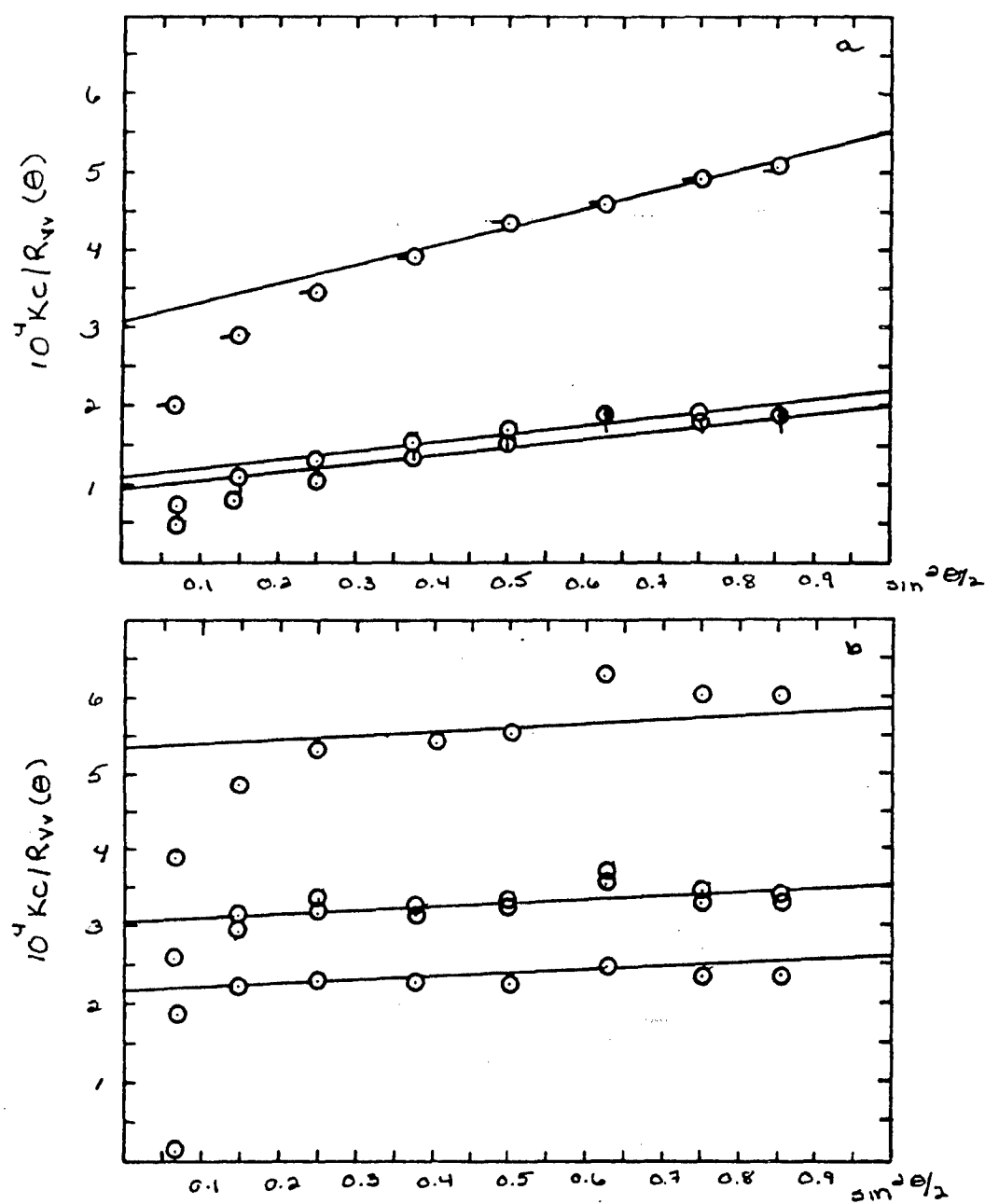
Figure 132: The a)uncentrifuged and b)centrifuged Vv components of the integrated intensity light scattering of SPBO 4/CSA at 633 nm and 25.0°C. O 0.0424 g/dl O 0.0360 g/dl Q 0.0244 g/dl O -0.0109 g/dl
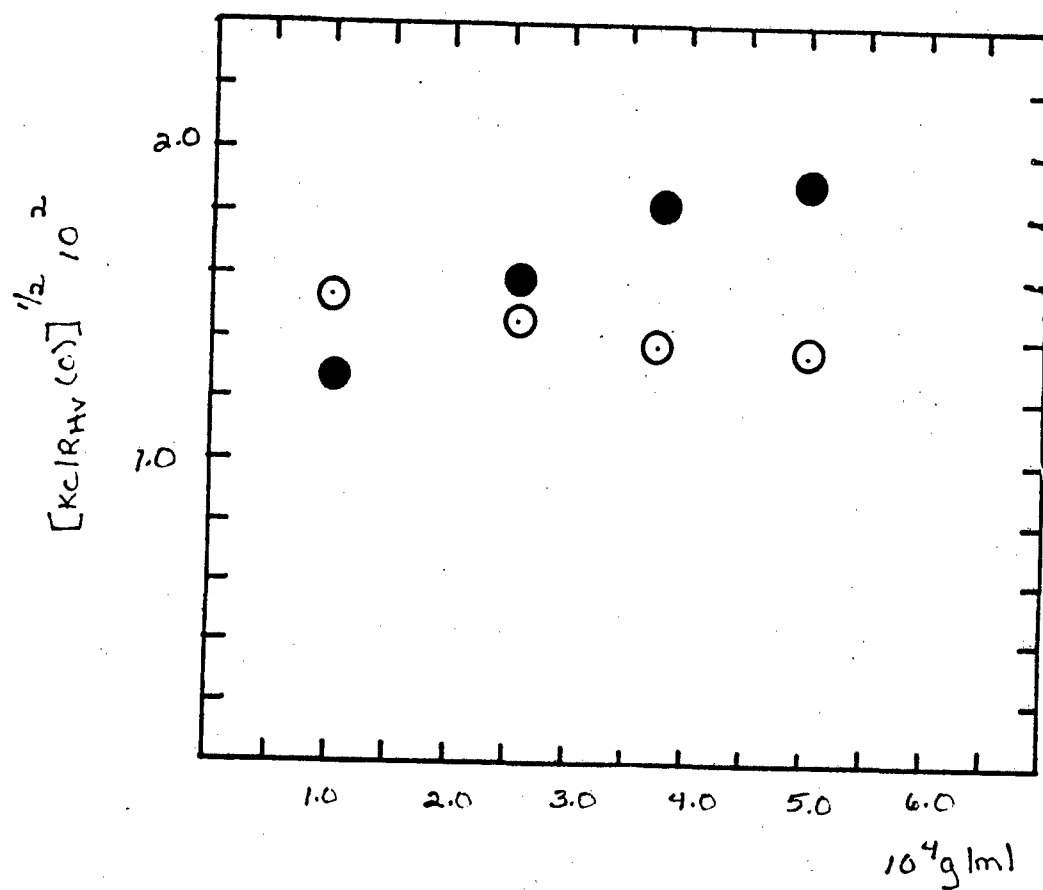
Figure 133: The concentration dependence of the Vv components of the integrated intensity light scattering of SPBO 4/CSA. ○ uncentrifuged ● centrifuged sonciated ○ uncentrifuged ● centrifuged
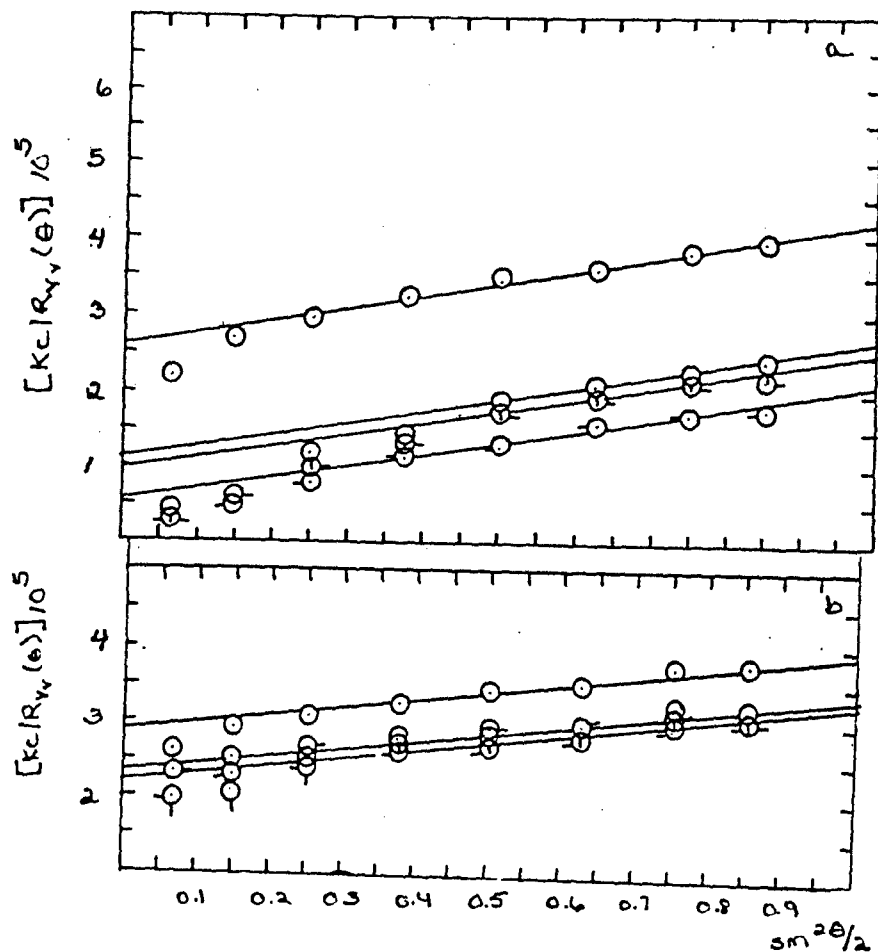
231

Figure 134: The a)uncentrifuged and b)centrifuged Hv components of the integrated
intensity light scattering of SPBO 4/CSA at 633 nm and
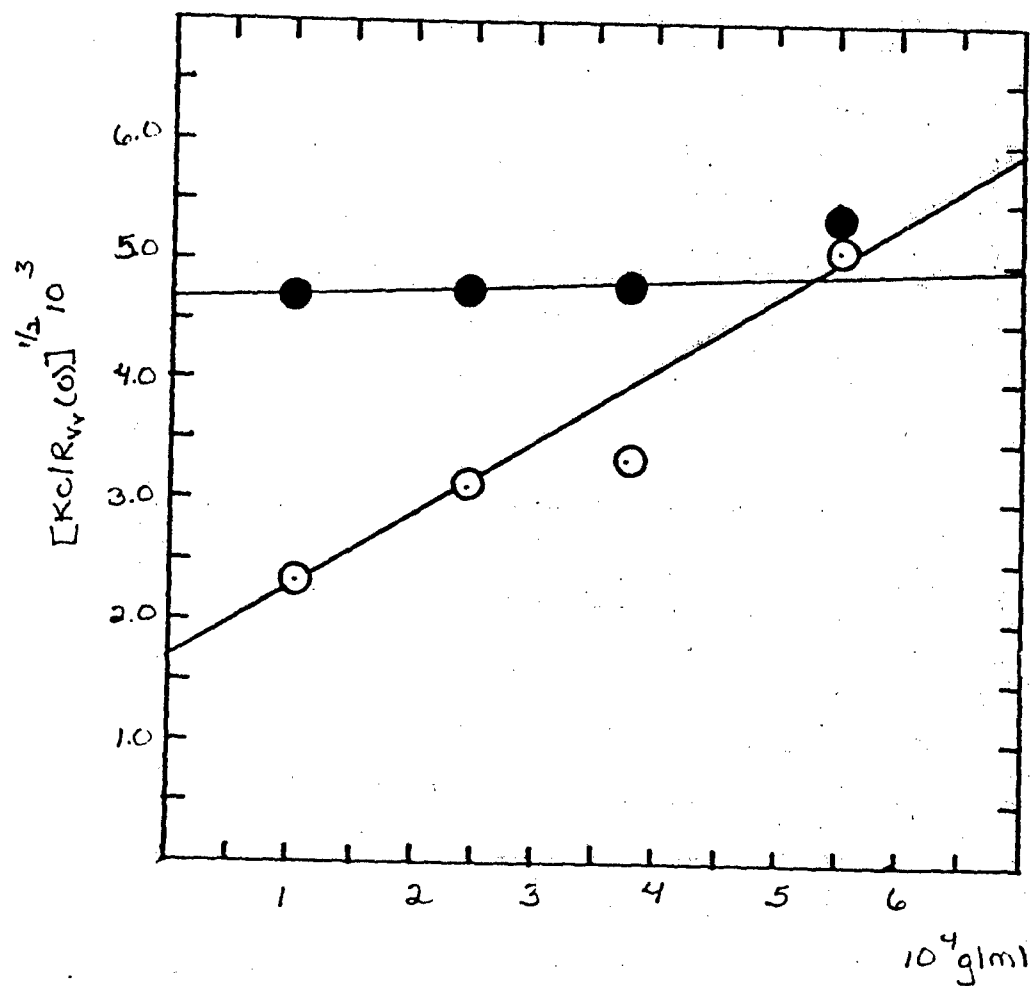25.0°C. O 0.0424 g/dl O-0.0360 g/dl Q 0.0244 g/dl-O 0.0109 g/dl

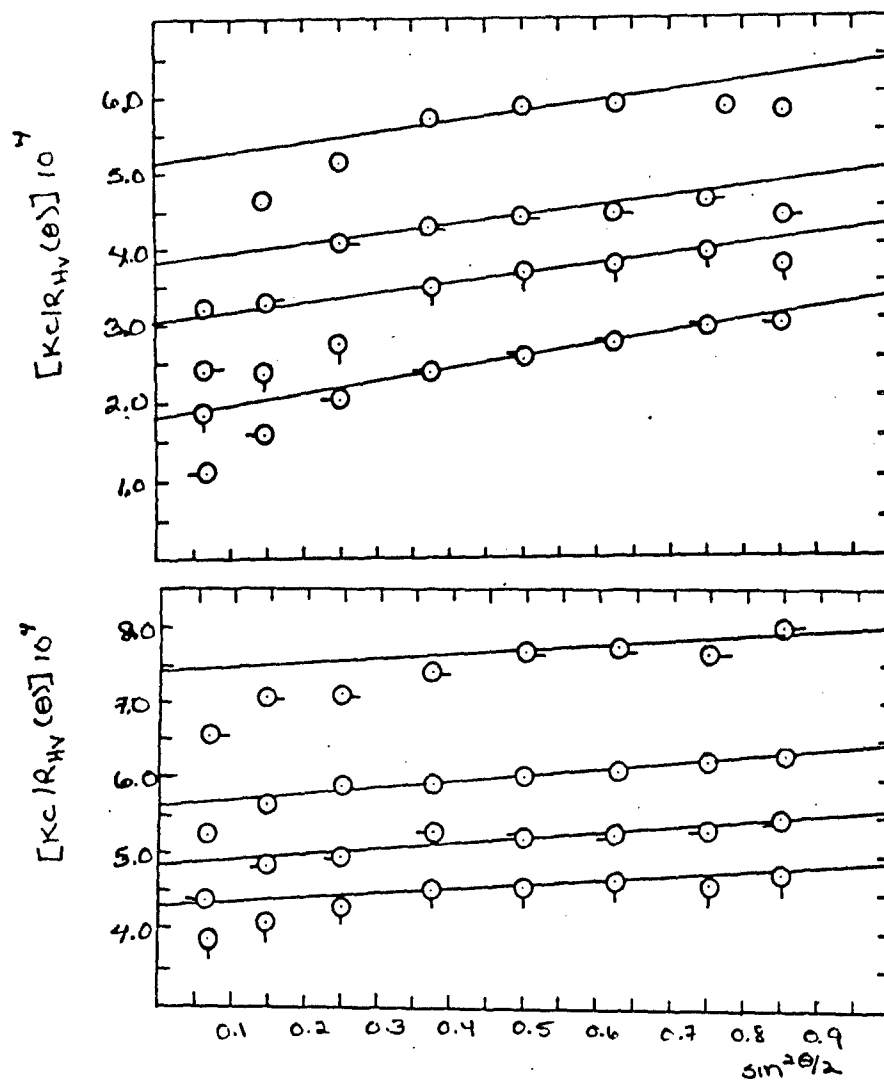**Figure 135:** The concentration dependence of the Hv components of the integrated intensity light scattering of SPBO 4/CSA. O uncentrifuged ● centrifuged sonicated O uncentrifuged ●—centrifuged
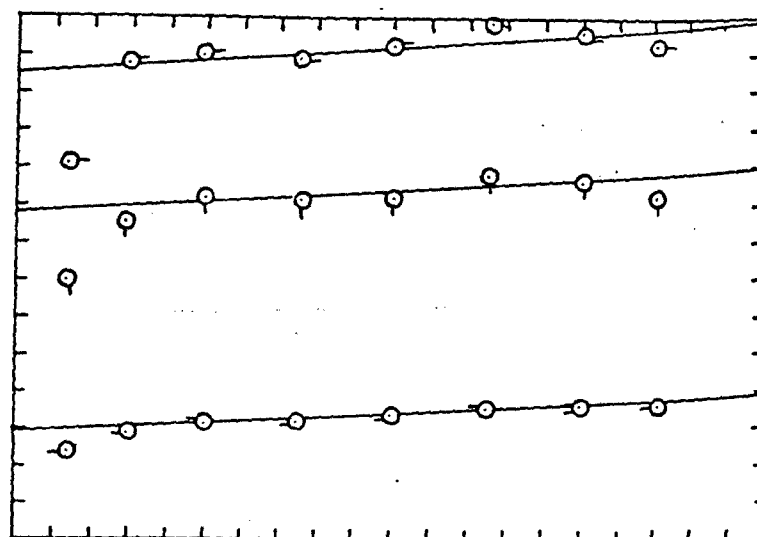
Figure 136: The a)uncentrifuged and b)centrifuged Vv components of the integrated intensity light scattering of sonicated SPBO 4/CSA at 633 nm and 25.0°C. O 0.0424 g/dl O−0.0360 g/dl ∅ 0.0244 g/dl −O 0.0109 g/dl .
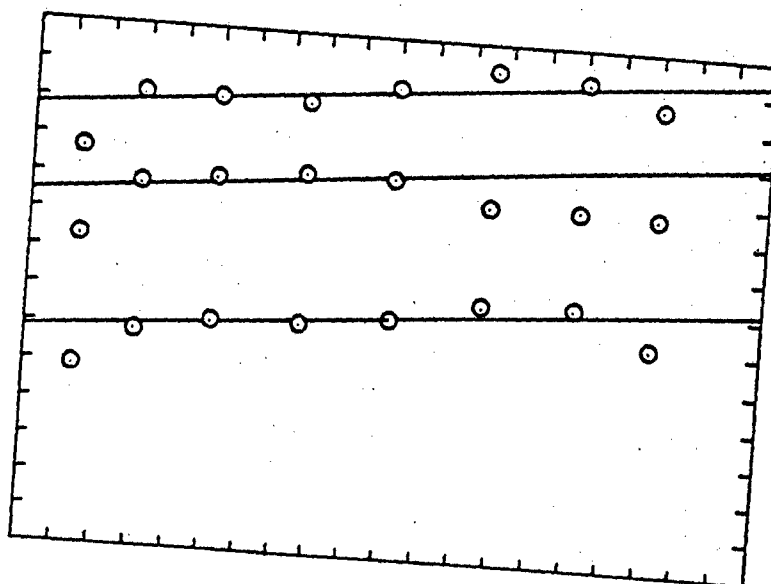
Figure 137: The a)uncentrifuged and b)centrifuged Hv components of the integrated intensity light scattering of sonicated SPBO 4/CSA at 633 nm and 25.0°C. O 0.0424 g/dl O-0.0360 g/dl Q 0.0244 g/dl-O 0.0109 g/dl
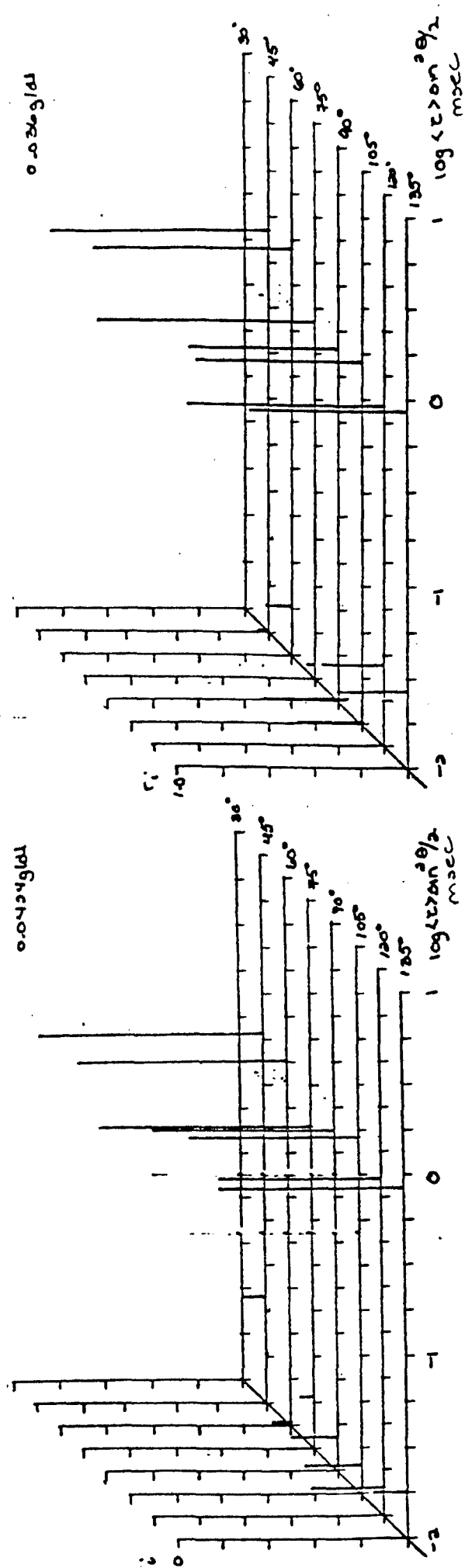
Figure 138: a)The concentration dependence of $\tau_i \sin^2 \theta/2$ of uncentrifuged SPBO-4/CSA
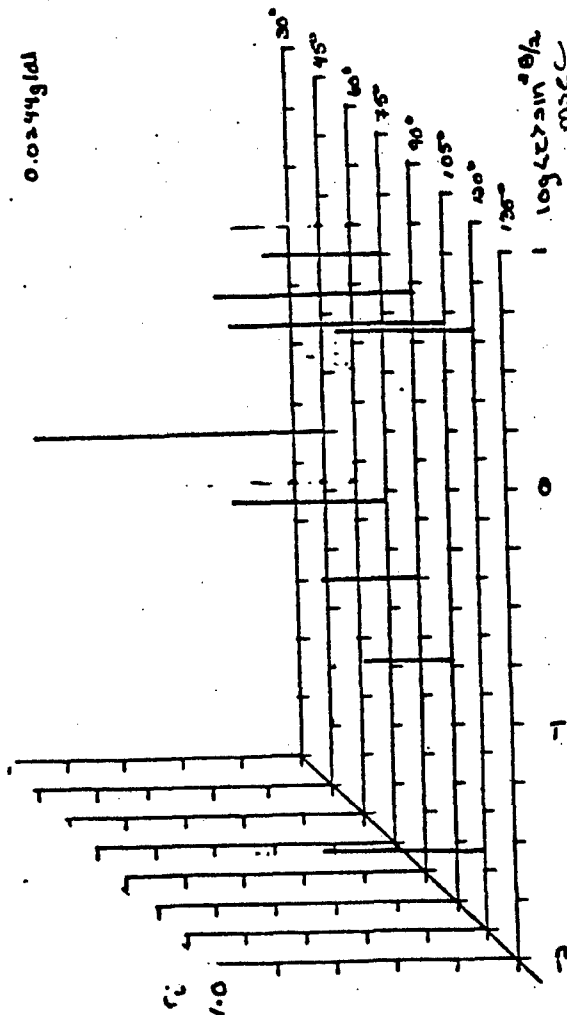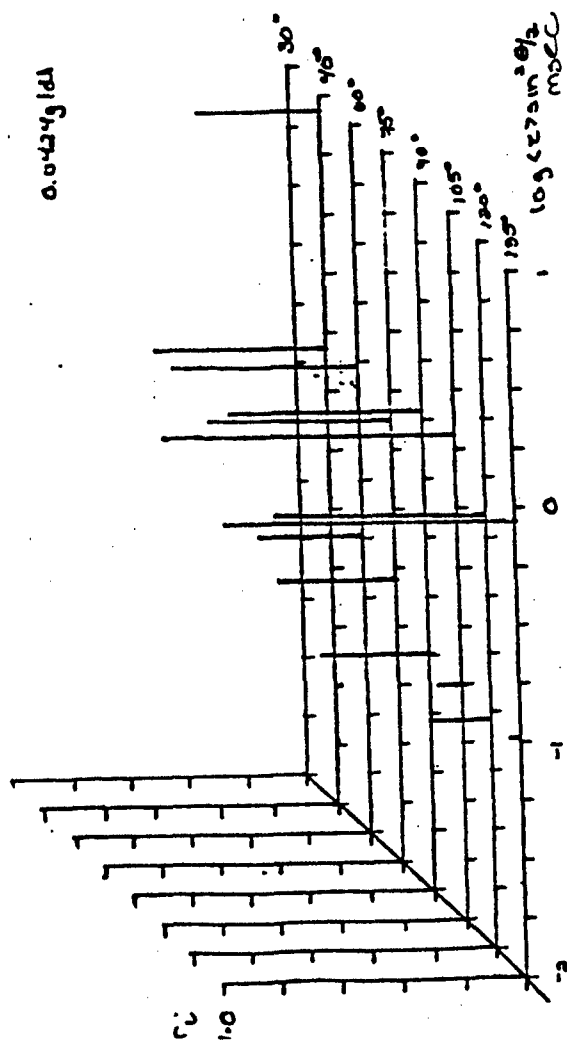
Figure 139: a)The concentration dependence of $\tau_i \sin^2 \theta/2$ of centrifuged SPBO-4/CSA

237
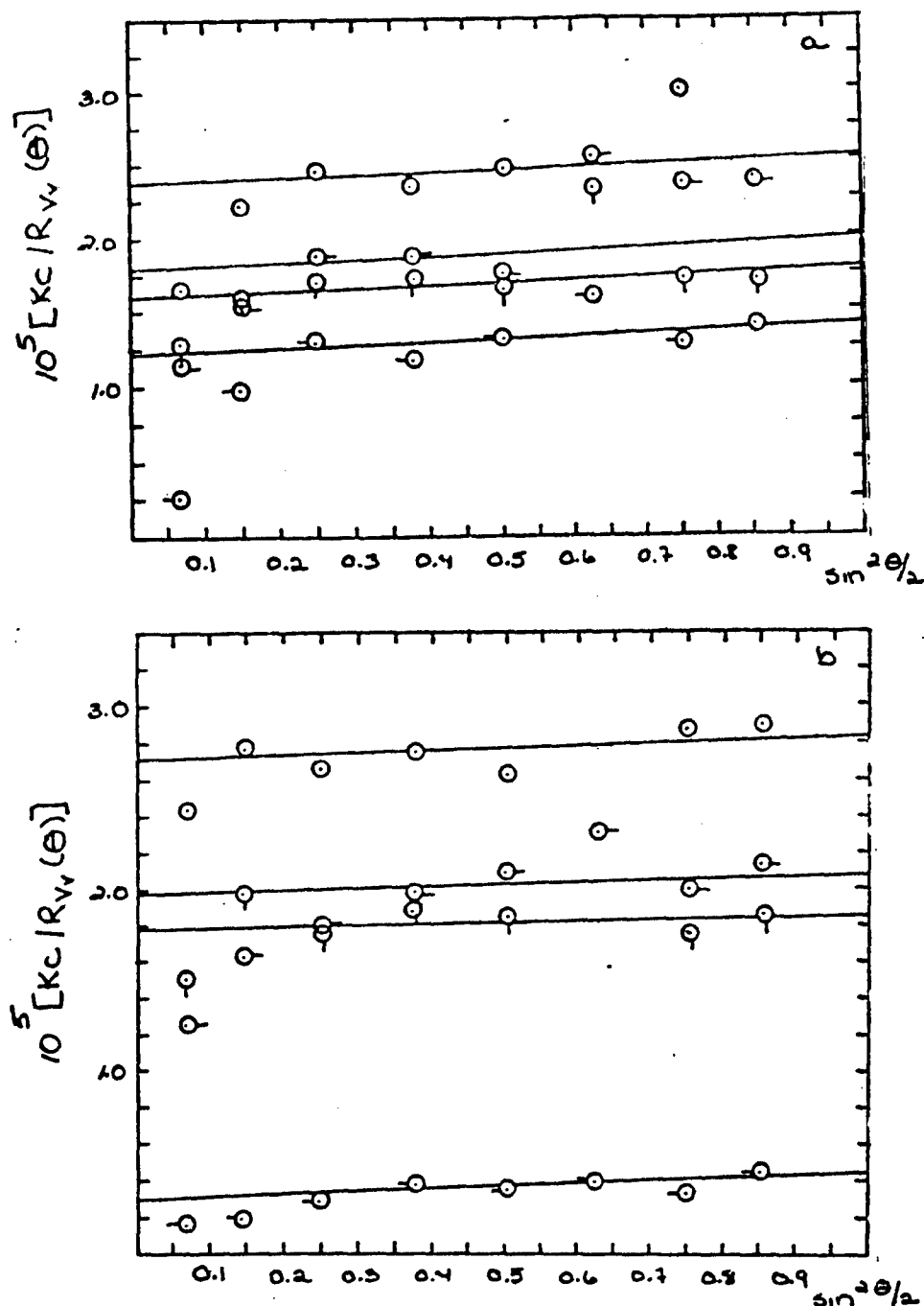
Figure 140: The a)uncentrifuged and b)centrifuged Vv components of the integrated intensity light scattering of SPBO 4/MSA at 514.5 nm and 25.0°C. O 0.0498 g/dl O–0.0376 g/dl ꝙ 0.0246 g/dl–O 0.0097 g/dl
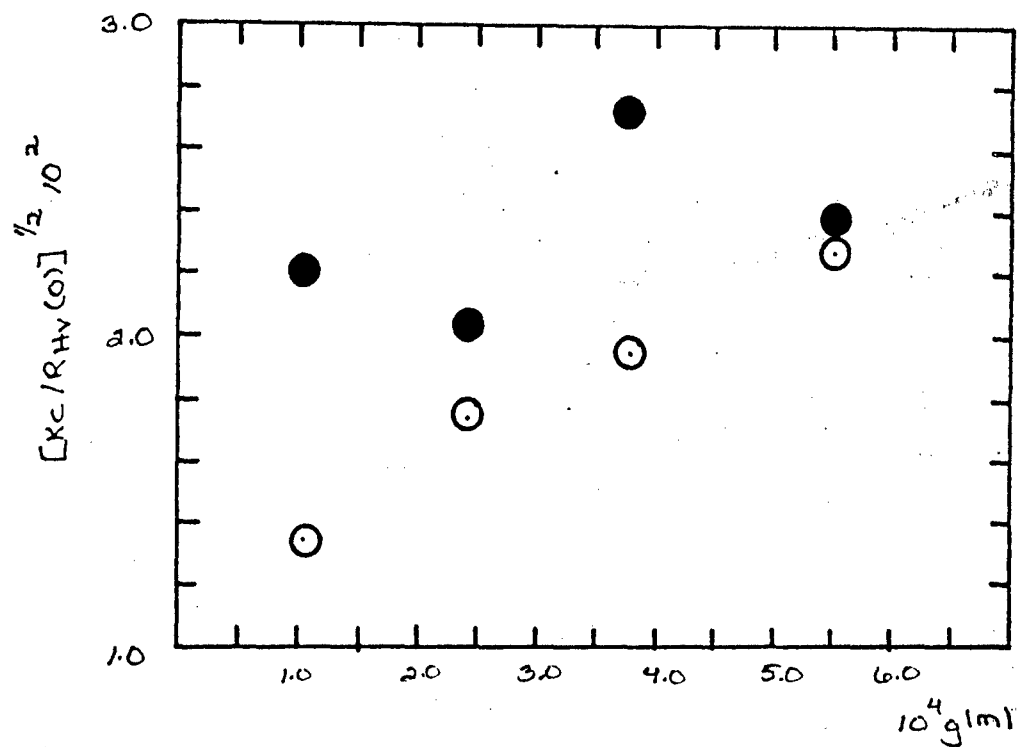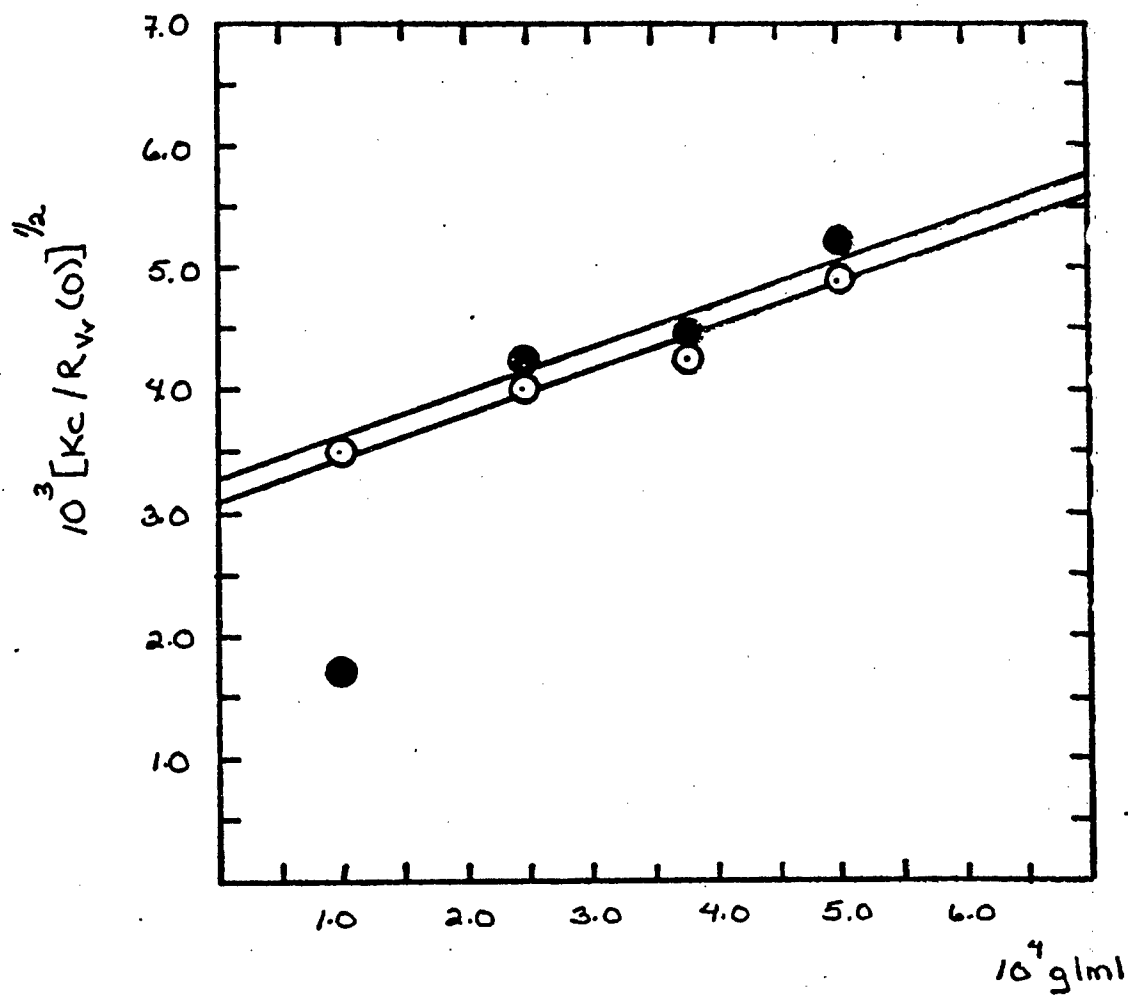
Figure 141: The concentration dependence of the Vv components of the integrated intensity light scattering of SPBO 4/MSA. O uncentrifuged
● centrifuged

Figure 142: a)The concentration dependence of $\tau_i \sin^2 \theta/2$ of uncentrifuged SPBO 4/MSA

240
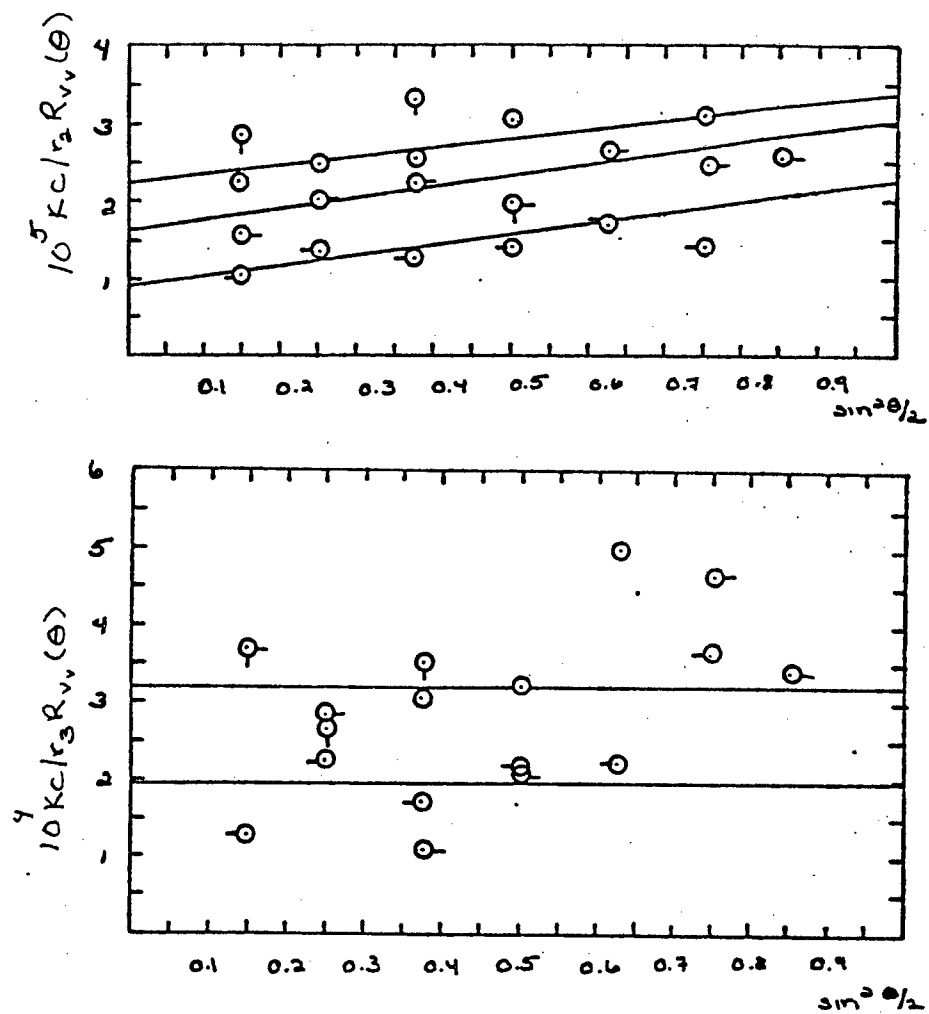
Figure 143:   The angular dependence for the uncentrifuged components of the Vv AILS of SPBO-4/MSA. O   0.0498g/dl   O- 0.0376 g/dl   Q   0.0246 g/dl O 0.0097g/dl
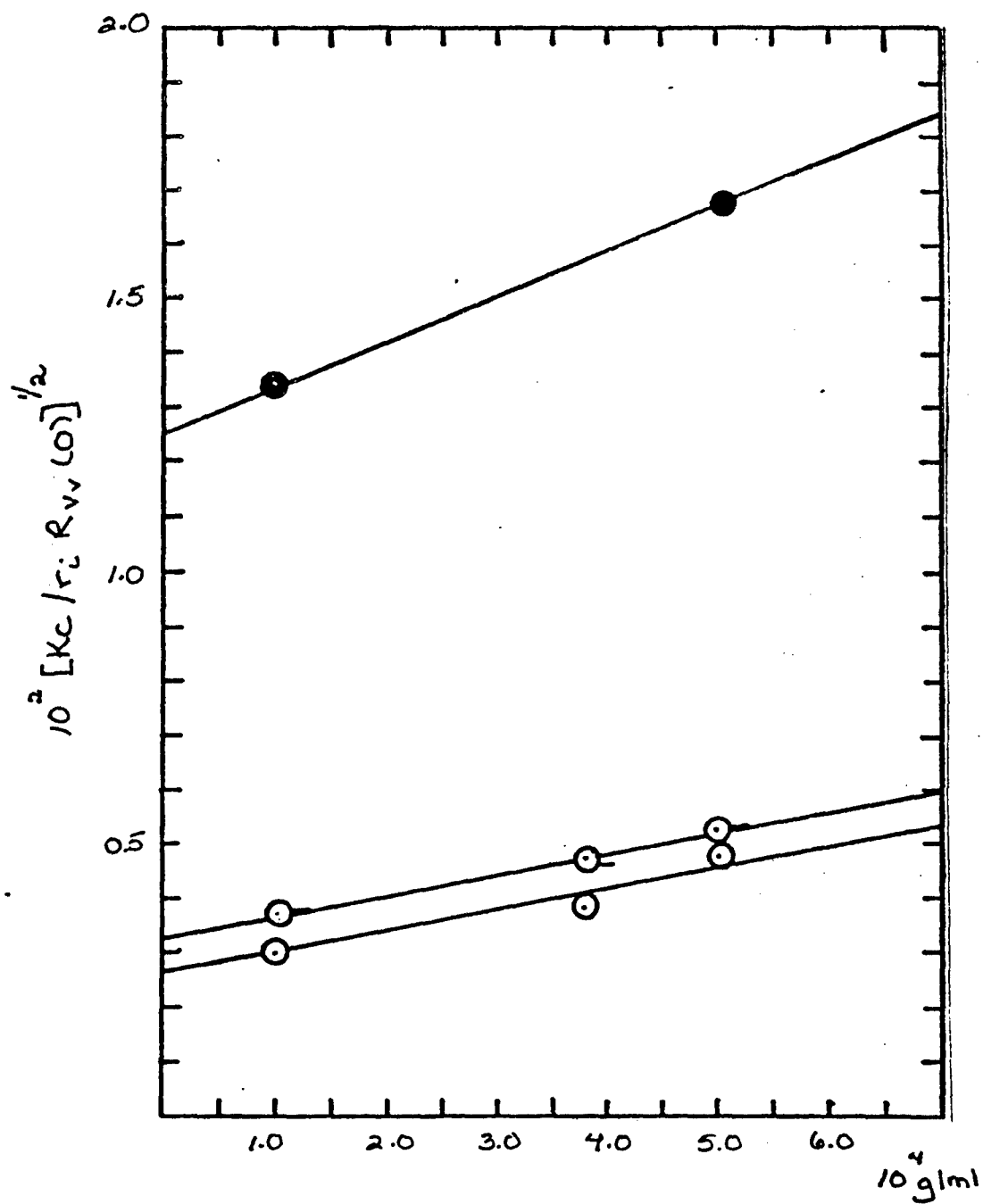
Figure 144 : The concentration dependence of the Vv components of the integrated
intensity light scattering of SPBO-4/MSA. O r_2 uncentrifuged
O-r_2 centrifuged ● r_3 uncentrifuged
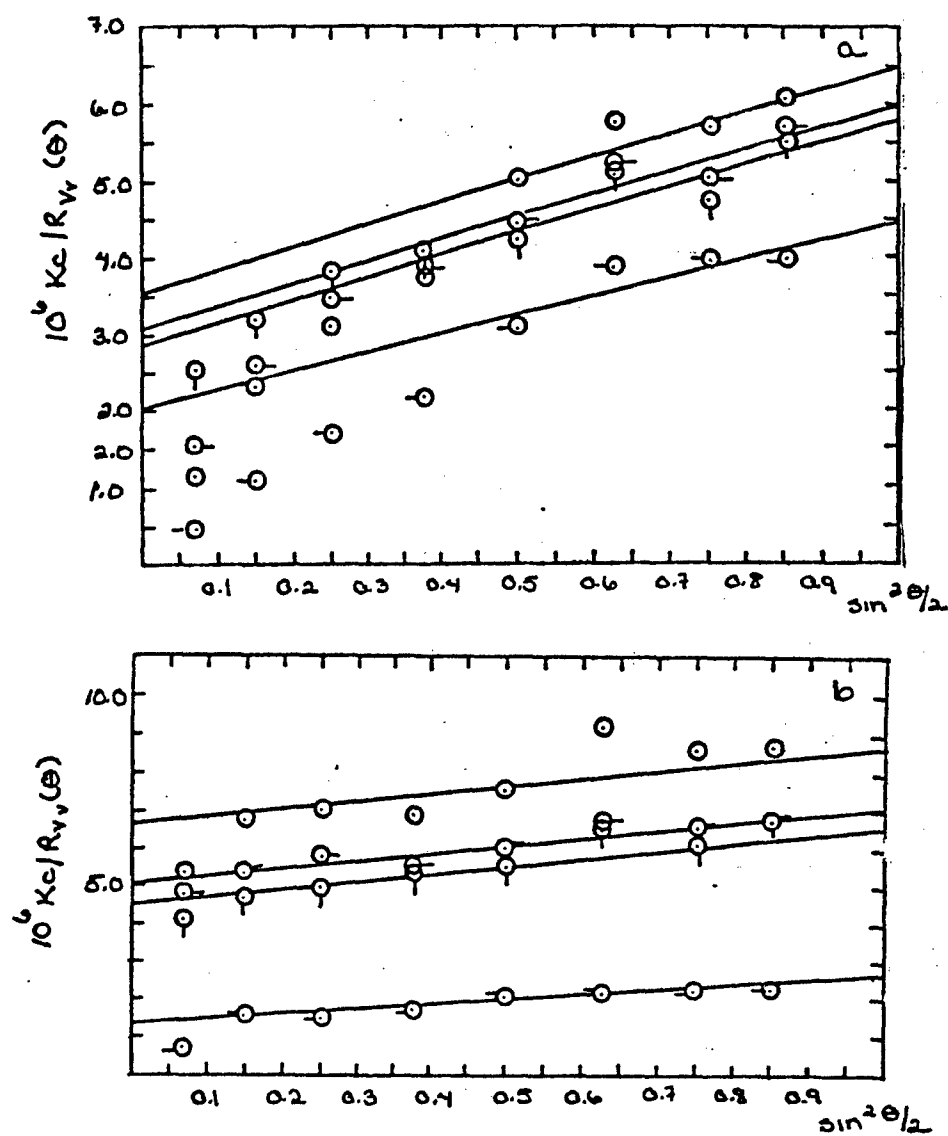
Figure 145: The a)uncentrifuged and b)centrifuged Vv components of the integrated intensity light scattering of SPBO 96/MSA at 514.5 nm and 25.0°C. O 0.0487 g/dl O–0.0389 g/dl Q 0.0236 g/dl–O 0.0092 g/dl

243
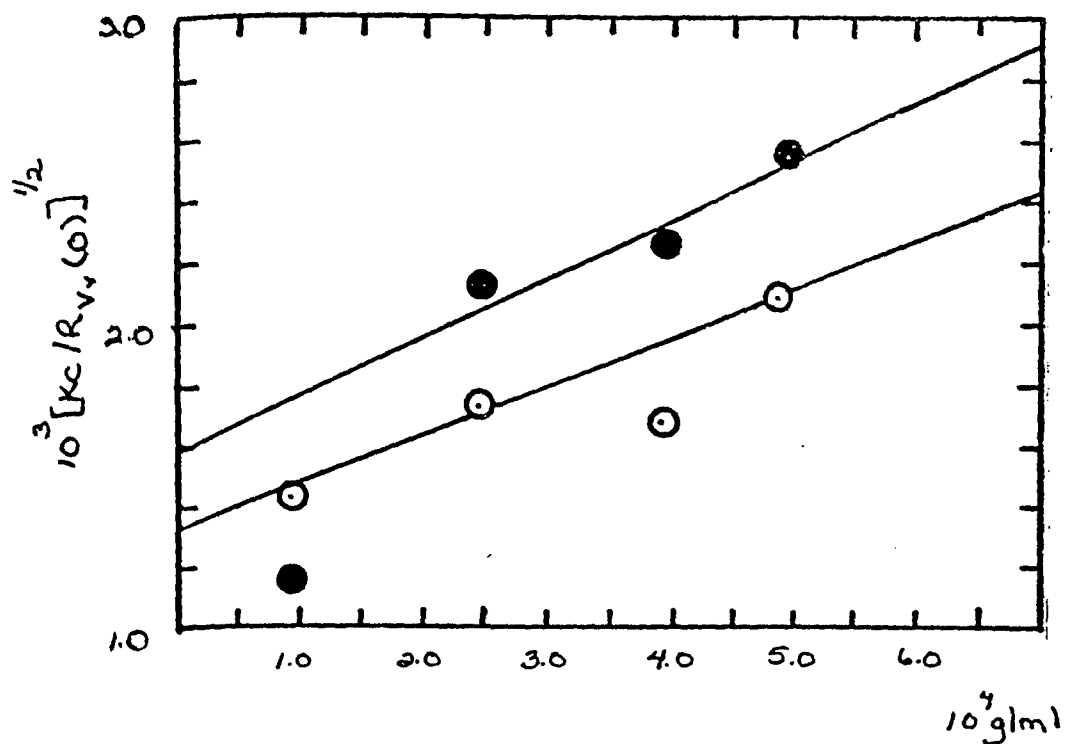
Figure 146: The concentration dependence of the Vv components of the integrated intensity light scattering of SPBO 96/MSA. O uncentrifuged ● centrifuged
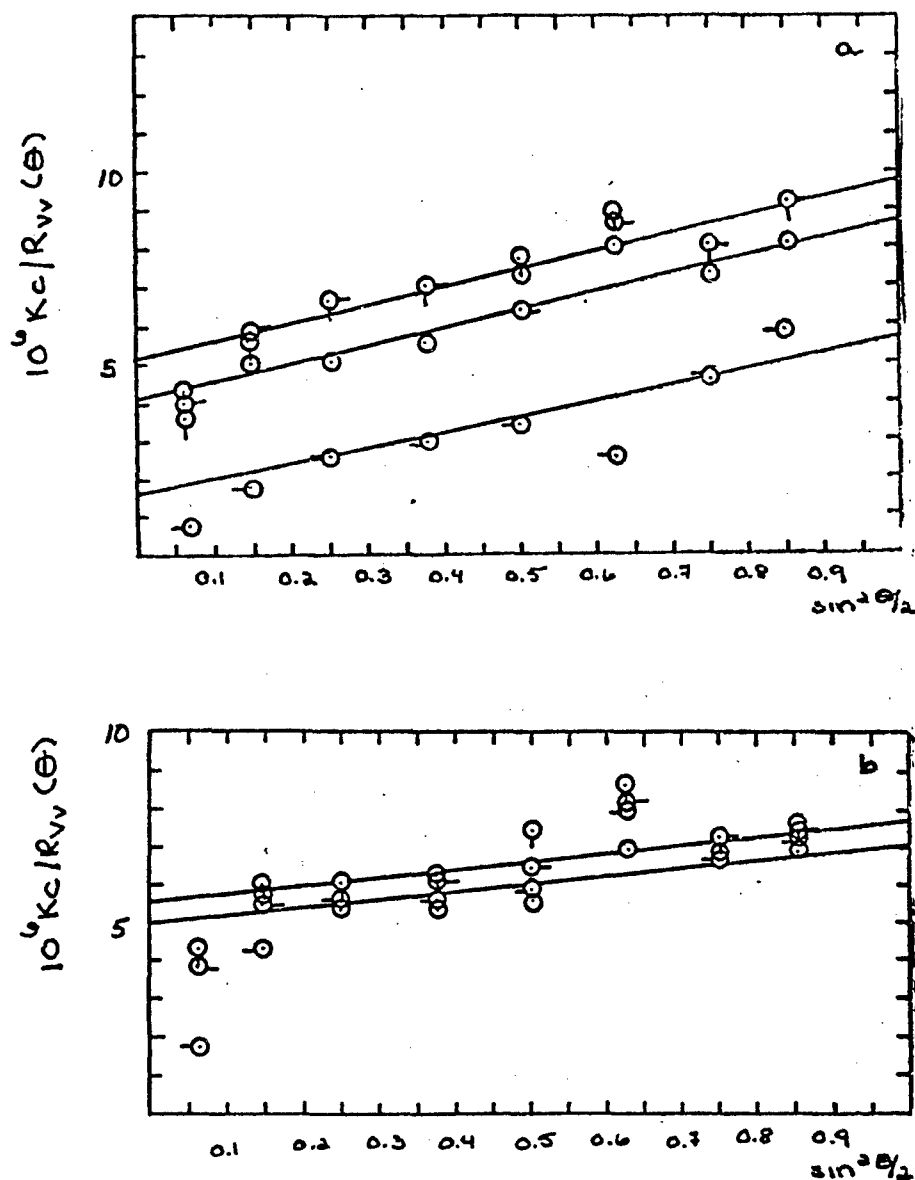
Figure 147: The a)uncentrifuged and b)centrifuged Vv components of the integrated intensity light scattering of sonciated SPBO-96/MSA at 514 nm and 25.0°C. O 0.0487 g/dl O-0.0389 g/dl Q 0.0236 g/dl-O 0.0092 g/dl
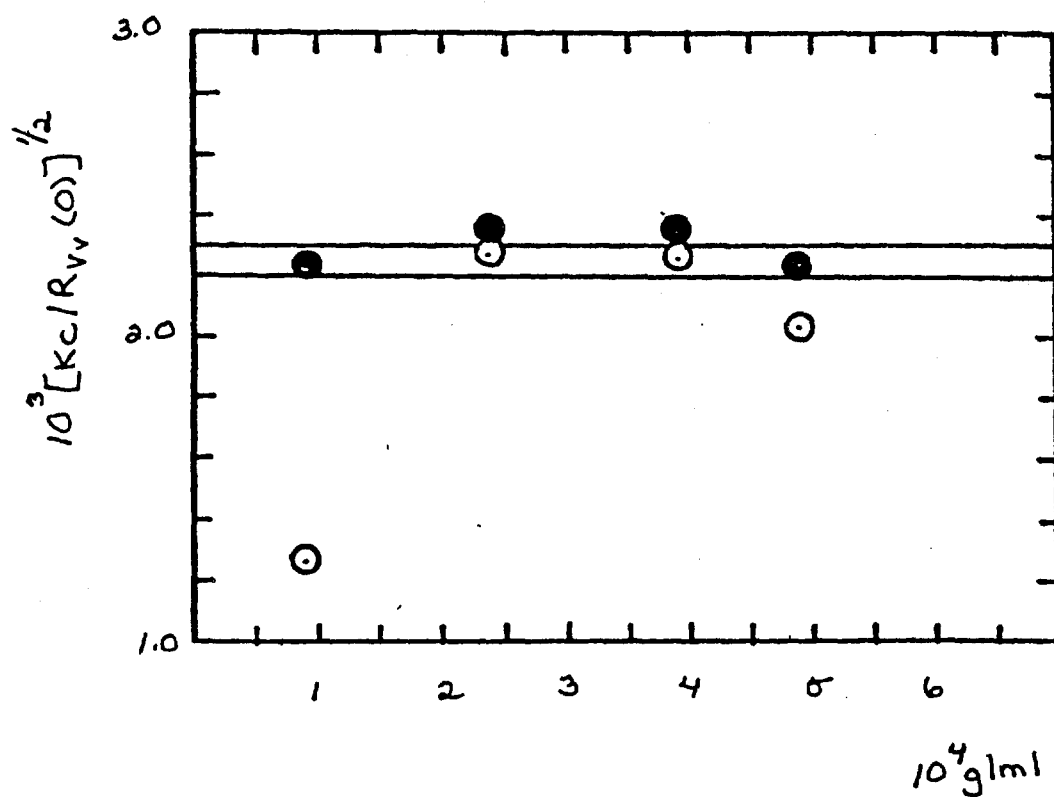
Figure 148: The concentration dependence of the Vv components of the integrated intensity light scattering of sonicated SPBO-96/MSA O uncentrifuged ● centrifuged
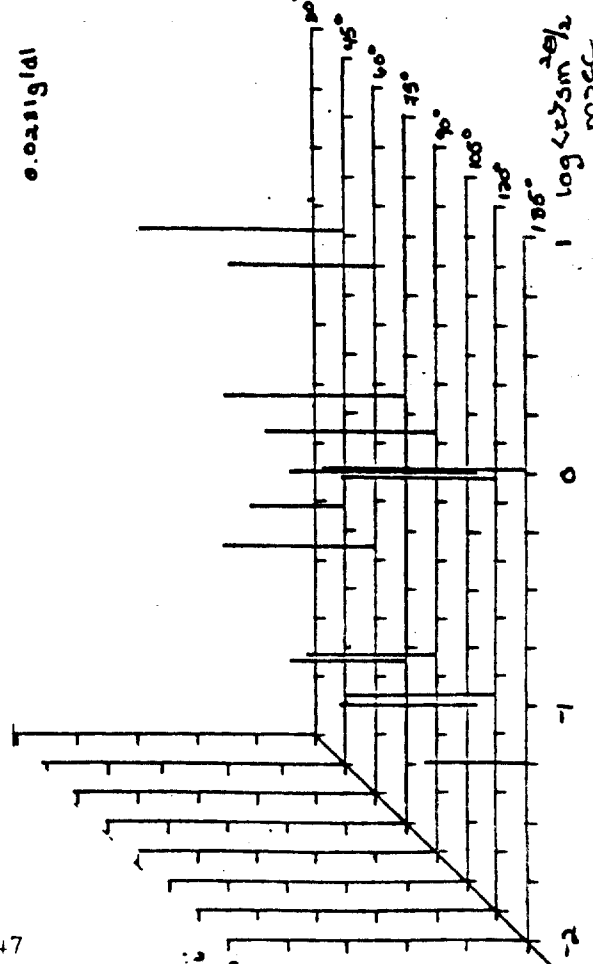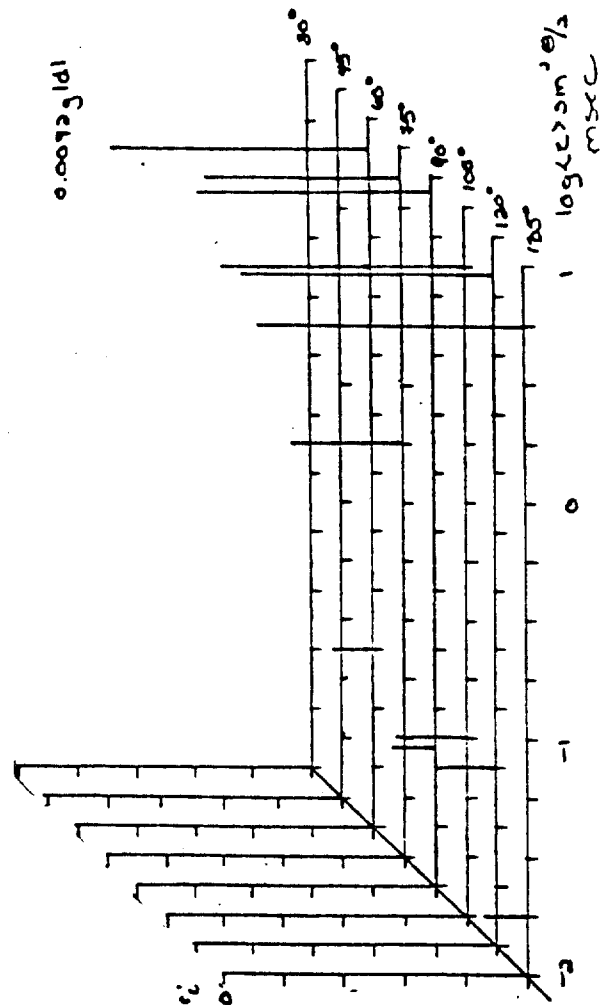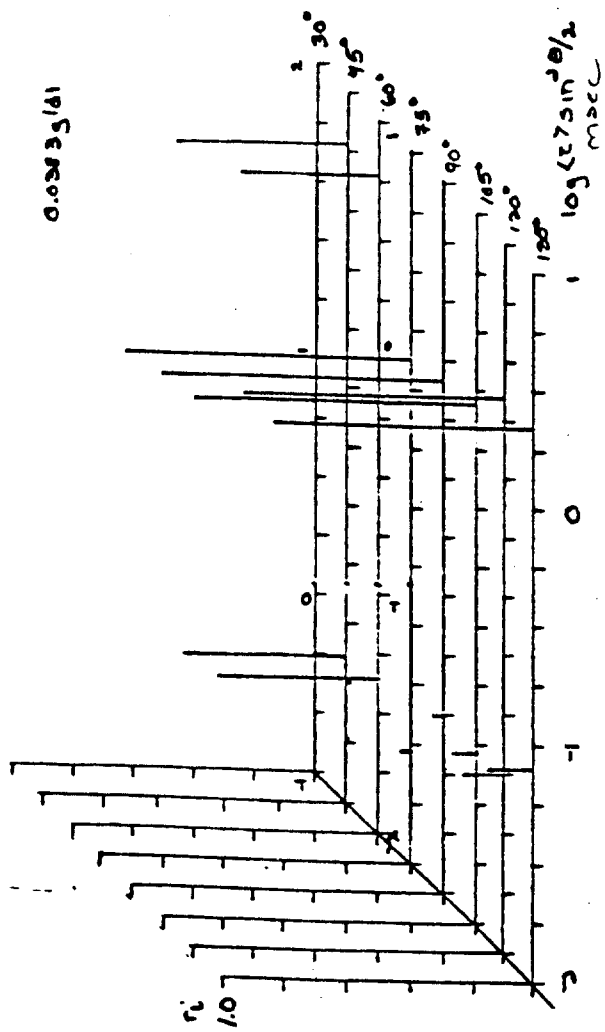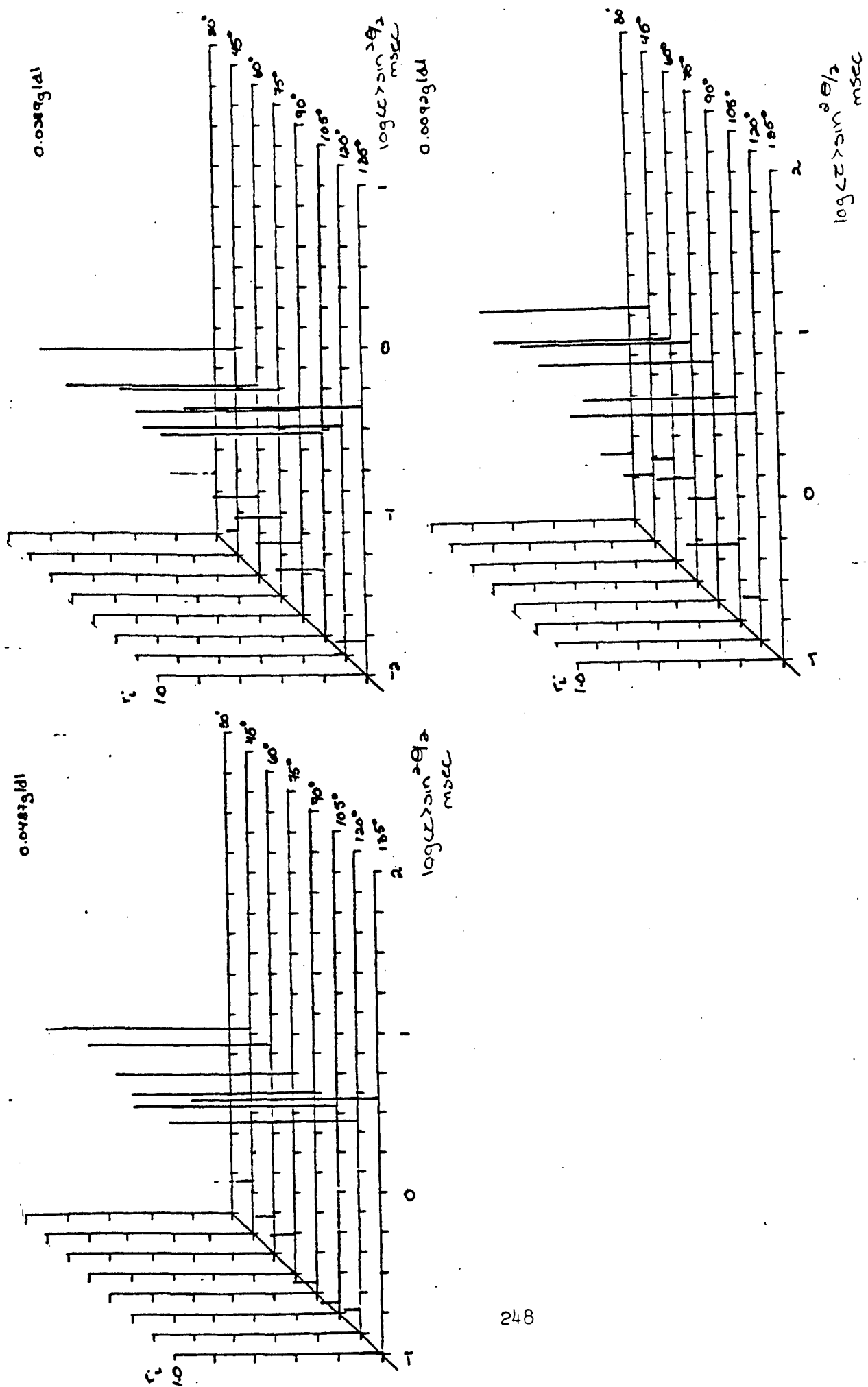
Figure 150 : a)The concentration dependence of $r_i \sin^2 \theta/2$ of centrifuged SPBO 96/MSA

248
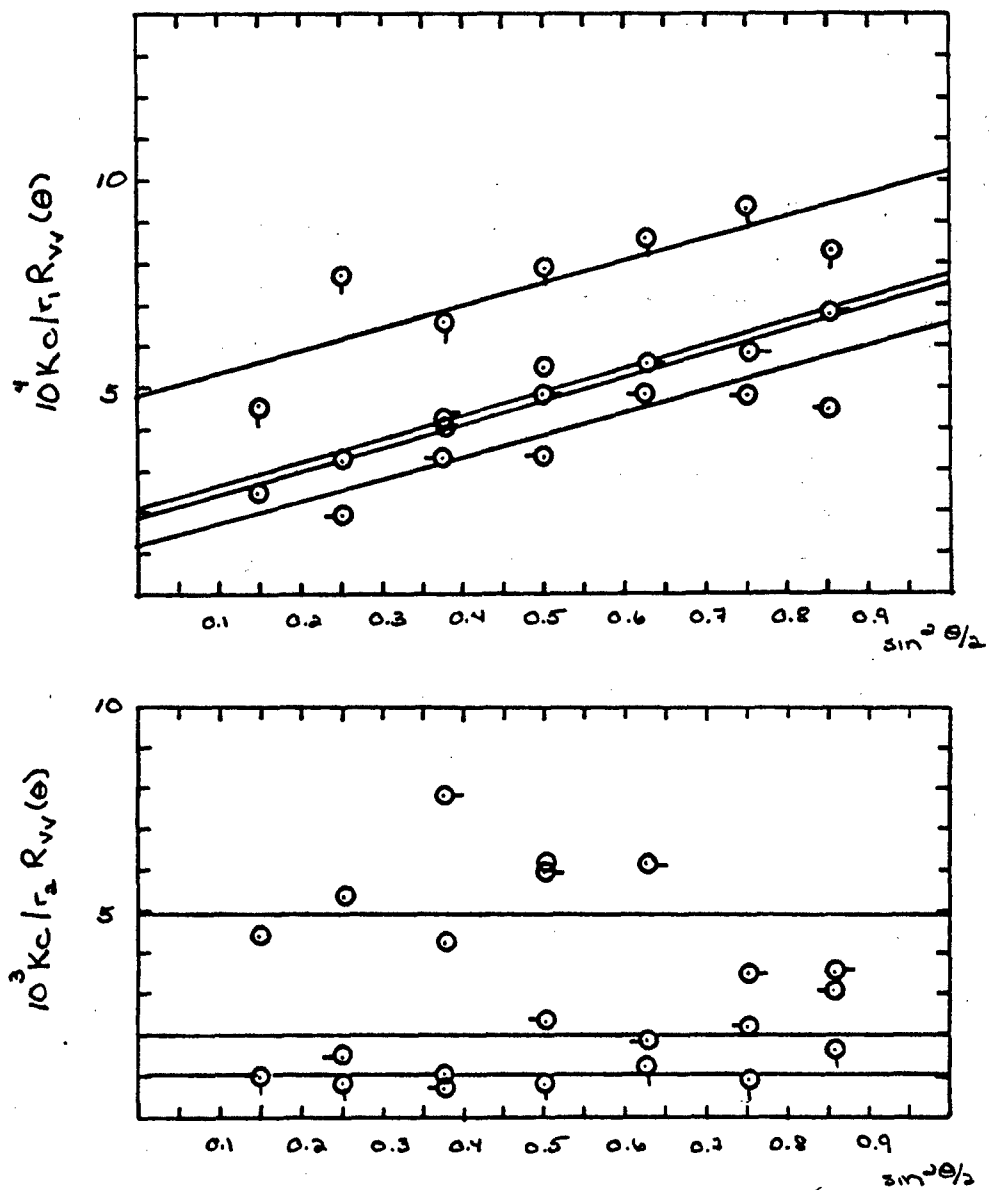
Figure 151: The angular dependence for the uncentrifuged components of the Vv AILS of SPBO-96. O 0.0487g/dl O- 0.0389 g/dl Q 0.0236 g/dl
-O 0.0092g/dl
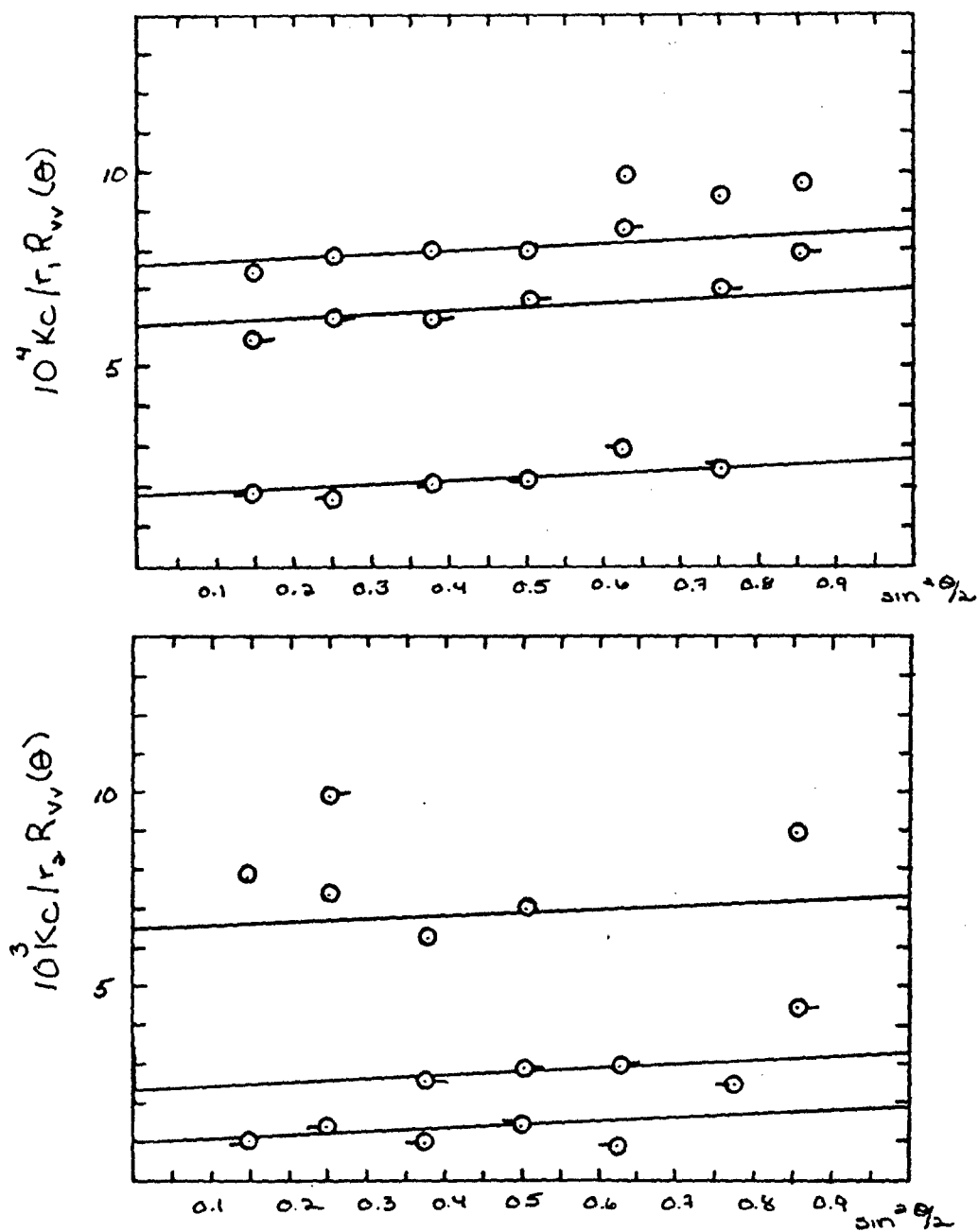
Figure 152: The angular dependence for the centrifuged components of the Vv AILS of SPBO-96. O 0.0487g/dl O- 0.0389 g/dl Q 0.0236 g/dl -O 0.0092g/dl
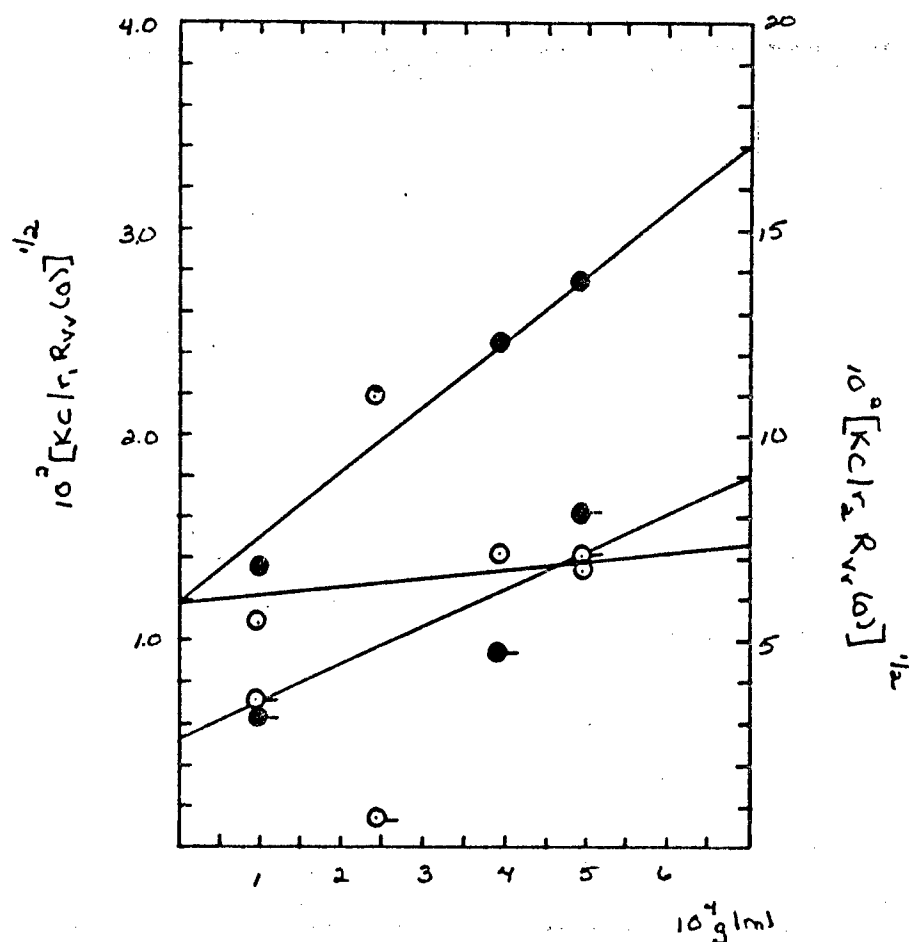
Figure 153: The concentration dependence of the Vv components of the integrated intensity light scattering of SPBO-96. O r_2 uncentrifuged ● r_2 centrifuged O-r_3 uncentrifuged ●-r_3 centrifuged
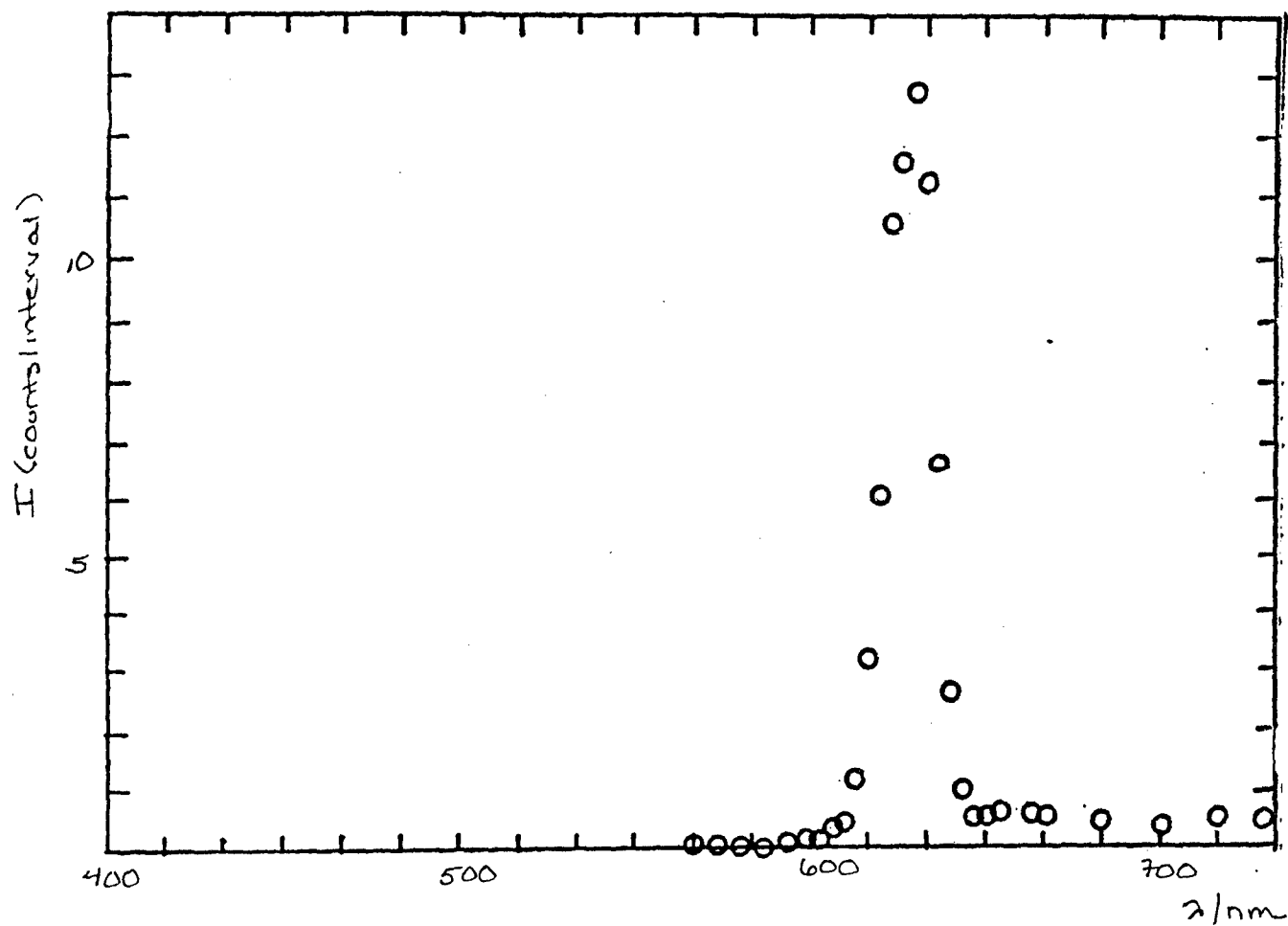
Figure 154:   Vv scattering and Vv emission spectra for SPBO–39/MSA excited at 633 nm and 25.0°C.
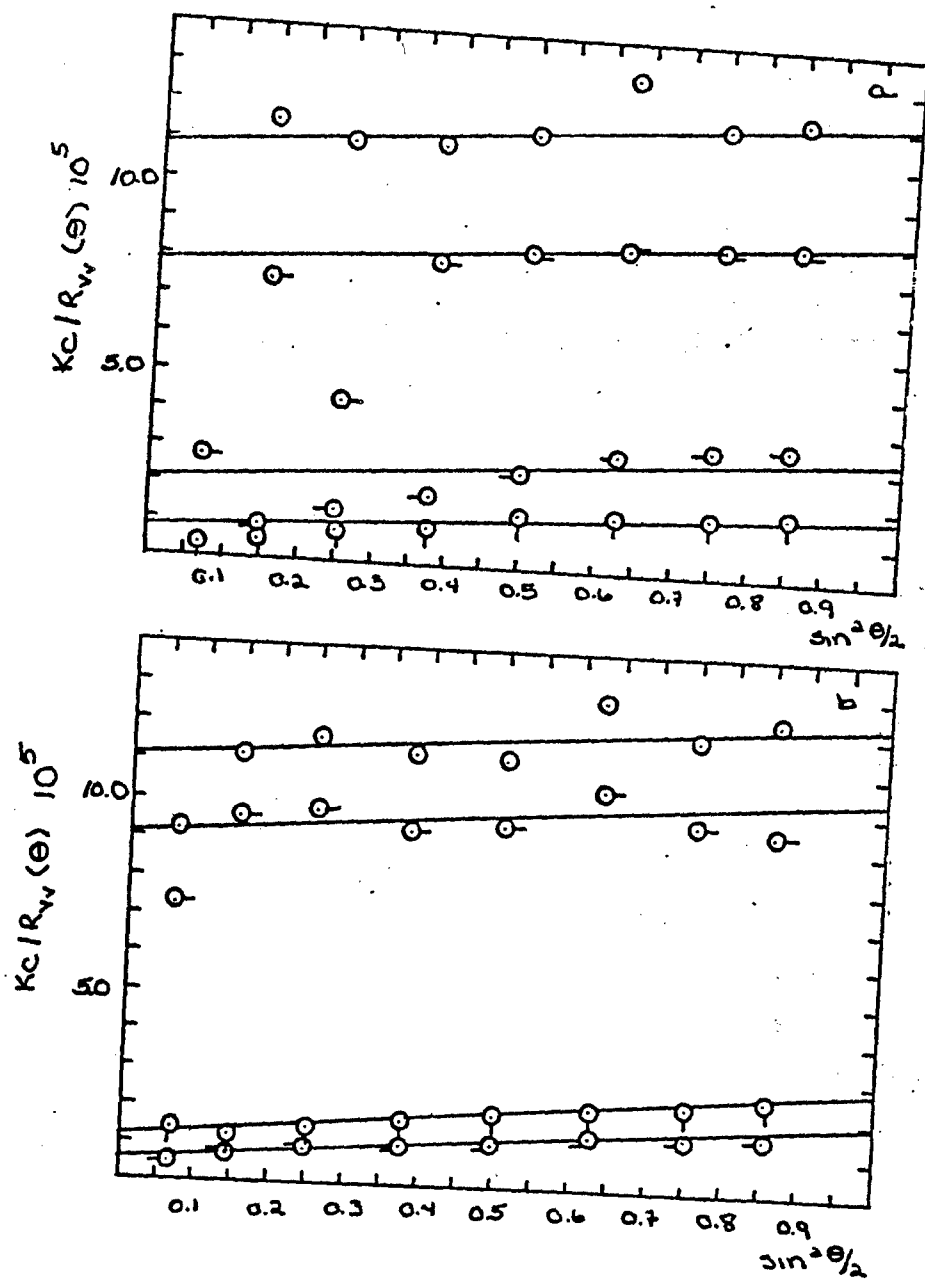
Figure 155: The a)uncentrifuged and b)centrifuged Vv components of the integrated intensity light scattering of SPBO 39/MSA at 633 nm and 25.0°C. O 0.0494 g/dl O–0.0383 g/dl Q 0.0204 g/dl–O 0.0106 g/dl
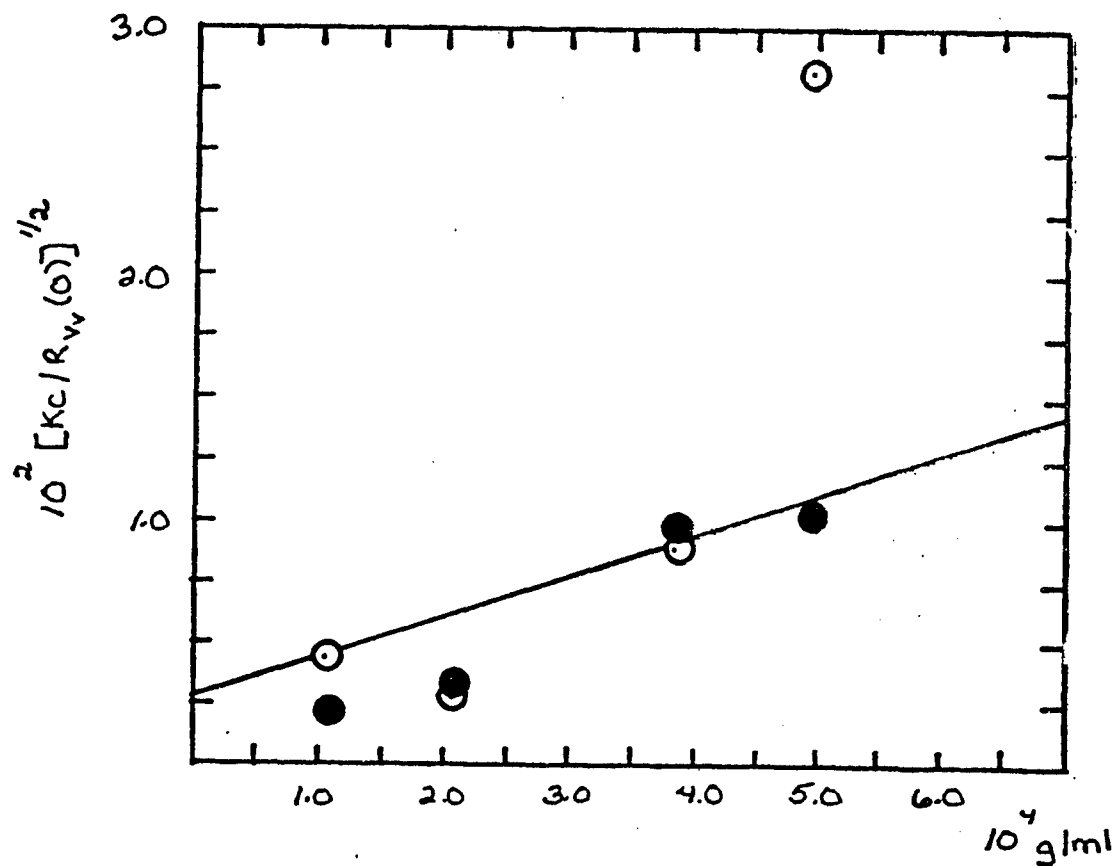
Figure 156: The concentration dependence of the Vv components of the integrated intensity light scattering of SPBO 39/MSA. O uncentrifuged
● centrifuged
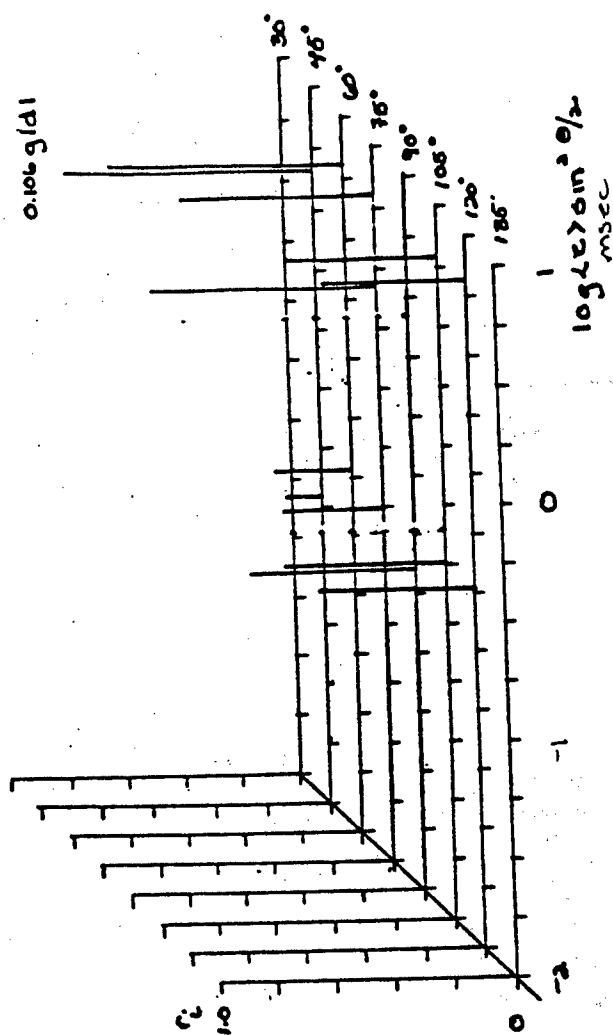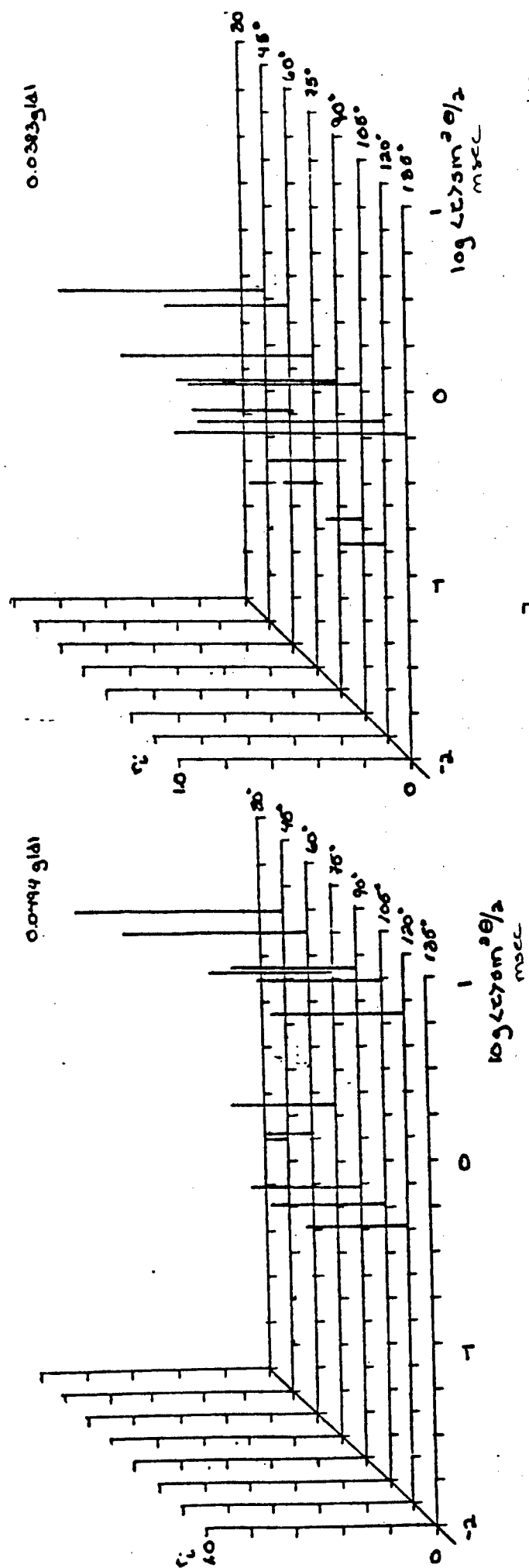
Figure 157: a)The concentration dependence of $\tau_i \sin^2 \theta/2$ of uncentrifuged SPBO 39/MSA

255
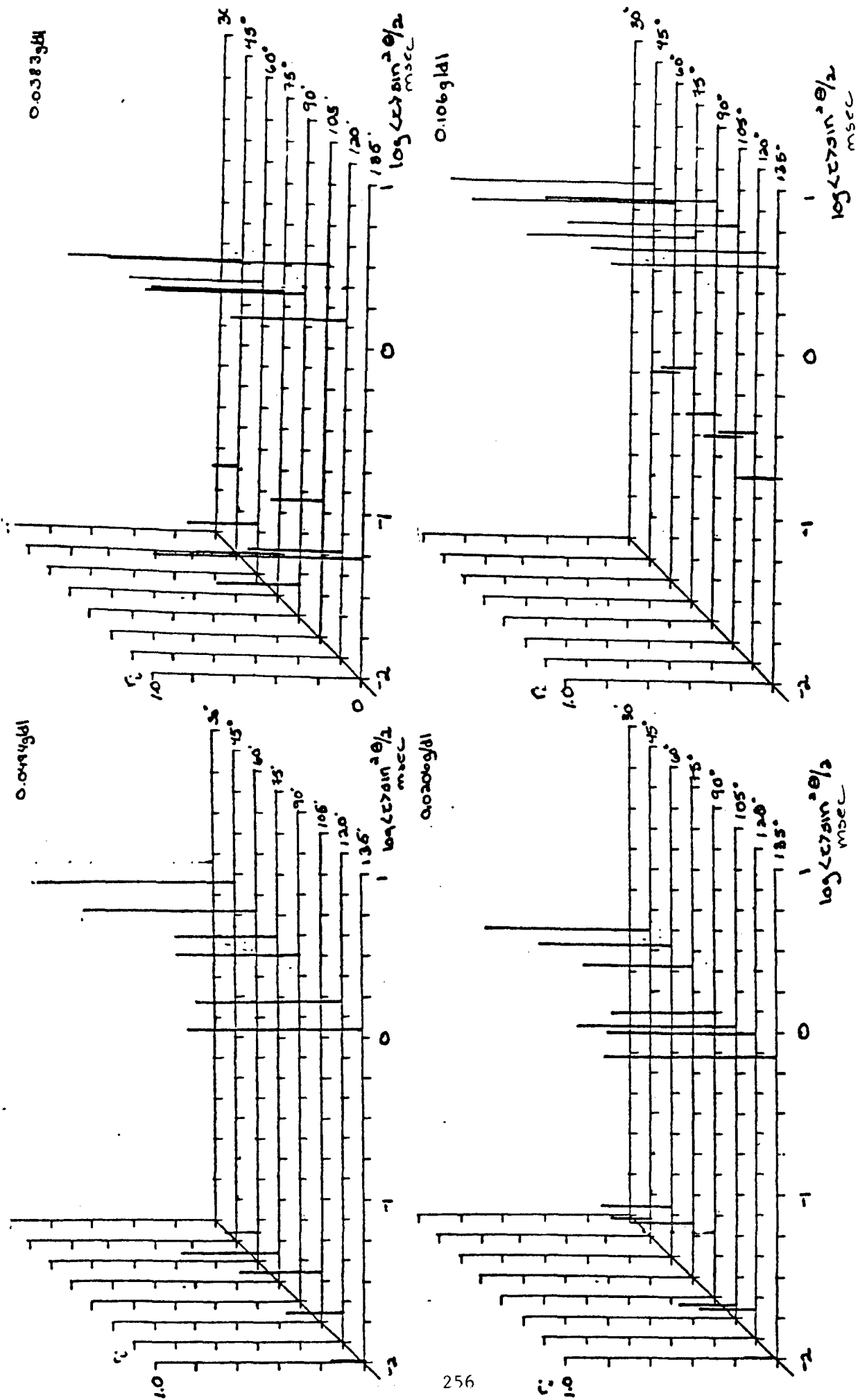
Figure 158: a)The concentration dependence of $\tau_i \sin^2 \theta/2$ of centrifuged SPBO 39/MSA.

256
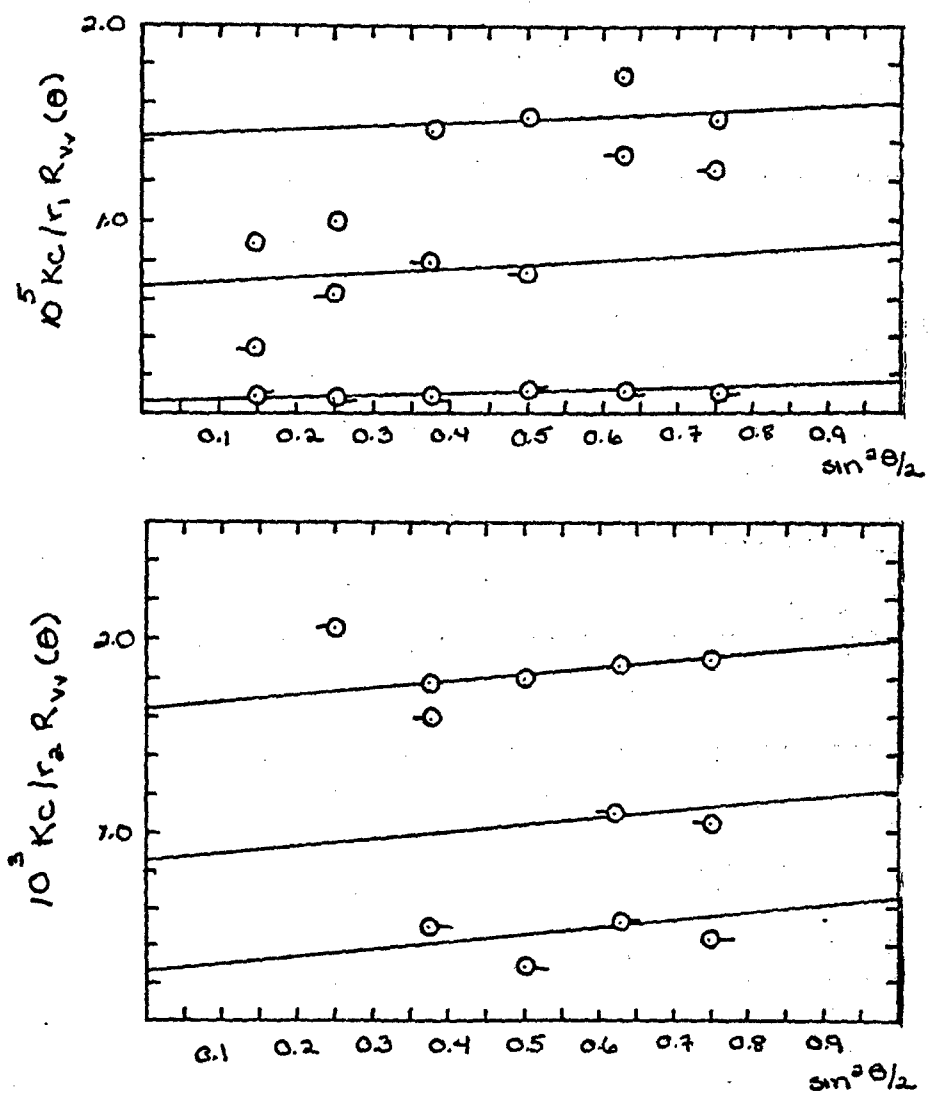
Figure 159: The angular dependence for the uncentrifuged components of the Vv AlLS of SPBO-39/MSA. O 0.0494g/dl O- 0.0383 g/dl Q 0.0204 g/dl -O 0.0106g/dl
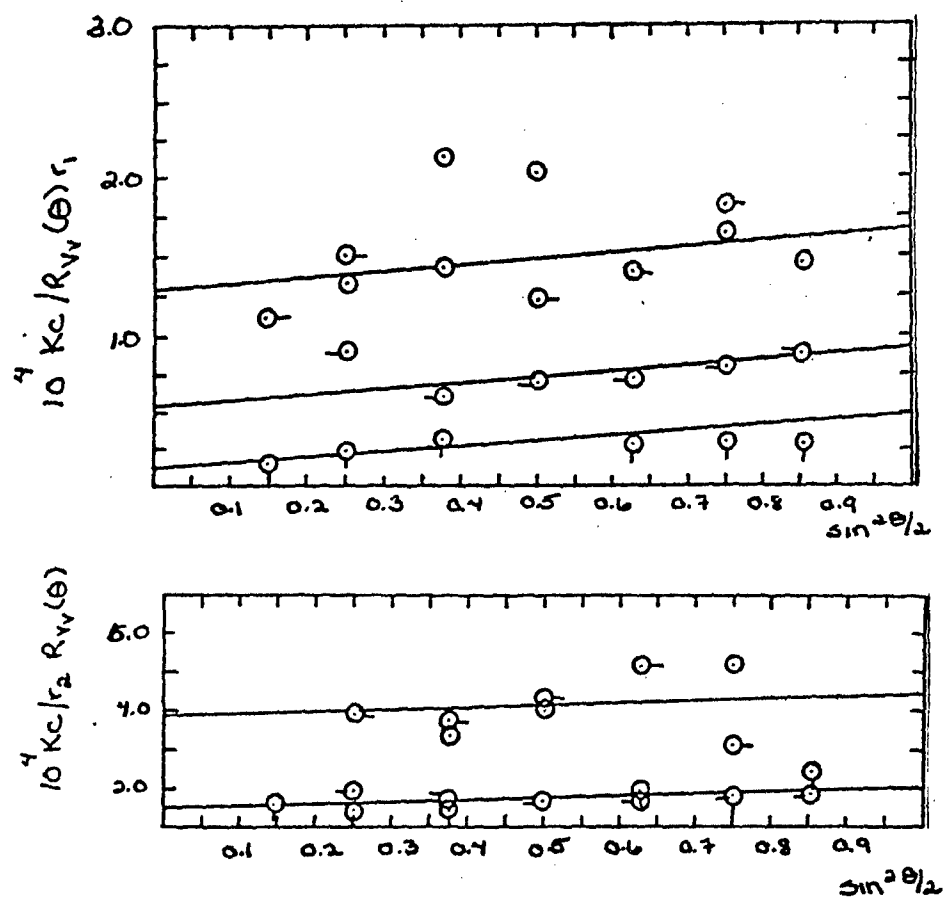
Figure 160: The angular dependence for the centrifuged components of the Vv AILS of SPBO–39/MSA. O   0.0494g/dl   O– 0.0383 g/dl   Q   0.0204 g/dl –O 0.0106g/dl
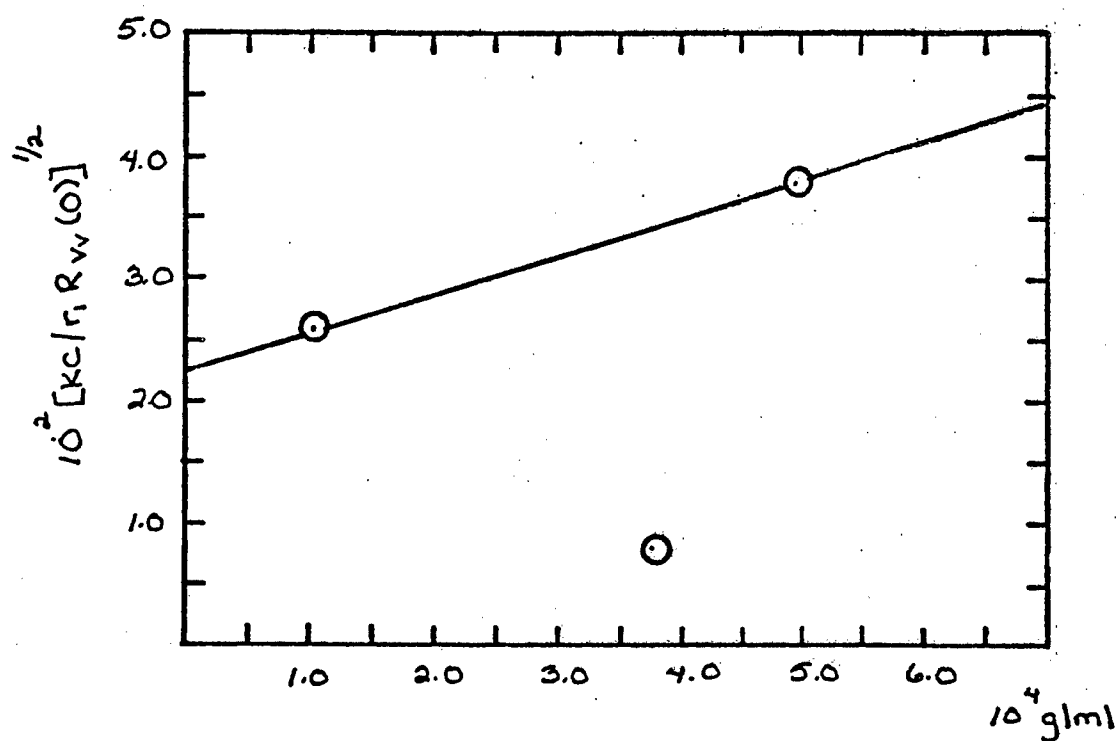
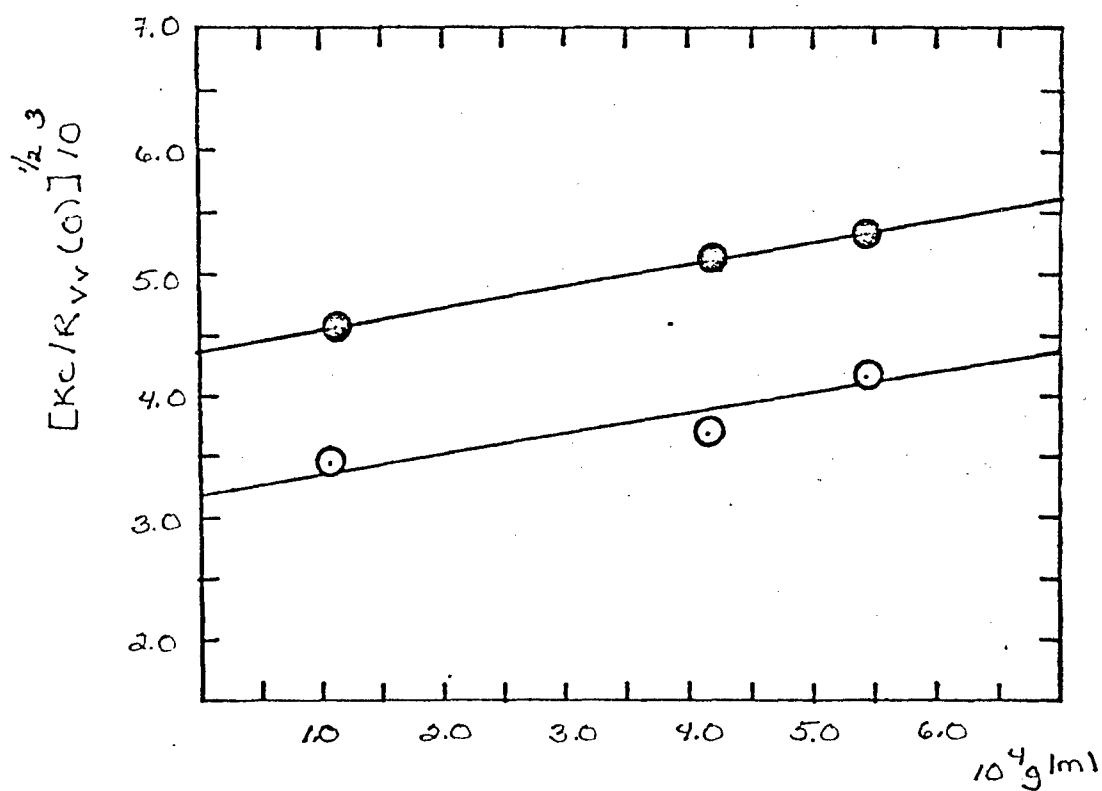**Figure** 161: The concentration dependence of the Vv components of the integrated intensity light scattering of SPBO-39/MSA. O r_2 uncentrifuged
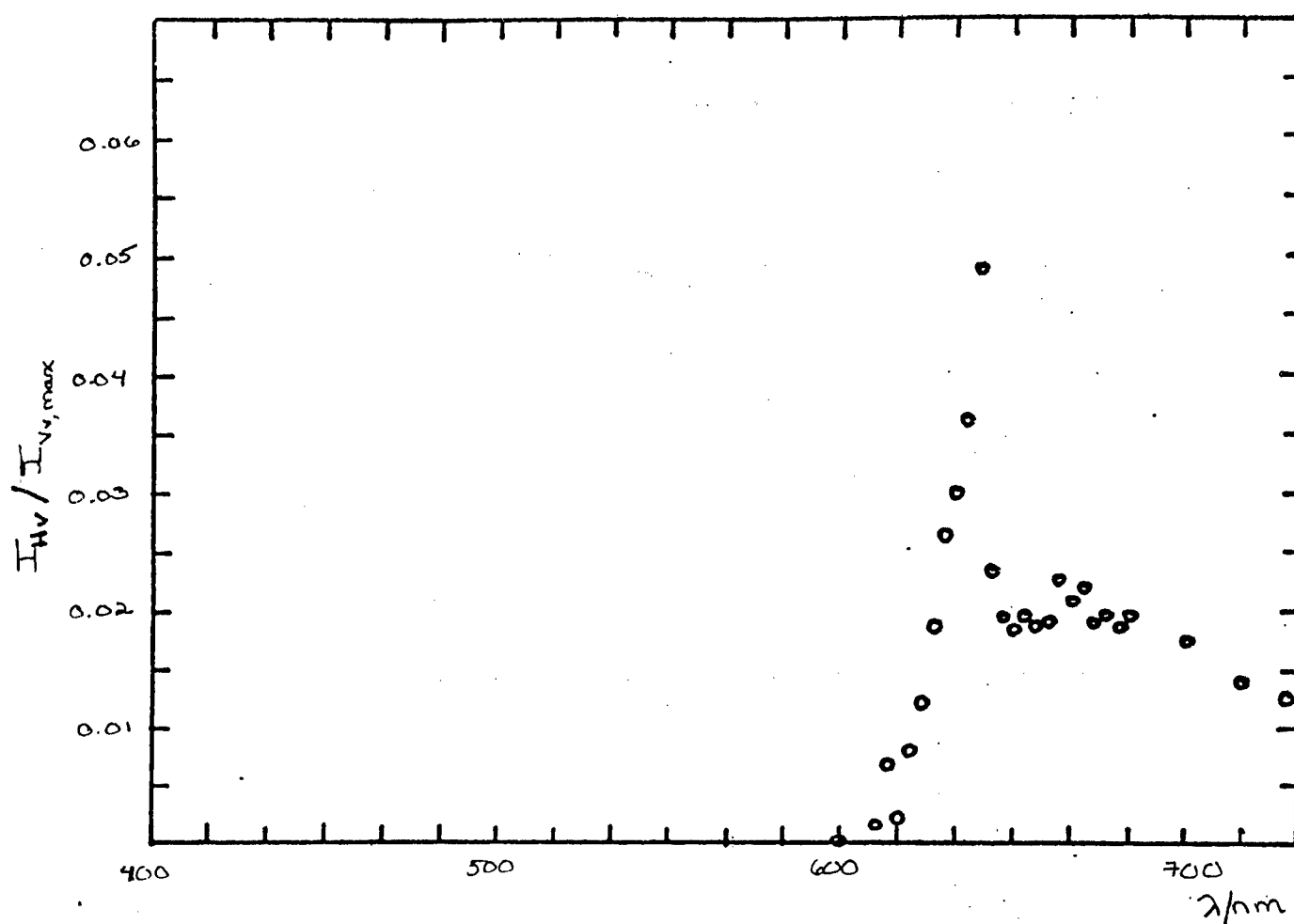
Figure 162: . Hv scattering and Hv emission spectra for SPBO−80 excited at 633 nm and 25.0°C.
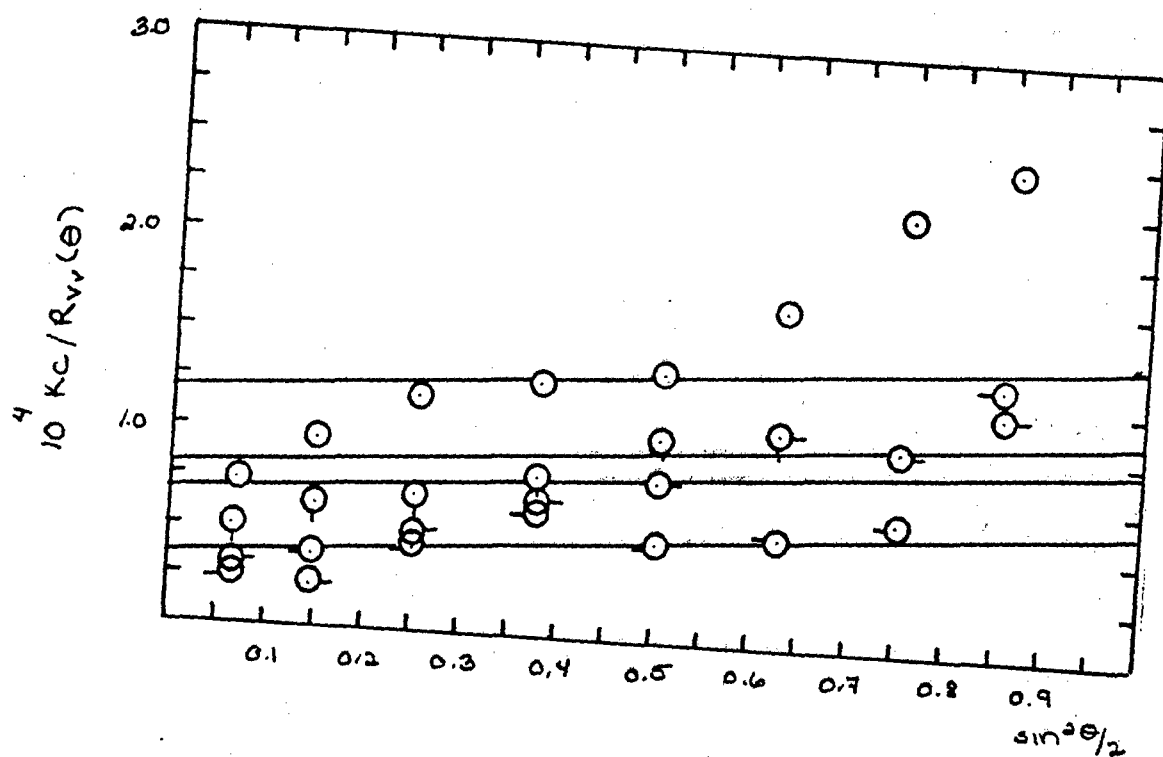
Figure 163: The aluncentrifuged Vv components of the integrated intensity light scattering of SPBO 80/MSA at 633 nm and 25.0°C. O 0.0511 g/dl O–0.0399 g/dl Q 0.0250 g/dl–O 0.0099 g/dl
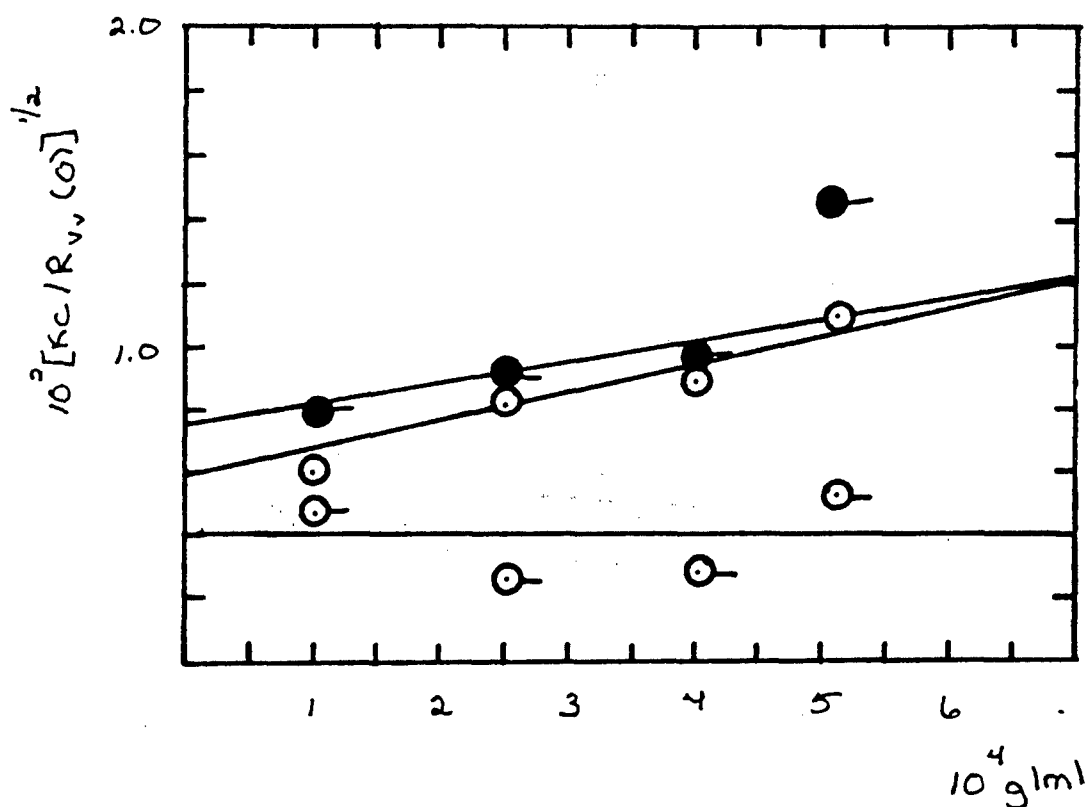
Figure 164: The concentration dependence of the Vv components of the integrated intensity light scattering of SPBO 80/MSA. O uncentrifuged sonicated O–uncentrifuged ● centrifuged
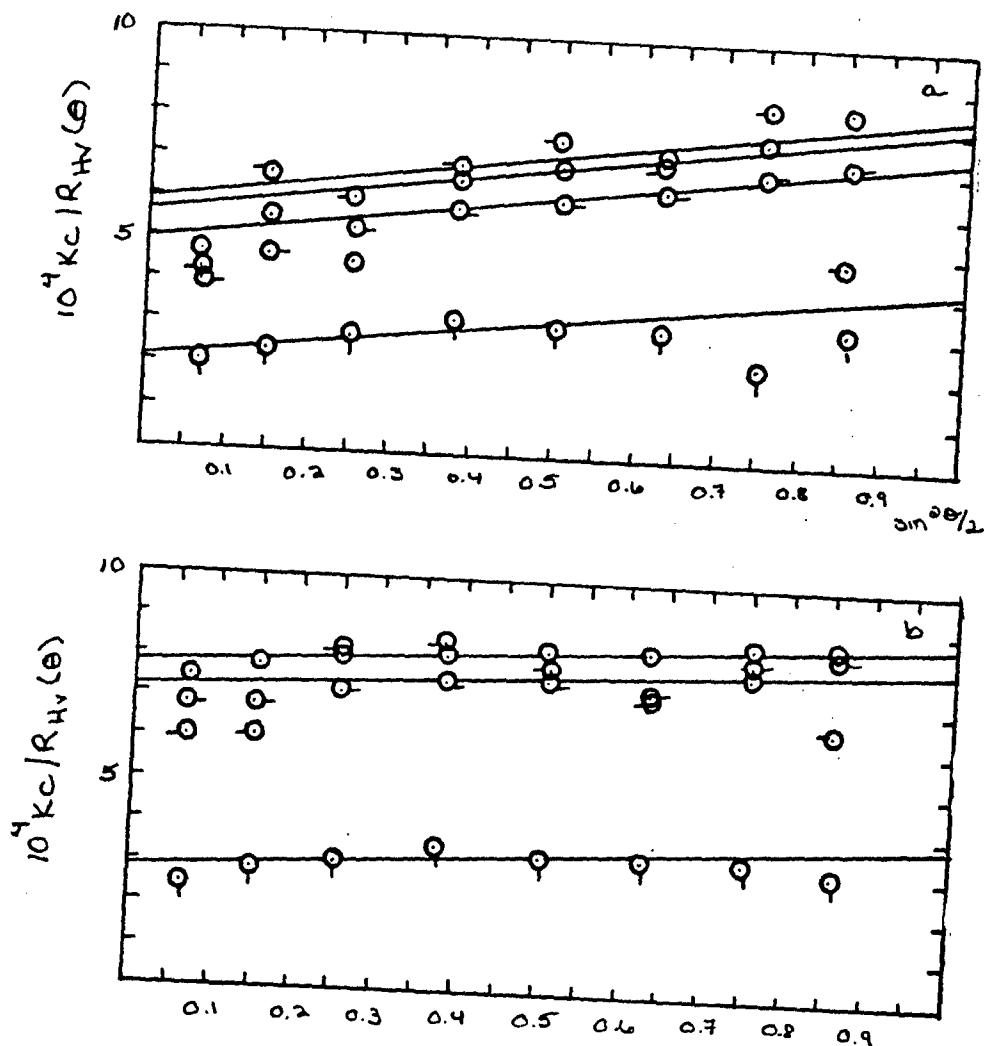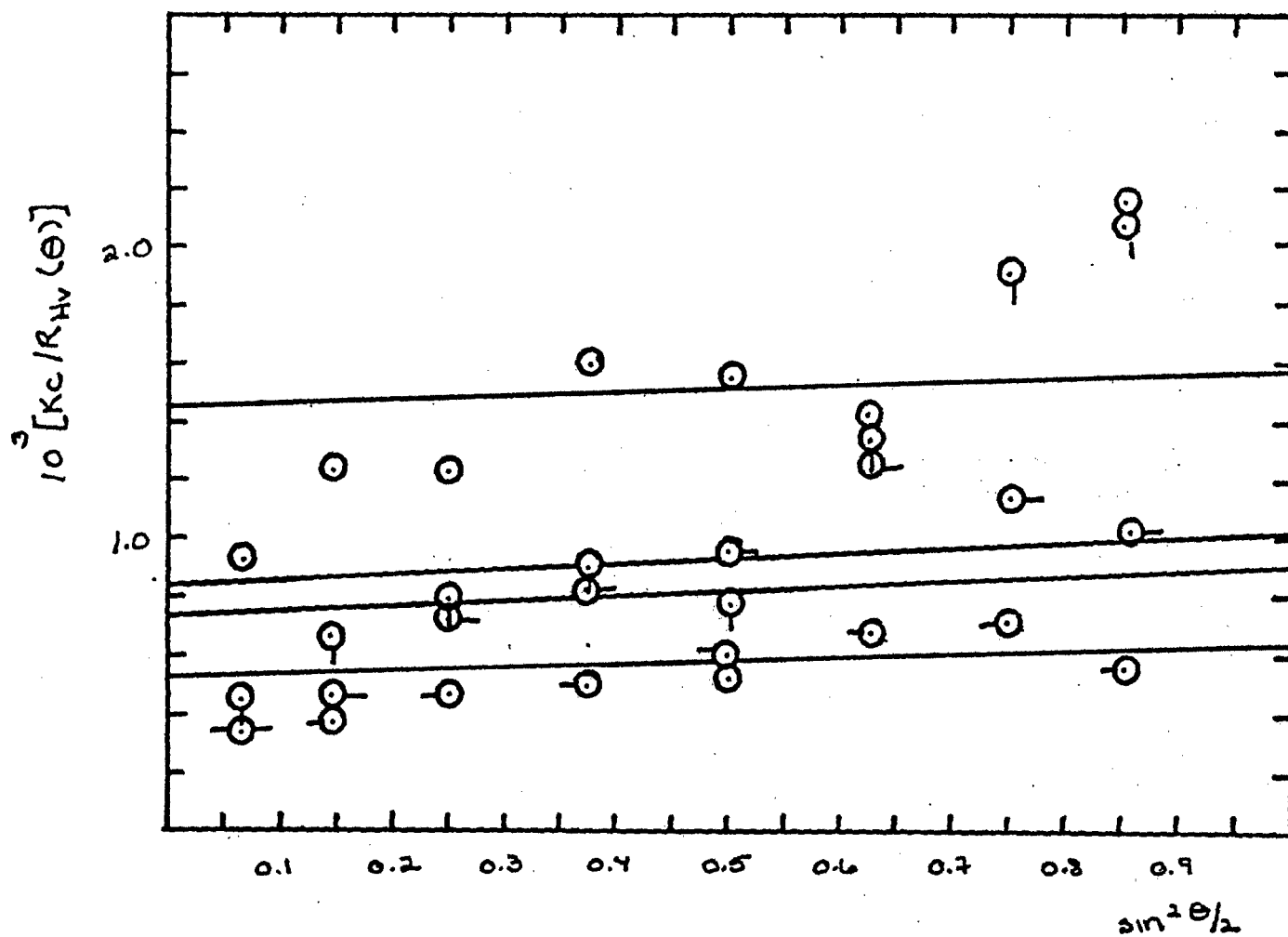
Figure 165: The a)uncentrifuged   Hv components of the integrated intensity light scattering of SPBO 80/MSA at 633 nm and 25.0°C. O 0.0511 g/dl O-0.0399 g/dl Q 0.0250 g/dl -O 0.0099 g/dl
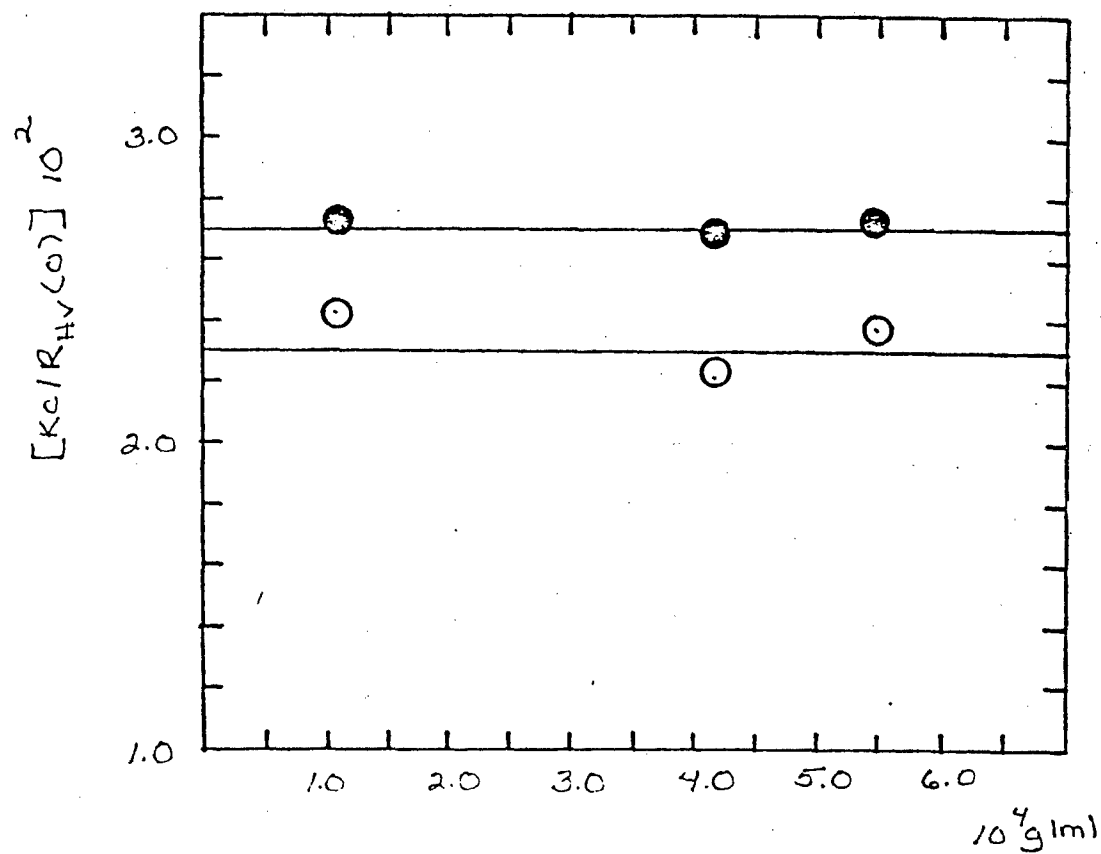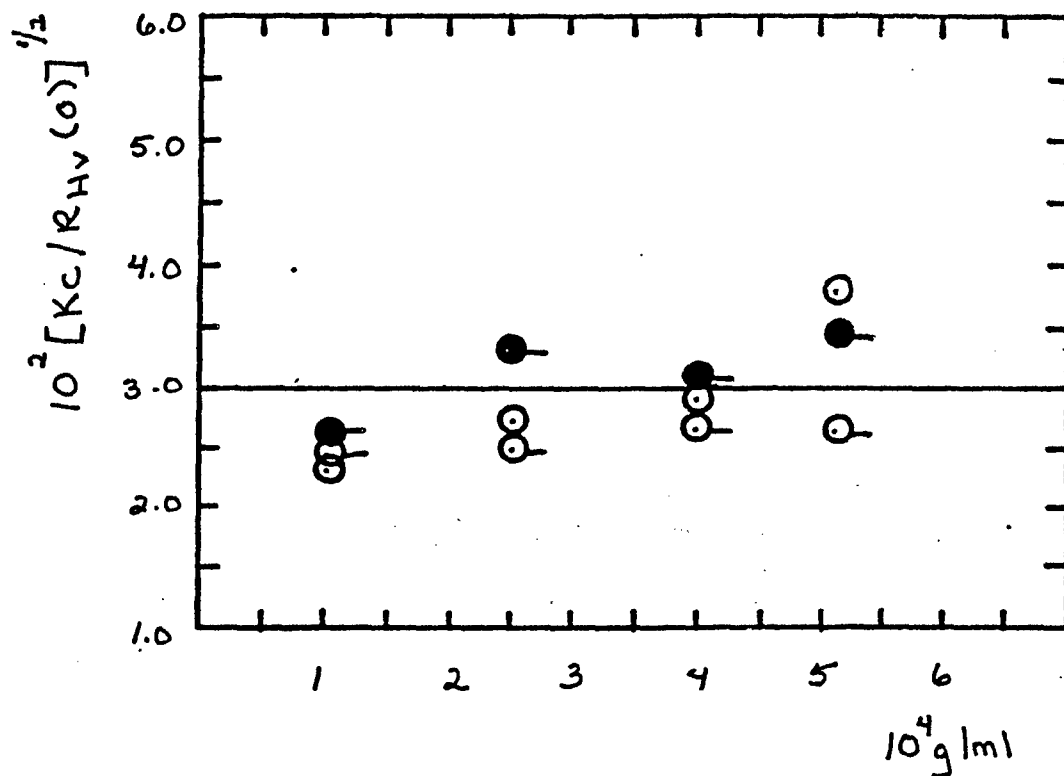
Figure 166 : The concentration dependence of the Hv components of the integrated intensity light scattering of SPBO 80/MSA. O uncentrifuged   sonicated O-uncentrifuged ●-centrifuged
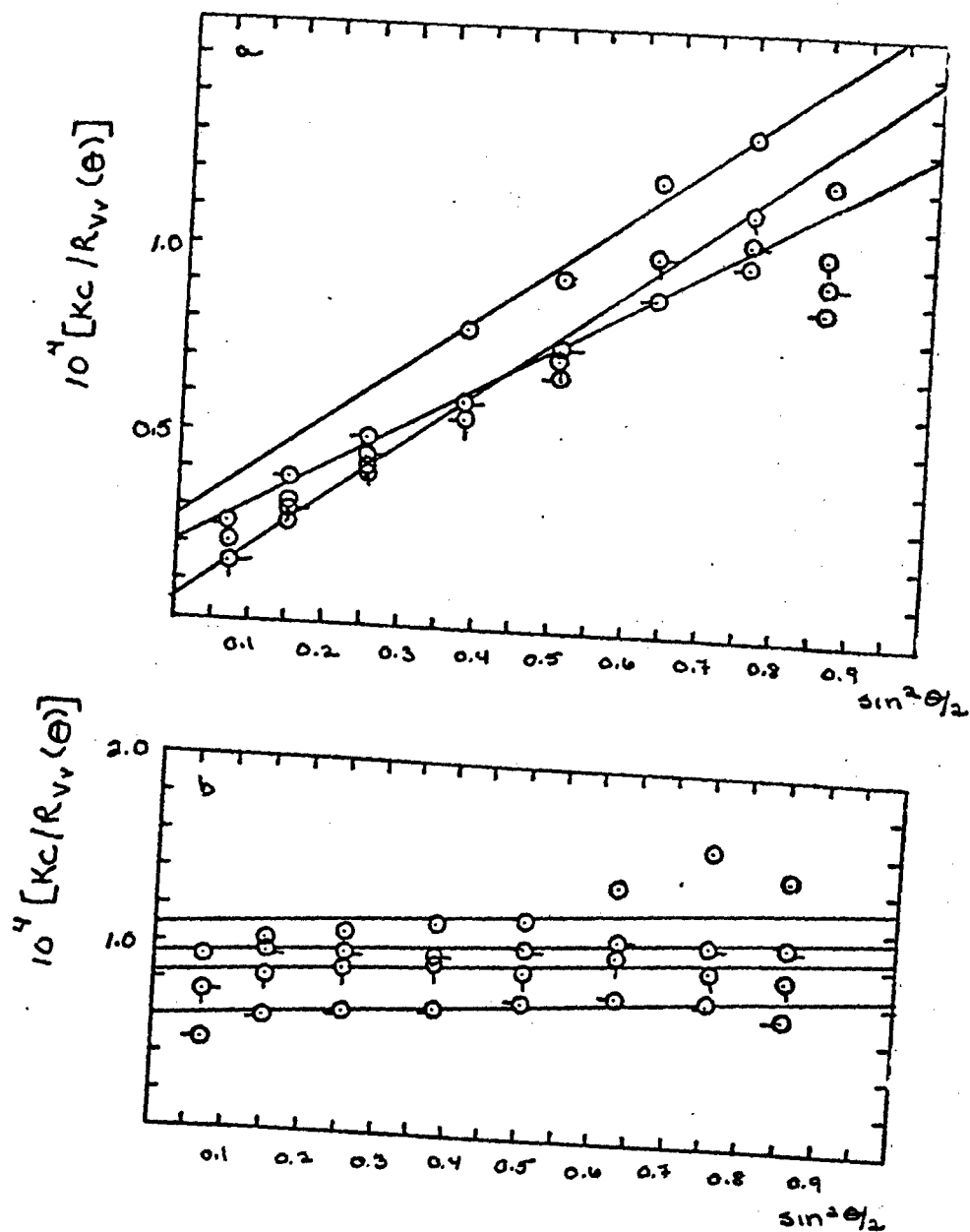
Figure 167: The a)uncentrifuged and b)centrifuged Vv components of the integrated intensity light scattering of sonicated SPBO-80/MSA at 633 nm and 25.0°C. O 0.0511 g/dl O–0.0399 g/dl Q 0.0250 g/dl –O 0.0099 g/dl
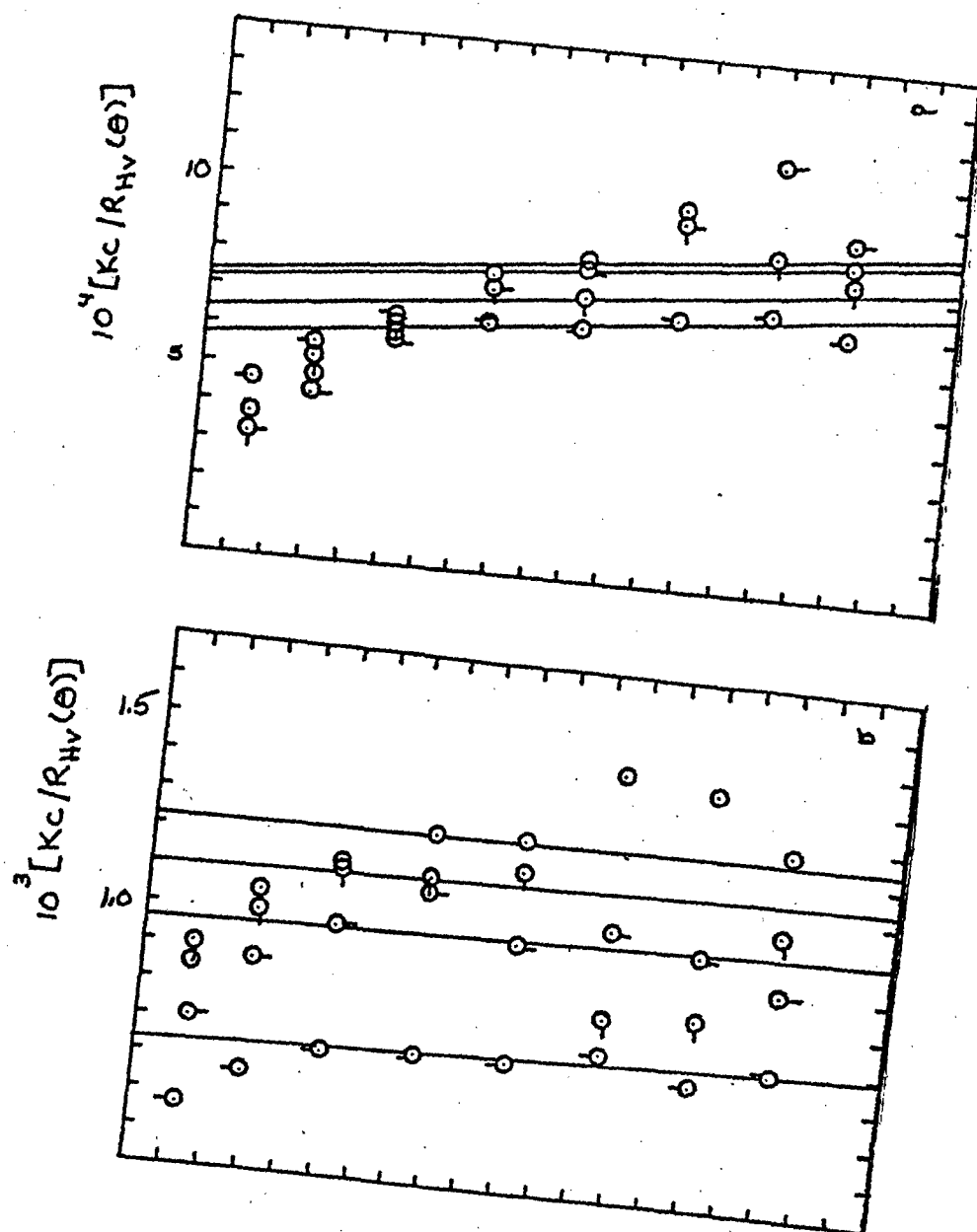
Figure 168: The a)uncentrifuged and b)centrifuged Hv components of the integrated intensity light scattering of sonicated SPBO-80/MSA at 633 nm and 25.0°C. O 0.0511 g/dl O-0.0399 g/dl Q 0.0250 g/dl-O 0.0099 g/dl
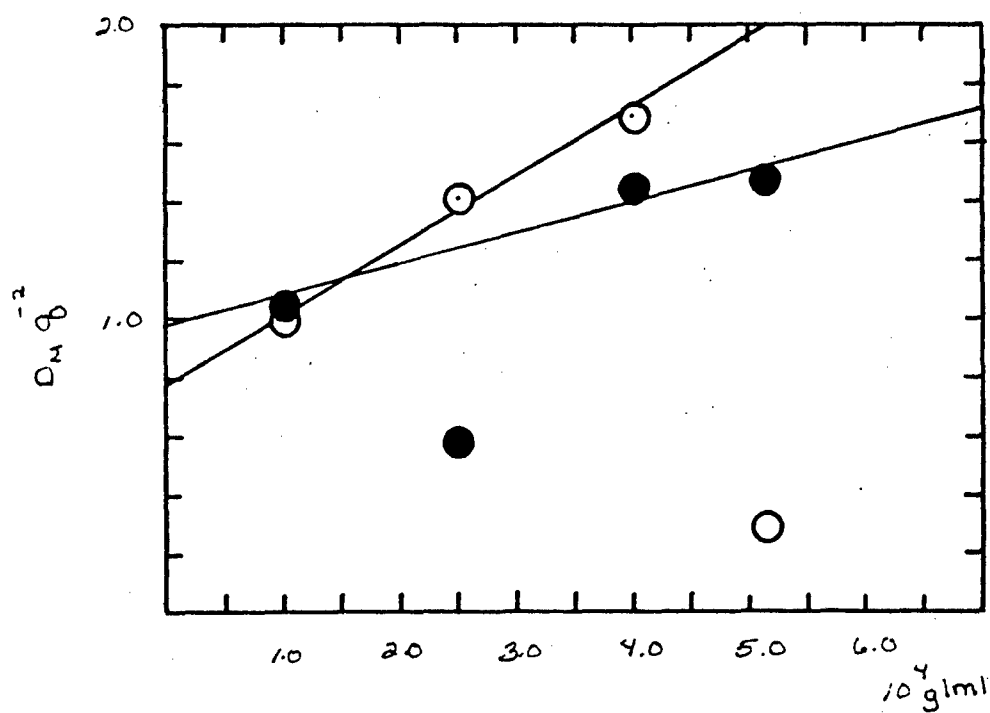
Figure 169:   The concentration dependence of the mutual diffusion coefficient D_M of SPBO-80/MSA
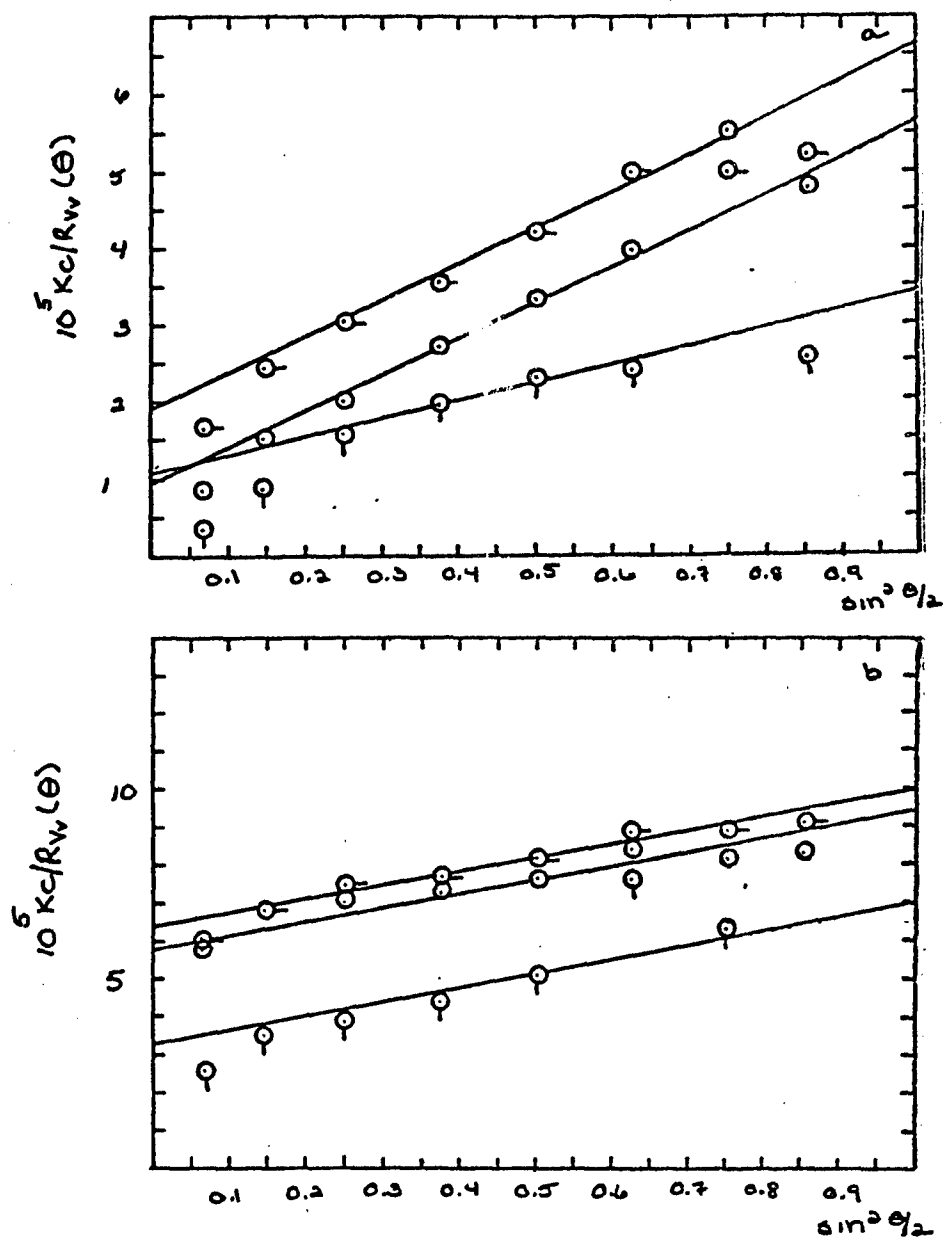
Figure 170: The a)uncentrifuged and b)centrifuged Vv components of the integrated intensity light scattering of sonicated SPBO 88/MSA at 633 nm and 25.0°C. O 0.0342 g/dl O–0.0202 g/dl Q 0.0062 g/dl
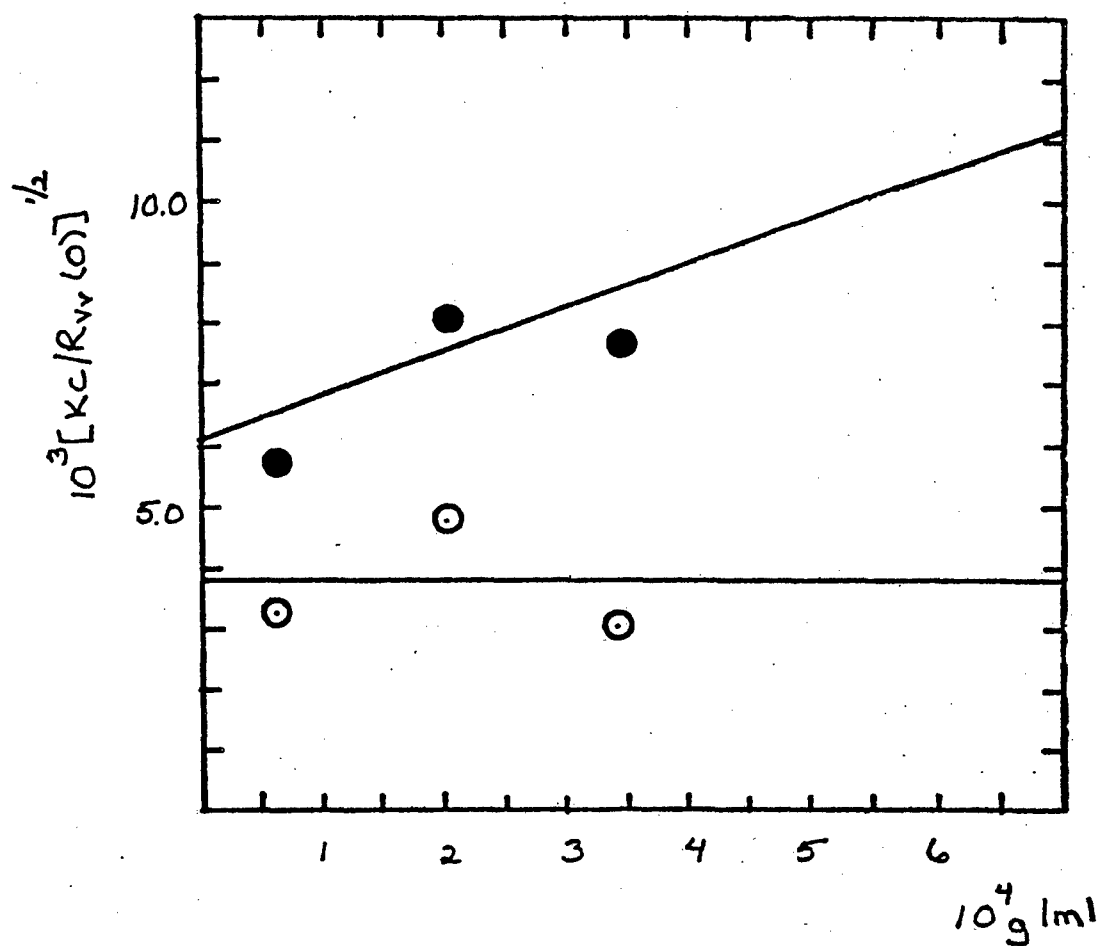
Figure 171: The concentration dependence of the Vv components of the integrated intensity light scattering of sonicated SPBO 88/MSA. O uncentrifuged ● centrifuged
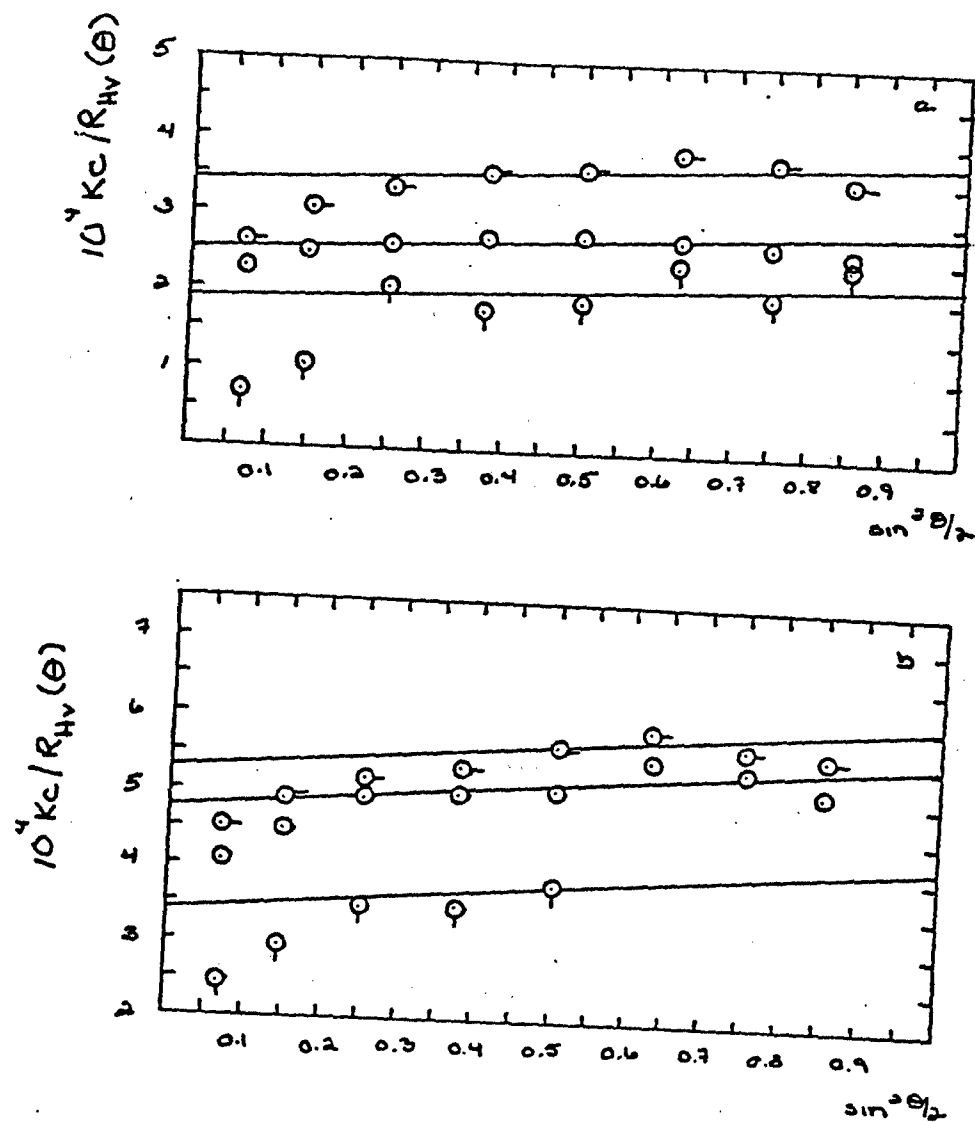
Figure 172: The a)uncentrifuged and b)centrifuged Hv components of the integrated intensity light scattering of sonicated SPBO 88/MSA at 633 nm and 25.0°C. O 0.0342 g/dl O-0.0202 g/dl Q 0.0062 g/dl
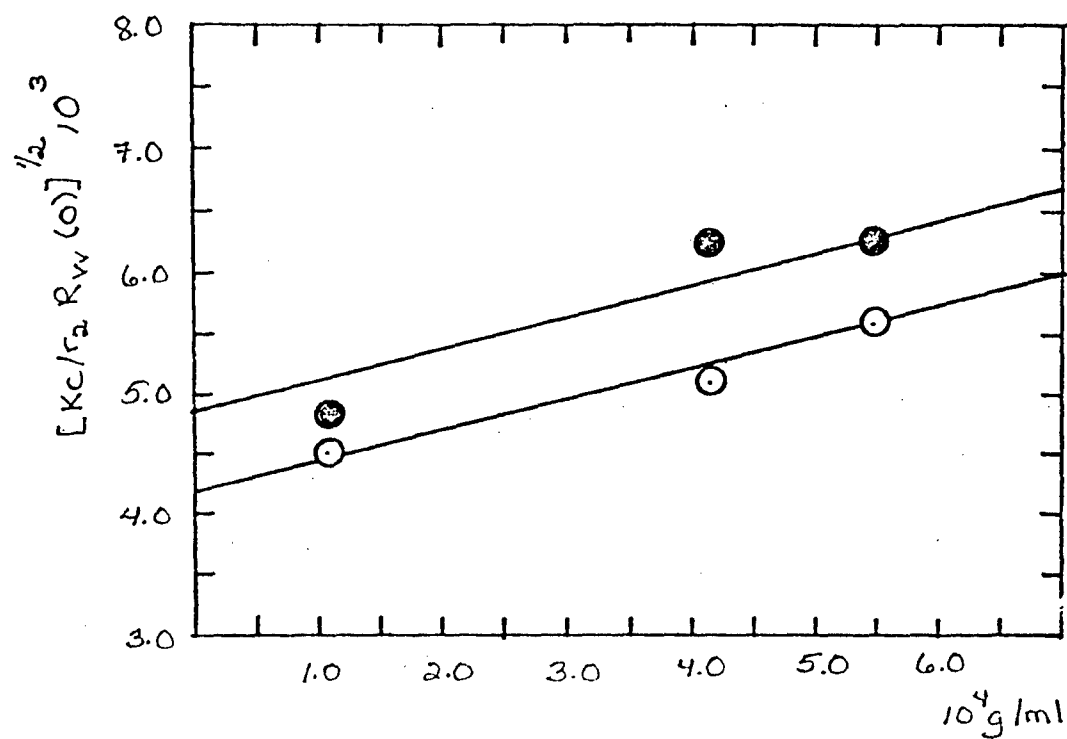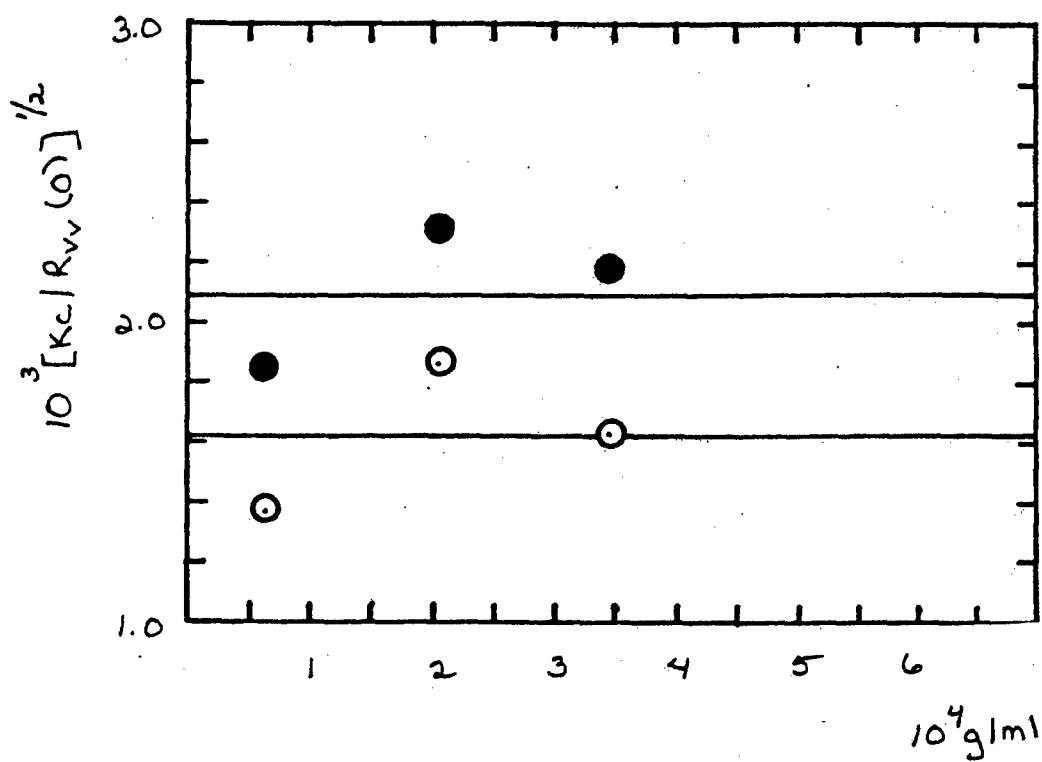
Figure 173: The concentration dependence of the Hv components of the integrated intensity light scattering of sonciated SPBO 88/MSA. O uncentrifuged ● centrifuged
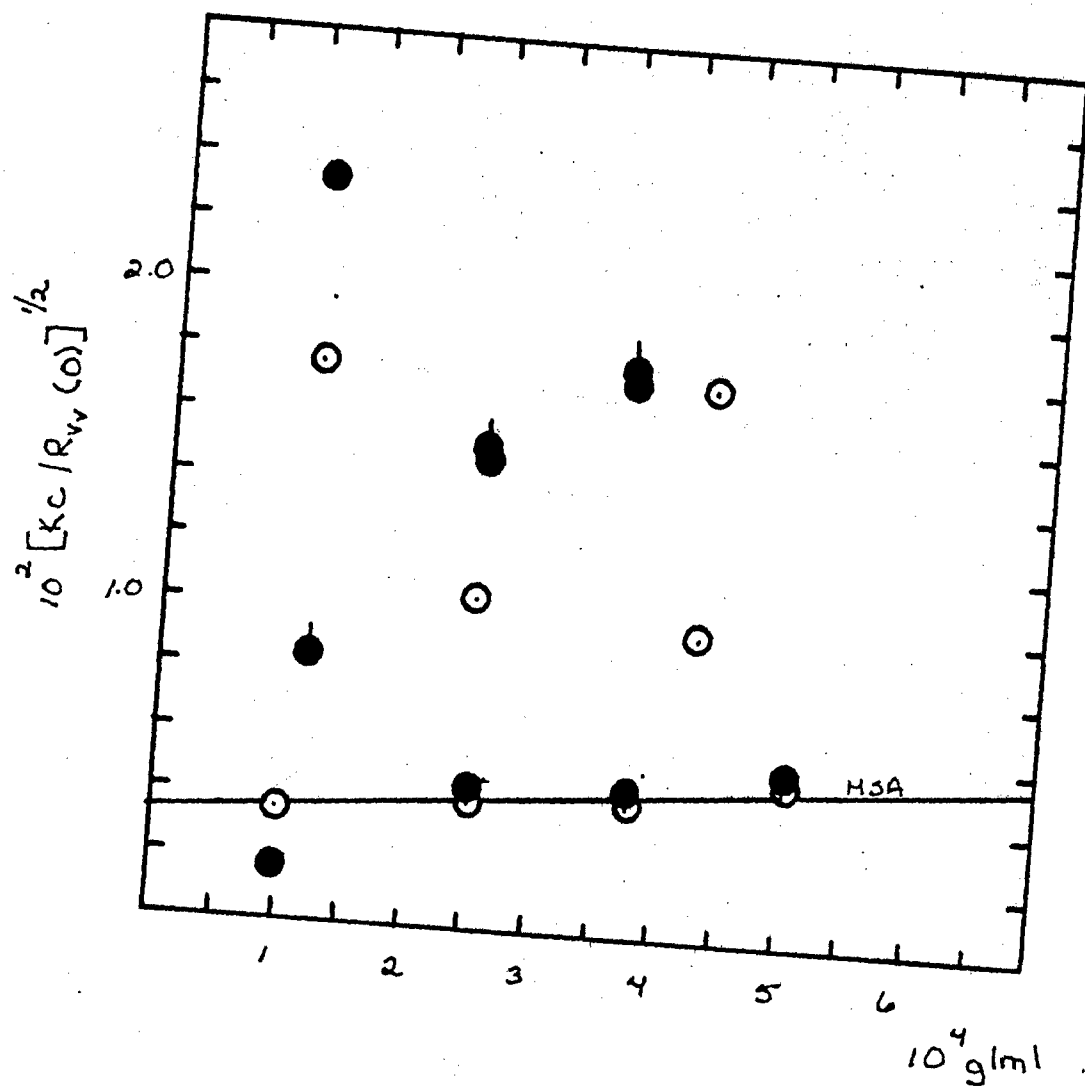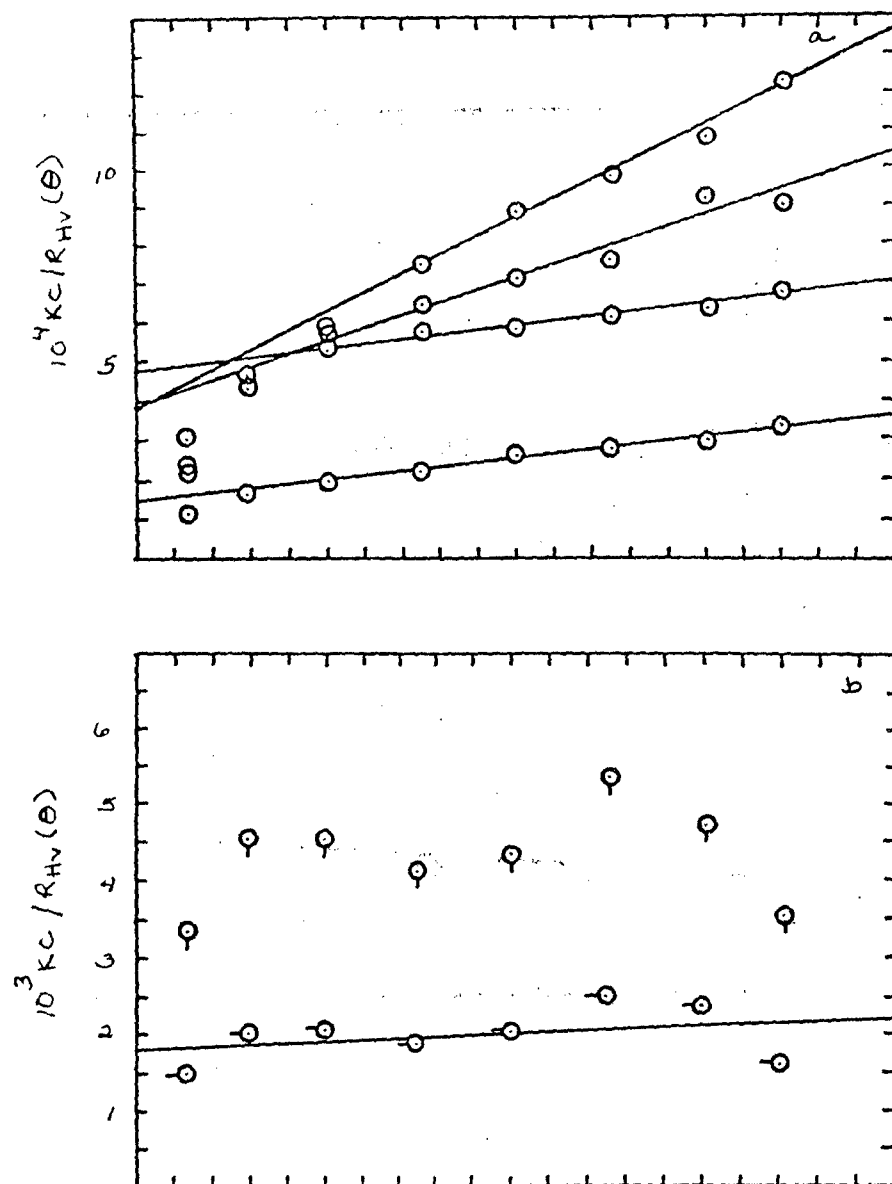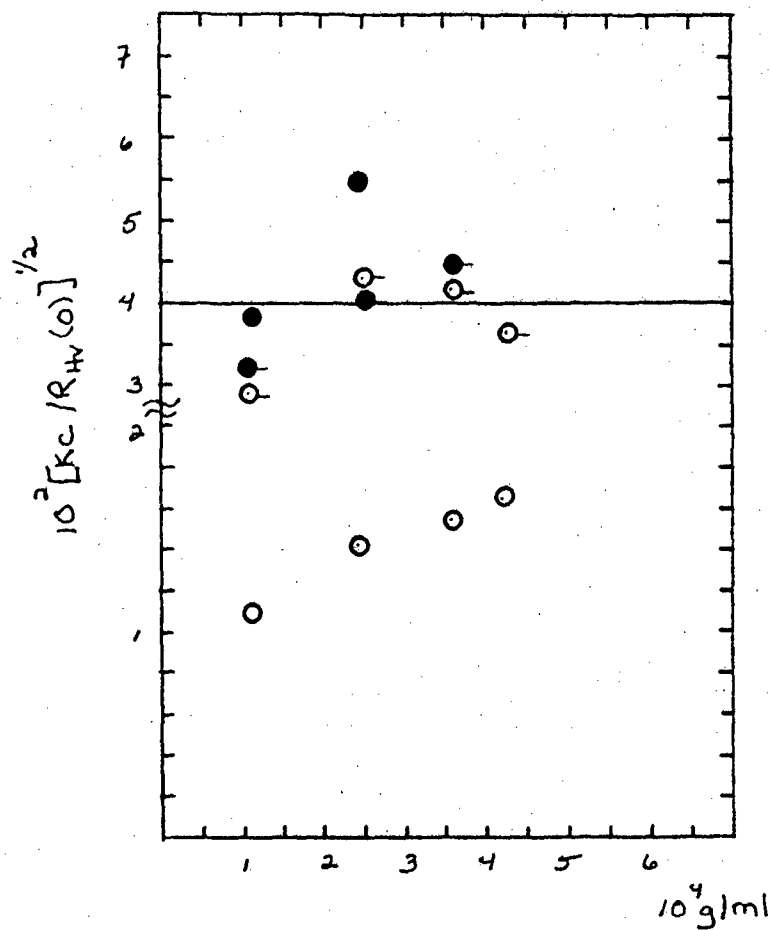
Figure 174: a) The concentration dependence of $\tau_i \sin^2 \theta/2$ of uncentrifuged SPBO 88/MSA.

Figure 175: a]The concentration dependence of $\tau_i \sin^2 \theta/2$ of centrifuged SPBO 88/MSA.

273

2. PART II

2.1 INTRODUCTION

In ref. 1[1], several steady-state rheological properties were studied in the linear and nonlinear response range for rodlike macroions in solution in protic sulfonic acids. The otherwise uncharged polymers are modified to become macroions in solution through protonation by the sulfonic acid. The rheological properties studied in ref. 1 included the dependence on shear rate κ of the steady-state viscosity η_κ, recoverable compliance R_κ and flow birefringence function $M_\kappa = \Delta n_\kappa^{(13)}/(\eta_\kappa \kappa)^2$, where $\Delta n_\kappa^{(13)}$ is the flow birefringence in the 1-3 plane. The parameters are defined in ref. 1 and elsewhere.[2-5] Here, we will report some transient rheological properties for solutions of the rodlike polymer poly(1,4-phenylene-2,6-benzobisthiazole), PBT:
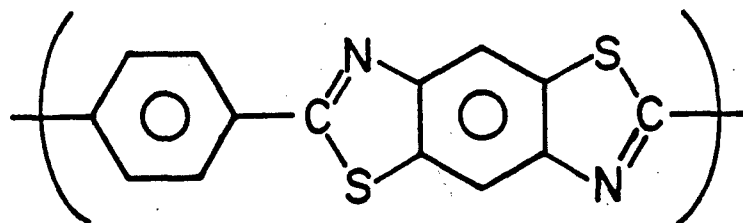
PBT

Transient properties obtained after initiation of flow include the nonlinear creep compliance $J_\sigma(t)$ and the viscosity growth function $\eta_\kappa(t)$ defined, respectively, as[5,6]

$$J_\sigma(t) = \gamma(t)/\sigma \tag{2.1}$$

$$\eta_\kappa(t) = \sigma(t)/\kappa \tag{2.2}$$

Here $\gamma(t)$ is the strain at time t after imposition of a shear stress σ and $\sigma(t)$ is the shear stress at time t after imposition of a steady rate of shear κ. Of course, for large t, both $\eta_\kappa(t)$ and $t/J_\sigma(t)$ are equal to η_κ.

Transient properties obtained after cessation of steady state flow include the recoverable compliance function $R_\sigma(t)$, the viscosity relaxation function $\hat{\eta}_\kappa(t)$ and the flow birefringence relaxation function $\hat{M}_\kappa(t)$ defined respectively, as

$$R_\sigma(t) = \gamma_R(t)/\sigma \qquad (2.3)$$

$$\hat{\eta}_\kappa(t) = \sigma(t)/\kappa \qquad (2.4)$$

$$\hat{M}(t) = \Delta n_\kappa^{(13)}(t)/(\eta_\kappa \kappa)^2 \qquad (2.5)$$

Here $\gamma_R(t)$ is the recovered strain at time t after cessation of steady flow at shear rate κ (shear stress $\sigma = \eta_\kappa \kappa$), $\sigma(t)$ is the shear stress at time t after cessation of steady flow at shear rate κ, and $\Delta n_\kappa^{(13)}(t)$ is the birefringence (in the 1,3 plane) at time t after cessation of steady flow at shear rate κ. For large t, $R_\sigma(t) = R_\kappa$, whereas both $\hat{\eta}_\kappa(t)$ and $\hat{M}(t)$ are zero. For t = 0, the latter are η_κ and $\hat{M}$, respectively.

For small κ or σ, linear viscoelastic behavior is expected,[5,6] for which one has the well-known relations

$$\lim_{\sigma=0} J_\sigma(t) = J_0(t) = R_0(t) + t/\eta_0 \qquad (2.6)$$

$$\lim_{\sigma=0} R_\sigma(t) = R_0(t) \qquad (2.7)$$

$$\lim_{\kappa=0} \eta_\kappa(t) = \eta_0(t) = \int_0^t G_0(u)du \qquad (2.8)$$

$$\lim_{\kappa=0} \hat{\eta}_\kappa(t) = \hat{\eta}_0(t) = \eta_0 - \eta_0(t) \qquad (2.9)$$

The creep compliance $J_0(t)$ and the linear modulus $G_0(t)$ are related through a convolution integral:

$$\int_0^t G_0(u) J_0(t - u)du = t \qquad (2.10a)$$

$$\int_0^t G_0(u)R_0(t-u)du = t \frac{\hat{\eta}_\kappa(t)}{\eta_0} + \tau_c \frac{N_0^{(1)}(t)}{R_0} \qquad (2.10b)$$

where $\tau_c = \eta_0 R_0$ and

$$N_0^{(1)}(t) = \eta_0^{-2} \int_0^t uG_0(u)du \qquad (2.11)$$

Equations 2.10 provide a means to compute $J_0(t)$ from $G_0(t)$ or vice versa[3,6,7], see below.

As described in ref. 1, according to the "stress-optic" law[8] M_κ is related to the first normal stress function $N_\kappa^{(1)}$ (with neglect of $\Delta n^{(23)}$ in comparison with $\Delta n^{(13)}$):

$$M_\kappa \sim 2\, \mathbb{C}'\, N_\kappa^{(1)} \tag{2.12}$$

Here, $N_\kappa^{(1)} = \nu^{(1)}/2(\kappa \eta_\kappa)^2$, where $\nu^{(1)}$ is the first normal stress difference for steady flow at shear rate κ, and the coefficient $\mathbb{C}'$ is about equal to the ratio $\mathbb{C}$ of the principal components of the refractive index and stress ellipsoids:[8,9]

$$\mathbb{C}' = \left(\frac{\cot 2\chi}{N_\kappa^{(1)} \eta_\kappa \kappa} \right) \mathbb{C} \sim \mathbb{C} \tag{2.13}$$

with χ the extinction angle locating the cross of isocline (the symbol S_κ was used to designate $N_\kappa^{(1)}$ in ref. 1). As indicated in Eqn. 2.13, the term in parenthesis is expected to be nearly unity. With Eqn 2.12, the limiting value M_0 of M_κ for small κ is given by $M_0 R_0^{-1} \sim 2\mathbb{C}'$. With the stress-optic law, $\mathbb{C}'$ is expected to be independent of polymer concentration or molecular weight for rodlike chains. For small κ, data on the limiting value of the flow birefringence $\Delta n^{(12)}$ in the 1-2 flow plane provide an alternative measure of $\mathbb{C}'$, with $\Delta n^{(12)}/\eta_{0\kappa} \sim 2\mathbb{C}'$.

2.2 EXPERIMENTAL

2.2.1 Materials

Polymers PBT 53 and 43 are described in ref. 1. Polymers PBT 72 and 72R are described in reference 10. The latter two represent examples of an otherwise common sample exposed to separate post-polymerization process histories. Sample 72R experienced several precipitation and redissolution cycles, whereas sample 72 was coagulated directly from the polymerization solution.

Methane sulfonic acid was distilled prior to use and stored away from contamination by atmospheric moisture. Polymers were dried *in vacuo* prior to use. Extreme caution was taken to prevent contamination of the solutions by moisture. Even modest amounts of water can lead to intermolecular association in acidic solution of heterocyclic polymers, with substantial effects on rheological properties.[11] Methods used here parallel those discussed in ref. 1.

The wire-suspension cone-and-plate rheometer[12] and the flow birefringence apparatus described in ref. 1 were used for most of the work reported here. A few data were also obtained with a Rheometrics model RMS 7200 rheometer, equipped with a Birnboim Correlator model DAS-IV, principally to permit estimation of the linear steady-state recoverable compliance. The apparatus was modified to retard the rate of contamination by moisture by use of the protective ring assembly described in ref. 1 (e.g., see Fig. 1 of ref. 1).

The temperature for the onset of the ordered nematic phase was determined by observation of the transmitted light with the sample between crossed polaroids in a microscope (approximately 100 x magnification). The sample was held in a special cell fabricated from rectangular glass tubing. (Vitro Dynamics, Inc., Rockaway, NJ). The sample thickness was 0.4 mm; use of cells ca. 0.02 mm thick produced a marked increase of the transition temperature, but no such effect was found for cells of the

thickness used.   The sample was sealed in the cell to prevent contamination by moisture.   After a rapid temperature scan (ca. 0.01K s^{-1}) to provide an approximate estimate for the transition temperature, the temperature was adjusted to give a nematic sample about 5-10 degrees below the transition temperature.   After equilibration, the temperature was slowly increased by increments (ca. 1K), allowing the necessary time for equilibration between increments; equilibration times varied from ca. 10 min to several hours, depending on the viscosity.   Stability of the anisotropic texture was taken as the criterion of equilibration.   The transition temperature was taken as the temperature for the disappearance of the last nematic domains.   After conversion to the isotropic state, the process was reversed, with slow cooling to confirm the transition temperature.   The process is more difficult, and it is easy to obtain supercooling, by as much as 5K for viscous samples.

2.3 RESULTS

The systems studied are identified in table 23. Values of η_0, R_0 and $M_0 R_0^{-1}$ are given in tables 24 and 25. Plots of η_κ/η_0, R_κ/R_0 and M_κ versus $\tau_c \kappa$ are given in figs. 176 to 180. As may be seen in the latter figures, reduced plots are obtained at various temperatures in every case but one. The exception is for a solution of PBT-53, $c = 32.3$ gKg^{-1}, at a temperature for which the solution has become nematic. This latter behavior is included for illustrative comparison only, and will not be considered further here; such behavior will be amplified in Part 3 of this series.

The reduced plots of η_κ/η_0, R_κ/R_0 and M_κ/R_0 versus $\tau_c \kappa$ are each nearly independent of c for a given polymer for the available example. Moreover, the curves for η_κ/η_0 and R_κ/R_0 versus $\tau_c \kappa$ to not differ markedly among the samples studied. The most marked difference among the reduced curves is for M_κ/R_0 versus $\tau_c \kappa$ for the different samples. Possible reasons for this are discussed below.

Plots of $\ln \eta_0/\eta_s$ and $\ln w_c$ versus T^{-1} are given in fig. 181. Here, w_c is the concentration for conversion from an isotropic state ($w \leq w_c$) at T to a nematic state ($w > w_c$) at T and η_s is the solvent viscosity. For methane sulfonic acid η_s is 7.67m Pa's at 313K and $\partial \ln \eta_s/\partial T^{-1} = 2800$K. As may be seen in fig. 181, $\partial \ln(\eta_0/\eta_s)/\partial T^{-1} = 1265$K for the isotropic samples studied. The data on w_c may also be fitted by an Arrheneus relation with $\partial \ln w_c/\partial T^{-1} = -433$K, and $w_c/$gkg^{-1} equal to 32.2, 32.3 and 34.9 at 313K for PBT 72, 53 and 43, respectively. With these results, $\partial \ln(\eta_0/\eta_s w_c^3)/\partial T^{-1} = 34$K is nearly negligible, see below. The product $[\eta]w_c \rho$ is equal to 81, 67 and 47 for PBT 72, 53 and 43, respectively (T = 313K).

As with earlier reports[13], $R_0 T$ is found to decrease with increasing w, and to be independent of T when w is well below w_c. However, as w_c is approached, $R_0 T$ increases with increasing w.

Data on $J_\sigma(t)$ are given in fig. 182 for PBT 53 (c = 25.5 gkg^{-1}). As with results

reported elsewhere for flexible chain polymers,[2,3] it appears that $J_\sigma(t) \sim J_0(t)$ for any stress for $t < t*$ decreases with increasing σ. As with flexible chain polymers, the strain $\gamma* = \gamma(t*) = \sigma J_\sigma(t*)$ is about independent of σ. Values of $\gamma*$ are discussed below.

The function $R_\sigma(t)$ is shown in fig. 183 for PBT-53, $c = 29.4$ gKg^{-1}. For small t, $R_\sigma(t)$ is independent of σ, but for large t, $R_\sigma(T)$ is decreased by increased σ. Similar behavior has been reported for flexible chain polymers.[2,3]

Data on $\eta_\kappa(t)$ obtained here display a broad, shallow maximum with increasing κ at a time t^+. It is found that t^+ decreases with increasing κ such that the strain $\gamma^+ = \kappa t^+$ is essentially independent of κ. Similar behavior is well known with linear polymers in the range of $\tau_c \kappa$ of interest here[6]. In every case, $\gamma^+ > \gamma*$. Possibly, $\eta_\kappa(t) \sim \eta_0(t)$ for $\kappa t < \gamma*$, similar to results reported[14] for flexible chain polymers, but our data at small t are not sufficiently precise to be certain of this.

Data on $\hat{\eta}_\kappa(t)/\eta_\kappa$ and $\hat{M}(t)/M_\kappa$ for two solutions at several temperatures are given in fig. 184. The data are represented in reduced form versus t/β_κ, where the reduction factors β_κ are shown as a function of $\tau_\kappa = \eta_\kappa R_\kappa$ in the inserts. For each function, the reduced curves superpose over the range of κ studied. The rate of relaxation of $\hat{M}_\kappa(t)/M_\kappa$ is considerably less than that of $\hat{\eta}_\kappa(t)/\eta_\kappa$; similar behavior has been reported[15] for flexible chain polymers.

Data on PBT-72R are included to demonstrate the dramatic effects of intermolecular association on the rheological behavior. This polymer, discussed in reference 10, is a form of PBT-72 in which (apparently) irreversible intermolecular association of the chains in (nearly) parallel array has been induced through the post-polymerization processing history. As might be expected with such aggregates, the aggregated species have significantly smaller η_0 for a given w and T.

2.4 DISCUSSION

2.4.1 Linear Viscoelastic Behavior

In the following we will consider a representation of the linear recoverable compliance $R_0(t)$ in terms of a discrete distribution of $n - 1$ retardation times. Together with η_0 and $\tau_c = \eta_0 R_0$, these will be converted to a discrete distribution of n relaxation times to facilitate computation of functions such as $\eta_0(t)$, $\hat{\eta}_0(t)$ and $\hat{M}_0(t)$. In the next section, the nonlinear creep compliance will be discussed in terms of a single-integral constitutive equation that permits computation of η_κ, $\eta_\kappa(t)$, $\hat{\eta}_\kappa(t)$, R_κ, $N_\kappa^{(1)}$, $N_\kappa^{(1)}(t)$ and $\hat{M}_\kappa(t)$ given the distribution of relaxation times. Finally, comparison of the behavior observed here with that given by mechanistic models will be considered.

In general, the linear creep compliance $J_0(t)$, equal to $R_0(t) + R_0 t/\tau_c$ (see Eqn. 2.6), can be represented in terms of a discrete set of 2n parameters including $\tau_c = \eta_0 R_0$ and $n - 1$ retardation times λ_i together with R_0 and $n - 1$ weight factors R_i, with

$$R_0(t) = R_0 + \sum_{}^{n-1} R_i \exp - t/\lambda_i \qquad (2.14)$$

where $\sum R_i \leq R_0$[5,6]; the contributions comprising $R_0 - \sum R_i$ represent terms with retardation times much shorter than the experimental time scale. By the use of methods based on Eqn. 2.10, these 2n parameters may be converted to an alternative set of 2n parameters comprising n relaxation times τ_i and n weight factors η_i such that, for example,[5,6]

$$\hat{\eta}_0(t) = \sum_1^n \eta_i \exp - t/\tau_i \qquad (2.15)$$

where $\eta_0 = \sum \eta_i$ and $(\sum \eta_i \tau_i^{-1})^{-1} = R_0 - \sum R_i$. Values of λ_i/τ_c and R_i/R_0 computed for the data in fig. 183 by use of "Procedure X"[16] are given in table 26, along with

τ_i/τ_c and η_i/η_0 computed from R_0, τ_c and the distribution of retardation times using a method described elsewhere.[3,7] The functions $R_0(t)/R_0$ and $\hat{\eta}_0(t)/\eta_0$ computed with these are shown in figs. 176 and 178. It would be difficult to extract the contribution with the longest relaxation time τ_1 by direct analysis of $\hat{\eta}_0(t)$ by, for example, use of Procedure X owing to experimental limitations at large t. In general, the reduced functions λ_i/τ_c, etc. are independent of temperature.

The linear viscoelastic data discussed above indicate that the distribution of retardation (or relaxation) times is broad. For example, for the average relaxation times $\tau^{(k)}$ defined by[17]

$$\tau^{(k)} = \Sigma' \eta_i \tau_i^{k-1} / \Sigma' \eta_i \tau_i^{k-2} \tag{2.16}$$

it is found that $\tau^{(2)}/\tau^{(1)} \sim 10$ for the data in fig. 183. Here the primes indicate that the summation is limited to the "terminal" relaxation time regime (e.g., the n terms of interest here). In the terms used above $\tau^{(2)} \sim \tau_c$ and $\tau^{(1)} \sim \eta_0 (\Sigma \eta_i \tau_i^{-1})^{-1} = \eta_0 (R_0 - \Sigma R_i)$.

With the use of the 'stress-optic' relation discussed in the Introduction, $\hat{M}_0(t)$ is expected to fit the relation (with neglect of $\Delta n_\kappa^{(23)}$):

$$\hat{M}_0(t) = \lim_{\kappa=0} \hat{M}_\kappa(t) \sim 2\,\mathbb{C}'\,\eta_0^{-2} \Sigma \eta_i \tau_i \exp - t/\tau_i \tag{2.17}$$

A plot of this function calculated with the η_i/η_0 and τ_i/τ_c given in table 26 is included as the curve in figs. 184-185; no data on $\hat{M}_0(t)$ are available for the solutions studied here, but an estimation of $\hat{M}_0(t)$ from data on $\hat{M}_\kappa(t)$ is considered below.

Following the methods discussed in ref. 1, a plot of $\eta_0/\eta_s M[\eta] a*^3$ versus $cL/M_L a*$ is given in fig. 185. Here, $c = w\rho$, with the solution density ρ approximately equal

to the solvent density ρ_s for the weight fraction w of polymer interest here, M_L = M/L is the mass per unit contour length and $a*$ is an empirical parameter chosen to fit the experimental data by the relation

$$\eta_0/\eta_s = KN_A^2 M[\eta] a*^3 X^3 (1 - BX)^{-2} \qquad (2.18)$$

where $X = cL/M_L a*$. The plot in fig. 185 was constructed using the data on $[\eta]$, L_η and $M_\eta = L_\eta M_L$ given in table 23. Data reported in ref. 1 are included for comparison. The data are well fitted by Eqn. 2.18, with the values of $w*/B$ = $a* M_L/L_\eta \rho B$ given in table 27 and $KB^{-3} = 1.5 \times 10^{-4}$. These values are conveniently deduced by comparison of bilogarithmic plots of $\eta_0/\eta_s M_\eta [\eta]$ versus cL_η/M_L with a similar plot of $(BX)^3(1 - BX)^{-2}$ versus BX (Eqn. 2.18). If these have the same shape, then the vertical and horizontal 'shifts' required to superpose the curves are equal to $\log KN_A^2(a*/B)^3$ and $\log a*/B$, respectively. As may be seen in table 27, values of w_c and $w*B^{-1}$ are equal within experimental error. The correspondence of ω_c and $w*B^{-1}$ and the temperature dependence of w_c provides a basis for the observed negligible temperature dependence of $\eta_0/\eta_s w_c^3$ remarked above.

With Eqn. 2.18, the substantial disparity between values of η_0 for PBT 72 and 72R at a given c and T, is subsumed in the parameter $w*B^{-1}$. Apparently, the suspected aggregation affects both η_0 and w_c.

2.4.2 Nonlinear Viscoelastic Behavior

In many ways the behavior observed here closely parallels that reported elsewhere[2,3] for flexible chain polymers. In the latter study, a single-integral constitutive equation of the BKZ type[18] was used to describe behavior for $J_\sigma(t)$, $\eta_\kappa(t)$, η_κ, R_κ, and $N_\kappa^{(1)}$. With $J_\sigma(t)$, it was found that $J_\sigma(t) \sim J_0(t)$ provided the total strain $\sigma J_\sigma(t)$ did not exceed a limiting value $\gamma*$, independent of σ. In accord with many other studies,[6] the strain $\gamma^+ = \kappa t$ for which $\partial \eta_\kappa(t)/\partial t$ is zero was found to be

independent of κ. It was found that γ^+ did not depend on polymer concentration over the range studied, but that $\gamma* \propto c^{-1}$. As may be seen in fig. 182, with the creep data on PBT solutions, it is also observed that $J_\sigma(t) \sim J_0(t)$ provided $\sigma J_\sigma(t) \leq \gamma*$. Moreover, as shown in fig. 186, $\gamma* \propto c^{-1}$.

As with flexible chain polymers,[3] the rheological behavior described above is accommodated by a BKZ-type single-integral equation which utilizes the linear viscoelastic modulus $G_0(t)$ and a strain function $F(|\gamma|)$ in the forms

$$G_0(t) = \frac{\partial \eta_0(t)}{\partial t} = \Sigma \; \eta_i \tau_i^{-1} \; \exp - t/\tau_i \tag{2.19}$$

$$F(|\gamma|) = \exp - m \; (|\gamma| - \gamma')/\gamma'' \tag{2.20}$$

where m is zero if $|\gamma| \leq \gamma'$ and unity otherwise. In terms of experimental parameters, $\gamma' = \gamma*$ and $\gamma'' = \gamma^+$. With this relation the steady-state functions are represented by the expressions[3]

$$\eta_\kappa = \Sigma \; \eta_i \; (1 - q_{\kappa,i}) \tag{2.21}$$

$$\eta_0 \eta_\kappa R_\kappa = \Sigma \; \eta_i \tau_i \; (1 - q_{\kappa,i} \; r_{\kappa,i}) \tag{2.22}$$

$$\eta_\kappa^2 N_\kappa^{(1)} = \Sigma \; \eta_i \tau_i \; (1 - q_{\kappa,i} \; p_{\kappa,i}) \tag{2.23}$$

285

The functions $q_{\kappa,i}$, $r_{\kappa,i}$ and $p_{\kappa,i}$, which depend on $\kappa\tau_i/\gamma''$ and $\alpha = \gamma'/\gamma''$, are given in the Appendix, along with a relation for $\eta_\kappa(t)$, but it may be noted that $q_{\kappa,i}$ is zero for $\kappa\tau_i < 1$, and approaches unity with increasing κ for $\kappa\tau_i > 1$. To a good approximation, $q_{\kappa,i}$, $r_{\kappa,i}$ and $p_{\kappa,i}$ each depend on $\beta\kappa\tau_i$, where $\beta^{-1} = \gamma''f$ with $f^2 = 1 + \alpha - \alpha^2/2$; typically, $f \sim 1$. Comparison of Eqns. 2.21 - 2.22 with data on solution of PBT 53 ($c = 29.4$ gKg^{-1}) are given in fig. 183, using the values of τ_i and η_i in table 26. The comparison is seen to be quite good, with the fits to Eqn. 2.21 and 2.22 giving $\beta^{-1} = 1.79$ (for $\alpha = 0.5$), in comparison with $\beta^{-1} = 2.5$ computed with the observed γ'/γ'' and γ'', using $\gamma' = \gamma*$ and $\gamma'' = \gamma^+$.

In general, η_κ is closely approximated by $[\eta_0(t)]_{\kappa t=1}$ such that[3]

$$\eta_\kappa \sim [\eta_0(t)]_{\kappa t=1} = \Sigma\, \eta_i\,(1 - \exp - 1/\kappa\tau_i) \tag{2.24}$$

and this approximation obtains with the data in fig. 176 and 178 as well. Equation 2.24 reflects the approximation $q_{\kappa,i} \sim \exp - 2/5\beta\kappa\tau_i$ and $\beta^{-1} \sim 2.5$. Equations 4.8 - 4.11 show that the dependence of η_κ/η_0 and R_κ/R_0 on $\tau_c\kappa$ for the κ of interest here is closely controlled by the distribution of relaxation times obtained for a linear response. The data in figs. 176-179 shows that η_κ/η_0 and R_κ/R_0 are similar for the several samples studied, but that distinct differences obtain among the samples, indicating differences in the distribution of relaxation times and/or the parameters γ' and γ'' in terms of Eqns. 2.21 - 2.22.

If Eqn. 2.12 is assumed, then data on M_κ/R_0 may be compared with $N_\kappa^{(1)}/R_0$ calculated with the single-integral constitutive relation. As shown in fig. 180a, the data on M_κ/R_0 versus $\tau_c\kappa$ for solutions of PBT-53 at several concentrations and temperatures form a single curve that can be fitted reasonably well using the estimate $\beta^{-1} = 1.79$ mentioned above, and $M_0/R_0 \sim 3.8$ MP$_a^{-1}$. The latter may be compared with the estimate $M_0/R_0 \sim 3$ MP$_a^{-1}$ given in table 25 based on data on

$\Delta n^{(12)}$ at lower concentrations of PBT-53. Discrepancies at small $\tau_c \kappa$ in fig. 180a may reflect experimental error in measuring small values of $\Delta n^{(13)}$. The data on M_κ / R_0 versus $\tau_c \kappa$ for PBT 72 and 72R are not too different from each other, but both lie below the data for PBT-53 for a given $\tau_c \kappa$, as do the data for PBT-43. Thus, the data for the latter three solutions indicate a more rapid decrease of M_κ with increasing $\tau_c \kappa$ than is observed with PBT-53. In terms of the proportionality $M_\kappa \propto N_\kappa^{(1)}$ of Eqn. 2.12, this corresponds to a broadened distribution of relaxation times for the latter three in comparison with PBT-53. Since the data on R_κ / R_0 and η_κ / N_0 versus $\tau_c \kappa$ do not support the postulate of broadened distribution, one may conclude that additional factors are involved, possibly having to do with the state of interchain association believed to obtain with some of the solutions.

The data in fig. 184 show that the relaxations $\hat{\eta}_\kappa(t)$ and $\hat{M}_\kappa(t)$ occur more rapidly with increasing κ, behavior also observed with flexible chain polymers. Moreover, the functions $\hat{\eta}_\kappa(t)/\eta_\kappa$ and $\hat{M}_\kappa(t)/M_\kappa$ can both be represented empirically in terms of a reduced time t/β_κ such that

$$\hat{\eta}_\kappa(t/\tau_c)/\eta_\kappa \sim \hat{\eta}_0(t/\beta_\kappa)/\eta_0 \qquad (2.25)$$

$$\hat{M}_\kappa(t/\tau_c)/M_\kappa \sim \hat{M}_0(t/\beta_\kappa)/M_0 \qquad (2.26)$$

According to Eqns. 2.25 and 2.26, bilogarithmic plots of $\hat{\eta}_\kappa(t)/\eta_\kappa$ and $\hat{M}_\kappa(t)/M_\kappa$ versus t/τ_c can each be superposed by 'shifts' along the log t/τ_c axis that give log β_κ/τ_c. For the data in figs. 184-185, $\beta_\kappa/\tau_c \sim (\tau_\kappa/\tau_c)^\nu$ with $\nu = 0.77$, where $\tau_\kappa = \eta_\kappa R_\kappa$.

In terms of the single-integral equation discussed above,

$$\hat{\eta}_\kappa(t) = \sum \eta_i (1 - q_{\kappa,i}) \exp - t/\tau_i \tag{2.27}$$

$$\eta_\kappa^2 \hat{N}_\kappa^{(1)}(t) = \sum \eta_i \tau_i (1 - q_{\kappa,i} p_{\kappa,i}) \exp - t/\tau_i \tag{2.28}$$

Thus, if

$$\hat{M}_\kappa(t) \sim 2 \, \mathbb{C}' \, \hat{N}_\kappa^{(1)}(t) \tag{2.29}$$

then both the stress and birefringence relaxation can be predicted with the single integral equation given data on η_i, τ_i and the nonlinear parameters γ' and γ''. Although it is not apparent in their form, numerical calculations with Eqns. 2.27 and 2.28 show that Eqn. 2.25 and 2.26 are approximately obey, with $\beta_\kappa \sim \tau_\kappa$ for the τ_i-distributions obtained here. By comparison, with the empirical behavior β_κ is a little larger for a given τ_κ. Nevertheless, the similarity between the experimental result and that observed with Eqns. 2.27 - 2.29 is satisfactory, given the limited accuracy of the η_i, τ_i set and the approximate nature of the single-integral constitutive equation obtained with Eqn. 2.19. It does not seem feasible to extract analytical approximations such as Eqns. 2.25 and 4.13 from Eqns. 2.27 - 2.29 given the approximate nature of the numerical comparisons. Nevertheless, with Eqns. 2.27 - 2.29, the enhanced relaxation rates with increased κ are attributed to the successive suppression of terms with long τ_i as κ increases, with the result that the remaining terms with shorter τ_i exhibit more rapid relaxation. For example, $q_{\kappa,i}$ is approximately given[3] by the relation

$$1 - q_{\kappa,i} \sim (1 + |\beta \kappa \tau_i|^\epsilon)^{-2/\epsilon} \tag{2.30}$$

where ϵ depends weakly on a(e.g., $\epsilon \sim f^2$). With this approximation, use of Eqn. 2.27 gives the result

$$\frac{\partial}{\partial \kappa} \frac{\partial \hat{\eta}_\kappa(t)}{\partial t} \sim \beta \Sigma \, \eta_i \frac{(\beta \kappa \tau_i)^{\epsilon - 1}}{[1 + |\beta \kappa \tau_i|^\epsilon]^{(2+\epsilon)/\epsilon}} \exp - t/\tau_i \qquad (2.31)$$

which is positive for all t and κ. In effect, with Eqns. 2.25 and 2.26, τ_κ is an approximate measure of the <u>effective</u> relaxation time following steady state flow at shear rate κ. With Eqn. 2.22,

$$\tau_\kappa = \frac{\Sigma \eta_i \tau_i (1 - q_{\kappa,i} \exp - \tau_\kappa/\tau_i)}{\Sigma \eta_i} \qquad (2.32)$$

so that τ_κ decreases with increasing κ.

The empirical behavior given by Eqns. 2.25 and 2.26 suggests that a set of pseudo-relaxation times and weights computed from pseudo-retardation times and weights obtained from $R_\sigma(t)$ for $\sigma = \eta_\kappa \kappa$ might be used to estimate $\hat{\eta}_\kappa(t)$ and $N_\kappa^{(1)}(t)$.

2.4.3 Molecular Aspects

The threshold volume fraction ϕ_c or concentration c_c for incipient separation of the ordered phase from the isotropic solution is expected to depend on chain length L and diameter d according to a relation of the forms[19-22]

$$\phi_c = (6A/L_w) k_D f(L/d) \qquad (2.33a)$$

$$c_c [\eta] \frac{\ln L_\eta/d}{L_\eta/d} = A(M_z/M_w)^{1/2} k_D f(L/d) \qquad (2.33b)$$

289

where k_D is a polydispersity factor, equal to unity for a monodispersed polymer, $f(L/d) \sim 1$ for large L/d, A is a constant and $L_\eta \sim (L_z L_w)^{1/2}$. In expressing Eqn. 2.33b, use is made of the relation[23]

$$M_L[\eta] = \pi N_A L_\eta^2 / 24 \ln(L_\eta/d) \qquad (2.34)$$

and c_c is calculated from the threshold volume fraction ϕ_c as $c_c = \bar{v}_2 \phi_c$ where the partial specific volume $\bar{v}_2$ is equal to $\pi N_A d^2/4 M_L$; data in reference 10 give $d \sim 0.5$ nm for PBT. For monodispersed polymers, theories of Onsager[19] and Flory[20] give A equal to 5/9 and 4/3, respectively. Calculations have been given for chains with a most probable[21] and a gaussian distribution[22] of L, with results, respectively, that can be represented by the expressions (for large L/d), $A(M_z/M_w)^{1/2} k_D \sim 6^{-1/2}$ and $A k_D \sim (4/3)(M_w/M_n)^{1/3}$. The experimental estimates of c_c may be higher than values given by Eqn. 2.33 owing to the limitations inherent in observing the onset of a birefringent phase. Experimental values of $c_c[\eta](d/L_\eta)\ln(L_\eta/d)$ obtained here (for T = 313K), calculated with $d = 0.5$ nm, range from 0.9 to 1.1. Thus, the experimental values of c_c seem to be in a range predicted by theory given the molecular weight distribution that obtains[24] with PBT and related polymers.

The correlation of the data for η_0 (c,L) with Eqn. 2.18 appears to be satisfactory. Equation 2.18 was obtained by Doi[25,26] using a model based on severe restrictions to rotational molecular motion owing to interchain (hard-core repulsive) interactions. The near correspondence of w*/B with w_c is in accord with this model. The experimental estimate of $K \sim 1.5 \times 10^{-4}$ is far smaller than the original estimate $K \sim 1$ of Doi, but is in better accord with a numerical estimate of the rotational diffusion of a rod moving in a milieu of randomly distributed rods.[27] The considerable variation of $[\eta]$, η_0 and w_c between PBT 72 and 72R is attributed to interchain

aggregation of the latter. Nevertheless, the dependence of the reduced parameter $\eta_0/M_\eta[\eta]$ on $cL_\eta/w^* \sim cL_\eta/w_c$ is found to be similar for the two polymers, indicating an approximate compensation for the effects of the aggregation on η_0 and w_c obtaining with PBT 72R.

The experimental values of $R_0 cRT/M_\eta$ are far larger than the value $R_0 cRT/M = 5/3$ given by the Doi and Edwards,[26] possibly owing to the effects of molecular weight distribution. The data on R_0 exhibit a previously reported effect:[13] R_0 decreases with increasing w for $w/w_c < 0.7$, then increases with increasing w. This behavior is predicted by a calculation of Marucci[28]; this treatment predicts that $R_0(t) \sim R_0$, which is not the behavior found here.

For small c, it is expected that[1,29]

$$\lim_{c=0} \mathbb{C} = \underline{\underline{\delta}}(\partial n/\partial c)M/RT \qquad (2.35)$$

where $\underline{\underline{\delta}}$ is the molecular anisotropy. For PBT in methane sulfonic acid $\underline{\underline{\delta}} \sim 0.6$ and the refractive index increment $\partial n/\partial c \sim 0.55$ mLg^{-1}.[10] Consequently, with Eqn. 2.17 for small c, $M_0 R_0^{-1} \sim 6.9$ MPa^{-1} if M_η is used, in comparison with the experimental value of ca. 3 MPa^{-1}.

A constitutive equation obtained by Doi and Edwards[26] for isotropic solutions of rodlike chains based on a mechanistic model similar to that leading to Eqn. 2.18 leads to a particularly simple result for $G_0(t)$: one relaxation time (e.g., $\eta_1 = \eta_0$ and $\tau_i = \tau_c$). The considerable disparity between this prediction and the behavior observed here may reflect the effects of molecular weight distribution. Alternatively, relaxation modes not included in the theoretical treatment may also contribute to $G_0(t)$. Possibilities for the latter may include the motions contributing to smaller K in Eqn. 2.18 than the theoretical expectation, or fluctuation in the local density of interchain interactions related to fluctuation in the local concentration.

The mechanistic treatment of Doi and Edwards leads to single-integral constitutive equation of the type employed here, with the exponential $G_0(t)$ and with $F(|\gamma|)$ that is fitted to within 10% by $(1 + \gamma^2/5)^{-1}$. For the calculations of interest here, Eqn. 2.20 provides a satisfactory fit to the theoretical estimate,[3] provided $\gamma' = 0.6$ and $\gamma'' = 2.13$ (e.g., $\beta^{-1} = 2.38$). Consequently, Eqns. 2.21 and 2.23 provide close representation of the expressions that would be obtained with the theoretical single-integral constitutive equation if the latter is generalized to use the empirical η_i, τ_i set and the experimental values of γ' and γ''. As shown in figs. 176-180, the functions η_κ/η_0, R_κ/R_0 and $M_\kappa/M_0 \sim N_\kappa^{(1)}/R_0$ computed with a single relaxation time and $\beta^{-1} = 2.38$ do not correspond to experiment. The theoretical constitutive equation discussed above employs the so-called "independent alignment approximation". For rodlike molecules, the results obtained with and without the use of this approximation are numerically quite similar for the functions of interest here.[30]

As with moderately concentrated solutions of flexible-chain polymers,[3] the observed $\gamma' \sim \gamma''$ exceed 0.6, and are proportional to c^{-1}, whereas the observed $\gamma'' \sim \gamma^+$ is not too far from 2.13, and does not depend on c. With flexible chain polymers it was suggested that the discrepancy between γ' and 0.6 might be attributed to a looseness in the pseudo-entanglement network caused by the finite chain length of the polymers studied (e.g., $cM/\rho M_c \sim 10$, where M_c is the critical chain length for which $\partial\ln\eta_0/\partial\ln cM$ changes from 1 to 3.4). A similar effect may be operative here such that γ' would approach 0.6 only if the rodlike chains were very long. In the latter case, however, with rodlike chains, an ordered state would develop, negating the comparisons being made here. Thus, with rodlike chains, the "universal" behavior may be unattainable.

Whereas molecular weight distribution may be a principal source of the distribution of τ_i noted above for the samples studied here. Contributions to the distribution could also arise from the postulated looseness of the network constraints to which

values of γ' larger than 0.6 are attributed. Thus, D_R, from which the relaxation time of the mechanistic model arises, is closely linked with the translational motion of a rodlike chain along its axis. Fluctuations in the distance over which this translation must occur might contribute to a distribution of τ_i, and such fluctuations could be enhanced if the chains are short, similar to the effect postulated for γ'.

As should be expected, the relaxations $\hat{\eta}_\kappa(t)$ and $\hat{N}_\kappa^{(1)}(t)$ are both much faster with the theoretical one-relaxation time model than is observed experimentally. With the theoretical model, $N_\kappa^{(1)}(t/\tau_c)/N_\kappa^{(1)}$ is independent of κ, whereas experimentally $N_\kappa^{(1)}(t/\beta_\kappa)/N_\kappa^{(1)}$ is essentially independent of κ, with $\beta_\kappa \sim \tau_\kappa \leq \tau_c$. In effect, τ_κ is a measure of the relaxation time for the deformed sample. With τ_κ given by Eqn. 2.32 and use of the approximation $1 - q_{\kappa,i} \approx \exp - 2/5 \, \beta\kappa\tau_i$, one obtains

$$\tau_\kappa/\tau_c \approx 1 - \hat{N}_0^{(1)}(\tau_\kappa + 2(5\beta\kappa)^{-1})/R_0 \tag{2.36}$$

where $\hat{N}_0^{(1)}(t)$ is given by the limit of Eqn. 2.28 for small κ. As κ is increased, τ_κ decreases owing to successive suppression of contributions from the largest τ_i.

Acknowledgement

Appendix

The functions $q_{\kappa,i}$, $r_{\kappa,i}$, and $p_{\kappa,i}$ in Eqns. 2.21- 2.23 are given by[3]

$$q_{\kappa,i} = (1 + af_i - f_i^2)\exp - g_i \tag{A1}$$

$$r_{\kappa,i} = \exp - R_\kappa \eta_\kappa /\tau_i \tag{A2}$$

$$p_{\kappa,i} = 1 - \frac{1 - f_i}{2} \; \frac{(f_i + g_i)^2 + f_i^2}{1 + af_i - f_i^2} \tag{A3}$$

where $f_i^{-1} = 1 + \tau_i \kappa /''$, $g_i = a\gamma''/\tau_i \kappa$ and $a = \gamma'/\gamma''$. For $a = 0$,[3,31].

$$(1 - q_{\kappa,i}) = (1 + \tau_i \kappa /\gamma'')^{-2} \tag{A4}$$

$$(1 - q_{\kappa,i}\, p_{\kappa,i}) = (1 + \tau_i \kappa /\gamma'')^{-3} \tag{A5}$$

References

1. S.-G. Chu, S. Venkatraman, G. C. Berry, and Y. Einaga, *Macromolecules* **1981,** *14,* No. 4, 939.

2. G. C. Berry, B. L. Hager, and C.-P. Wong, *Macromolecules* **1977,** *10,* 361.

3. K. Nakamura, G. C. Berry, and C.-P. Wong, *J. Polym. Sci., Polymer Phys.* in press

4. H. Markovitz and G. C. Berry, *Ind. Eng. Chem. Prod. Res. Div.* **1978,** *17(2),* 95.

5. H. Markovitz, in *"Am. Inst. Phys. 50th Anniversary Physics Vade Mecum",* Ed., H. L. Anderson, Am. Inst. Phys., New York, 1981, Chapter 19.

6. J. D. Ferry, *Viscoelastic Properties of Polymers,* Wiley, New York, NY, 3rd Ed., 1980.

7. R. Sips, *J. Polym. Sci.* **1951,** *7* 191.

8. H. Janeschitz-Kriegl, *Adv. Polym. Sci.* **1969,** *6,* 170.

9. B. D. Coleman, E. H. Dill, and R. A. Toupin, *Arch. Ration. Mech. Anal.* **1970,** *39,* 358.

10. C. C. Lee, S.-G. Chu, and G. C. Berry, *J. Polym. Sci., Polym. Phys. Ed.* **1983,** *21,* 1573.

11. C.-P. Wong and G. C. Berry, *Polymer* **1979,** *20,* 229.

12. G. C. Berry and C.-P. Wong, *J. Polym. Sci., Polym. Phys. Ed.* **1975,** *13,* 1761.

13. G. C. Berry, P. Metzger, D. B. Cotts, and S.-G. Chu, *British Polym. J.* **1980,** *16,* 947.

14. E. V. Menezes and W. W. Graessley, *Rheol. Acta* **1980,** *19,* 38.

15. K. Osaki, N. Bessho, T. Kojimoto, and M. Kurata, *J. Rheology* **1979,** *23,* 457.

16. A. V. Tobolsky,, *Properties and Structure of Polymers,* Wiley, New York, 1960, p. 188.

17. W. W. Graessley, *Adv. Polym. Sci.* **1974,** *20,* 229.

18. B. Bernstein, E. A. Kearsley, and L. J. Zapas, *Trans. Soc. Rheol.* **1963,** *7,* 391.

19. L. Onsager, *Am. N.Y. Acad. Sci.* **1949,** *51,* 627.

20. P. J. Flory, *J. Proc. R. Soc. London, Ser. A* **1956,** *234,* 73.

21. P. J. Flory and R. S. Frost, *Macromolecules* **1978**, *11*, 1126.

22. J. K. Moscicki and G. Williams, *Polymer* **1982**, *23*, 588.

23. H. Yamakawa, *Modern Theory of Polymer Solutions*, Harper and Row, New York **1971**, p. 180.

24. G. C. Berry and D. B. Cotts, *Macromolecules* **1981**, *14*, 930.

25. M. Doi, *J. Phys. (Paris)* **1975**, *36*, 607.

26. M. Doi and S. F. Edwards, *J. Chem. Soc., Faraday Trans. 2* **1978**, *74*, 560.

27. A. Keller and J. A. Odell, to be published.

28. C. Marrucci, *Polymer Preprints, Am. Chem. Soc.* **1982**, *23*(2), 4.

29. V. N. Tsvetkow, et al. "Structure of Macromolecules in Solution" (English Translation); National Lending Library for Science and Technology: Boston Spa, England, 1971; Vol. 3, Chapter 7.

30. N. Y. Kuzuu and M. Doi, *Polymer J.* **1980**, *12*, 883.

31. H. M. Laun, *Rheol. Acta* **1978**, *17*, 1.

Table 23 Polymer Solutions Used in This Study

Polymer	$[\eta]/mLg^{-1}$	L_{η}/nm[a]	Range w/gkg^{-1}	Range T/K
PBT 72	1770	135	25.4-29.4	297-331
PBT 72R	1100	100	29.6	296-331
PBT 53	1400	118	1.49-32.3	283-333
PBT 43	900	95	29.4-31.5	288-297

a) $L_{\eta} = M_{\eta}/M_{L}$, where $M_{L} = 220$ dalton nm^{-1} and $L_{\eta} = [\eta]/K_{\eta})^{1.8}$
with $K_{\eta} = 0.26$ mLg^{-1}.[10]

Table 24 Rheological Parameters for Solutions of Rodlike Polymers

Polymer	w/gkg^{-1}	T/K	$\eta_0 A^{-1}/kPa\cdot s$ [a]	$R_0 cRT/M_\eta$ [b]
72	25.4	328	3.94	83
	25.4	312	3.67	86
	25.4	297	3.77	85
	29.4	331	27.5	55
	29.4	312	31.3	61
72R	29.6	331	1.71	(28/37)
	29.6	312	1.99	(31/41)
	29.6	296	2.42	33/44
53	25.5	333	1.89	(60)
	25.5	313	1.83	(60)
	25.5	303	1.73	(62)
	25.5	296	2.10	64
	25.5	286	1.89	69
	28.0	333	6.81	57
	28.0	311	6.30	58
	28.0	293	5.81	(58)
	29.4	313	7.15	70
	29.4	296	7.64	78
	29.4	285	6.80	107
	317	333	13.2	85
	31.7	313	20.7	82
	32.3[c]	283	5.59	130
	32.3	294	4.54	112
	32.3	316	5.24	97
	32.3	333	4.83	102
43[d]	29.4	297	0.098	11.8
	29.4	288	0.093	14.0
	31.5	296	0.11	15.3
	31.5	291	0.12	17.2
	31.5	288	0.12	18.1

(a) $A = \exp E(T_r^{-1} - T^{-1})$ with $E = 4065K$ and $T_r = 297K$.

(b) R_0 in parenthesis calculated as τ_c/η_0 with τ_c determined from fit of η_κ/η_0 versus κ with curves of η_κ/η_0 versus $\tau_c\kappa$.

(c) Nematic solutions for $T \leq 292K$.

(d) R_0 determined as $\lim_{\omega=0} J'(\omega)$.

Table 25 Rheological and Rheooptical Parameter Solutions of Rodlike Polymer (PBT-53)

w/gkg^{-1}	T/K	$\eta_0/\text{Pa·s}$	$R_0 cRT/M^a$	$M_0 R_0^{-1}/\text{MPa}^{-1}$ [b]
1.49	297	0.145	14.6	3.03
2.10	297	0.340	13.6	2.72
2.80	297	0.580	15.0	3.02
3.50	297	0.780	14.8	--

(a) R_0 determined as $\lim_{\tau_c \omega = 0} J'(\omega)$.

(b) $M_0 R_0^{-1}$ was calculated as $\Delta n^{(12)}/\eta_\kappa \kappa$

for small κ.

Table 26   Retardation and Relaxation Spectra

λ_i/τ_c [a]	R_i/R_0	τ_i/τ_c	η_i/η_0
PBT-53; w = 29.4 gkg^{-1}			
2.580	0.580	3.251	0.231
0.210	0.280	0.494	0.480
0.0175	0.130	0.0615	0.092
		0.0010	0.092
PBT-53; w = 25.5 gkg^{-1}			
5.248	0.430	5.732	0.094
1.022	0.290	1.354	0.258
0.240	0.174	0.381	0.253
0.080_5	0.035	0.098_8	0.084
		0.025_2	0.312

(a) $\tau_c cRT/M_n$ is 134 and 596 for c/gkg^{-1} equal to 255 and 596, respectively.

Table 27 Critical Concentrations for Solutions of Rodlike Polymers

Polymer	T/K	w_c/gkg^{-1} [a]	w^*B^{-1}/gkg^{-1} [b]	Bw_c/w^*
PBT-72	296	29.7	27.5	1.08
	313	32.2	28.9	1.11
	333	34.9	30.4	1.15
PBT-72R	296	--	36.5	
	313	--	38.3	
	333	--	40.3	
PBT-53	296	29.9	31.5	0.95
	313	31.7	32.9	0.96
	333	34.9	34.9	1.00
PBT-43	296	32.2	38.8	0.83
	313	34.9	40.7	0.86
	333	37.9	42.9	0.88

(a) The concentration for formation of the ordered phases interpolated using the relation $w_c = k \exp - 433/T$, with k equal to 128.4, 128.8 and 139.2 for PBT 72, 53, and 43, respectively.

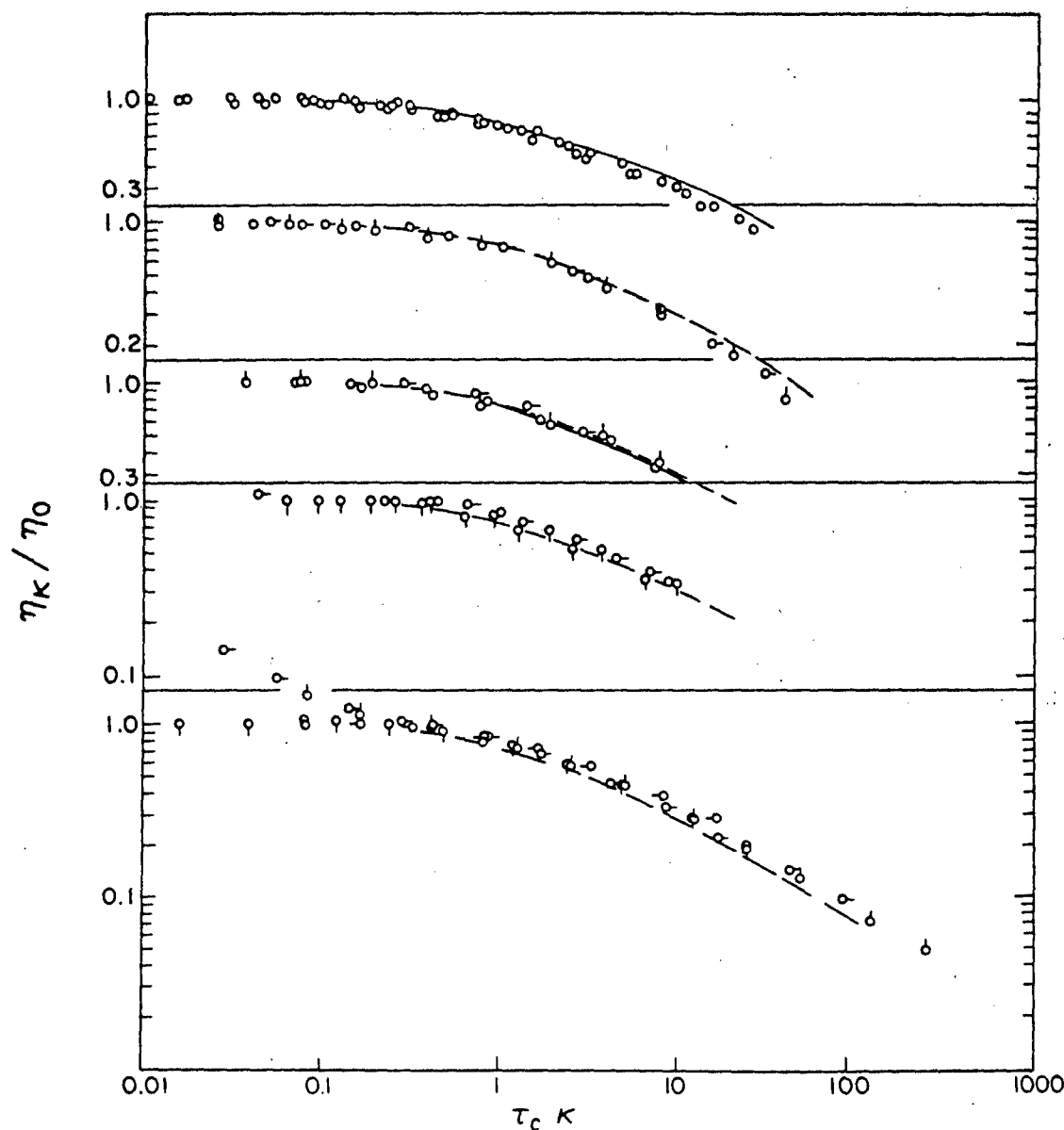(b) Obtained by a fit of Eqn. 4.5 with data on η_0, as described in the text.

Figure 176: The reduced steady-state viscosity η_κ/η_0 versus the reduced shear rate $\tau_c\kappa$ for solutions of PBT-53 in methane sulfonic acid. From top to bottom:25.5 gkg^{-1} (Ó, O-, O, Q, Q for 12.5, 23, 30, 40, 60 C, resp.); 28.0 gkg^{-1} (O-, Ó for 38, 60, resp.); 29.4 gkg^{-1} (O, Ó, O- for 12, 21, 40 C, resp.); 31.7 gkg^{-1} (O-, Q for 40, 60 C, resp.); and 32.3 gkg^{-1} (8, 19, 43, 60 C for Ó, O-, Q, -O, resp).

The solid curves represent Eqn. 2.21 using the η_i and τ_i in table 26. The dashed curves represent the data for the solution with w = 25.5 gkg^{-1} to facilitate comparison of the data at various w.
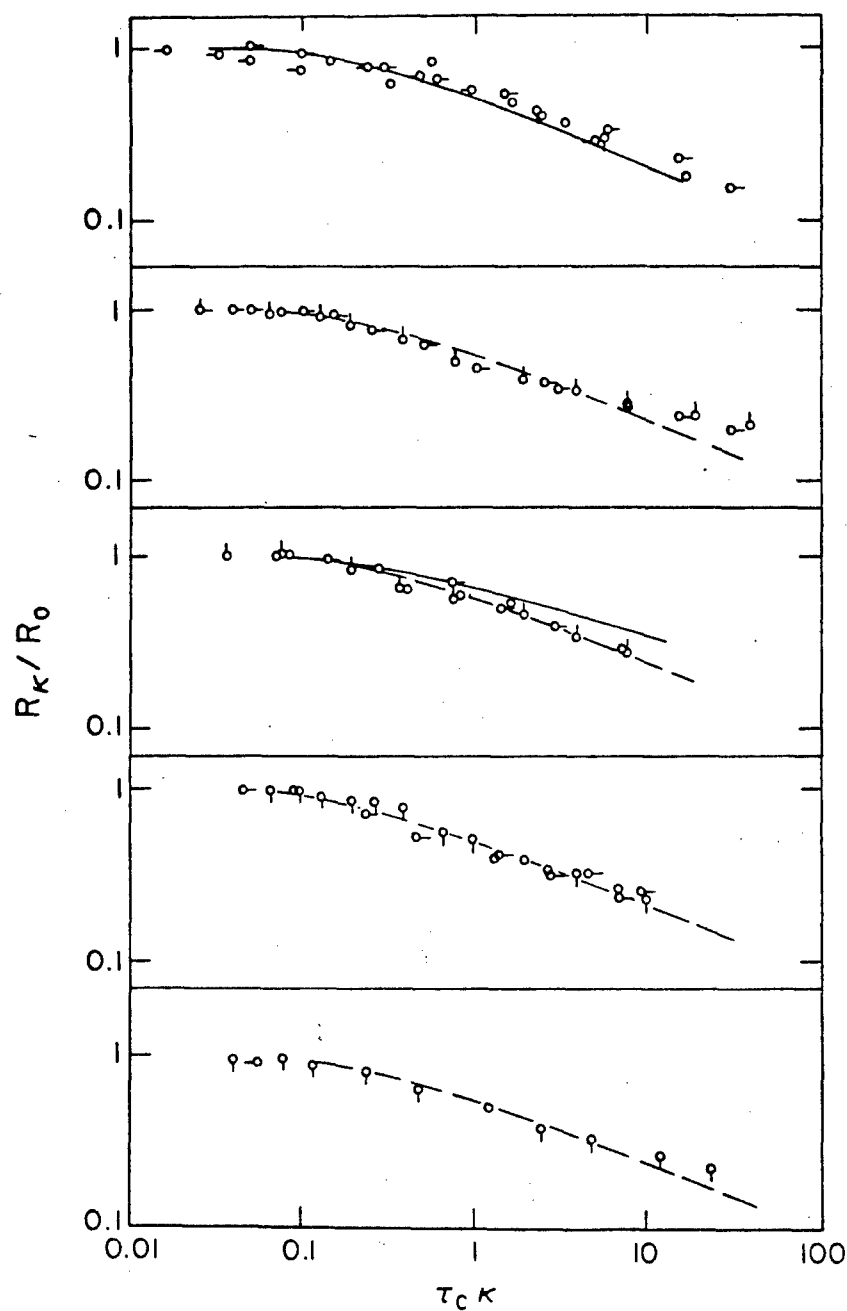
Figure 177: The reduced steady-state recoverable compliance R_κ/R_0 versus the reduced shear rate $\tau_c \kappa$ for the solutions identified in the caption to fig. 176. The solid curves represent Eqn2.22 using the η_i and τ_i in table 26. The dashed curves represent the data for the solution with $c = 25.5$ gkg^{-1} to facilitate comparison of the data at various w.
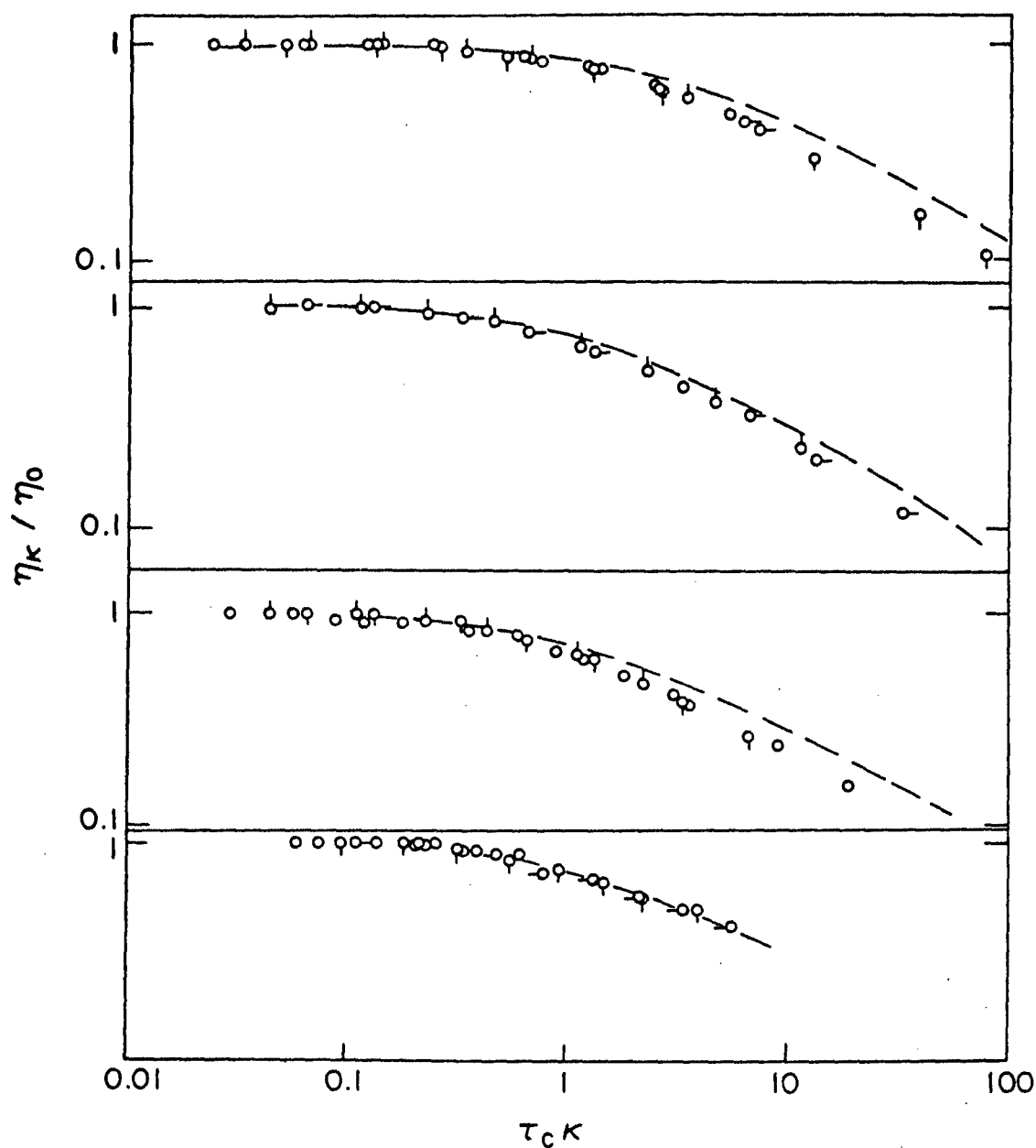
Figure 178: The reduced steady-state viscosity η_κ/η_0 versus the reduced shear rate $\tau_c \kappa$ for solutions of PBT polymers in methane sulfonic acid. From top to bottom: PBT-72, 25.4 gkg^{-1} (φ, O-, $\dot{O}$ for 24, 39, 55 C, resp.); PBT-72, 29.4 gkg^{-1}, (O; $\dot{O}$ for 39, 58 C, resp.); PBT-72-R, 29.6 gkg^{-1} ($\dot{O}$, φ, O for 23, 39, 58 C); PBT-43, 31.5 gkg^{-1} (-O, φ, O-, O for 10, 14.5, 18, 23.5 C, resp.). The dashed curves represent the data for PBT-53, c = 25.5 gkg^{-1}.
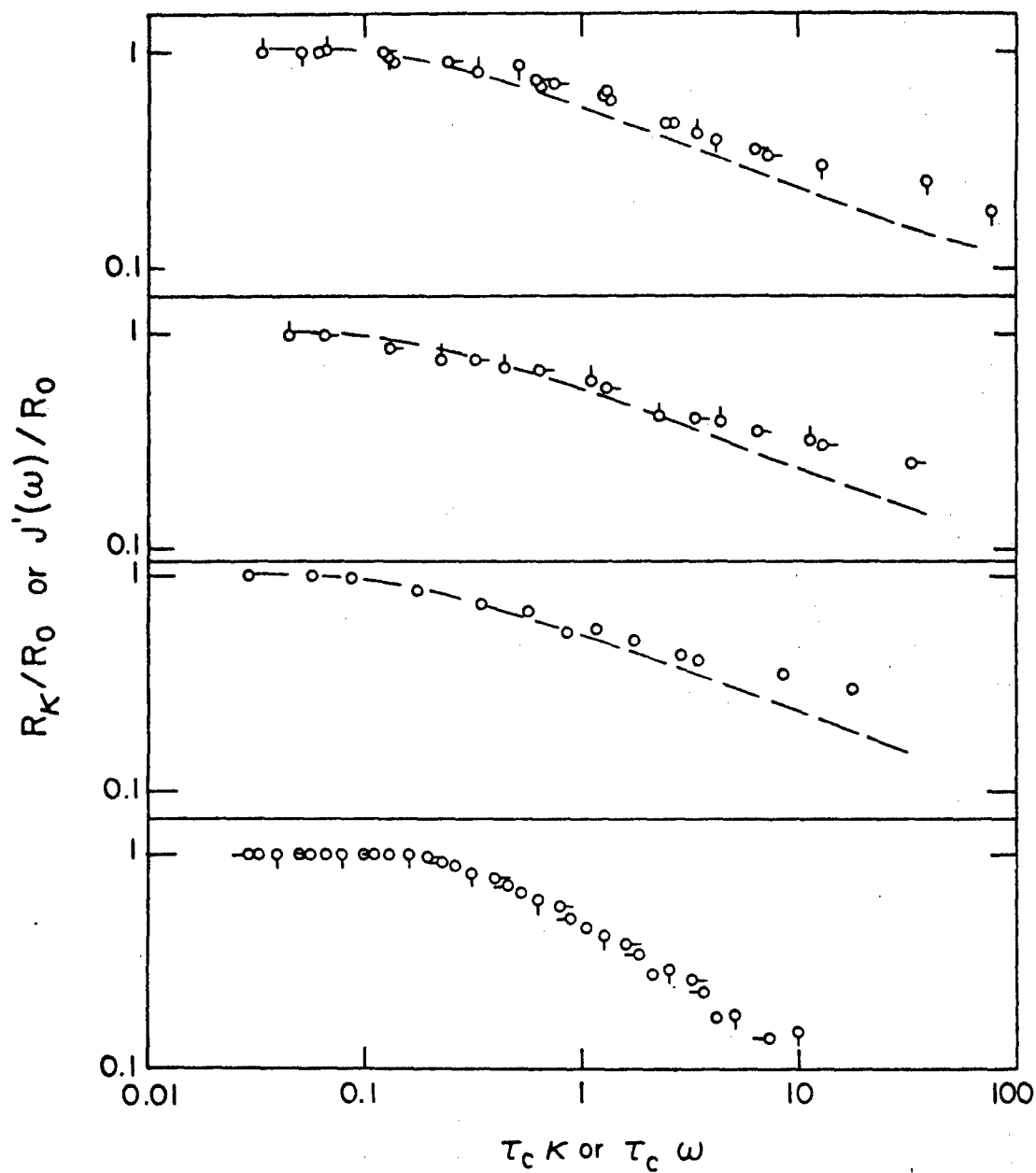
Figure 179: The upper three panels give the reduced steady-state recoverable compliance R_κ/R_0 versus
the reduced shear rate $\tau_c \kappa$; the lowest panel gives the reduced dynamic compliance $J'(\omega)/R_0$ versus the reduced frequency $\tau_c \omega$. The data are for
the solution in the corresponding panels identified in the caption to fig. 178.
The dashed curves represent the data for PBT-53, w = 25.5 gkg^{-1}.

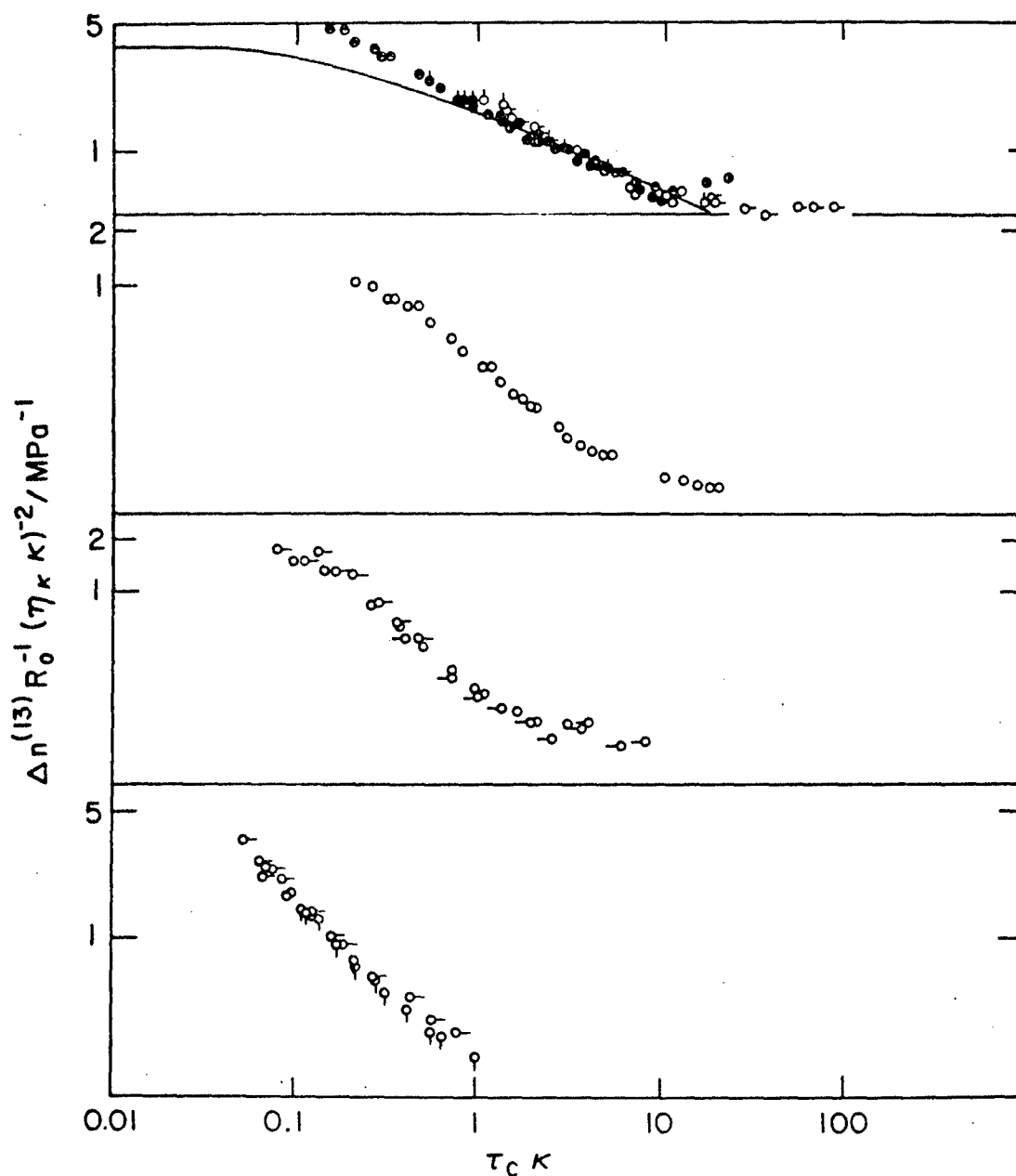**Figure** 180: The flow birefringence function versus the reduced shear rate $\tau_c\kappa$ for solution of PBT in methane sulfonic acid.
From top to bottom: PBT-53, 25.5 gkg^{-1},
(•, ♭ for 23,40 C, resp.), 28.0 gkg^{-1} (•,60 C), 29.4 gkg^{-1} (O, O- for 23,40 c, resp.),
31.7 gkg^{-1} (O, 40 C); PBT-72, 25.4 gkg^{-1} (Q, O- for 39, 55 C, resp.);
PBT-72R, 29.6 gkg^{-1} (-O, O, O- for 23, 39 and 60 C, resp.); and PBT-43
(31.5 gkg^{-1}, Q, O- for 15, 23 C,
resp.). The solid curve represents Eqn. 2.12
with Eqn. 2.28 using the η_i and τ_i in table 26.
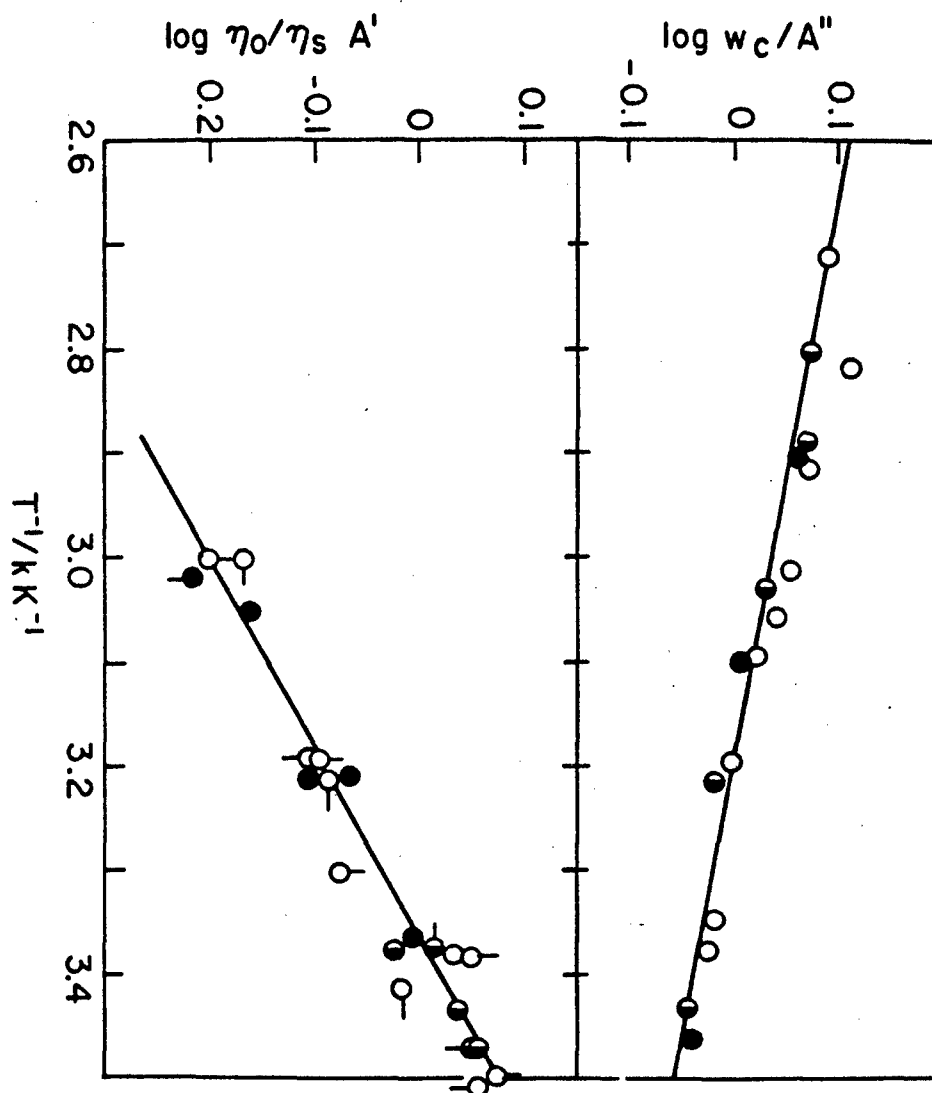
Figure 181: Temperature dependence of the viscosity η_0 relative to that η_s of methane sulfonic acid, and the concentration w_c for the onset of the nematic phase. In the figures, A' and A" are the values of η_0/η_s and w_c, respectively, for T = 313K. The symbols denote PBT-53, O; PBT-72, ● and PBT-43, ◑.
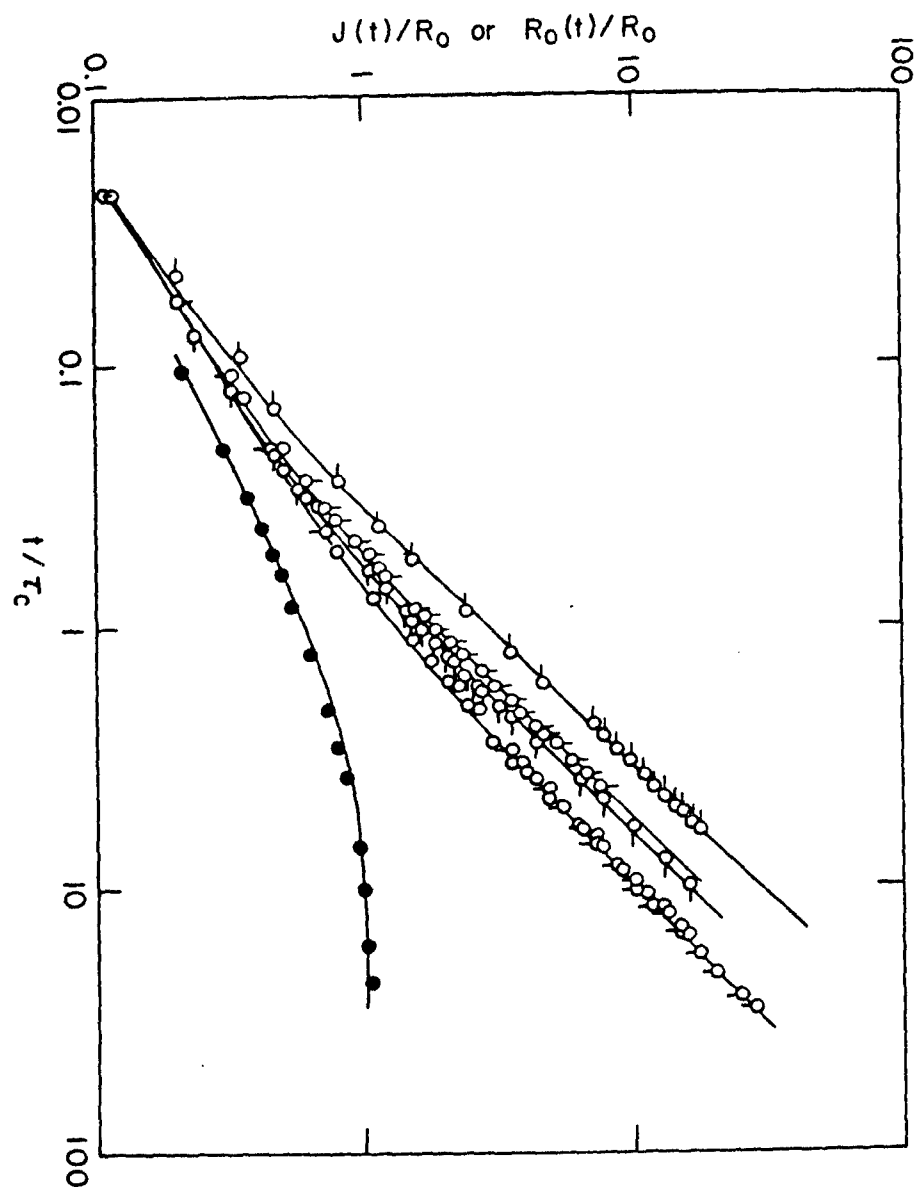
Figure 182: The reduced creep compliance $J_\sigma(t)/R_0$ (open circles) and recoverable compliance $R_0(t)/R_0$ (filled circles) versus the reduced time t/τ_c for a solution of PBT-53 in methane sulfonic acid, w = 25.5 gkg^{-1}. The symbols O($\bullet$), O, O-, O, -O denote stress σ/Pa equal to 2.8, 15.2, 68.3, 78.7 and 145, resp. The data for O($\bullet$) are at 23 C; all others at 13 C.
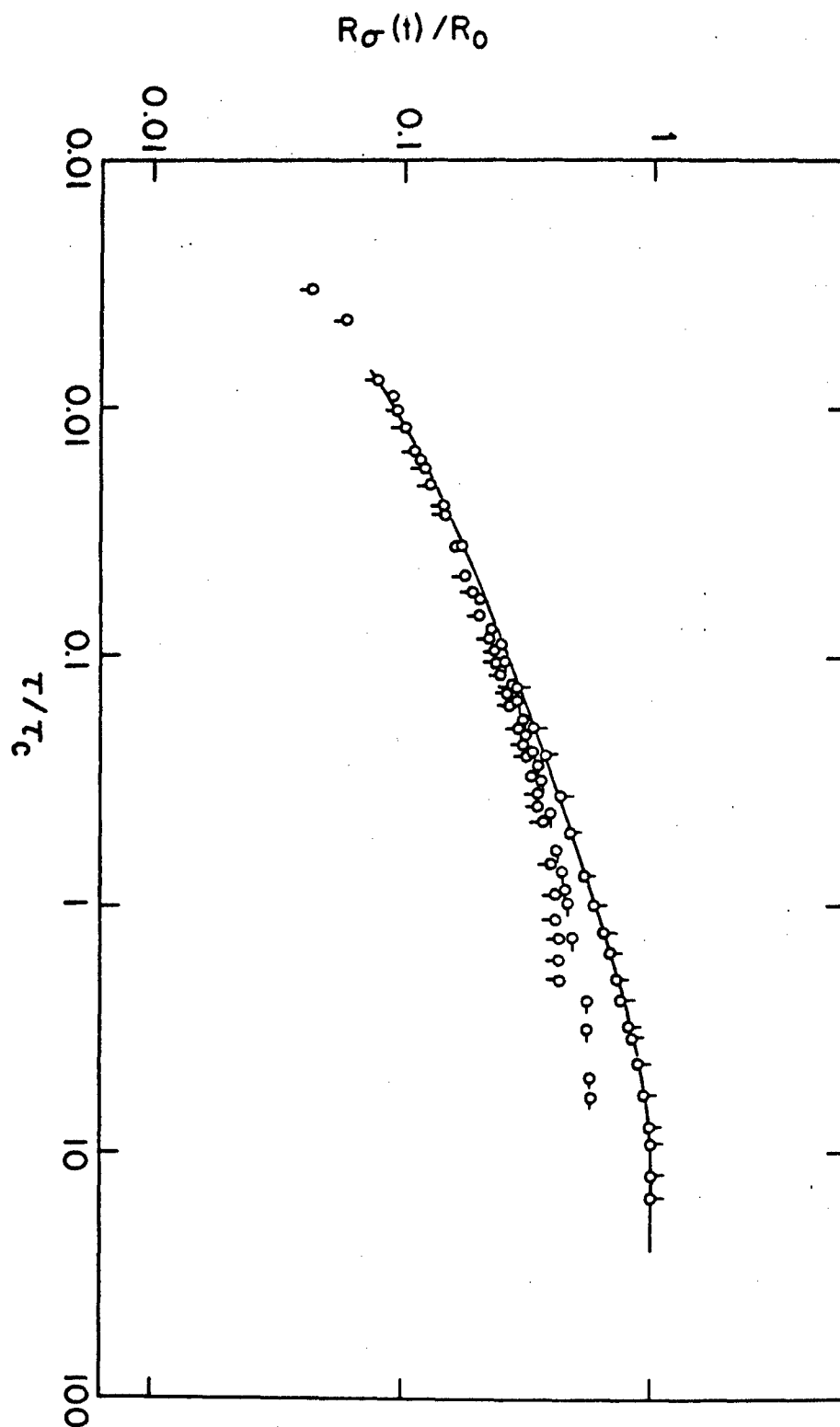
Figure 183: The reduced recoverable compliance function $R_\sigma(t)/R_0$ versus the reduced time t/τ_c for a solution of PBT-53 in methane sulfonic acid, $W = 29.4$ gkg$^{-\alpha}$. The stress σ/Pa is 6.6 (O), 39.3 (O-), and 57.5 (Q) with $T = 40°$, $20°$, and $40°$C, respectively. The curve represents Eqn. 2.14 with the R_i and λ_i given in table 26.
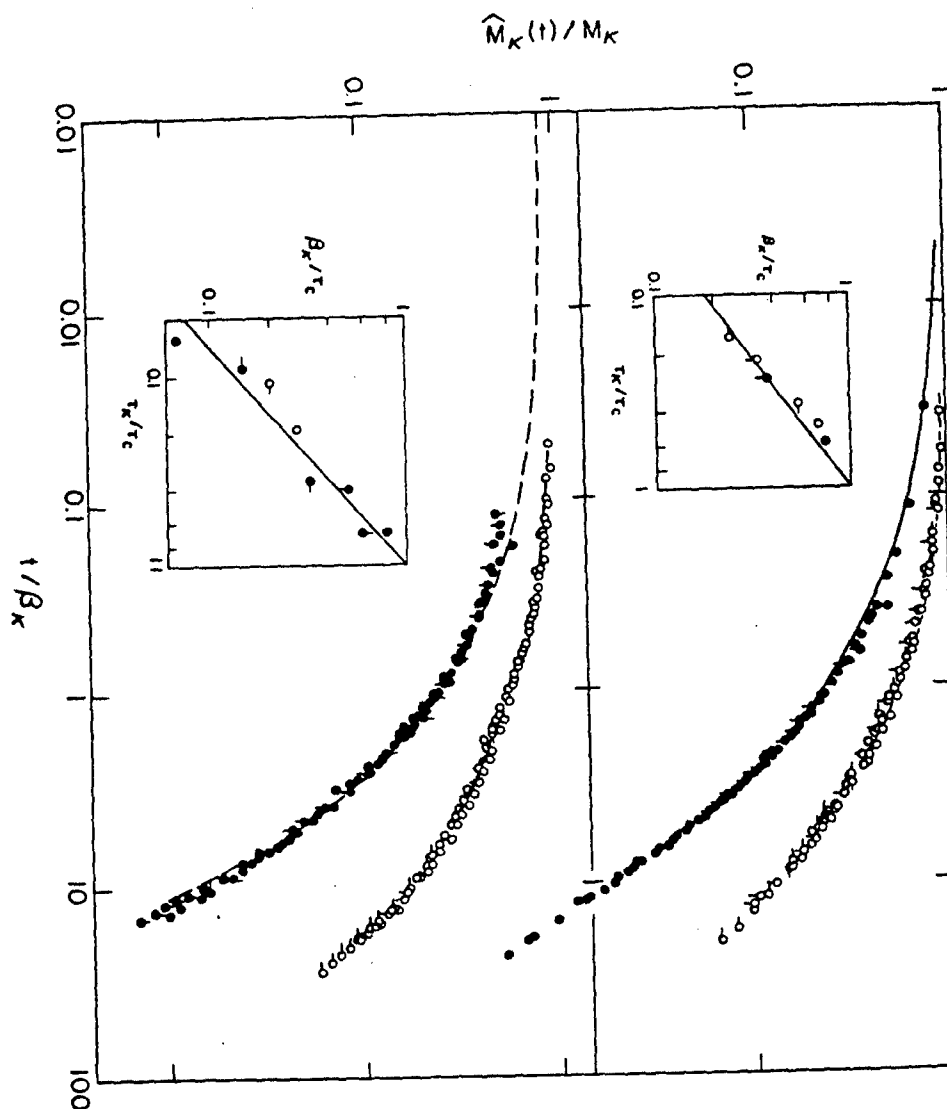
Figure 184: The reduced flow birefringence relaxation function $\hat{M}_\kappa(t)/M_\kappa$ (filled circle) and stress relaxation function $\hat{\eta}_\kappa(t)/\eta_\kappa$ (open circle) for PBT-72, 25.4 gkg^{-1} (top) and PBT-53, 29.4 gkg^{-1} (bottom) in methane sulfonic acid. For PBT-72, κ/s^{-1} is 0.0208 (O), 0.0358 (O-), 0.0726 (Q), 0.100 (-O), 0.0126 (•), 0.0502 (•), all at 39 C. For PBT-53, κ/s^{-1} is 0.0227 (O), 0.0455 (O-), 0.0851 (Q), 0.186 (-O), 0.0050 (•), 0.0126 (•), 0.0502 (-•), all at 21°C, and 0.0050 (•), 0.0252 (•-).
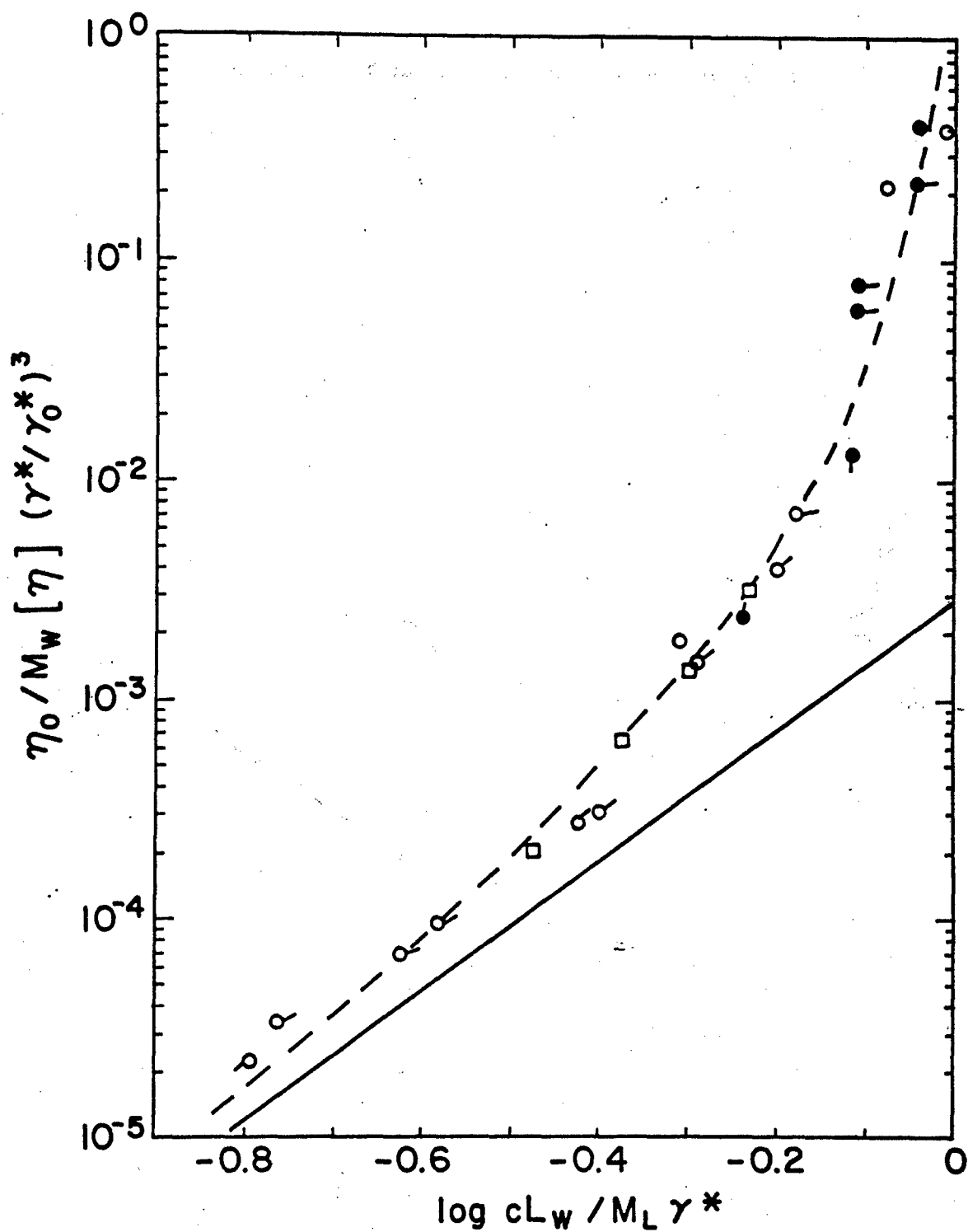
310

Figure 185: The reduced viscosity as a function of concentration c and chain length L. Here γ^* is the value of cL_W/M_L for the maximum in η_0 and γ_0^* is a constant.
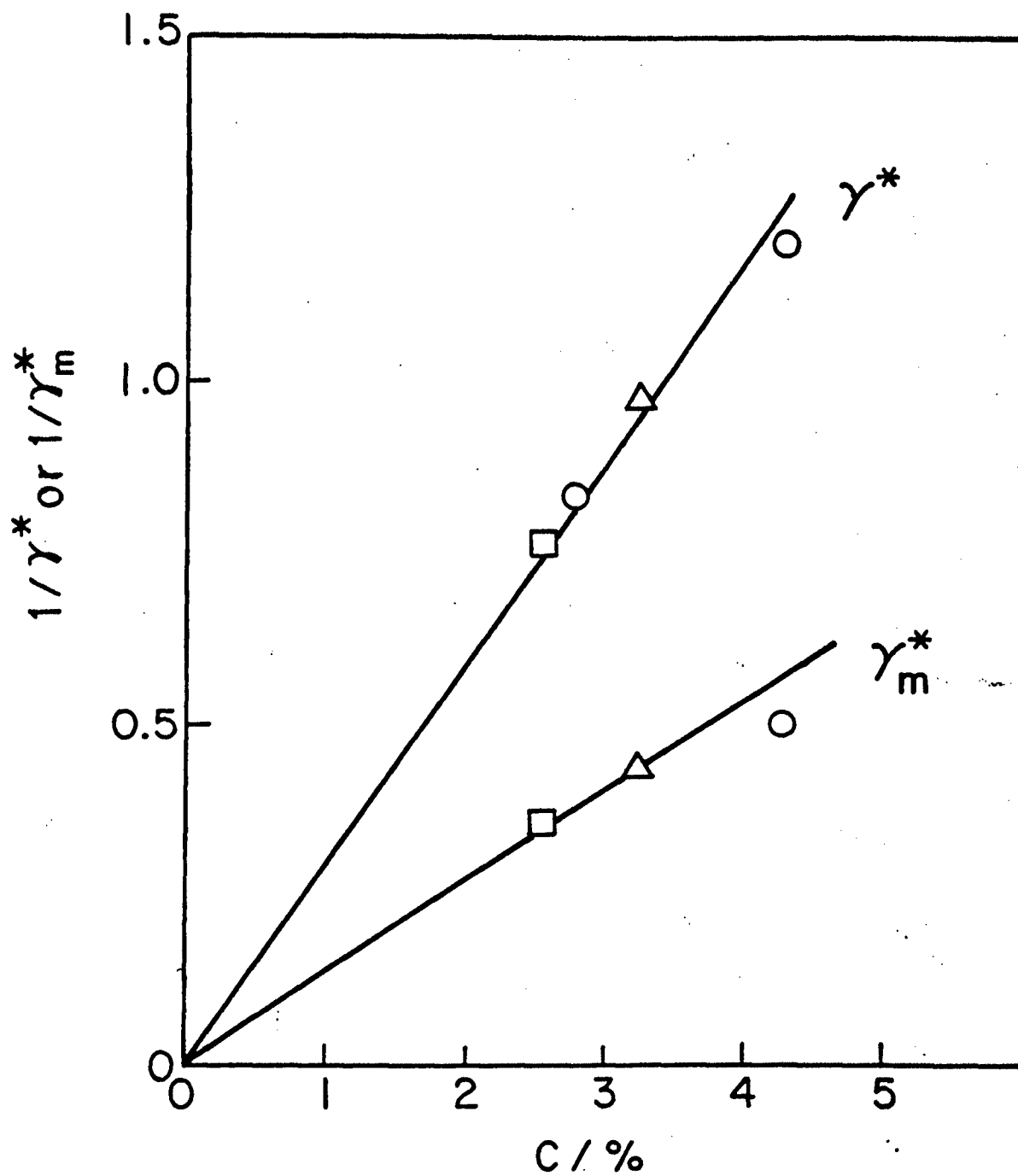
Figure 186: The critical strain γ^* for the onset of nonlinear behavior as a function of concentration in weight percent.

312